

AD-A076 502

MISSOURI UNIV-KANSAS CITY DEPT OF PHYSICS

F/O 20/8

MOLECULAR AND CRYSTALLINE ELECTROMAGNETIC PROPERTIES OF SELECTE--ETC(U)

AUG 79 M R QUERRY

DAA029-76-6-185

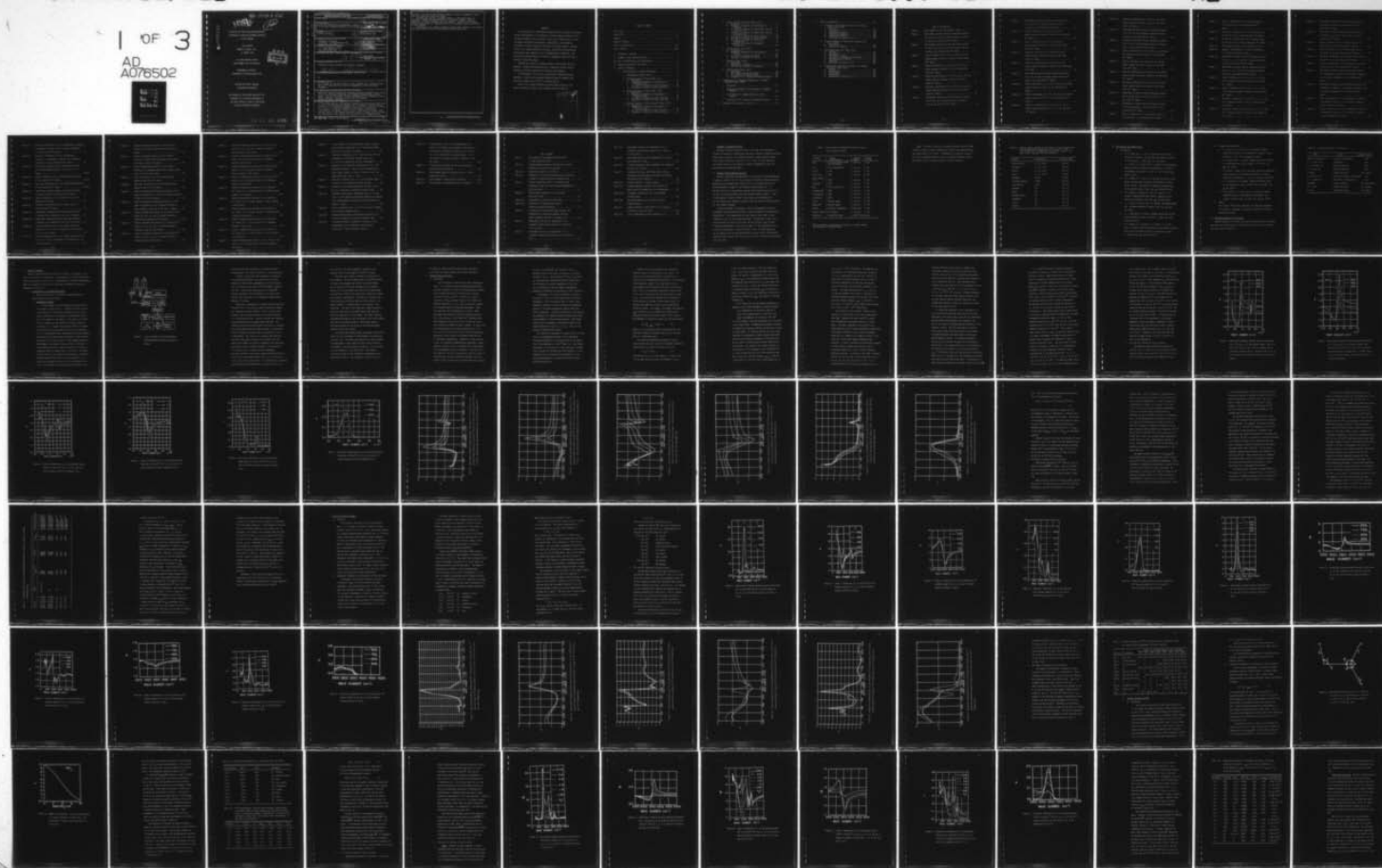
UNCLASSIFIED

ARO-13739.9-05X

NL

1 OF 3

AD  
A076502



AD A 076502

LEVEL 11

ARO 13739.9-GSX

12

MOLECULAR AND CRYSTALLINE ELECTROMAGNETIC  
PROPERTIES OF SELECTED CONDENSED MATERIALS  
IN THE INFRARED

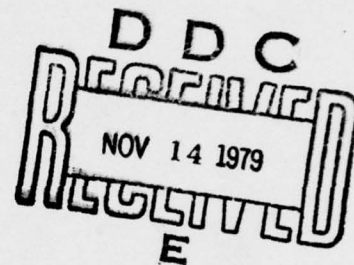
FINAL REPORT

MARVIN R. QUERRY, Ph.D.

30 AUGUST 1979

U.S. ARMY RESEARCH OFFICE

GRANT NUMBER DAAG 29-76-GS-0185



DEPARTMENT OF PHYSICS  
UNIVERSITY OF MISSOURI-KANSAS CITY

APPROVED FOR PUBLIC RELEASE:

DISTRIBUTION UNLIMITED.

THE FINDINGS IN THIS REPORT ARE NOT TO BE  
CONSTRUED AS AN OFFICIAL DEPARTMENT OF  
THE ARMY POSITION, UNLESS SO DESIGNATED  
BY OTHER AUTHORIZED DOCUMENTS.

79 11 13 033

Unclassified

SECURITY CLASSIFICATION OF THIS PAGE (When Data Entered)

REPORT DOCUMENTATION PAGE		READ INSTRUCTIONS BEFORE COMPLETING FORM
1. REPORT NUMBER	2. GOVT ACCESSION NO.	3. RECIPIENT'S CATALOG NUMBER
4. TITLE (and Subtitle)		5. TYPE OF REPORT & PERIOD COVERED
Molecular and Crystalline Electromagnetic Properties of Selected Condensed Materials in the Infrared.		Final Report 1 Apr 1976-30 Jun 1979
7. AUTHOR(s)		6. PERFORMING ORG. REPORT NUMBER
Marvin R. Querry		
9. PERFORMING ORGANIZATION NAME AND ADDRESS		8. CONTRACT OR GRANT NUMBER(s)
Department of Physics University of Missouri-Kansas City Kansas City, Mo. 64110		DAAG29-76-G-185
11. CONTROLLING OFFICE NAME AND ADDRESS		10. PROGRAM ELEMENT, PROJECT, TASK AREA & WORK UNIT NUMBERS
U. S. Army Research Office Post Office Box 12211 Research Triangle Park, NC 27709		R&D Project No. & Title HTL61102BH57-01 Atmospheric & Terrestrial
14. MONITORING AGENCY NAME & ADDRESS (if different from Controlling Office)		12. REPORT DATE
		30 August 1979
		13. NUMBER OF PAGES
15. SECURITY CLASS. (of this report)		15a. DECLASSIFICATION/DOWNGRADING SCHEDULE
Unclassified		NA
16. DISTRIBUTION STATEMENT (of this Report)		
Approved for public release; distribution unlimited.		
17. DISTRIBUTION STATEMENT (of the abstract entered in Block 20, if different from Report)		
NA		
18. SUPPLEMENTARY NOTES		
The findings in this report are not to be construed as an official Department of the Army position, unless so designated by other authorized documents.		
19. KEY WORDS (Continue on reverse side if necessary and identify by block number)		
Refractive Index; Infrared; Zinc chloride solutions, phosphoric Acid, Nitric Acid, Oils, Alcohols, limestone, and polymethyl Methacrylate, natural waters. Optical properties, infrared; Montmorillonite, Colemanite, Kernite, Kaolin, Lampblack, Activated charcoal and wood charcoal, Refractive index of graphite.		
20. ABSTRACT (Continue on reverse side if necessary and identify by block number)		
By using water as a reflectance standard, relative specular reflectance spectra in the infrared were measured for 38 materials including aqueous solutions of zinc chloride, phosphoric acid, and nitric acid, and for diesel fuel, fog oil, tetramethyl-tetraphenyl-trisiloxane, 1-hexadecanol, 1-octadecanol, 1-eicosanol, rutile, lucite, limestone, and natural waters. Spectral values of the complex refractive indices, suitable for Mie scattering computations, were computed and tabulated by use of Kramers-Kronig		

DD FORM 1 JAN 73 1473

EDITION OF 1 NOV 65 IS OBSOLETE

Unclassified  
SECURITY CLASSIFICATION OF THIS PAGE (When Data Entered)

409 501

Lau

analysis. The spectra were further analyzed in terms of fundamental intra- and inter-molecular vibrational modes.

Transmittance spectra of powders pressed in a KBr matrix were also measured. Powders were montmorillonite, colemanite, Kernite, Kaolin, Lampblack, activated charcoal, and wood charcoal. Analysis of the transmittance spectra was not completed but is still underway during continuation of this research

Tabulations of all complex refractive indices were supplied to the Aerosol/Obsecration Science Group at the Aberdeen Proving Ground, Md.

# ABSTRACT

By using water as a reflectance standard, relative specular reflectance spectra were measured for 38 materials including aqueous solutions of zinc chloride, phosphoric acid, and nitric acid, and for diesel fuel, fog oil, tetramethyl-tetraphenyl-trisiloxane, 1-hexadecanol, 1-octadecanol, 1-eicosanol, rutile, plexiglas, limestone, and natural waters. Spectral values of the complex refractive indices, suitable for Mie-scattering computations, were computed by use of Kramers-Kronig techniques. The spectra were further analyzed in terms of fundamental intra- and inter-molecular vibrational modes.

Transmittance spectra of powders pressed in KBr pellets were also measured. Powders were montmorillonite, colemanite, kernite, kaolin, lampblack, activated charcoal, wood charcoal, and aluminum.

An investigation of the optical properties of graphite was also completed. Values for the complex refractive index of graphite were obtained throughout the  $10^{-3}$ - $10^6$  ev spectral region.

Values of all complex refractive indices were supplied to the Aerosol/Obscuration Science Group, Aberdeen Proving Ground, Md.

Accession For	
NTIS GRA&I	<input checked="checked" type="checkbox"/>
DDC TAB	<input type="checkbox"/>
Unannounced	<input type="checkbox"/>
Justification	
By	
Institution/	
Availability Codes	
Dist	Avail and/or special

A

# TABLE OF CONTENTS

Title Page . . . . .	1
Form DD 1473 . . . . .	ii
Abstract . . . . .	iv
Table of Contents. . . . .	v
List of Illustrations. . . . .	viii
List of Tables . . . . .	xviii
I. Statement of Problem. . . . .	1
II. Summary of Most Important Results . . . . .	1
III. List of Publications and Presentations. . . . .	5
IV. Personnel Employed on the Project . . . . .	6
V. Report of Research. . . . .	8
A. Investigations of Infrared Reflectance . . . . .	8
1. Experimental methods (Fig. 1) . . . . .	8
2. Aqueous Solutions of $ZnCl_2$ (Figs. 2-13)	
a. Objectives . . . . .	12
b. Background Information for Discussion of $ZnCl_2$ Solutions. . . . .	13
c. R(v) and N(v) Spectra for $ZnCl_2$ Solutions. . . .	19
d. Discussion of Spectra of $ZnCl_2$ Solutions . . . .	32
3. Aqueous Solutions of $H_3PO_4$ (Figs. 14-30)	
a. Objective. . . . .	39
b. Background Information for Discussion of $H_3PO_4$ Solutions. . . . .	39
c. R(v) and N(v) Spectra for $H_3PO_4$ Solutions. . . .	42
d. Discussion of Spectra for $H_3PO_4$ Solutions. . . .	60
4. Aqueous Solutions of $HNO_3$ Solutions (Figs. 31-38)	
a. Objectives . . . . .	61
b. Background Information for Discussion of $HNO_3$ Solutions. . . . .	62
c. R(v) and N(v) Spectra for $HNO_3$ Solutions . . . .	67
d. Discussion of Spectra for $HNO_3$ Solutions . . . .	68

5.	Organic Liquids and Solids (Figs. 39-53)	
a.	Objectives . . . . .	80
b.	Background Information for Discussion of Organics. . . . .	81
c.	R( $\nu$ ) and N( $\nu$ ) Spectra for Diesel Fuel, Fog Oil, and DC-704 Oil. . . . .	84
d.	Discussion of Spectra for Diesel Fuel, Fog Oil, and DC-704 Oil. . . . .	84
e.	R( $\nu$ ) and N( $\nu$ ) Spectra for Solid Alcohols . . . . .	99
f.	Discussion of Spectra for Solid Alcohols . . . . .	99
g.	R( $\nu$ ) and N( $\nu$ ) Spectra for Polymethyl- methacrylate. . . . .	100
h.	Discussion of Spectra for Polymethyl- methacrylate. . . . .	107
6.	Natural Rutile (Figs. 54-56)	
a.	Objectives . . . . .	109
b.	Background Information for Discussion of Rutile. . . . .	109
c.	R( $\nu$ ) and N( $\nu$ ) Spectra for Rutile . . . . .	110
d.	Discussion of Spectra for Rutile . . . . .	114
7.	Limestone (Figs. 57-60)	
a.	Objectives . . . . .	115
b.	Preparation of Samples . . . . .	117
c.	R( $\lambda$ ) and N( $\lambda$ ) Spectra for Limestone. . . . .	118
8.	Natural Waters (Figs. 61-67)	
a.	Objectives . . . . .	126
b.	R( $\lambda$ ) Spectra for Natural Waters. . . . .	133
c.	N( $\lambda$ ) Spectra for Natural Waters. . . . .	137
d.	Discussion of R( $\lambda$ ) Spectra for Natural Waters. . . . .	140
B.	Investigations of Infrared Transmittance of Powdered Materials (Figs. 68-80)	
1.	Objectives. . . . .	152
2.	Background Information for Discussion of Powdered Materials. . . . .	152
3.	T( $\nu$ ) Spectra for Powdered Materials in KBR Pellets. . . . .	157
4.	Discussion of T( $\nu$ ) Spectra for Powdered Materials . . . . .	157
C.	References for Sections V.A. and V.B. . . . .	174

D.	Other Investigations . . . . .	179
1.	Attenuation Coefficients of Water in the Visible Region (Figs. 81-82)	
a.	Abstract . . . . .	179
b.	Introduction . . . . .	180
c.	Experimental Methods . . . . .	183
d.	Theoretical Background . . . . .	187
e.	Experimental Results . . . . .	198
f.	References for Section V.D.1. . . . .	200
2.	Optical Properties of Crystalline Graphite ( $E_1C$ ) (Figs. 83-88)	
a.	Introduction . . . . .	202
b.	Spectra for Graphite . . . . .	206
3.	Thin Wedge Shaped Cell (Figs. 89-90)	
a.	Abstract . . . . .	211
b.	Introduction . . . . .	212
c.	Description of Cell. . . . .	214
d.	Calculation of Maximum Cell Thickness. . . . .	219
e.	Some Experimental Results. . . . .	221
f.	Conclusion . . . . .	224
g.	References for Section V.D.3 . . . . .	225
4.	Microprocessor Controlled Interface for a Desktop Calculator (Figs. 91-94)	
a.	Abstract . . . . .	226
b.	Introduction . . . . .	227
c.	System Design. . . . .	231
d.	Performance. . . . .	246
e.	References for Section V.D.4. . . . .	247

# LIST OF ILLUSTRATIONS

Figure 1.	Block diagram of the reflectometer system . . . . .	9
Figure 2.	Near-normal incidence relative reflectance spectra for 20.3, 29.4, and 40.2 percent aqueous solutions of $\text{ZnCl}_2$ in the $270\text{--}2,500\text{ cm}^{-1}$ region. . . . .	20
Figure 3.	Near-normal incidence relative reflectance spectra for 20.3, 29.4, and 40.2 percent aqueous solutions of $\text{ZnCl}_2$ in the $2,500\text{--}5,000\text{ cm}^{-1}$ region . . . . .	21
Figure 4.	Index of refraction $n(\nu)$ for 20.3, 29.4, and 40.2 percent aqueous solution of $\text{ZnCl}_2$ in the $270\text{--}2,500$ $\text{cm}^{-1}$ region . . . . .	22
Figure 5.	Index of refraction $n(\nu)$ for 20.3, 29.4, and 40.2 percent aqueous solutions of $\text{ZnCl}_2$ in the $2,500\text{--}$ $5,000\text{ cm}^{-1}$ region . . . . .	23
Figure 6.	Extinction coefficient $k(\nu)$ for 20.3, 29.4, and 40.2 percent aqueous solutions of $\text{ZnCl}_2$ in the $270\text{--}$ $2,500\text{ cm}^{-1}$ region . . . . .	24
Figure 7.	Extinction coefficient $k(\nu)$ for 20.3, 29.4, and 40.2 percent aqueous solutions of $\text{ZnCl}_2$ in the $2,500\text{--}$ $5,000\text{ cm}^{-1}$ region . . . . .	25
Figure 8.	Near-normal incidence relative reflectance spectra for 50, 65, and 75 percent aqueous solutions of $\text{ZnCl}_2$ in the $300\text{--}2,500\text{ cm}^{-1}$ region. . . . .	26

Figure 9.	Near-normal incidence relative reflectance spectra for 50, 65, and 75 percent aqueous solutions of $\text{ZnCl}_2$ in the $2,500\text{--}5,000\text{ cm}^{-1}$ region . . . . .	27
Figure 10.	Index of refraction $n(\nu)$ for 50, 65, and 75 percent aqueous solutions of $\text{ZnCl}_2$ in the $300\text{--}2,500$ $\text{cm}^{-1}$ region . . . . .	28
Figure 11.	Index of refraction $n(\nu)$ for 50, 65, and 75 percent aqueous solutions of $\text{ZnCl}_2$ in the $2,500\text{--}$ $5,000\text{ cm}^{-1}$ region . . . . .	29
Figure 12.	Extinction coefficient $k(\nu)$ for 50, 65, and 75 percent aqueous solutions of $\text{ZnCl}_2$ in the $2,500\text{--}$ $5,000\text{ cm}^{-1}$ region . . . . .	30
Figure 13.	Extinction coefficient $k(\nu)$ for 50, 65, and 75 percent aqueous solutions of $\text{ZnCl}_2$ in the $2,500\text{--}5,000$ $\text{cm}^{-1}$ region . . . . .	31
Figure 14.	Near-normal incidence relative reflectance spectra for 5, 10, 20, and 40 percent aqueous solutions of $\text{H}_3\text{PO}_4$ in the $300\text{--}2,500\text{ cm}^{-1}$ region. . . . .	43
Figure 15.	Index of refraction $n(\nu)$ for 5, 10, 20, and 40 percent aqueous solutions of $\text{H}_3\text{PO}_4$ in the $300\text{--}2,500\text{ cm}^{-1}$ region. . . . .	44
Figure 16.	Index of refraction $n(\nu)$ for 5, 10, 20, and 40 percent aqueous solutions of $\text{H PO}$ in the $2,500\text{--}5,000\text{ cm}^{-1}$ region. . . . .	45
Figure 17.	Extinction coefficient $k(\nu)$ for 5, 10, 20, and 40 percent aqueous solutions of $\text{H PO}$ in the $300\text{--}2,500$ $\text{cm}^{-1}$ region . . . . .	46

Figure 18.	Extinction coefficient $k(\nu)$ for 5, 10, 20, and 40 percent aqueous solutions of $\text{H}_3\text{PO}_4$ in the 2,500-5,000 $\text{cm}^{-1}$ region . . . . .	47
Figure 19.	Near-normal incidence relative reflectance spectra for 50, 65, 75, and 85 percent aqueous solutions of $\text{H}_3\text{PO}_4$ in the 300-2,500 $\text{cm}^{-1}$ region . . . . .	48
Figure 20.	Near-normal incidence relative reflectance spectra for 50, 65, 75, and 85 percent aqueous solutions of $\text{H}_3\text{PO}_4$ in the 2,500-5,000 $\text{cm}^{-1}$ region. . . . .	49
Figure 21.	Index of refraction $n(\nu)$ for 50, 65, 75, and 85 percent aqueous solutions of $\text{H}_3\text{PO}_4$ in the 300-2,500 $\text{cm}^{-1}$ region . . . . .	50
Figure 22.	Index of refraction $n(\nu)$ for 50, 65, 75, and 85 percent aqueous solutions of $\text{H}_3\text{PO}_4$ in the 2,500-5,000 $\text{cm}^{-1}$ region . . . . .	51
Figure 23.	Extinction coefficient $k(\nu)$ for 50, 65, 75, and 85 percent aqueous solutions of $\text{H}_3\text{PO}_4$ in the 300-2,500 $\text{cm}^{-1}$ region . . . . .	52
Figure 24.	Extinction coefficient $k(\nu)$ for 50, 65, 75, and 85 percent aqueous solutions of $\text{H}_3\text{PO}_4$ in the 2,500-5,000 $\text{cm}^{-1}$ region . . . . .	53
Figure 25.	Near-normal incidence relative reflectance spectra for 85 percent $\text{H}_3\text{PO}_4$ , at 25°C and -10°C, in the 300-2,500 $\text{cm}^{-1}$ region . . . . .	54
Figure 26.	Near-normal incidence relative reflectance spectra for 85 percent $\text{H}_3\text{PO}_4$ , at 25°C and -10°C, in the 2,500-5,000 $\text{cm}^{-1}$ region . . . . .	55
Figure 27.	Index of refraction $n(\nu)$ for 85 percent $\text{H}_3\text{PO}_4$ , at 25°C and -10°C, in the 300-2,500 $\text{cm}^{-1}$ region. . . . .	56

Figure 28.	Index of refraction $n(\nu)$ for 85 percent $\text{H}_3\text{PO}_4$ , at $25^\circ\text{C}$ and $-10^\circ\text{C}$ , in the $2,500\text{--}5,000\text{ cm}^{-1}$ region. . . . .	57
Figure 29.	Extinction coefficient $k(\nu)$ for 85 percent $\text{H}_3\text{PO}_4$ , at $25^\circ\text{C}$ and $-10^\circ\text{C}$ , in the $300\text{--}2,500\text{ cm}^{-1}$ region . . .	58
Figure 30.	Extinction coefficient $k(\nu)$ for 85 percent $\text{H}_3\text{PO}_4$ , at $25^\circ\text{C}$ and $-10^\circ\text{C}$ , in the $2,500\text{--}5,000\text{ cm}^{-1}$ region . .	59
Figure 31.	The planar structure of $\text{HNO}_3$ [from Ref. (23)] . . . .	63
Figure 32.	Degree of dissociation $\alpha$ vs. molar concentration M of aqueous solutions of $\text{HNO}_3$ . . . . .	64
Figure 33.	Near-normal incidence relative reflectance spectra for 0.5, 1, 2, 4, 8, and 15.7 M aqueous solutions of $\text{HNO}_3$ in the $310\text{--}2,500\text{ cm}^{-1}$ region. . . . .	69
Figure 34.	Near-normal incidence relative reflectance spectra for 0.5, 1, 2, 4, 8, and 15.7 M aqueous solutions of $\text{HNO}_3$ in the $2,500\text{--}5,000\text{ cm}^{-1}$ region. . . . .	70
Figure 35.	Index of refraction $n(\nu)$ for 0.5, 1, 2, 4, 8, and 15.7 M aqueous solutions of $\text{HNO}_3$ in the $310\text{--}2,500$ $\text{cm}^{-1}$ region . . . . .	71
Figure 36.	Index of refraction $n(\nu)$ for 0.5, 1, 2, 4, 8, and 15.7 M aqueous solutions of $\text{HNO}_3$ in the $2,500\text{--}5,000$ $\text{cm}^{-1}$ region . . . . .	72
Figure 37.	Extinction coefficient $k(\nu)$ for 0.5, 1, 2, 4, 8, and 15.7 M aqueous solutions of $\text{HNO}_3$ in the $310\text{--}2,500$ $\text{cm}^{-1}$ region . . . . .	73
Figure 38.	Extinction coefficient $k(\nu)$ for 0.5, 1, 2, 4, 8, and 15.7 M aqueous solutions of $\text{HNO}_3$ in the $2,500\text{--}5,000$ $\text{cm}^{-1}$ region . . . . .	74

Figure 39.	Near-normal incidence relative reflectance spectra for diesel fuel, fog oil, and DC-704 oil in the 300-2,500 $\text{cm}^{-1}$ region . . . . .	85
Figure 40.	Near-normal incidence relative reflectance spectra for diesel fuel, fog oil, and DC-704 oil in the 2,500-5,000 $\text{cm}^{-1}$ region . . . . .	86
Figure 41.	Index of refraction $n(\nu)$ for diesel fuel, fog oil, and DC-704 oil in the 300-2,500 $\text{cm}^{-1}$ region . . . . .	87
Figure 42.	Index of refraction $n(\nu)$ for diesel fuel, fog oil, and DC-704 oil in the 2,500-5,000 $\text{cm}^{-1}$ region . . . . .	88
Figure 43.	Extinction coefficient $k(\nu)$ for diesel fuel, fog oil, and DC-704 oil in the 300-2,500 $\text{cm}^{-1}$ region . . . . .	89
Figure 44.	Extinction coefficient $k(\nu)$ for diesel fuel, fog oil, and DC-704 oil in the 2,500-5,000 $\text{cm}^{-1}$ region . . . . .	90
Figure 45.	Near-normal incidence relative reflectance spectra for 1-hexadecanol (palmityl), 1-octadecanol (stearyl), and 1-eicosanol (arachidyl) in the 300-2,500 $\text{cm}^{-1}$ region. . . . .	93
Figure 46.	Near-normal incidence relative reflectance spectra for 1-hexadecanol (palmityl), 1-octadecanol (stearyl), and 1-eicosanol (arachidyl) in the 2,500-5,000 $\text{cm}^{-1}$ region. . . . .	94
Figure 47.	Index of refraction $n(\nu)$ for 1-hexadecanol (palmityl), 1-octadecanol (stearyl), and 1-eicosanol (arachidyl) in the 300-2,500 $\text{cm}^{-1}$ region. . . . .	95
Figure 48.	Index of refraction $n(\nu)$ for 1-hexadecanol (palmityl), 1-octadecanol (stearyl), and 1-eicosanol (arachidyl) in the 2,500-5,000 $\text{cm}^{-1}$ region. . . . .	96

Figure 49.	Extinction coefficient $k(\nu)$ for 1-hexadecanol (palmityl), 1-octadecanol (stearyl), and 1-eicosanol (arachidyl) in the $300\text{--}2,500\text{ cm}^{-1}$ region. . . . .	97
Figure 50.	Extinction coefficient $k(\nu)$ for 1-hexadecanol (palmityl), 1-octadecanol (stearyl), and 1-eicosanol (arachidyl) in the $2,500\text{--}5,000\text{ cm}^{-1}$ region. . . . .	98
Figure 51.	Near-normal incidence relative reflectance spectrum for polymethyl-methacrylate in the $300\text{--}5,000\text{ cm}^{-1}$ region. . . . .	101-102
Figure 52.	Index of refraction $n(\nu)$ for polymethyl-methacrylate in the $300\text{--}5,000\text{ cm}^{-1}$ region. . . . .	103-104
Figure 53.	Extinction coefficient $k(\nu)$ for polymethyl-methacrylate in the $300\text{--}5,000\text{ cm}^{-1}$ region. . . . .	105-106
Figure 54.	Near-normal incidence relative reflectance spectrum of natural rutile in the $300\text{--}5,000\text{ cm}^{-1}$ region. . . .	111
Figure 55.	Index of refraction $n(\nu)$ for natural rutile in the $300\text{--}5,000\text{ cm}^{-1}$ region . . . . .	112
Figure 56.	Extinction coefficient $k(\nu)$ for natural rutile in the $300\text{--}5,000\text{ cm}^{-1}$ region . . . . .	113
Figure 57.	Near-normal incidence absolute reflectance spectrum of Bethany Falls Limestone in the $0.2\text{--}17\text{ }\mu\text{m}$ region . .	120
Figure 58.	Near-normal incidence absolute reflectance spectrum of Bethany Falls Limestone in the $17\text{--}32.8\text{ }\mu\text{m}$ region .	121
Figure 59.	Real and imaginary parts of the complex refractive index $N(\lambda) = n(\lambda) + ik(\lambda)$ for Bethany Falls Limestone in the $0.2\text{--}17\text{ }\mu\text{m}$ region . . . . .	122
Figure 60.	Real and imaginary parts of the complex refractive index $N(\lambda) = n(\lambda) + ik(\lambda)$ for Bethany Falls Limestone in the $17\text{--}32.8\text{ }\mu\text{m}$ region . . . . .	123

Figure 61.	Relative reflectance spectra at $70.03^\circ$ angle of incidence for natural ocean waters in the 2-20 $\mu\text{m}$ region. . . . .	134
Figure 62.	Relative reflectance spectra at $70.03^\circ$ angle of incidence for water from the Dead Sea and the Great Salt Lake in the 2-20 $\mu\text{m}$ region . . . . .	135
Figure 63.	Relative reflectance spectra at $70.03^\circ$ angle of incidence for a phosphate water sample (Alafia River, Fla.) in the 2-20 $\text{cm}^{-1}$ region . . . . .	136
Figure 64.	Index of refraction $n(\lambda)$ for six natural water samples in the 2-20 $\text{cm}^{-1}$ region . . . . .	138
Figure 65.	Extinction coefficient $k(\lambda)$ for six natural water samples in the 2-20 $\text{cm}^{-1}$ region . . . . .	139
Figure 66.	Relative and absolute reflectance spectra at $70.03^\circ$ angle of incidence for 1, 3, and 5 M aqueous solutions of NaCl in the 2-20 $\mu\text{m}$ region . . . . .	141
Figure 67.	Relative and absolute reflectance spectra at $70.03^\circ$ angle of incidence for 0.5 M aqueous solutions of $\text{NaNO}_3$ , $\text{NH}_4\text{H}_2\text{PO}_4$ , and $\text{K}_2\text{SO}_4$ in the 2-20 $\mu\text{m}$ region. . .	142
Figure 68.	Relative transmittance spectra in the 300-5,000 $\text{cm}^{-1}$ region for 0.01, 0.1, and 1.0 percent mixtures of Montmorillonite pressed in KBr pellets. . . . .	158
Figure 69.	Relative transmittance spectra in the 300-5,000 $\text{cm}^{-1}$ region for 0.01, 0.1, and 1.0 percent mixtures of Colemanite pressed in KBr pellets . . . . .	159
Figure 70.	Relative transmittance spectra in the 300-5,000 $\text{cm}^{-1}$ region for 0.01, 0.1, and 1.0 percent mixtures of Kernite pressed in KBr pellets. . . . .	160

Figure 71.	Relative transmittance spectra in the 300-5,000 $\text{cm}^{-1}$ region for 0.01, 0.1, and 1.0 percent mixtures of Kaolin pressed in KBr pellets . . . . .	161
Figure 72.	Relative transmittance spectrum in the 300-5,000 $\text{cm}^{-1}$ region for a 0.002 percent mixture of lampblack pressed in KBr pellets, . . . . .	162
Figure 73.	Relative transmittance spectrum in the 285-5,000 $\text{cm}^{-1}$ region for a 0.002 percent mixture of activated charcoal pressed in KBr pellets . . . . .	163
Figure 74.	Relative transmittance spectrum in the 300-5,000 $\text{cm}^{-1}$ region for a 0.02 percent mixture of wood charcoal pressed in KBr pellets, . . . . .	164
Figure 75.	Relative transmittance spectrum in the 1,665-5,000 $\text{cm}^{-1}$ region for a 2 percent mixture of aluminum powder pressed in KBr pellets. . . . .	165
Figure 76.	Relative transmittance spectrum in the 1,665-5,000 $\text{cm}^{-1}$ region for a 2 percent mixture of Kaolin pressed in KBr pellets. . . . .	166
Figure 77.	Relative transmittance spectrum in the 1,665-5,000 $\text{cm}^{-1}$ region for a 2 percent mixture of Montmorillonite pressed in KBr pellets, . . . . .	167
Figure 78.	Relative transmittance spectrum in the 1,665-5,000 $\text{cm}^{-1}$ region for a 2 per cent mixture of Colemanite pressed in KBr pellets, . . . . .	168
Figure 79.	Relative transmittance spectrum in the 1,665-5,000 $\text{cm}^{-1}$ region for a 2 percent mixture of Illite pressed in KBr pellets. . . . .	169
Figure 80.	Relative transmittance spectrum in the 1,665-5,000 $\text{cm}^{-1}$ region for a 2 percent mixture of Kernite pressed in KBr pellets . . . . .	170

Figure 81.	A block diagram of the instrumentation used to measure the attenuation coefficient $\alpha(\lambda)$ of deionized filtered water in the 418.6-640.3 nm region . . . . .	182
Figure 82.	A graphical comparison of $\alpha(\lambda)$ (solid circles) from the investigation of deionized filtered water, with $\alpha(\lambda)$ and $\alpha(\lambda)a$ obtained by previous investigators . .	193
Figure 83.	Logarithm of the extinction coefficient $k(\xi)$ vs. $\xi$ for crystalline graphite: electric field perpendicular to c-axis ( $E_{\perp}C$ ), energy $\xi$ in units of electron volts, and energy range from 1 mev to 1 Mev. . . . .	203
Figure 84.	Extinction coefficient $k(\xi)$ vs. $\xi$ in the energy region 1 mev-40 ev for crystalline graphite with $E_{\perp}C$ . . . .	204
Figure 85.	Evaluation of the effective-electron sum rule for the $k(\xi)$ vs. $\xi$ spectrum of crystalline graphite ( $E_{\perp}C$ ) . .	205
Figure 86.	Logarithm of the index of refraction $n(\xi)$ vs. $\xi$ in the 1 mev to 1 Mev range for crystalline graphite as obtained from a Kramers-Kronig analysis of the $k(\xi)$ spectrum in Figure 83. ( $E_{\perp}C$ ). . . . .	208
Figure 87.	Index of refraction $n(\xi)$ vs. $\xi$ in the 1 mev-40 ev region for crystalline graphite ( $E_{\perp}C$ ). . . . .	209
Figure 88.	Normal-incidence absolute reflectance spectrum in the 1 mev-40 ev region for crystalline graphite ( $E_{\perp}C$ ) . .	210
Figure 89.	An exploded drawing of components comprising a thin wedge-shaped cell for measuring the attenuation coefficient of highly absorbent liquids . . . . .	215

Figure 90.	Cross-sectional view of thin wedge-shaped cell; showing cell windows, liquid samples, and spacer; in the vertical orientation in which the cell is used. In (a) the liquid fills the vertex region. In (b) the liquid is virtually displaced a distance $x$ from the vertex. . . . .	220
Figure 91.	Interconnection diagram for the calculator/micro- processor interface system. . . . .	232
Figure 92.	Block diagram depicting principles used to control peripheral devices . . . . .	233
Figure 93.	Block diagram of Communications Interface . . . . .	238
Figure 94.	Block diagram of Experimental Control Interface . . .	240

# LIST OF TABLES

Table I.	Bulk materials investigated during the term of Grant DAAG29-76-G-0185. . . . .	2
Table II.	Powdered samples pressed in KBr pellets for which transmittance spectra were measured. . . . .	4
Table III.	Personnel employed on the project. . . . .	7
Table IV.	Parameters for intra- and inter-molecular vibrations of water in aqueous solutions containing $\text{ZnCl}_2$ . . . .	36
Table V.	Central frequencies $\nu(\text{cm}^{-1})$ of infrared active vibrational bands and tentative band assignments for $\text{H}_3\text{PO}_4$ solutions. . . . .	61
Table VI.	Previous band assignments for nitric-acid vapor and liquid . . . . .	66
Table VII.	Stoichiometry of nitric-acid solutions. . . . .	66
Table VIII.	Parameters for intramolecular bands of selected nitric-acid solutions . . . . .	76
Table IX.	Infrared active vibrational modes, species, and frequencies of n-paraffins compiled from the normal coordinate analysis in Reference (33) . . . . .	83
Table X.	Wave-number positions and assignments of the strongest infrared bands observed in the spectra of the alcohols. . . . .	91
Table XI.	Wave-number positions and assignments of the strongest infrared bands observed in the spectrum of PTMA . . . . .	92

Table XII.	Wave-number positions and assignments for the strongest infrared bands observed in the spectra of the alcohols . . . . .	100
Table XII.	Wave-number positions and assignments for infrared bands observed in PMMA. . . . .	108
Table XIV.	Classical-dispersion theory parameters for Limestone, Calcite, and Dolomite . . . . .	125
Table XV.	Inorganic molecules, vibrational modes, central wavelength and wave-number positions, half widths, are relative band strengths . . . . .	128
Table XVI.	Chemical analysis of natural waters . . . . .	131
Table XVII.	Powdered materials pressed in KBr pellets for which relative transmittance $T(\nu)$ was measured. . . .	157
Table XVIII.	Attenuation coefficients $\alpha(\lambda)$ for deionized filtered water. . . . .	194
Table XIX.	Calculated maximum cell thickness for some common solvents . . . . .	222
Table XX.	Lambert absorption coefficients $\alpha(\nu)$ for aqueous solutions of $\text{ZnCl}_2$ and $\text{H}_3\text{PO}_4$ . . . . .	223
Table XXI.	List of abbreviations used in Section V.C.4. . . . .	228

## I. Statement of Research Problem

Research conducted during the term of this Grant was measurement of infrared reflectance or transmittance spectra of selected condensed materials, computational analysis of the measured spectra to obtain spectral values of the complex refractive index  $N(\nu) = n(\nu) + ik(\nu)$  of those materials, and further analysis of the spectra in terms of fundamental intra- and inter-molecular vibrational modes.

## II. Summary of Most Important Results

The most significant accomplishments of this project are determinations of spectral values of  $N(\nu)$  of bulk natural and artificial aerosol/obscurant materials, and providing these values of  $N(\nu)$  to scientists within the aerosol/obscuration program at the Aberdeen Proving Ground, Md. We measured and sent, to the Aberdeen Proving Ground spectral values of  $N(\nu)$  for each of the thirty-eight solids and liquids listed in Table I. Most of the materials listed in Table I were chosen for investigation by Mr. Hugh Carlon, CSL, Aberdeen Proving Ground, who was the technical monitor for this research program.

Current knowledge of the manner in which electromagnetic radiation propagates through aerosols/obscurants is based primarily on Mie-scattering computations. Such computations are only possible when there is prior knowledge of  $N(\nu)$  for the aerosol/obscurant. The spectral values of  $N(\nu)$  obtained during the term of this Grant are now routinely used for Mie-scattering computations by scientists at many U.S. Army Laboratories and by many DOD contractors. Tabulated values of  $N(\nu)$  for these materials can be obtained from the Aerosol/Obscuration Science Office, DRDAR-CLB-PS, Aberdeen Proving Ground, Md. 21010; or by consulting publications associated with this Grant.

TABLE I. Bulk materials investigated during the term of  
Grant DAAG29-76-G-0185.

Material	Sample Concentration	Spectral Range	Obtained n + 1k
H <sub>3</sub> PO <sub>4</sub>	5,10,20,40,50,65,75,85%, Cold 85% sample.	2-33 $\mu$ m	Yes
ZnCl <sub>2</sub>	20,30,40,50,65,75%	2-33 $\mu$ m	Yes
Fog Oil	100%	2-33 $\mu$ m	Yes
Diesel Fuel	100%	2-33 $\mu$ m	Yes
DC-704 Silicon Oil	100%	2-33 $\mu$ m	Yes
Plexiglas	100%	2-33 $\mu$ m	Yes
HNO <sub>3</sub>	0.5,1,2,4,8,15.7 M	2-33 $\mu$ m	Yes
1-hexadecanol	100%	2-33 $\mu$ m	Yes
1-octadecanol	100%	2-33 $\mu$ m	Yes
1-eicosanol	100%	2-33 $\mu$ m	Yes
Futile	Natural sample	2-33 $\mu$ m	Yes
Limestone*	Natural sample	2-33 $\mu$ m	Yes
Water*	purified & deionized	42-.64 $\mu$ m	Yes
Natural Waters*	six samples	2-20 $\mu$ m	Yes
Graphite*	crystalline (E <sub>1</sub> C)	1.24x10 <sup>-6</sup> -1240 $\mu$ m	Yes

\* Denotes materials investigated for which only partial support  
was provided by DAAG29-76-G-0185.

Table II contains a listing of powdered materials pressed in KBr pellets for which infrared transmittance spectra were measured during the latter months of the Grant. Determination of spectral values of  $N(\nu)$  for the powdered materials was not completed during the term of this Grant, but is continuing during a follow-on Contract.

TABLE II. Powdered samples pressed in KBr pellets for which transmittance spectra were obtained during the latter months of Grant DAAG 29-76-G-0185. Determination of spectral values of  $n+ik$  has not been completed for these materials.

Material	Concentration	Spectral Range
Montmorillonite	1, 0.1, 0.01%	2-40 $\mu\text{m}$
Colemanite	1, 0.1, 0.01%	2-40 $\mu\text{m}$
Kernite	1, 0.1, 0.01%	2-40 $\mu\text{m}$
Kaolin	1, 0.1, 0.01%	2-35 $\mu\text{m}$
Lampblack	0.002%	2-35 $\mu\text{m}$
Activated Charcoal	0.002%	2-35 $\mu\text{m}$
Wood Charcoal	0.02%	2-35 $\mu\text{m}$
Aluminum	2%	2-6 $\mu\text{m}$
Kaolin	2%	2-6 $\mu\text{m}$
Montmorillonite	2%	2-6 $\mu\text{m}$
Colemanite	2%	2-6 $\mu\text{m}$
Illite	2%	2-6 $\mu\text{m}$
Kernite	2%	2-6 $\mu\text{m}$

### III. Publications and Presentations

#### A. Publications

1. M. R. Querry and I. L. Tyler, "Reflectance and complex refractive indices in the infrared for aqueous solutions of nitric acid", J. Chem. Phys. 72, (in press).
2. J. B. Ross, I. L. Tyler, and M. R. Querry, "A microcomputer-based interface to expand the capabilities of a desktop programmable calculator," J. Phys. E: Sci. Instrum. 12, 266-267 (1979).
3. M. R. Querry, P. G. Cary, R. C. Waring, "Split-pulse laser method for measuring attenuation coefficients of transparent liquids: application to deionized filtered water in the visible region," Appl. Opt. 17, 3587-3592 (1978).
4. M. R. Querry, G. Osborne, K. Lies, R. Jordon, & R. M. Coveney, "Complex refractive index of limestone in the visible and infrared," Appl. Opt. 17, 353-356 (1978).
5. I. L. Tyler, G. Taylor, and M. R. Querry, "Thin-Wedge-shaped cell for highly absorbent liquids," Appl. Opt. 17, 960-963 (1978).
6. I. L. Tyler and M. R. Querry, "Complex refractive indices in the infrared for  $\text{ZnCl}_2$  in water," J. Chem. Phys. 68, 1230-1236 (1977).
7. M. R. Querry, W. E. Holland, R. C. Waring, L. M. Earls and M. D. Querry, "Relative reflectance and complex refractive index in the infrared for saline environmental waters," J. Geophys. Res. 82, 1425-1433 (1977).

B. Presentations (abstracts)

1. G. M. Hale, I. L. Tyler, and M. R. Querry, "Complex refractive indices in the infrared for selected oils and alcohols," J. Opt. Soc. Am. 68, 1403 (1978).
2. M. R. Querry and I. L. Tyler, "Complex refractive indices in the infrared for  $H_3PO_4$  in water," J. Opt. Soc. Am. 68, 1404 (1978).
3. G. M. Hale, K. Biagi, and W. Holland, "Classical dispersion theory applied to the infrared reflectance of calcite, dolomite, and limestone," J. Opt. Soc. Am. 68, 1403 (1978).
4. I. L. Tyler and M. R. Querry, "Complex refractive index in the infrared for  $ZnCl_2$  in water," Bull. Am. Phys. Soc. 22, 641 (1977).
5. M. R. Querry, I. L. Tyler, and W. E. Holland, "Complex refractive index in the infrared for phosphoric acid ( $H_3PO_4$ ) in water," Bull. Am. Phys. Soc. 22, 641 (1977).

C. Thesis

Roy D. Holt, "The optical properties of crystalline graphite",  
M. S. Thesis, Department of Physics, University of Missouri-  
Kansas City (1979).

IV. Personnel Employed on the Project

Persons employed on the Grant, persons who received pay as consultants and persons who participated in the project but were not paid from grant funds are listed in Table III.

TABLE III. Personnel Employed on the Project.

Name	Postion	Degrees Received
Marvin R. Querry, Ph.D.	Principal Investigator	none
I. L. Tyler, Ph.D.	Investigator	none
W. E. Holland, M.S.	Research Associate	none
G. M. Hale, M.S.	Research Associate	none
K. Biagi	Student Assistant	B.S. Physics
J. B. Ross, Ph.D.	Consultant (digital electronics)	none
M. D. Querry, M.S.	Consultant (illustrations)	none
Tom Baird	Student Assistant	B.S. Engineering
P. G. Cary	Unpaid Participant	M.S. Physics
R. Holt	Unpaid Participant	M.S. Physics

## V. Report of Research

Research conducted during the term of the Grant, for purposes of this report, is divided into three parts: Investigations of Infrared Reflectance which are presented in Section V.A., Investigations of Infrared Transmittance which are presented in Section V.B., and Other Investigations which are presented in Section V.D.

### A. Investigations of Infrared Reflectance

Here, in Section V.A., we present the investigations of those materials listed in Table I.

#### 1. Experimental Methods

A block diagram of the reflectometer and data acquisition system is shown in Fig. 1. Radiant flux from a glower G was chopped at C and was then focussed by an f/5 optical system, consisting of plane mirror  $M_1$  and spherical mirror  $M_2$ , on the surface of the sample S. The angle of incidence  $\theta$  was 6.2 degrees for the central ray from  $M_2$  incident on the surface of S. Radiant flux reflected from S was imaged by an identical optical system ( $M_3$  and  $M_4$ ) on the entrance slit of a Perkin-Elmer Ebert double-pass grating monochromator. The entrance slits were manually adjusted to assure spectral resolution  $\nu/\Delta\nu$  of 100 or better. After passage through the monochromator, the radiant flux was optically filtered to remove higher diffraction orders, and was then focussed on a thermopile detector equipped with a CsI window. The signal from the detector was synchronously processed by a Princeton Applied Research (PAR) Model 124 lock-in amplifier. The analog output signal from the Model 124 was applied to the input of a PAR Model 260 analog-to-digital converter (ADC).

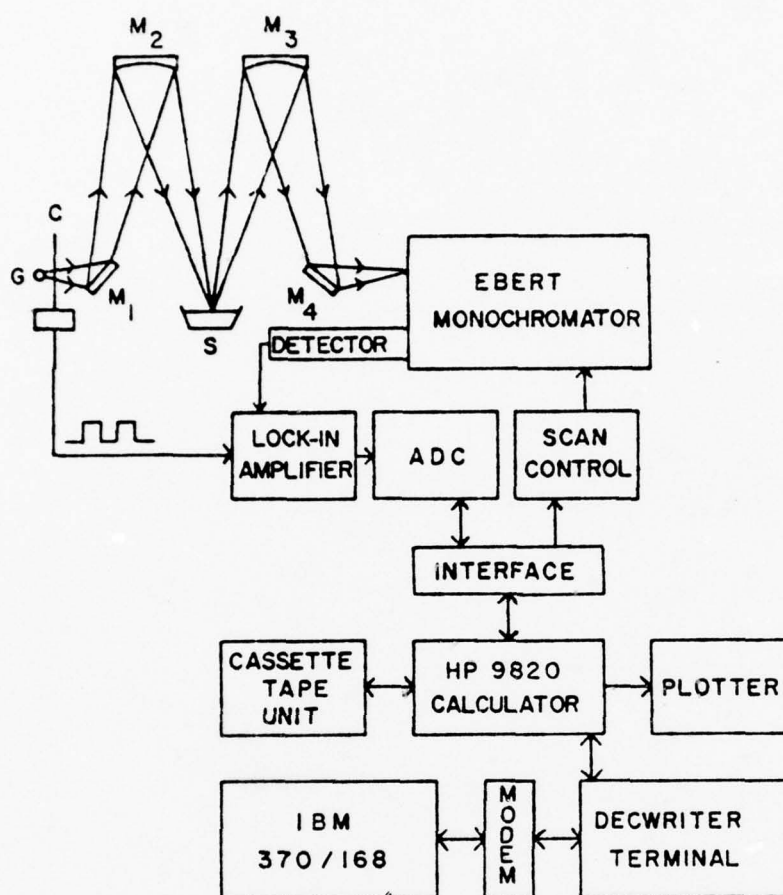


Figure 1. A block diagram of the reflectometer-spectrophotometer and data acquisition system.

which both digitized the signal and inserted an index corresponding to the spectral position of the monochromator.

In order to facilitate data acquisition and analysis the system described above was interfaced to a Hewlett-Packard (HP) Model 9820A programmable calculator equipped with an HP 9862A plotter and an HP11223A magnetic cassette tape unit. This entire system was then interfaced<sup>19/</sup> through a decwriter L-36 TSO terminal to an IBM 370/168 computer which was used for the subsequent Kramers-Kronig analysis of the data.

During this investigation we measured relative specular reflectance  $R(v) = R(v)_s / R(v)_w$ , where s denotes the sample and w denotes the water standard. Prior to use the water standard w was purified, deionized, and filtered through a 0.2  $\mu\text{m}$  Millipore filter. Aqueous solutions were prepared using purified water and reagent grade chemicals. The aqueous solutions and purified water were placed in separate petri dishes which served as sample holders. Each dish was filled to precisely the same level as determined by use of a cathetometer. The levels of all samples were monitored routinely during data collection and purified water was added to the samples as needed to compensate for evaporation. Each sample was also stirred thoroughly at the beginning of a spectral scan to assure isotropic homogeneity. Data were acquired at 200 equally spaced wavelength positions in each of the wavelength regions 2-3, 3-4, 4-6, 6-8, 8-10, 10-15, 15-20, 20-30, and 30-40  $\mu\text{m}$ . For some samples, individual relative reflectance measurements were made at 30.15, 32.2,

34.0, and 37.1  $\mu\text{m}$ , where atmospheric absorption was a minimum, rather than throughout the 30-40  $\mu\text{m}$  region.

Procedures were slightly different for handling the solid samples. The solid samples were placed one-at-a-time on a small three-legged stand within the reflectometer. The top surface of the water standard and the polished surface of the solid sample were placed at the same height by adjusting the legs of the stand while viewing the surface edge through a cathetometer. Additionally, the beam from a He-Ne laser was reflected from the level surface of the water standard to a fiducial mark on the ceiling of the laboratory. The legs of the stand were further adjusted to bring the laser beam to the same fiducial mark when the water was replaced by a solid sample. The latter leveling adjustments were made so that the height of the solid surface was also at the proper position. Reflectance spectra were then acquired for the solids at the same wavelength positions as for the liquids.

All spectra were obtained with the samples at about 27°C, except for one cold sample of 85% phosphoric acid which was of about -10°C. The reflectance spectra  $R(\nu)$  were converted from wavelength to wave number and then plotted either by the HP9862A, a Tektronix graphics terminal, or by a calcomp plotter interfaced to the IBM 370/168. The standard deviations, based on three independent measurements, were generally  $\pm 0.005 R(\nu)$  but increased to about  $\pm 0.01 R(\nu)$

in relatively narrow spectral regions where atmospheric water vapor and carbon dioxide were strongly absorbing.

## 2. Aqueous Solutions of $\text{ZnCl}_2$

### a. Objectives

The two principal objectives for this investigation were: (1) to measure central frequencies, half-widths, and band strengths of intra- and inter-molecular infrared active vibrational modes of liquid water in aqueous solutions of  $\text{ZnCl}_2$ ; and (2) to obtain, for aqueous solutions of  $\text{ZnCl}_2$ , spectral values of the complex refractive index  $N(\nu)_s = n(\nu)_s + ik(\nu)_s$  which are suitable for computing basic Mie scattering parameters. These two objectives were accomplished as follows. First, the near-normal incidence relative reflectance spectra  $R(\nu) = R(\nu)_s / R(\nu)_w$  in the  $270\text{--}5000\text{ cm}^{-1}$  spectral region were measured for 20.3, 29.4, 40.2, 50, 65, and 75 per cent solutions by weight of  $\text{ZnCl}_2$  in water. In moles/liter the concentrations of the three solutions are 1.77 M, 2.8 M, 4.19 M, 5.75 M, 8.82 M, and 11.65 M, respectively. Subscripts s and w refer to the aqueous solutions and to pure water, respectively. Spectra  $R(\nu)$  were analyzed by use of a subtractive Kramers-Kronig algorithm to obtain spectral values for  $\Delta\phi(\nu)$  the differences in phase shifts for electromagnetic waves of frequency  $\nu$  reflected from the surface of the  $\text{ZnCl}_2$  solutions and from the surface of the water which was the reflectance standard. Spectral values of  $N(\nu)_s$  for the  $\text{ZnCl}_2$  solutions were then computed

by use of an algorithm<sup>7/</sup> that uses  $R(\nu)$ ,  $\Delta\phi(\nu)$ , a measured value for the angle of incidence  $\theta$ , and known values<sup>2/</sup> of  $N(\nu)_w$ . The influence of  $\text{ZnCl}_2$  on the intra- and inter-molecular vibrational modes of liquid water was determined by critical examination of  $R(\nu)$  and  $k(\nu)_s$  throughout the spectral region investigated.

b. Background Information for Discussion of  $\text{ZnCl}_2$  Solutions.

A knowledge of the optical properties of aqueous solutions of  $\text{ZnCl}_2$  is of both theoretical and practical importance. From the practical point of view, clouds composed of droplets of such solutions are occasionally present in localized geographical regions within the earth's atmosphere. Analytical prediction of the scattering parameters for radiation passing through such clouds relies primarily on Mie scattering theory. This theory requires prior knowledge of the spectral values of the complex refractive index  $N(\nu)_s = n(\nu)_s + ik(\nu)_s$  of the materials comprising the aerosol.

The theoretical importance of aqueous  $\text{ZnCl}_2$  solutions lies in a long-standing interest in the complicated structural properties of liquid water and in the formation of autocomplexes of the  $\text{Zn}^{2+}$  metal ion. The present knowledge of the structure of liquid water and of aqueous  $\text{ZnCl}_2$  solutions is reviewed here, with emphasis on those properties that provide greater understanding of the accurate measurements of infrared reflectance spectra described hereinafter.

Several intra- and inter-molecular vibrational bands are clues to the structure of the liquid. For instance, the infrared reflectance spectrum  $R(\nu)_w$  of liquid water, and Kramers-Kronig analysis of that spectrum, provide spectral values of the phase shift  $\phi(\nu)_w$  of electromagnetic waves reflected from the liquid surface. Then by use of an appropriate algorithm spectral values of  $N(\nu)_w$  for liquid water are calculated from  $\phi(\nu)_w$  and  $R(\nu)_w$ . The spectrum thus obtained for the extinction coefficient  $k(\nu)_w$  of water is particularly useful in further investigations of inter- and intra-molecular vibrational modes. For example, one obtains the frequency  $\nu_{\max}$  at which  $k(\nu)_w$  is a maximum for infrared active vibrational bands, the spectral width  $\Gamma$  (full width at half maximum) of vibrational bands, and the band strength

$$S_b = \frac{1}{\rho_0} \int_{\text{band}} k(\nu)_w d\nu, \quad (1)$$

where  $\rho_0$  is the molecular density (molecules/cm<sup>3</sup>), and where the integral is evaluated over the full spectral width of a vibrational band.

The infrared transmittance spectrum of liquid water provides spectral values for the Lambert absorption coefficient  $\alpha(\nu)_w$ , which is related to  $k(\nu)_w$  by

$$\alpha(\nu)_w = 4\pi\nu k(\nu)_w, \quad (2)$$

Differentiation of  $\alpha(\nu)_w$  with respect to  $\nu$  shows, that for the same vibrational band, the maximum for  $\alpha(\nu)_w$

occurs at a higher frequency  $\nu$  than the maximum for  $k(\nu)_w$ . Thus in the scientific literature there are slight, but implicit, disagreements as to the central frequency  $\nu_{\max}$  of some vibrational bands because some investigators work entirely with  $\alpha(\nu)_w$  and others work entirely with  $k(\nu)_w$ . Noting this implicit difference in obtaining central frequencies  $\nu_{\max}$  of vibrational bands, we relate to  $k(\nu)_w$  the subsequent discussions of central band frequencies  $\nu_{\max}$ , half widths  $\Gamma$ , and band strengths  $S_b$ .

In the vapor state the  $H_2O$  monomer possesses  $C_{2v}$  symmetry and has three fundamental vibrational modes:

- $\nu_1(A_1)$  symmetrical O-H stretch at  $3656\text{ cm}^{-1}$ ,
- $\nu_2(A_1)$  O-H-O bending motion at  $1594\text{ cm}^{-1}$ , and
- $\nu_3(B_1)$  antisymmetric O-H stretch at  $3756\text{ cm}^{-1}$ .

It is very doubtful that the  $H_2O$  monomer, per se, exists in the liquid state. Hydrogen-bonded temporal clusters of several  $H_2O$  molecules, however, are believed to exist in liquid water. An infrared spectrum of liquid water therefore is interpreted in terms of bands associated with the intra-molecular vibrations of  $H_2O$  molecules, and in terms of inter-molecular lattice vibrations of the clusters. For example, the infrared spectrum of liquid water at  $27^\circ\text{C}$  possesses a band, designated as  $\nu_2$ , that is associated with the O-H-O bending motion. The  $\nu_2$  band has a central frequency  $\nu_{\max}$  of  $1640\text{ cm}^{-1}$ , a half width  $\Gamma$  of  $110\text{ cm}^{-1}$ , and a band strength  $S_b$  of

$(4.5 \pm 0.8) \times 10^{-22} \text{ cm}^2/\text{molecule}$ . The symmetric and antisymmetric O-H stretching vibrations, designated  $\nu_1$  and  $\nu_3$ , respectively, and the first overtone  $2\nu_2$  which may be in Fermi resonance with one of the O-H stretching vibrations, provide broad overlapping bands in relatively close spectral proximity to one another. The bands associated with  $\nu_1$ ,  $\nu_3$ , and  $2\nu_2$  are grouped together for purposes of analyzing the infrared spectrum; together they provide a very broad band with central frequency  $\nu_{\text{max}}$  of  $3395 \text{ cm}^{-1}$ , a half width  $\Gamma$  of  $390 \text{ cm}^{-1}$ , and a combined band strength  $S_b$  of  $(3.65 \pm 0.08) \times 10^{-21} \text{ cm}^2/\text{molecule}$ .

The structure of the temporal clusters of  $\text{H}_2\text{O}$  molecules in liquid water is not fully understood at this time. However, one recent model<sup>3/</sup> is useful when interpreting the infrared spectrum of liquid water. The model, regarded by its authors as not being definitive until further experimental verification is obtained, consists of an  $\text{H}_2\text{O}$  molecule hydrogen-bonded with  $C_{2v}$  symmetry in a temporal cluster of four first and twelve second nearest neighboring  $\text{H}_2\text{O}$  molecules. A normal coordinate and Monte Carlo analysis of this structure yielded six principal lattice vibrational modes with a total of thirty different vibrational species. According to the normal coordinate analysis the six principal lattice vibrations occur at ca. 75, 165, 219, 450, 550, and  $722 \text{ cm}^{-1}$ . In the infrared spectrum of liquid water, assuming that the

seventeen molecule cluster with  $C_{2v}$  symmetry has significant validity, the lattice vibrational modes near 450, 550, and  $722\text{ cm}^{-1}$  provide broad overlapping bands that collectively give a broader band designated as the librational band  $\nu_L$ . From infrared spectra obtained for liquid water at  $27^\circ\text{C}$  the parameters for the  $\nu_L$  band are  $\nu_{\text{max}} = 580\text{ cm}^{-1}$ ,  $\Gamma = 500\text{ cm}^{-1}$ , and  $S_b = (7.2 \pm 1.5) \times 10^{-21}\text{ cm}^2/\text{molecule}$ . Similar parameters for the other three principal lattice vibrations have not been measured because infrared reflectance and transmittance spectra of water are difficult to obtain in the region below  $300\text{ cm}^{-1}$ .

Of particular relevance to the investigation of  $\text{ZnCl}_2$  solutions was the fact that the nature of water molecules in the liquid state could also be investigated through effects that monatomic and polyatomic ions have on the intra- and inter-molecular vibrations of the temporal clusters. The ions are sources of electric fields that interact with the electric dipole moments of neighboring water molecules within the hydrogen-bonded temporal clusters. In infrared reflectance spectra  $R(\nu)_s$  of aqueous solutions, and in associated spectra  $N(\nu)_s$ , the averaged effects of such interactions are observed as (1) shifts in the central frequencies  $\nu_{\text{max}}$  of the various intra- and inter-molecular vibrational bands, and (2) as changes in  $S_b$  the infrared band strength associated with each vibrational band. Investigations of these effects are described in several previous articles,<sup>4-7/</sup>

D. E. Irish<sup>8/</sup> previously reviewed the physical and chemical properties of fused salts and electrolyte solutions of  $\text{ZnCl}_2$ . Raman spectra were the primary basis for deducing the chemical properties, but several references to infrared studies were also included. Based on the review by Irish, and the pertinent publications<sup>9-18/</sup> referred to therein, we note that aqueous solutions of  $\text{ZnCl}_2$  contain the polyatomic constituents  $\text{ZnCl}^+$ ,  $\text{ZnCl}_2$ ,  $\text{ZnCl}_3^-$ ,  $\text{ZnCl}_4^{2-}$ , and  $\text{Zn}(\text{H}_2\text{O})_6^{2+}$  in addition to hydrated species of some of these autocomplexes. The diatomic ion  $\text{ZnCl}^+$  has a vibrational frequency of ca.  $305 \text{ cm}^{-1}$  and occurs in solutions of less than 4M concentration. The linear molecule  $\text{ZnCl}_2$ , which occurs in solutions of greater than 4M concentration, has three fundamental vibrational modes: (1) the  $\nu_1$  Zn-Cl symmetric stretch at ca.  $305 \text{ cm}^{-1}$ , (2) the  $\nu_2$  Cl-Zn-Cl bending mode at ca.  $101 \text{ cm}^{-1}$ , and (3) the  $\nu_3$  Zn-Cl anti-symmetric stretch at ca.  $505 \text{ cm}^{-1}$ . The  $\nu_1$  mode is Raman active and the  $\nu_2$  and  $\nu_3$  modes are infrared active. No evidence from Raman or infrared studies exists to either prove or disprove the existence of  $\text{ZnCl}_3^-$  in aqueous solutions of  $\text{ZnCl}_2$ . The anion  $\text{ZnCl}_4^{2-}$ , which exists in solutions of less than 10 M concentration, possesses the nine fundamental vibrational modes characteristic of tetrahedral molecules:  $\nu_1(\text{A}_1)$  at  $278 \text{ cm}^{-1}$ ,  $\nu_2(\text{E})$  at ca.  $100 \text{ cm}^{-1}$ ,  $\nu_3(\text{F}_2)$  at ca.  $280 \text{ cm}^{-1}$ , and  $\nu_4(\text{F}_2)$  at ca.  $122 \text{ cm}^{-1}$ . All modes are Raman active, but only the  $\nu_3(\text{F}_2)$  and  $\nu_4(\text{F}_2)$  triply degenerate modes

are infrared active. The octahedral cation  $\text{Zn}(\text{H}_2\text{O})_6^{2+}$ , which exists in solutions of less than 13 M concentration, possesses three Raman active vibrational species  $A_{1g}$ ,  $E_g$ , and  $T_{2g}$  and two triply degenerate  $T_{1u}$  infrared active vibrational species. Irish observed a Raman band at ca.  $390\text{ cm}^{-1}$  which was assigned to the  $A_{1g}$  species. Infrared active modes attributed to  $\text{Zn}(\text{H}_2\text{O})_6^{2+}$  were observed in  $\text{ZnSO}_4 \cdot 7\text{H}_2\text{O}$  by use of the KBr disk method by Nakagawa and Shimanouchi.<sup>9/</sup> They assigned an  $\text{OH}_2$  wagging vibration to a band at  $541\text{ cm}^{-1}$ , a Zn-O stretching vibration to a band at  $364\text{ cm}^{-1}$ ; and an  $\text{OH}_2$  rocking vibration that was calculated to occur at  $620\text{ cm}^{-1}$  was not observed possibly because of overlap with the band due to the  $\nu_4(\text{F}_2)$  mode of  $\text{SO}_4^{2-}$ . In aqueous solutions of greater than 10 M concentration a polynuclear aggregate of  $\text{ZnCl}_4$  tetrahedra, comparable to that of crystalline  $\text{ZnCl}_2$ , was observed by Irish to possess Raman active vibrational modes at ca. 90, 230, 335, and  $280\text{ cm}^{-1}$ . Evidence of the water structure also persists in Raman spectra for  $\text{ZnCl}_2$  solutions up to about 10 M concentration.

c.  $R(\nu)$  and  $N(\nu)$  Spectra for  $\text{ZnCl}_2$  Solutions

The measured relative reflectance spectra  $R(\nu)$  for the 1.77, 2.8, and 4.19 M  $\text{ZnCl}_2$  solutions are presented in Figs. 2 and 3, and  $R(\nu)$  for the 5.75, 8.82, and 11.65 M  $\text{ZnCl}_2$  solutions are presented in Figs. 3

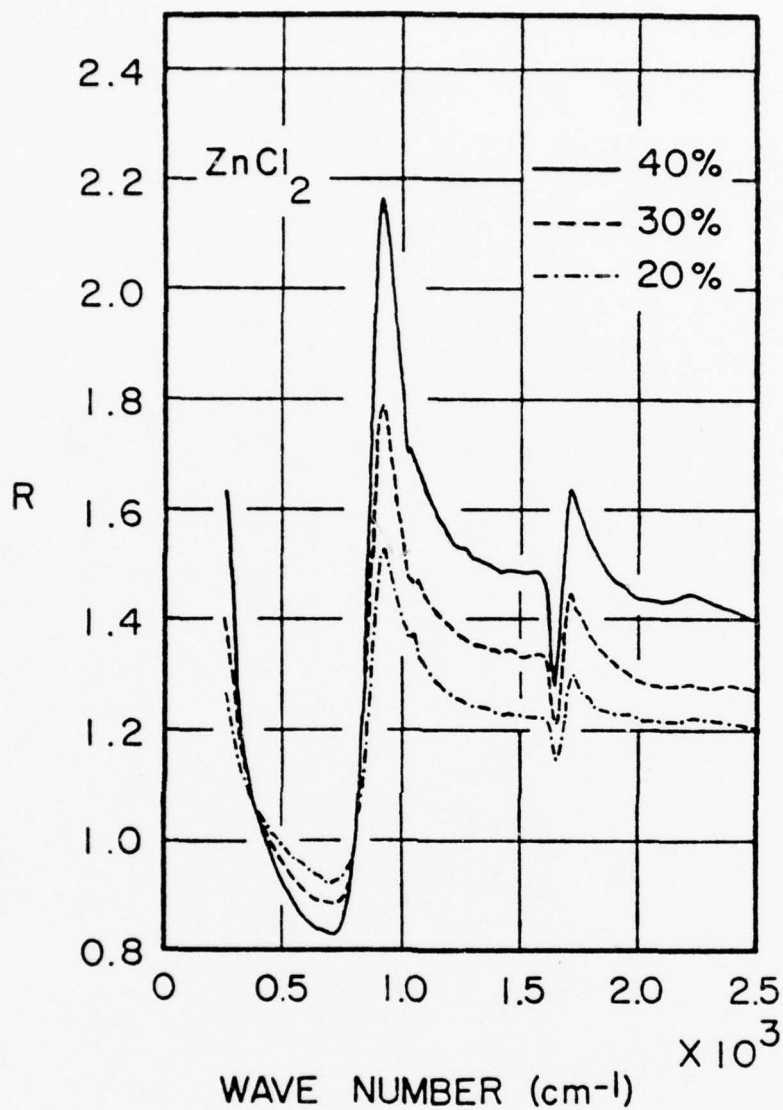


Figure 2. Near-normal incidence relative specular reflectance  $R(\nu) = R(\nu)_s / R(\nu)_w$  in the spectral region from 270 to 2500  $\text{cm}^{-1}$  for 20.3, 29.4, and 40.2 percent aqueous solutions containing  $\text{ZnCl}_2$ . Nominal values of 20, 30, and 40 percent are listed in the key for the various spectra.

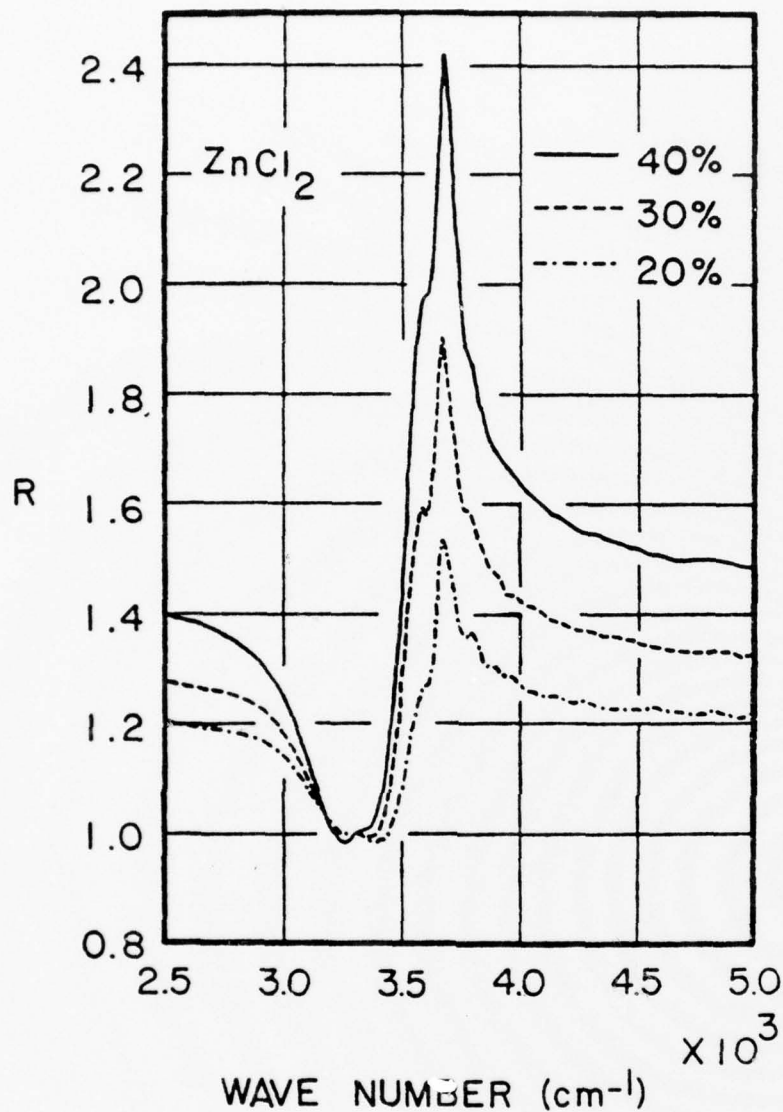


Figure 3. Near-normal incidence relative specular reflectance  $R(\nu) = R(\nu)_s / R(\nu)_w$  in the spectral region from 2500 to 5000  $\text{cm}^{-1}$  for 20.3, 29.4, and 40.2 percent aqueous solutions containing  $\text{ZnCl}_2$ . Nominal values of 20, 30, and 40 percent are listed in the key for the various spectra.

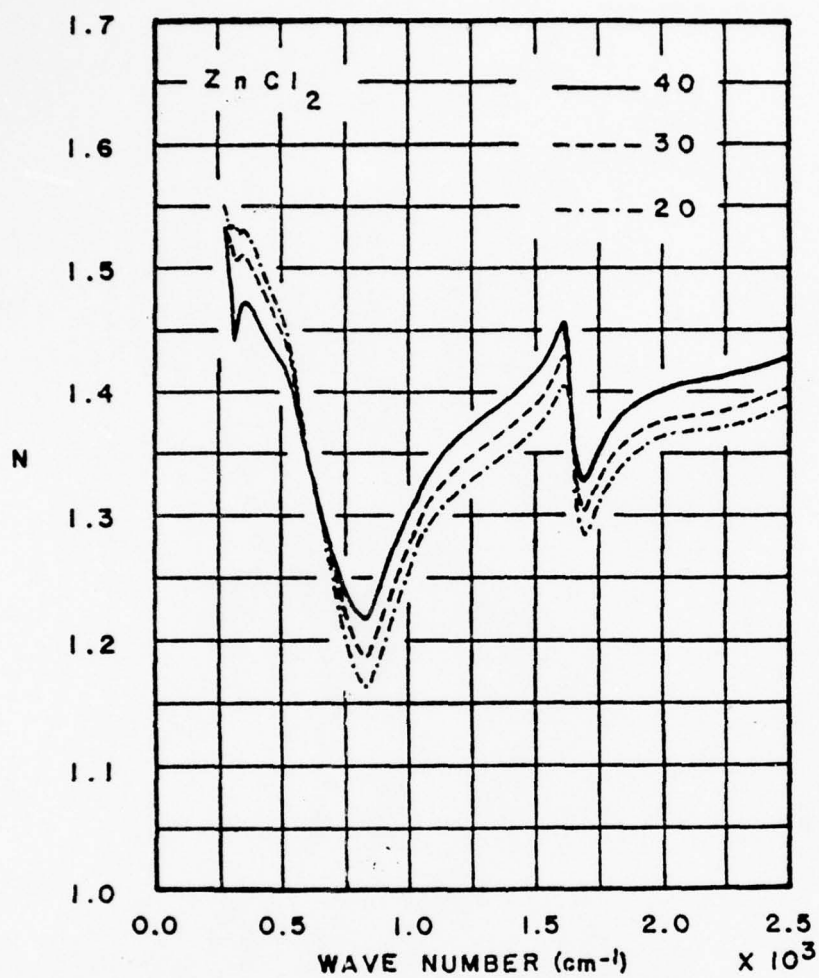


Figure 4. Index of refraction  $n(v)_s$  in the spectral region from 270 to 2500  $cm^{-1}$  for 20.3, 29.4, and 40.2 percent aqueous solutions containing  $ZnCl_2$ .

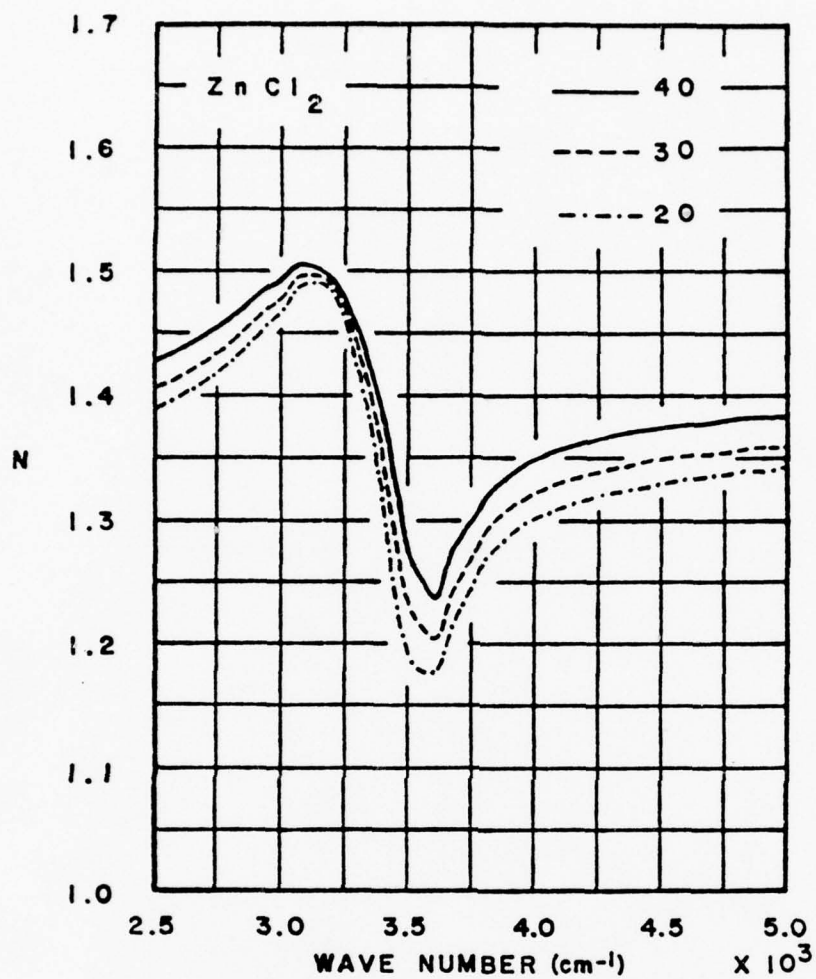


Figure 5. Index of refraction  $n(v)_s$  in the spectral region from 2500 to 5000  $\text{cm}^{-1}$  for 20.3, 29.4, and 40.2 percent aqueous solutions containing  $\text{ZnCl}_2$ .

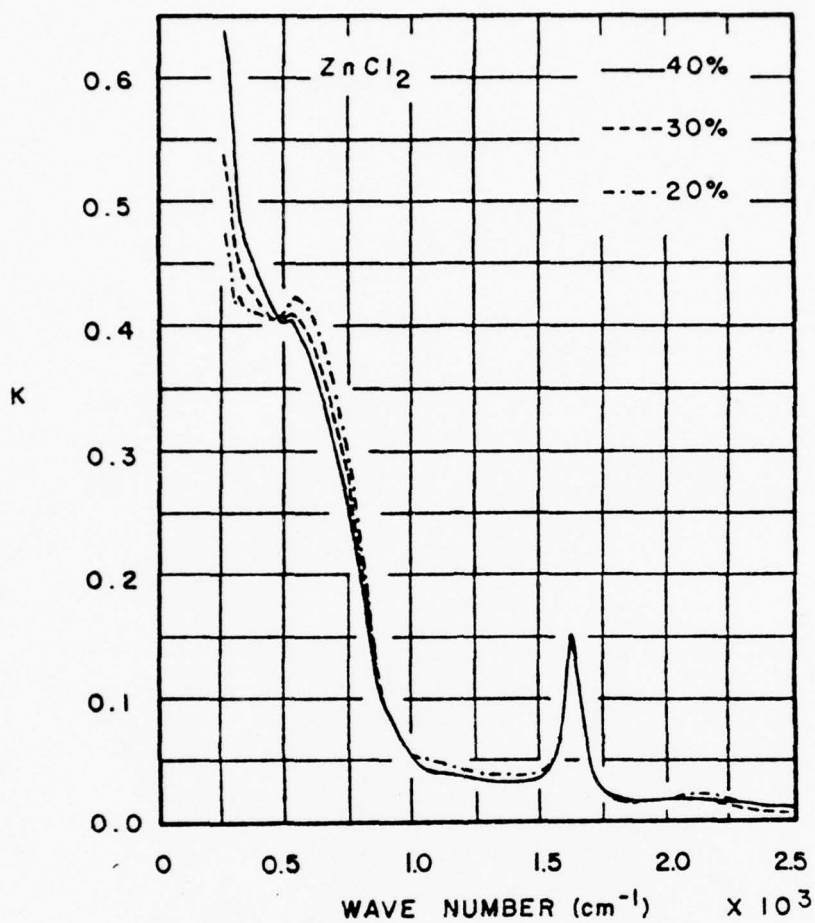


Figure 6. Extinction coefficient  $k(\nu)_s$  in the spectral region from 270 to 2500  $\text{cm}^{-1}$  for 20.3, 29.4, and 40.2 percent aqueous solutions containing  $\text{ZnCl}_2$ .

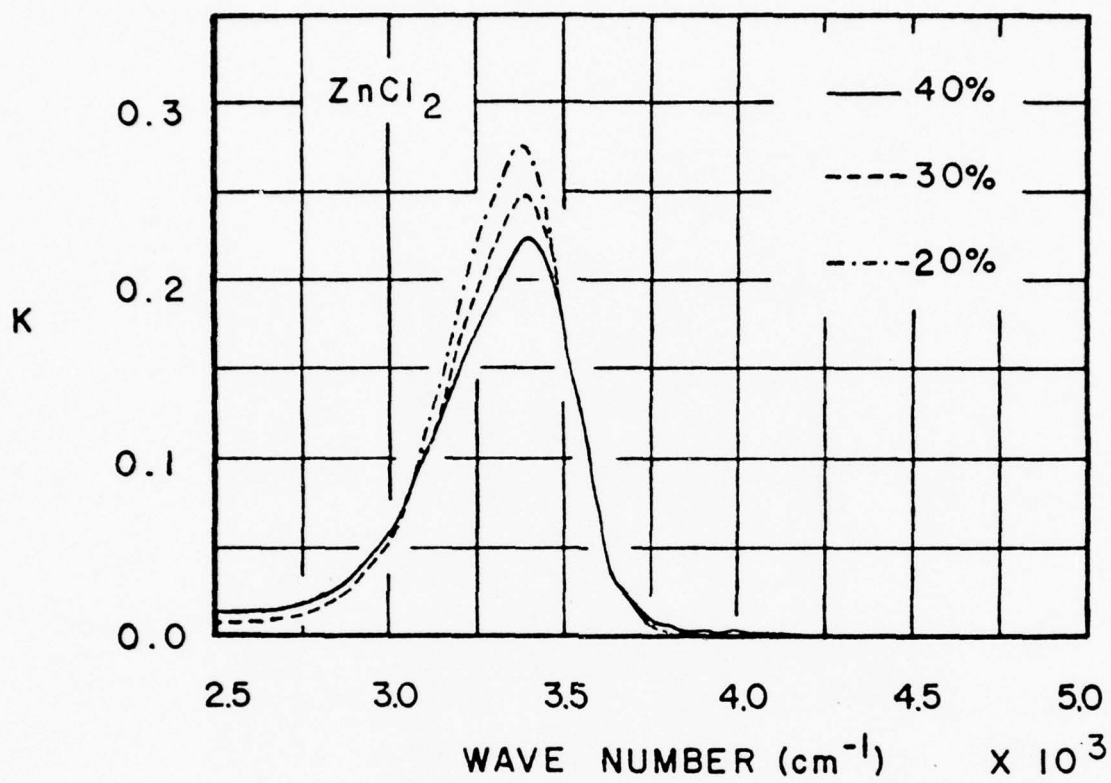


Figure 7. Extinction coefficient  $k(\nu)_s$  in the spectral region from 2500 to 5000  $\text{cm}^{-1}$  for 20.3, 29.4, and 40.2 percent aqueous solutions containing  $\text{ZnCl}_2$ .

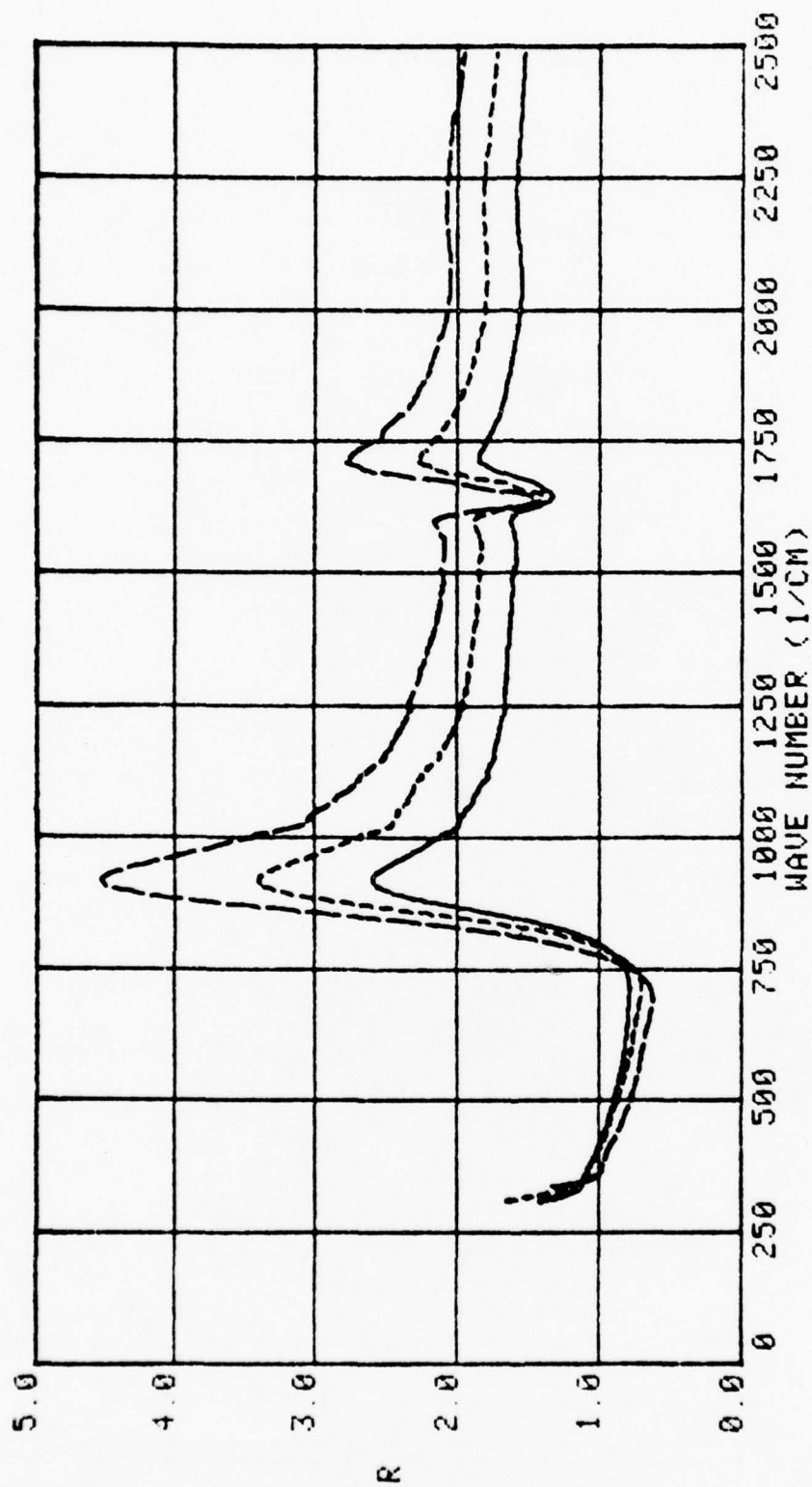


Figure 8. Near-normal incidence relative specular reflectance  $R(\nu) = R(\nu)_g/R(\nu)_w$  in the spectral range from 300 to 2,500  $\text{cm}^{-1}$  for 50, 65, and 75 percent aqueous solutions of  $\text{ZnCl}_2$ : 50%-solid line, 65% short-dashed line, and 75% long-dashed line.

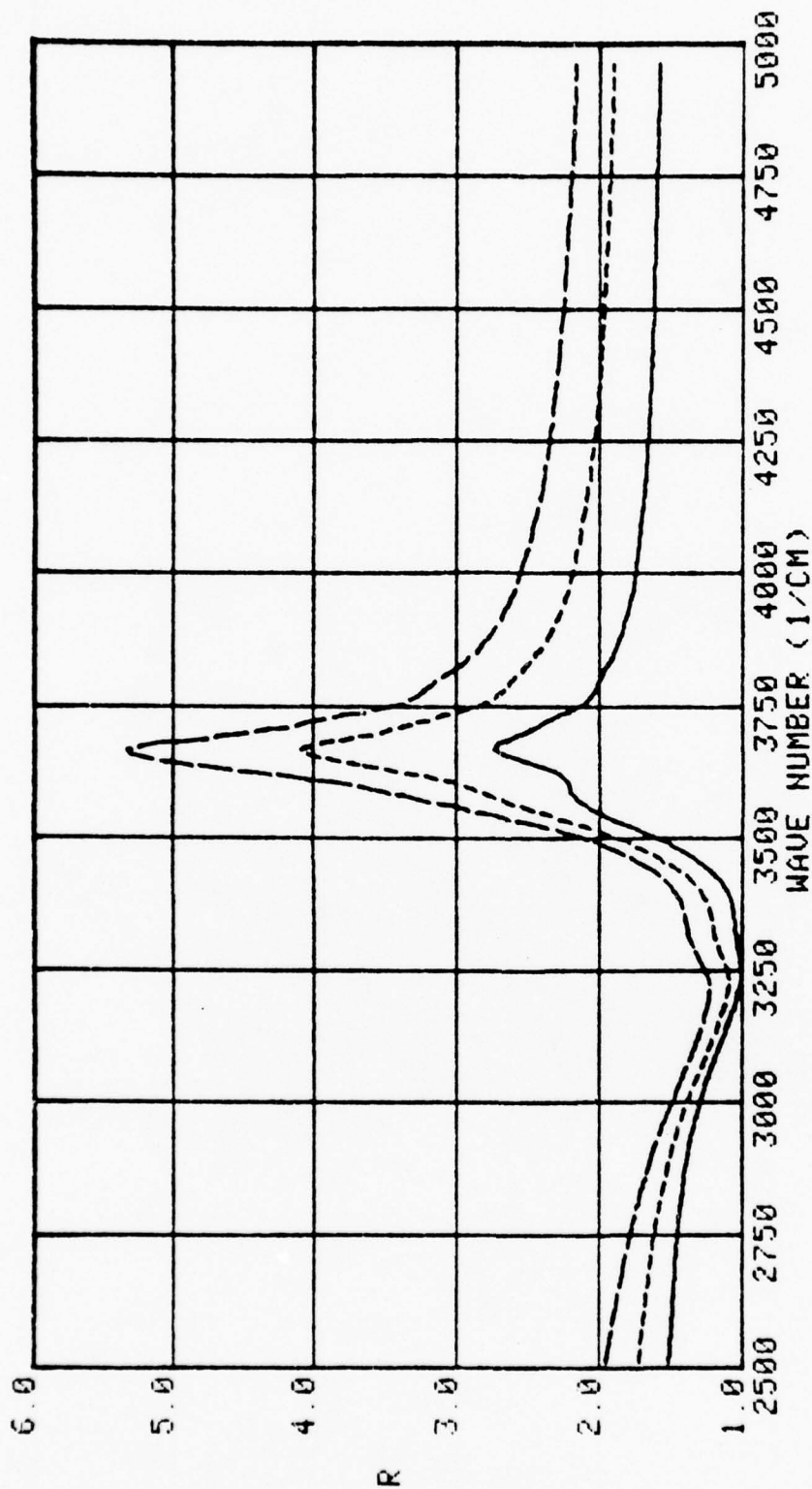


Figure 9. Near-normal incidence relative specular reflectance  $R(\nu) = R(\nu)_s / R(\nu)_w$  in the spectral range from 2,500 to 5,000  $\text{cm}^{-1}$  for 50, 65, and 75 percent aqueous solutions of  $\text{ZnCl}_2$ : 50% solid line, 65% short-dashed line, and 75% long-dashed line.

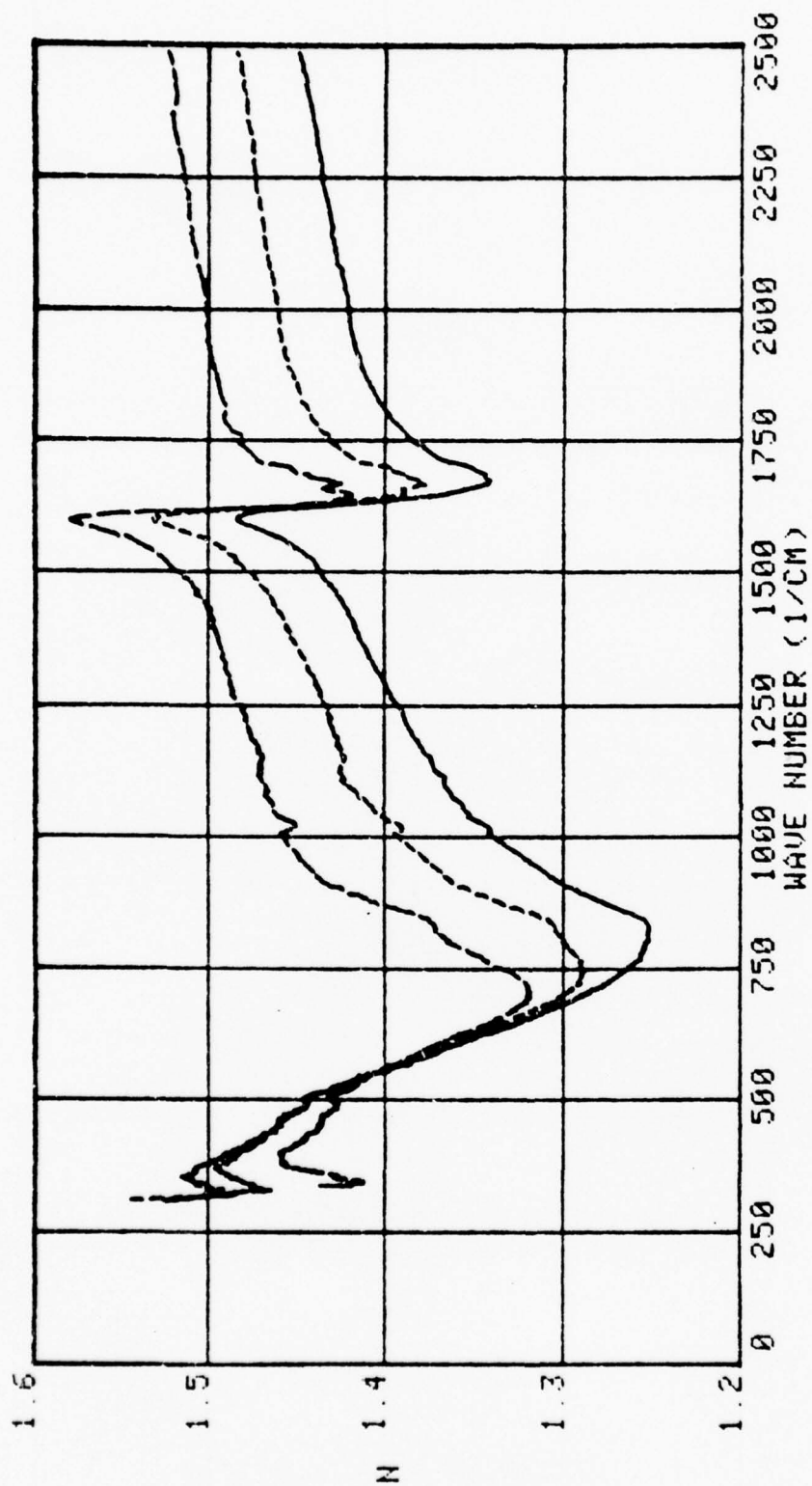


Figure 10. Index of refraction  $n(\nu)$  for 50, 65, and 75 percent aqueous solutions of  $\text{ZnCl}_2$  in the 300-2,500  $\text{cm}^{-1}$  spectral range: 50% solid line, 65% short-dashed line, and 75% long-dashed line.

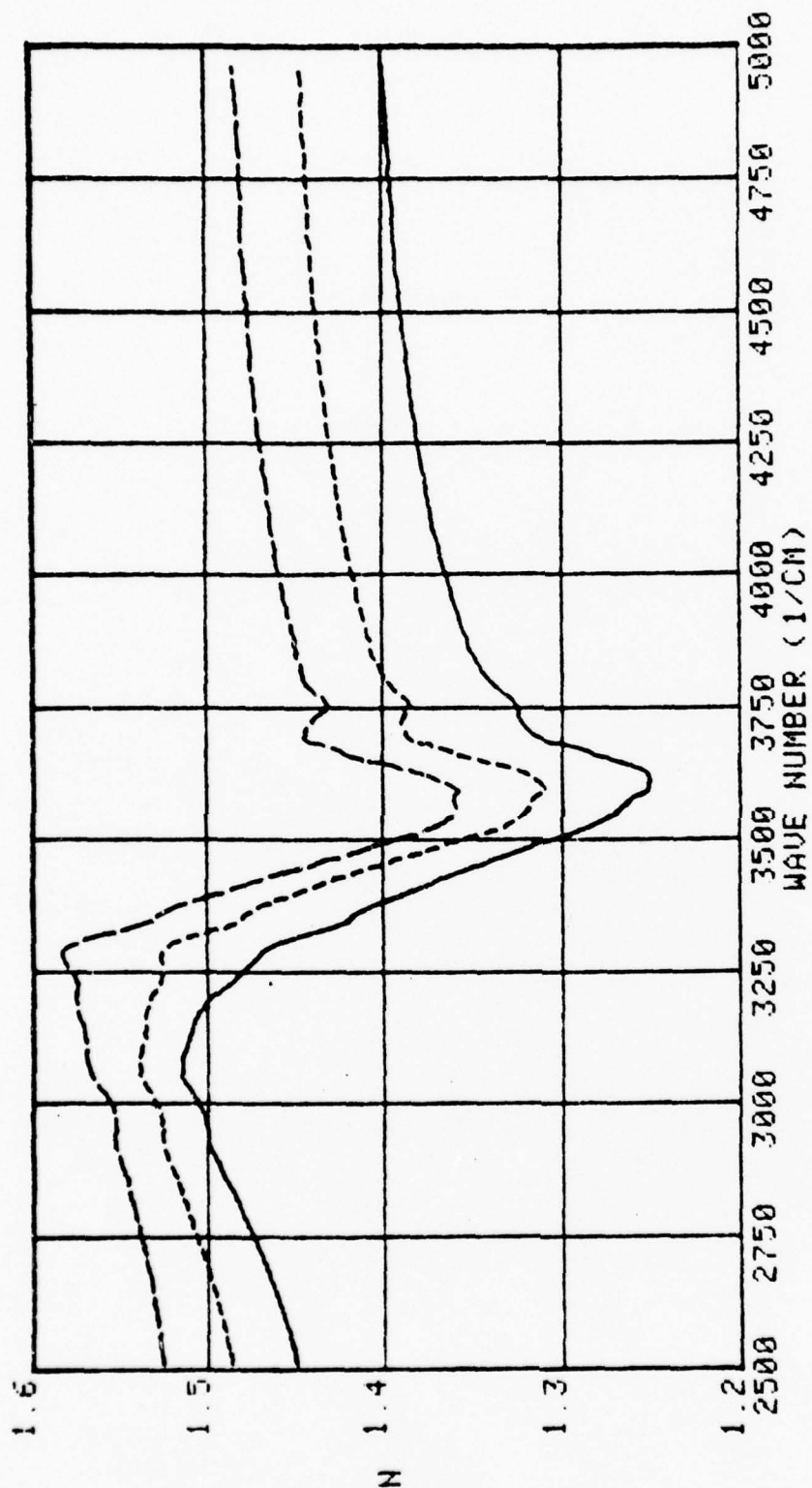


Figure 11. Index of refraction  $n(\nu)$  for 50, 65, and 75 percent aqueous solutions of  $\text{ZnCl}_2$  in the 2,500-5,000  $\text{cm}^{-1}$  spectral range: 50% solid line, 65% short-dashed line, and 75% long-dashed line.

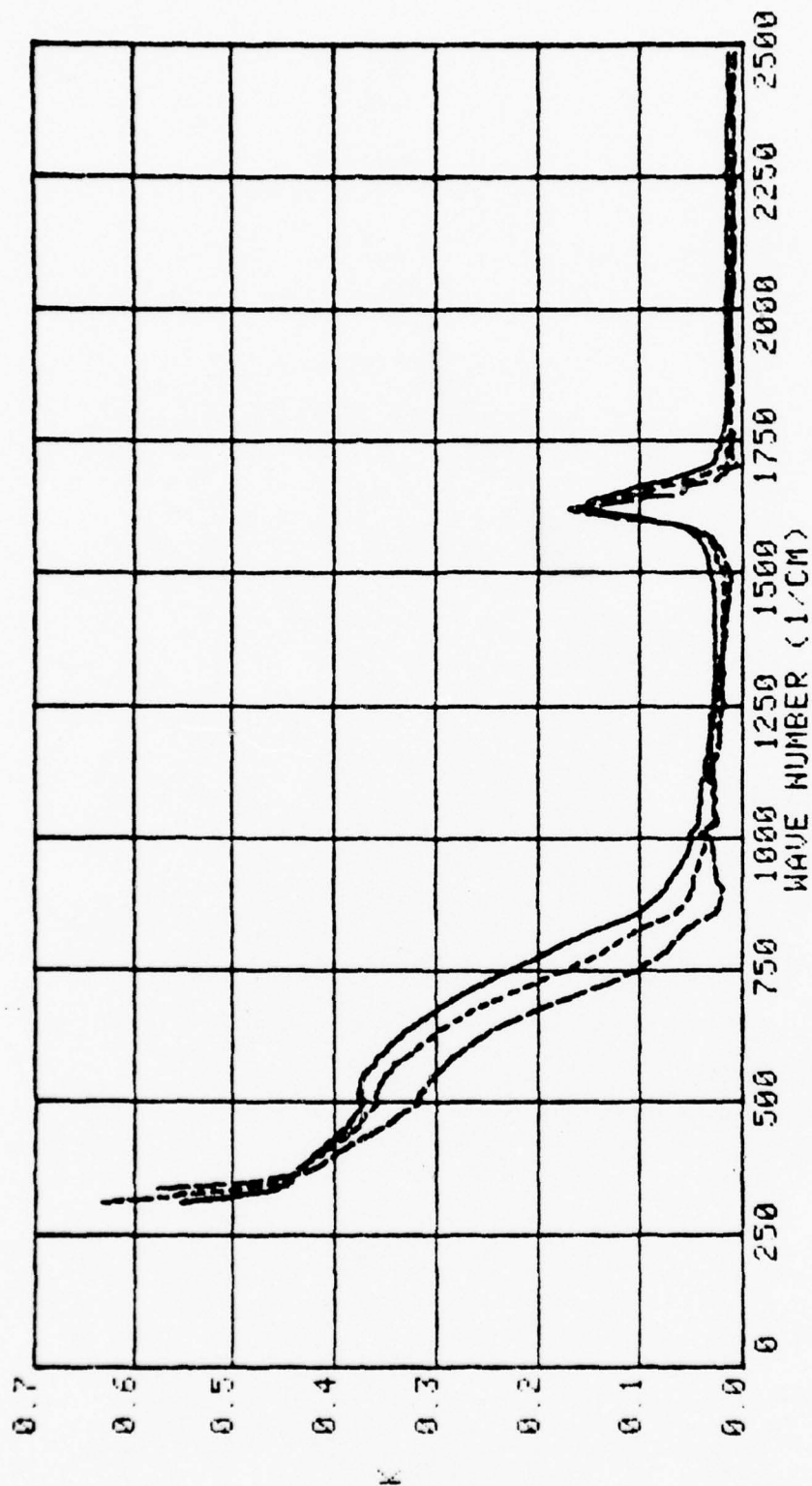


Figure 12. Extinction coefficient  $k(\nu)$  for 50, 65, and 75 percent aqueous solutions of  $\text{ZnCl}_2$  in the 300-2,500  $\text{cm}^{-1}$  spectral range: 50% solid line, 65% short-dashed line, and 75% long-dashed line.

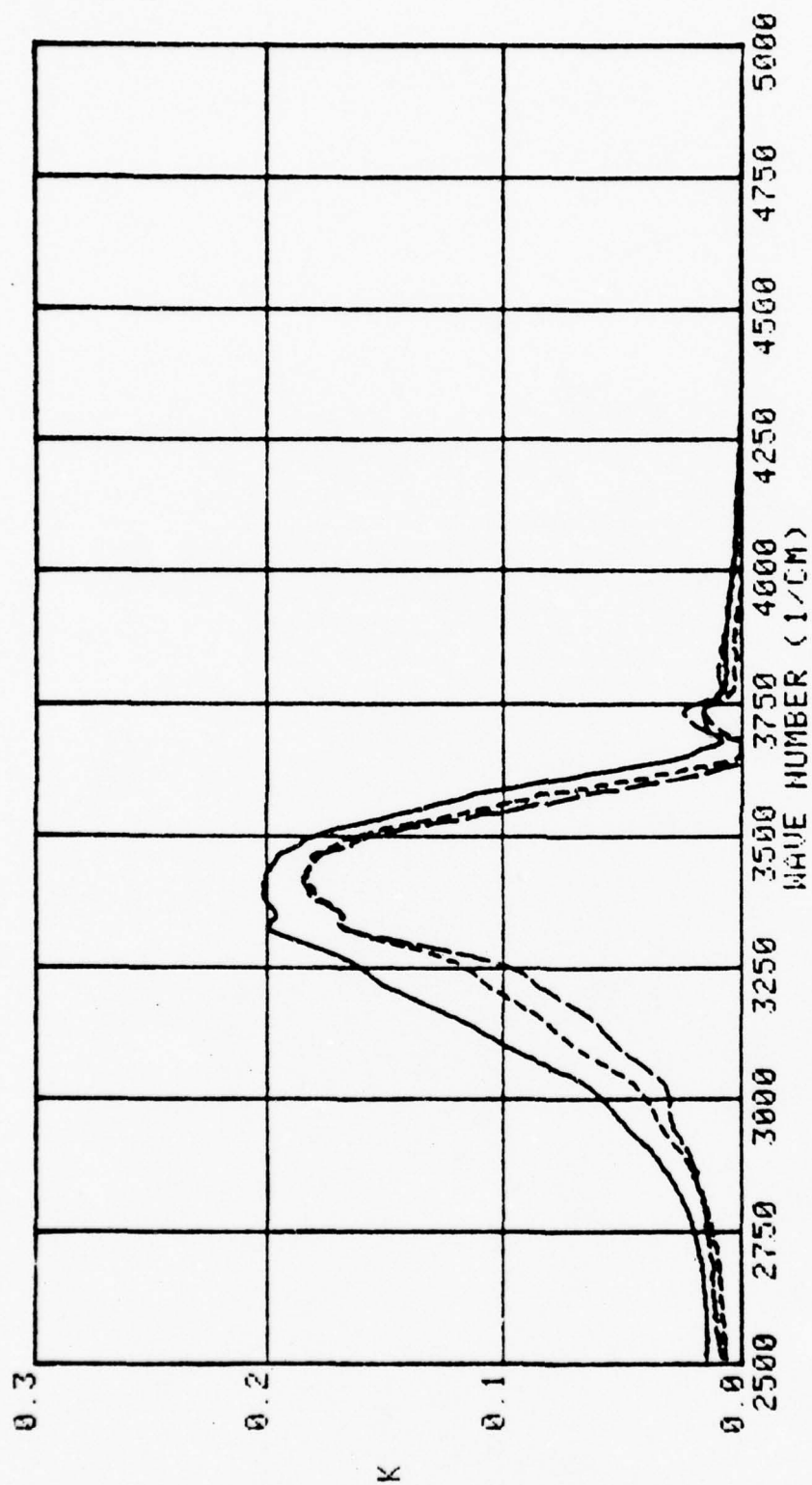


Figure 13. Extinction coefficient  $k(\nu)$  for 50, 65, and 75 percent aqueous solutions of  $\text{ZnCl}_2$  in the 2,500–5,000  $\text{cm}^{-1}$  spectral range: 50% solid line, 65% short-dashed line, and 75% long-dashed line.

and 9. The  $R(\nu)$  spectra were phase-shift analyzed by use of the Kramers-Kronig relation

$$\Delta\phi(\lambda_0) = \text{Prin.}(\lambda_0/\pi) \int_0^{\infty} \{\ln[R(\lambda)]/(\lambda_0^2 - \lambda^2)\} d\lambda, \quad (3)$$

where  $\Delta\phi(\lambda_0)$  is the difference in phase shift for electromagnetic waves of wavelength  $\lambda_0$  reflected from the surfaces of the sample and the water. The portions of the integral in Eq. (3), beyond the region in which data were acquired, were evaluated analytically by assuming constant relative reflectance  $R(\lambda) = R(\lambda_{\min})$  in the region  $0 \leq \lambda \leq \lambda_{\min}$  and  $R(\lambda) = R(\lambda_{\max})$  in the region  $\lambda_{\max} < \lambda < \infty$ .

Spectral values of  $N(\lambda)$  were then obtained for each solution by use of the results from the Kramers-Kronig analysis as input to a previously published algorithm. Values of  $N(\lambda)$  are presented in Figs. 4-7 for the 10, 20, and 30%  $\text{ZnCl}_2$  solutions, and in Figs. 10-13 for the 50, 65, and 75%  $\text{ZnCl}_2$  solutions.

d. Discussion of Spectra of  $\text{ZnCl}_2$  Solutions

Significant hydrolysis of  $\text{Zn}^{2+}$  does not occur in aqueous solutions<sup>10,19/</sup> of  $\text{ZnCl}_2$ . Thus the infrared bands of  $\text{Zn}(\text{H}_2\text{O})_6^{2+}$  at 620, 541, and 364  $\text{cm}^{-1}$  provide only weak contributions to the spectra shown in Figs. 2-13.

Raman intensity studies by Irish *et al.*<sup>10/</sup> indicate that below 4 M concentration that  $\text{ZnCl}^+$  and  $\text{ZnCl}_4^{2-}$  are predominate, and that concentrations of  $\text{ZnCl}_2$  are

insignificant.  $\text{ZnCl}^+$  is present in concentrations of about 1.3, 0.4, and 0. M in the 1.77, 2.8, and 4.19 M  $\text{ZnCl}_2$  solutions, respectively.  $\text{ZnCl}_4^{2-}$  is present in concentrations of about 0.3, 0.8, and 1.6 M in the 1.77, 2.8, and 4.19 M  $\text{ZnCl}_2$  solutions, respectively. In the 4.19 M aqueous  $\text{ZnCl}_2$  solution the  $\text{ZnCl}_2$  molecule, per se, is present at about 0.1 M concentration. In the infrared spectra obtained for the 1.77, 2.8, and 4.19 M solutions in the region from 270 to 5000  $\text{cm}^{-1}$  we expect, in addition to bands due to the water structure, broad infrared active bands at 305  $\text{cm}^{-1}$  due to  $\text{ZnCl}^+$ , at 280  $\text{cm}^{-1}$  due to the  $\nu_3(\text{F}_2)$  mode of  $\text{ZnCl}_4^{2-}$ , and in the 4.19 M solution weak contributions at 505  $\text{cm}^{-1}$  due to the  $\nu_3$  antisymmetric stretch of  $\text{ZnCl}_2$ . Additionally, ions  $\text{Zn}^{2+}$  and  $\text{Cl}^-$  will effect the positions and strengths of infrared bands due to the water structure.

The Raman intensity studies by Irish et al.<sup>10/</sup> also indicate that, for concentrations above 4 M, the species  $\text{Zn}^{2+}$ ,  $\text{ZnCl}_2$ , and  $\text{ZnCl}_4^{2-}$  are predominate.  $\text{ZnCl}_2$  is present in respective concentrations of about 0.4 and 1.9 M in the 5.75 and 8.82 M  $\text{ZnCl}_2$  solutions. The concentration of  $\text{ZnCl}_2$  for the 11.65 M solution is not known but probably exceeds 2M.  $\text{ZnCl}_4^{2-}$  is present in concentrations of about 2.2, 2.7, and 3.7 M in the 5.75, 8.82, and 11.65 M solutions, respectively. Thus,

in the infrared spectra for the 5.75, 8.82, and 11.65 M solutions we expect, in addition to bands due to water, broad infrared bands at  $280\text{ cm}^{-1}$  due to the  $\nu_3(\text{F}_2)$  mode of  $\text{ZnCl}_4^{2-}$  and at  $505\text{ cm}^{-1}$  due to the  $\nu_3$  anti-symmetric stretch of  $\text{ZnCl}_2$ . Additionally, the  $\text{Zn}^{2+}$  ions will effect the positions and strengths of the infrared bands due to water.

The relative reflectance spectra shown in Figs. 2, 3, 8, and 9 possess three general spectral features of the same type. For example, the feature extending from 270 to ca.  $1350\text{ cm}^{-1}$  and centered at ca.  $800\text{ cm}^{-1}$ . This feature is characterized by a decrease in the magnitude of the relative reflectance in the region from 270 to about  $720\text{ cm}^{-1}$ , an increase in relative reflectance in the region from about 720 to about  $900\text{ cm}^{-1}$ , and then a decrease in relative reflectance in the region from about 900 to about  $1350\text{ cm}^{-1}$ . The two other similarly shaped spectral features are centered at ca. 1680 and  $3500\text{ cm}^{-1}$ . These features are due primarily to different water content of the aqueous solutions. Note also that the relative reflectance of liquid water would be 1.0 throughout the spectrum.

The three spectral features are characterized in the spectra  $n(\nu)_s$  vs.  $\nu$  shown in Figs. 4, 5, 10, and 11 as regions of anomalous dispersion, and as peaks in the spectra  $k(\nu)_s$  vs.  $\nu$  shown in Figs. 6, 7, 12, and 13.

In applying the Kramers-Kronig analysis to the relative reflectance spectra  $R(\nu)$  we assumed that in the wave-number region from 0 to  $270\text{ cm}^{-1}$  that  $R(\nu) = R(270\text{ cm}^{-1})$ . This is a somewhat poor assumption because there are other infrared active vibrational modes of polyatomic constituents of Zn and Cl beyond  $270\text{ cm}^{-1}$ . Additionally, the full influence of the  $\text{ZnCl}^+$  band at  $305\text{ cm}^{-1}$  and the  $\text{ZnCl}_4^{2-}$  band at  $280\text{ cm}^{-1}$  extend to wave numbers below  $270\text{ cm}^{-1}$ , the beginning of the relative reflectance spectra collected in these experiments. Also, the  $505\text{ cm}^{-1}$  band of  $\text{ZnCl}_2$  occurs in the spectral region of the strong  $\nu_L$  band of water. Therefore, it is virtually impossible to extract any information about  $\text{ZnCl}^+$ ,  $\text{ZnCl}_2$ , and  $\text{ZnCl}_4^{2-}$  from these spectra except that the rapid increase in relative reflectance in the region from  $600$  to  $270\text{ cm}^{-1}$  is undoubtedly due in part to infrared activity of these three polyatomic constituents. Reflectance spectra in the region below  $270\text{ cm}^{-1}$ , obtained by Fourier Transform techniques and then joined with the spectra reported in this paper, can provide additional knowledge of the infrared parameters of  $\text{ZnCl}^+$  and  $\text{ZnCl}_4^{2-}$  in these solutions. The increase in relative reflectance from about  $700\text{ cm}^{-1}$  to  $270\text{ cm}^{-1}$  is also due to the  $\nu_L$  band of liquid water shifting to lower wave numbers as the  $\text{ZnCl}_2$  concentration increases.

The assumption that  $R(\nu) = R(270\text{ cm}^{-1})$  throughout the spectral region from 0 to  $270\text{ cm}^{-1}$  will have small influence on values computed for  $n(\nu)_s$  and  $k(\nu)_s$  for

TABLE IV. Parameters for intra- and inter-molecular vibrations of water in aqueous solutions containing  $\text{ZnCl}_2$ .

Solution	Band	$\nu_{\text{max}} (\text{cm}^{-1})$	$\Gamma (\text{cm}^{-1})$	$k(\nu)_{\text{max}}$	$S_b (\text{cm}^2/\text{H}_2\text{O molecule})$
20.3% (1.77 M)	$\nu_1, \nu_3, 2\nu_2$	3396	387+5	0.275	$(3.84 \pm 0.06) \times 10^{-21}$
29.4% (2.8 M)		3398	404+5	0.249	$(3.62 \pm 0.09) \times 10^{-21}$
40.2% (4.19 M)		3407	436+5	0.223	$(3.68 \pm 0.08) \times 10^{-21}$
20.3% (1.77 M)	$\nu_2$	1636	99+4	0.144	$(4.07 \pm 0.30) \times 10^{-22}$
29.4% (2.8 M)		1634	94+4	0.147	$(4.10 \pm 0.29) \times 10^{-22}$
40.2% (4.19 M)		1631	92+4	0.151	$(4.43 \pm 0.21) \times 10^{-22}$
20.3% (1.77 M)	$\nu_L$	545+4	548+5	0.422	$(5.23 \pm 0.12) \times 10^{-21}$ [7.35x10 <sup>-21</sup> ]
29.4% (2.8 M)		538+4	552+5	0.411	$(6.00 \pm 0.06) \times 10^{-21}$ [7.85x10 <sup>-21</sup> ]
40.2% (4.19 M)		526+4	550+5	0.405	$(6.09 \pm 0.06) \times 10^{-21}$ [7.10x10 <sup>-21</sup> ]

greater than about  $500\text{ cm}^{-1}$ .

The spectra  $k(\nu)_s$  vs.  $\nu$  shown in Figs. 6, 7, 12, and 13 provide parameters  $k(\nu)_{\max}$ ,  $\nu_{\max}$ ,  $\Gamma$ , and  $S_b$  listed in Table IV for the infrared bands  $\nu_L$ ,  $\nu_2$ , and the combined contributions of  $\nu_1$ ,  $\nu_3$ , and  $2\nu_2$  of liquid water. Referring to Table IV we note for the infrared band comprising intra-molecular vibrations  $\nu_1$ ,  $\nu_3$ , and  $2\nu_2$  that as the  $\text{ZnCl}_2$  concentration increases,  $\nu_{\max}$  shifts to higher frequencies,  $\Gamma$  increases,  $k(\nu)_{\max}$  decreases, and  $S_b$  decreases and then either increases or remains about the same. Similarly, as the  $\text{ZnCl}_2$  concentration increases, we note for the infrared band comprising intra-molecular vibration  $\nu_2$  that  $\nu_{\max}$  shifts to lower frequencies,  $\Gamma$  decreases,  $k(\nu)_{\max}$  increases, and  $S_b$  increases. We also note from Fig. 6 that the contribution of the  $\nu_2$  band to  $k(\nu)$  is superimposed with a general absorption which decreases slowly from  $1000$  to  $2400\text{ cm}^{-1}$ . This general absorption is due to temporal water clusters and is possibly due in part to water molecules coordinated with  $\text{Zn}^{2+}$  ions. The general absorption also contributes to the values tabulated for  $k(\nu)_{\max}$  for the  $\nu_2$  band. For the  $\nu_L$  band comprising inter-molecular vibrations, as the  $\text{ZnCl}_2$  concentration increases,  $\nu_{\max}$  shifts to lower frequencies,  $\Gamma$  remains about the same,  $k(\nu)_{\max}$  decreases, and  $S_b$  increases. Two values of  $S_b$  are tabulated for the  $\nu_L$  band in each solution; the lower value in Table IV denotes deletion of the general absorption which was manually

extended into the spectral region spanned by the  $\nu_L$  band, and the higher value includes the contribution from this general absorption. The integration indicated in Eq. (1) was made manually in each case by use of a planimeter. The limits on the integrals were from 2600 to 4000  $\text{cm}^{-1}$  for the  $\nu_1$ ,  $\nu_3$ , and  $2\nu_2$  band, from 1280 to 1810  $\text{cm}^{-1}$  for the  $\nu_2$  band, and from  $\nu_{\text{max}}$  to 1140  $\text{cm}^{-1}$  for the  $\nu_L$  band. Parameters  $\Gamma$  and  $S_b$  for the  $\nu_L$  band were obtained by considering only the high-frequency side of the band and then multiplying the results by 2 before entry in Table IV. The increase in  $S_b$  measured for the  $\nu_L$  band of liquid water shown in Table IV is probably due to infrared activity of  $\text{Zn}(\text{H}_2\text{O})_6^{2+}$  at 620 and 541  $\text{cm}^{-1}$  in all three solutions, and also to infrared activity of  $\text{ZnCl}_2$  at 505  $\text{cm}^{-1}$  in the 4.19 M solution.

Parameters  $\Gamma$  and  $S_b$  were not measured for the  $\nu_L$  water band in the 5.75, 8.82, and 11.7 M solutions, because of significant contributions of unknown magnitude due to bands associated with  $\text{ZnCl}_2$  and  $\text{ZnCl}_4^{2-}$ .

### 3. Aqueous Solutions of $H_3PO_4$

#### a. Objectives

The principal objectives for this investigation were: (1) to obtain, for aqueous solutions of  $H_3PO_4$ , spectral values of  $N(\nu) = n(\nu) + ik(\nu)$  which were suitable for computing Mie-scattering parameters, and (2) to measure central frequencies, half-widths, and band strengths of inter- and intra-molecular infrared-active vibrational modes of liquid water,  $H_3PO_4$ , and molecular products of due to dissociation of  $H_3PO_4$  in aqueous solution. The methods used to accomplish these objectives were the same as those described in Section V.A.2.a. Nine phosphoric acid samples were investigated: 5, 10, 20, 40, 50, 65, 75 solutions, an 85% solution at 25°C, and an 85% solution at about -10°C. In terms of molar concentrations the  $H_3PO_4$  solutions were 0.52, 1.07, 2.27, 5.12, 6.81, 9.78, 12.08, and 14.65M, respectively.

#### b. Background Information for Discussion of $H_3PO_4$ Solutions

Knowledge of the optical properties of aqueous solutions of  $H_3PO_4$  is of both practical and basic importance. From the practical point of view, clouds, which are ultimately composed of  $H_3PO_4$ , are produced in the earth's atmosphere by combustion of white, yellow, or red phosphorus. Computation of radiation transport through such clouds relies primarily on Mie-scattering theory, which requires prior knowledge of  $N(\nu)$  of the cloud's constituents.

The basic importance of aqueous  $\text{H}_3\text{PO}_4$  solutions lies in an interest in the hydrogen bonded structure of liquid water and the stoichiometry of acid solutions. Present knowledge of the structure of liquid water, as it applies to this investigation, was reviewed in Section V.A.2.b. The known structure and stoichiometry of aqueous solutions of  $\text{H}_3\text{PO}_4$  are reviewed here, with emphasis on those properties providing greater understanding of the accurate measurements of infrared reflectance spectra described hereinafter.

Preston and Adams<sup>20/</sup> investigated Raman spectra of aqueous solutions of  $\text{H}_3\text{PO}_4$  ranging in concentration from 0.005 M to 15.6 M. They found that the Raman spectra could be reasonably accounted for by liquid water, undissociated  $\text{H}_3\text{PO}_4$ , and the anion  $\text{H}_2\text{PO}_4^-$ . The degree of dissociation, according to their investigations, falls from about 0.5 at 0.01 M concentration to 0.1 in the 1-2 M range of concentrations, and remains at about 0.1 up to concentrations of 15.7 M. Based on a molecular model of  $\text{H}_3\text{PO}_4$  of the form  $\text{OPX}_3$ , where X designates O-H, possessing  $\text{C}_{3v}$  symmetry, Preston and Adams assigned the following bands:

$\nu_1(\text{A}_1)$	885 $\text{cm}^{-1}$	$\text{PX}_3$	symmetric stretch
$\nu_2(\text{A}_1)$	498 $\text{cm}^{-1}$	$\text{PX}_3$	deformation
$\nu_3(\text{A}_1)$	1165 $\text{cm}^{-1}$	PO	stretch
$\nu_4(\text{E})$	1007 $\text{cm}^{-1}$	$\text{PX}_3$	asymmetric stretch
$\nu_5(\text{E})$	500 $\text{cm}^{-1}$	$\text{PX}_3$	deformation
$\nu_6(\text{E})$	370 $\text{cm}^{-1}$	$\text{PX}_3$	bend.

These bands would also be infrared active.

The  $\text{OPX}_3$  molecular model, however, does not provide for O-H vibrations. The reduced representation of molecular  $\text{H}_3\text{PO}_4$  with  $\text{C}_{3v}$  point group symmetry is

$$\Gamma = 5A_1 + A_2 + 6E.$$

The  $A_1$  species are: O-H stretch, P-O stretch, P-O<sub>3</sub> stretch, PO<sub>3</sub> deformation, P-O-H inplane bend, and P-O-H out-of-plane bend. The  $A_2$  species is a P-O-H out-of-plane bend. And, the doubly degenerate E species are: O-H stretch, P-O<sub>3</sub> stretch, PO<sub>3</sub> deformation, P-O-H inplane bend, and P-O-H out-of-plane bend. The  $A_1$  and E species are infrared and Raman active, and the  $A_2$  species is inactive. In the absence of previous normal coordinate analysis of  $\text{H}_3\text{PO}_4$ , we are currently undertaking a normal coordinate analysis to better assign the bands of  $\text{H}_3\text{PO}_4$ .

The structure of the anion  $\text{H}_2\text{PO}_4^-$  is not clearly understood in aqueous solutions, and the possibility of hydrogen bonding makes it doubtful that the anion, per se, exists in the solutions. However, as with the  $\text{HNO}_3$  solutions which are discussed in Section V.A.4., the infrared spectra of  $\text{H}_3\text{PO}_4$  will also be characterized by bands due to  $\text{H}_2\text{PO}_4^-$ . The anion  $\text{H}_2\text{PO}_4^-$  cannot possess symmetry greater than  $\text{C}_{2v}$ , for which the reduced representation is

$$\Gamma = 6A_1 + 2A_2 + 4B_1 + 3B_2.$$

The  $A_1$ ,  $B_1$ , and  $B_2$  species are infrared active. If the symmetry is  $\text{C}_2$ , rather than  $\text{C}_{2v}$ , then the reduced representation is

$$\Gamma = 8A + 7B;$$

and the A and B species are infrared active.

Chapman and Thirlwell<sup>21/</sup> previously investigated the infrared and Raman spectra of orthophosphates and assigned the following bands for  $H_2PO_4^-$ :

2900-3000 $cm^{-1}$	O-H stretch
2380 $cm^{-1}$	O-H stretch
1830 $cm^{-1}$	Combination band
1230 $cm^{-1}$	P-O-H in-plane deformation
1076 $cm^{-1}$	$PO_3$ stretch
988 $cm^{-1}$	$PO_3$ stretch
862 $cm^{-1}$	P-O-H stretch
520- 590 $cm^{-1}$	OPO bending
455 $cm^{-1}$	OPO bending.

c. R(v) and N(v) Spectra of  $H_3PO_4$  Solutions.

The measured relative reflectance spectra R(v) in the spectral region from 0-2,500  $cm^{-1}$  for 5, 10, 20, and 40 per cent solutions of  $H_3PO_4$  are presented in Fig. 14. The R(v) spectra for these four relatively weak aqueous solutions varied little from a value of  $R(v) = 1.0$  throughout the 2,500-5,000  $cm^{-1}$  region, and therefore are not presented graphically in this report. The R(v) spectra for 50, 65, 75, and 85 per cent aqueous solutions of  $H_3PO_4$  are presented in Figs. 19 and 20, and the R(v) spectra for the 85 per cent solution at 25°C and -10°C are presented in Figs. 25 and 26.

The relative reflectance spectrum of each solution was analyzed by use of the Kramers-Kronig techniques

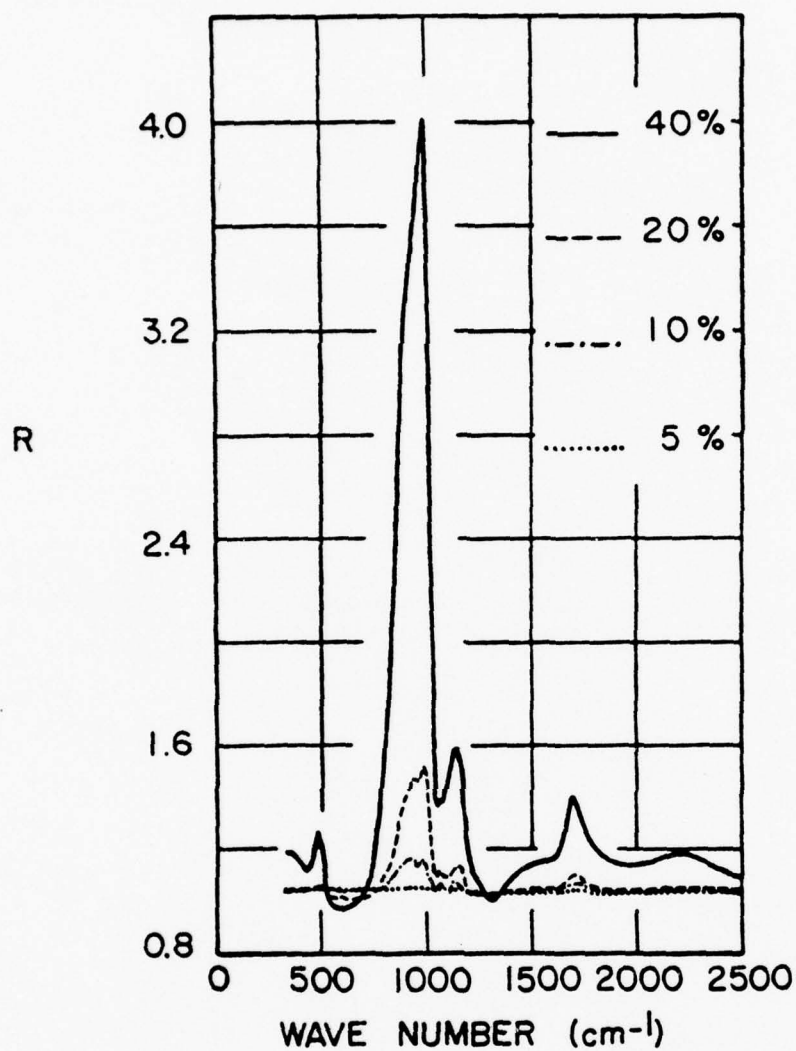


Figure 14. Near-normal incidence relative specular reflectance  $R(\nu)$  in the 300-2,500  $\text{cm}^{-1}$  spectral range for 5, 10, 20, and 40 percent aqueous solutions of  $\text{H}_3\text{PO}_4$ .

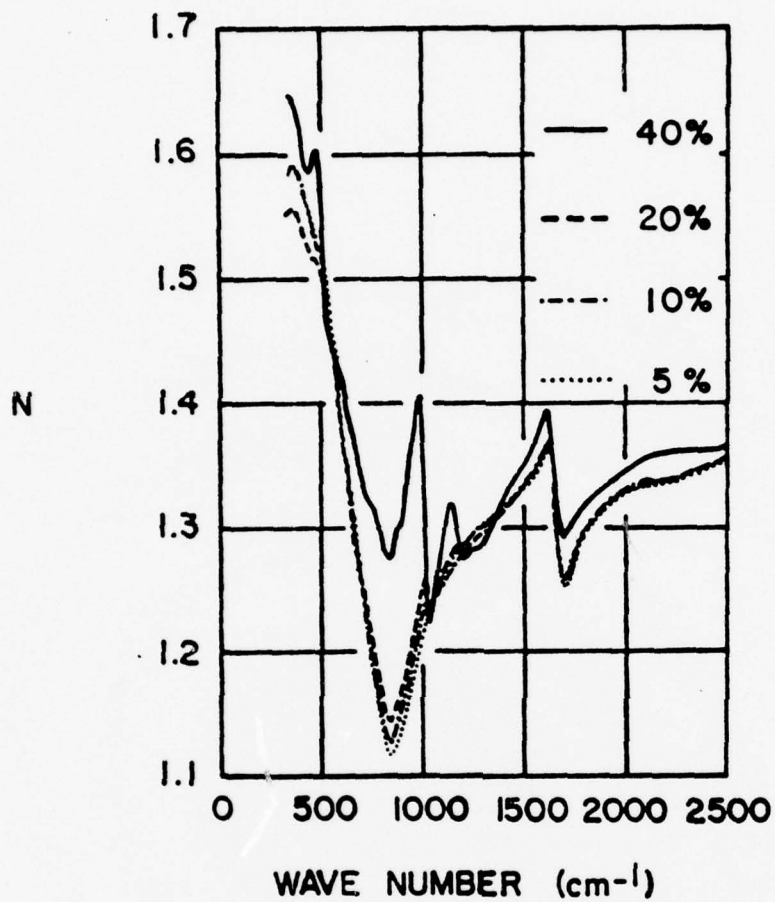


Figure 15. Index of refraction  $n(\nu)$  in the 300-2,500  $\text{cm}^{-1}$  spectral range for 5, 10, 20, and 40 percent aqueous solutions of  $\text{H}_3\text{PO}_4$ .

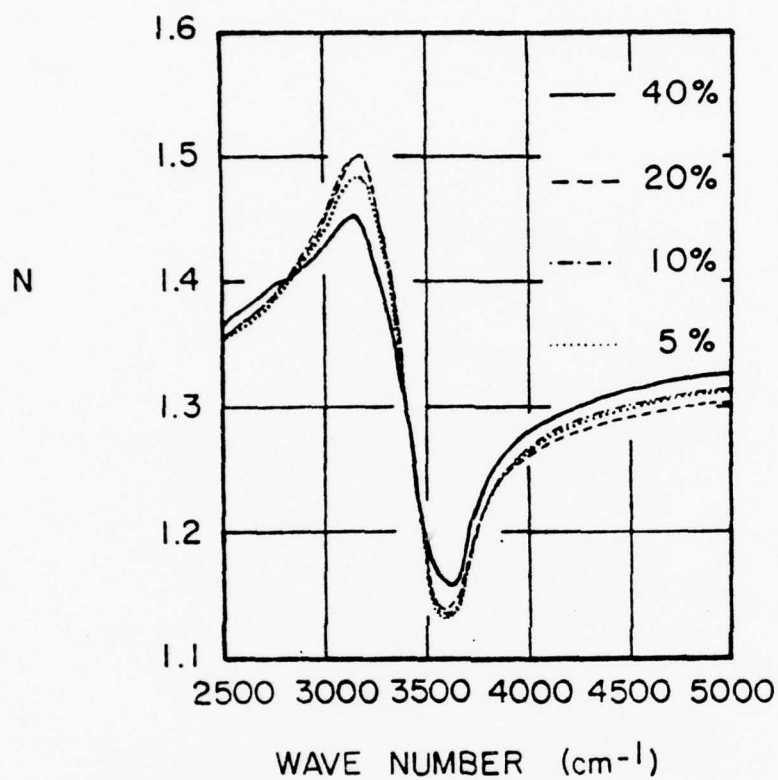


Figure 16. Index of refraction  $n(\nu)$  in the 2,500-5,000  $\text{cm}^{-1}$  spectral range for 5, 10, 20, and 40 percent aqueous solutions of  $\text{H}_3\text{PO}_4$ .

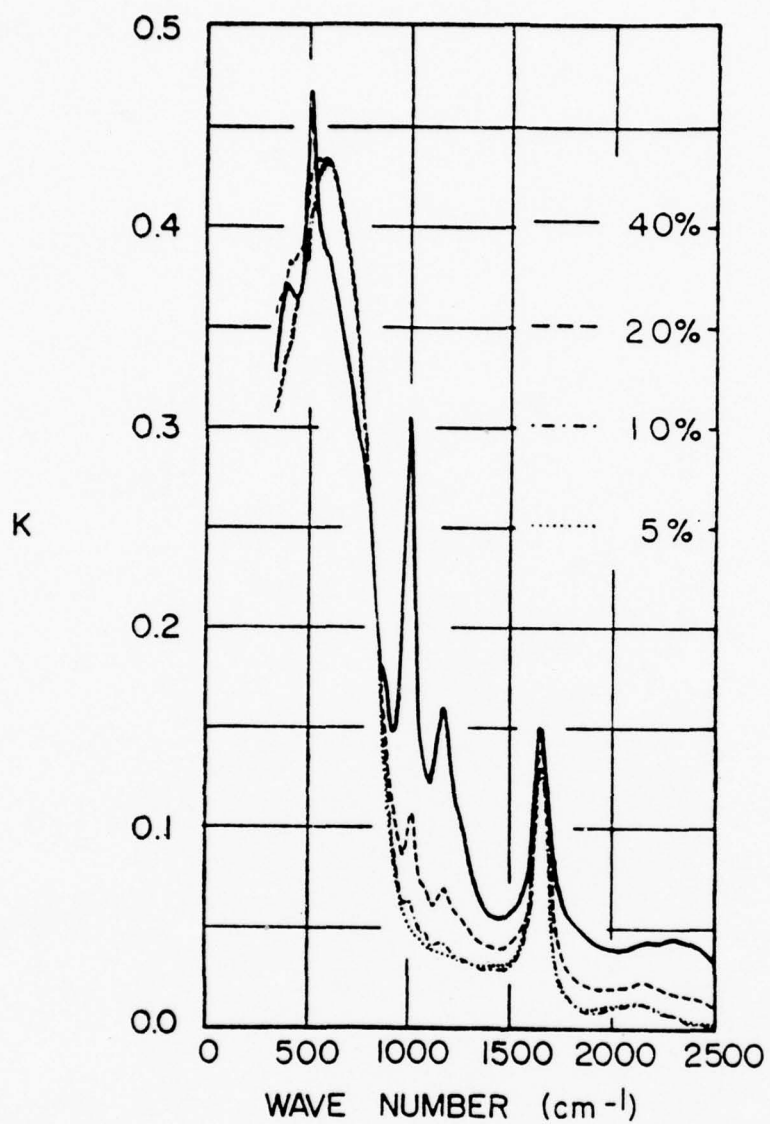


Figure 17. Extinction coefficient  $k(\nu)$  in the 300-2,500  $\text{cm}^{-1}$  spectral range for 5, 10, 20, and 40 percent aqueous solutions of  $\text{H}_3\text{PO}_4$ .

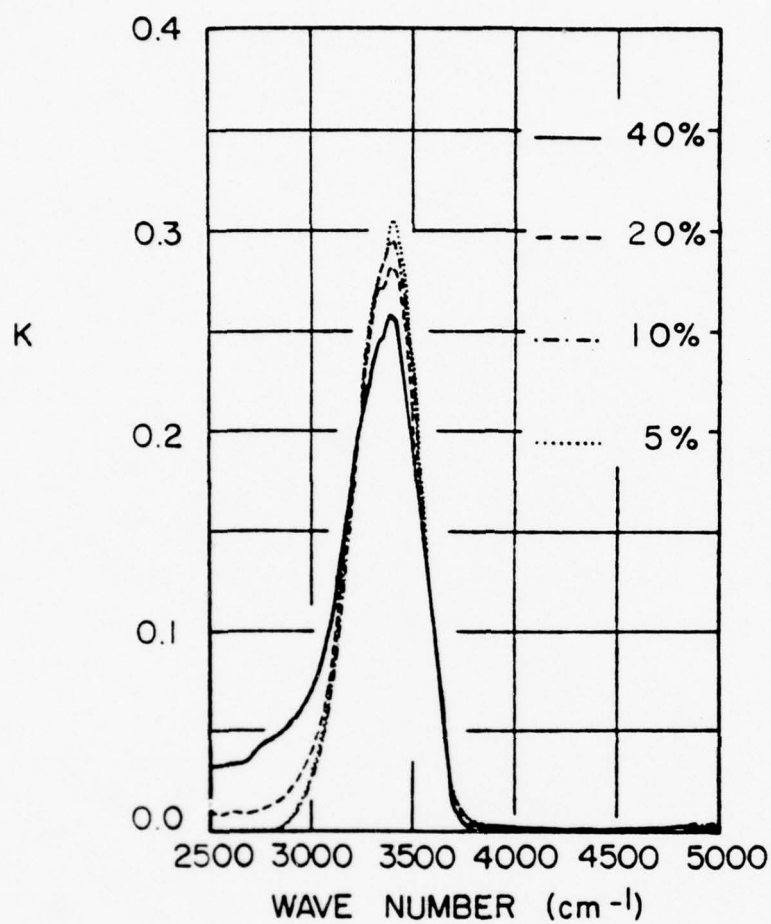


Figure 18. Extinction coefficient  $k(\nu)$  in the 2,500-5,000  $\text{cm}^{-1}$  spectral range for 5, 10, 20, and 40 percent aqueous solutions of  $\text{H}_3\text{PO}_4$ .

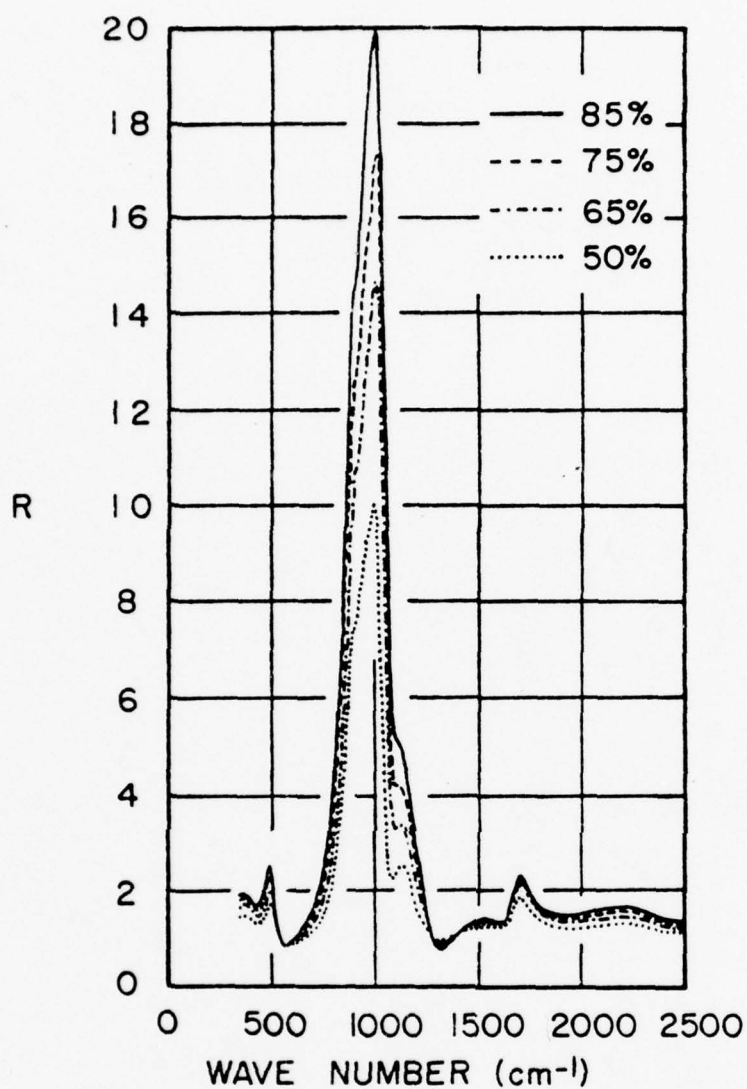


Figure 19. Near-normal incidence relative reflectance  $R(\nu)$  in the 300-2,500  $\text{cm}^{-1}$  spectral range for 50, 65, 75, and 85 percent aqueous solutions of  $\text{H}_3\text{PO}_4$ .

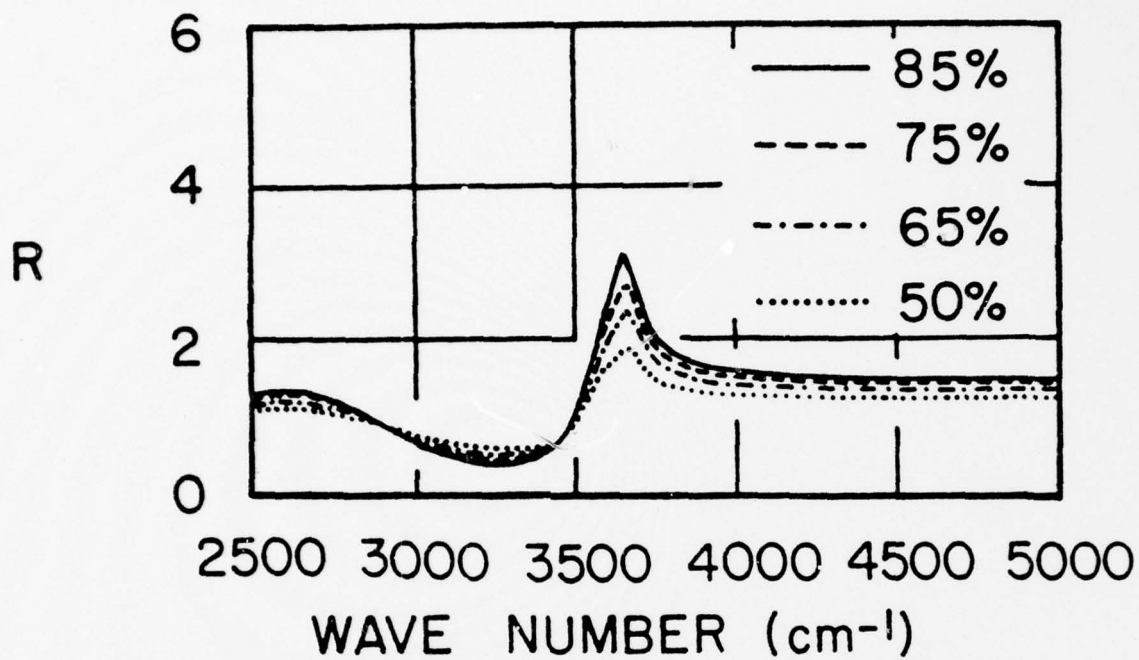


Figure 20. Near-normal incidence relative specular reflectance  $R(\nu)$  in the 2,500-5,000  $\text{cm}^{-1}$  spectral range for 50, 65, 75, and 85 percent aqueous solutions of  $\text{H}_3\text{PO}_4$ .

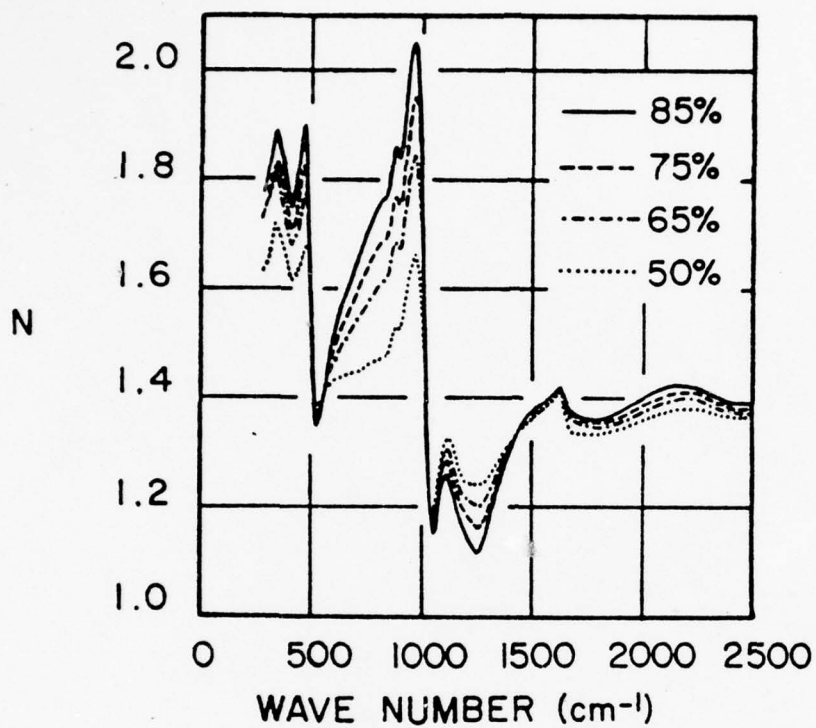


Figure 21. Index of refraction  $n(\nu)$  in the  $300\text{--}2,500\text{ cm}^{-1}$  spectral range for 50, 65, 75, and 85 percent aqueous solutions of  $\text{H}_3\text{PO}_4$ .

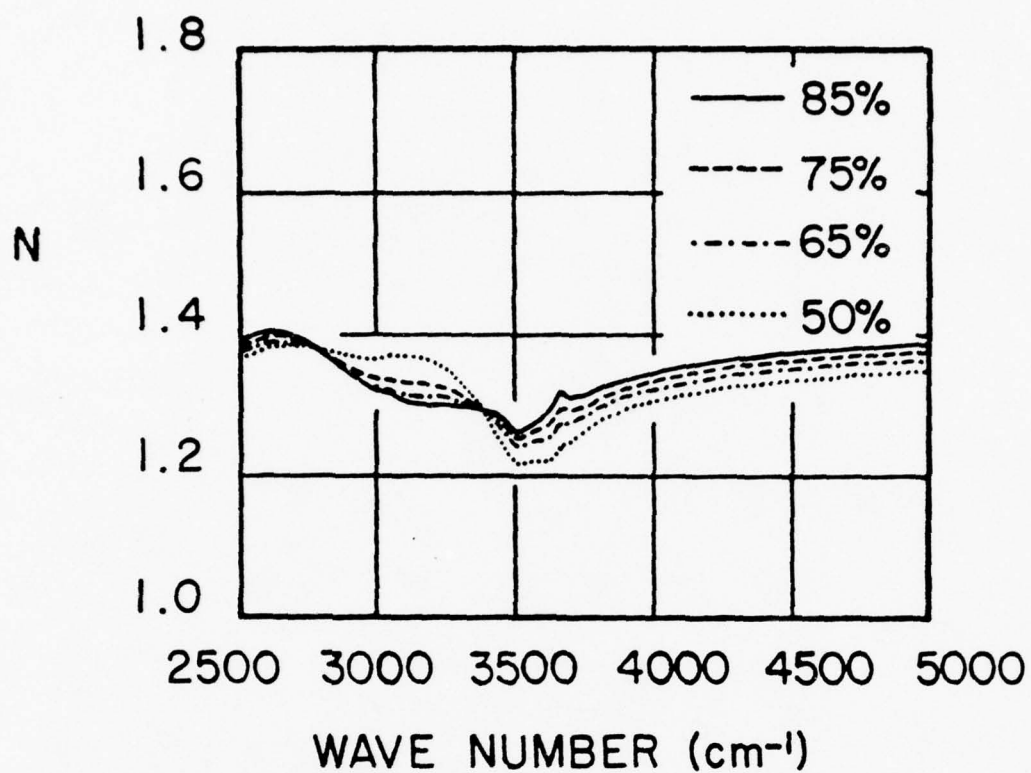


Figure 22. Index of refraction  $n(\nu)$  in the 2,500-5,000  $\text{cm}^{-1}$  spectral range for 50, 65, 75, and 85 percent aqueous solutions of  $\text{H}_3\text{PO}_4$ .

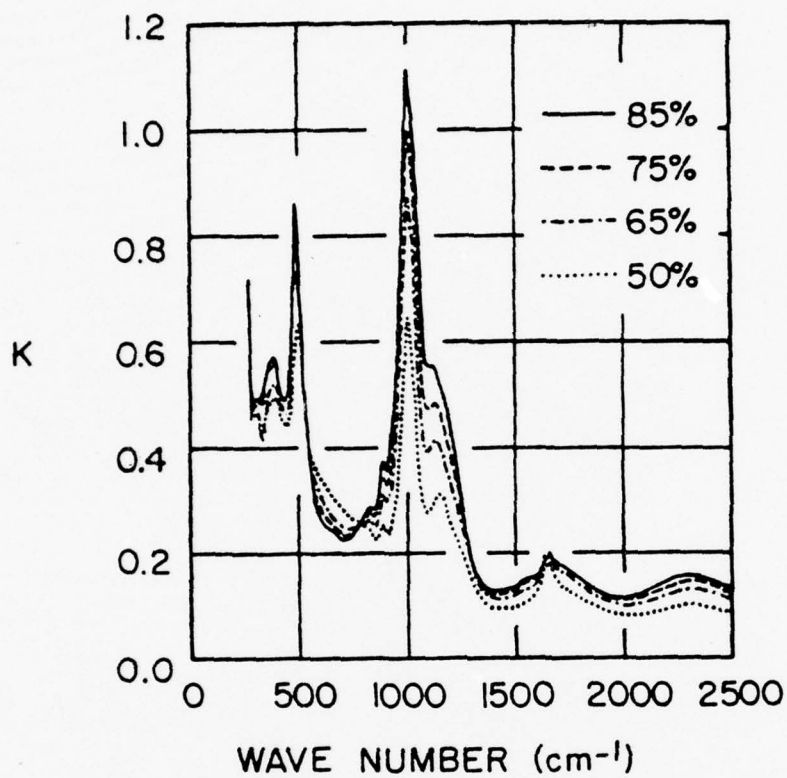


Figure 23. Extinction coefficient  $k(\nu)$  in the 300-2,500  $\text{cm}^{-1}$  spectral range for 50, 65, 75, and 85 percent aqueous solutions of  $\text{H}_3\text{PO}_4$ .

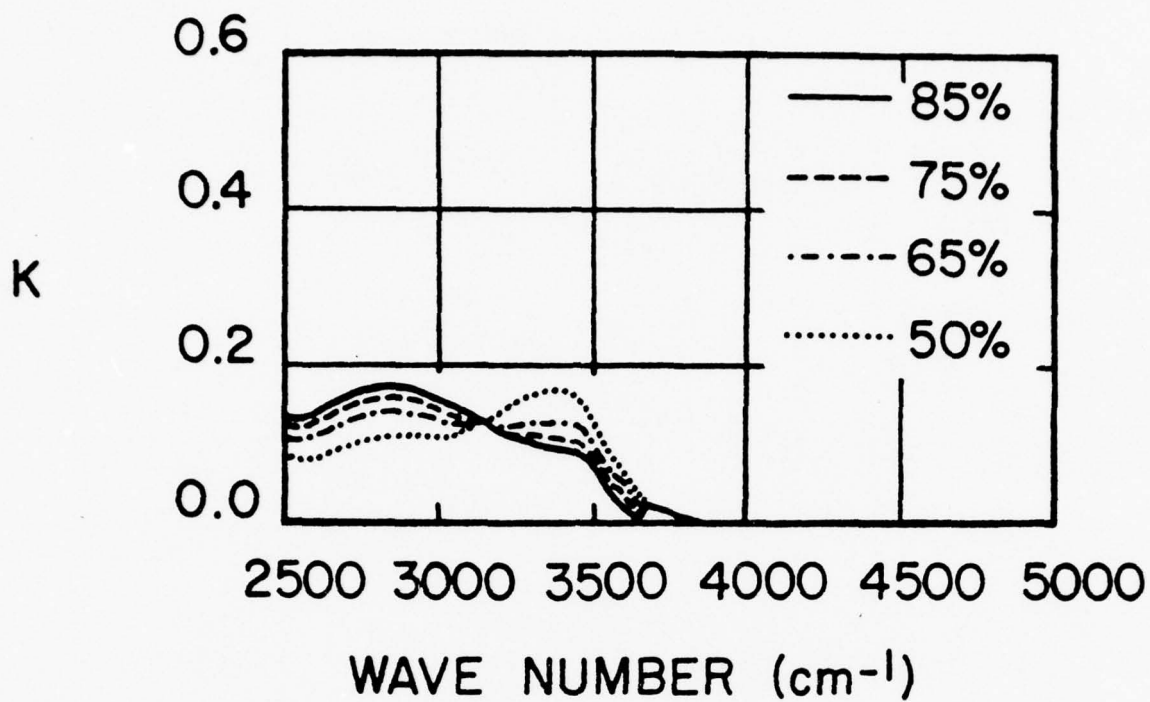


Figure 24. Extinction coefficient  $k(\nu)$  in the 2,500–5,000  $\text{cm}^{-1}$  spectral range for 50, 65, 75, and 85 percent aqueous solutions of  $\text{H}_3\text{PO}_4$ .

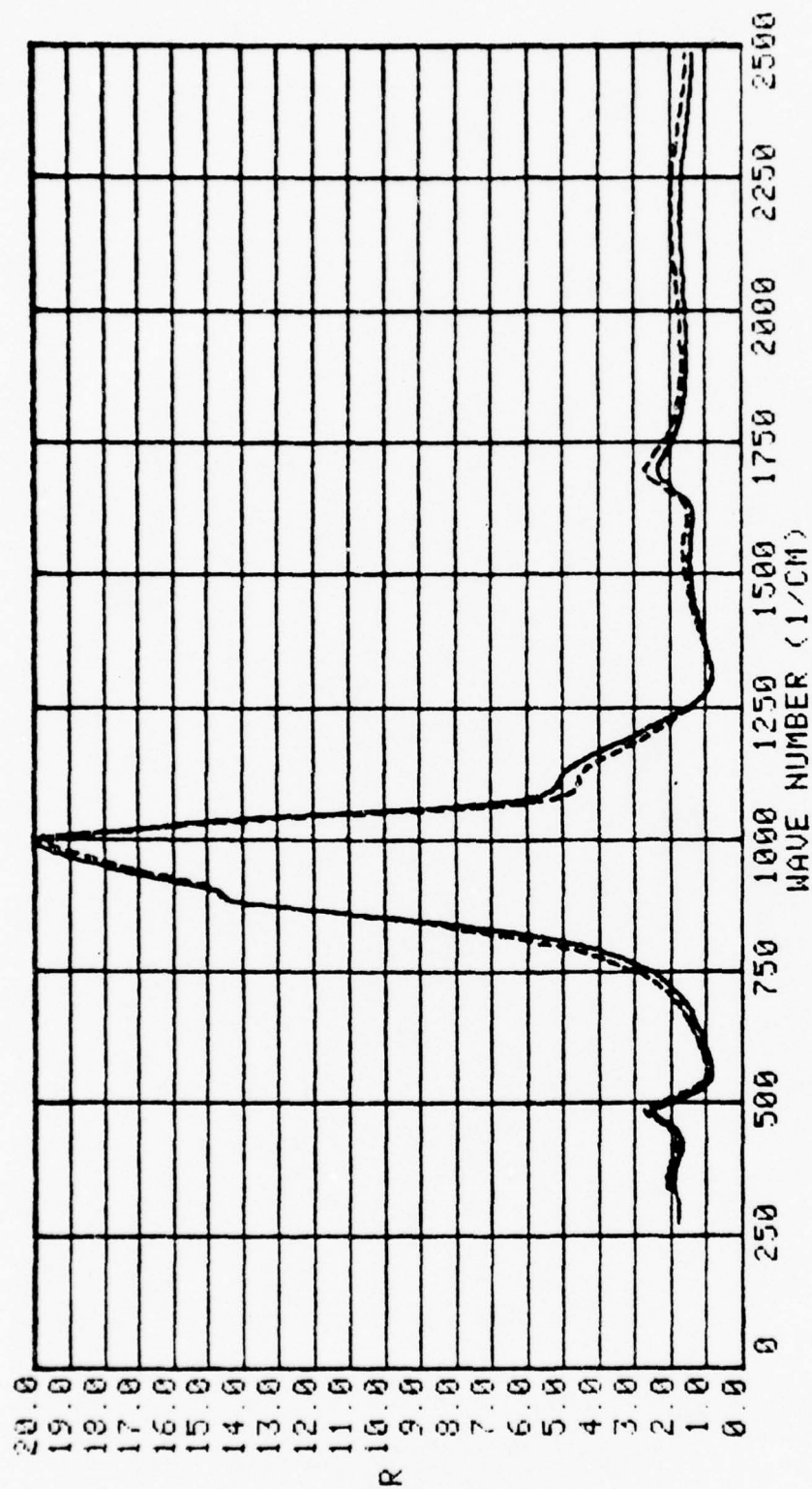


Figure 25. Near-normal incidence relative specular reflectance  $R(\nu)$  in the 300-2,500  $\text{cm}^{-1}$  spectral range for 85 percent aqueous solutions of HPO at  $25^\circ\text{C}$  (solid line) and  $-10^\circ\text{C}$  (dashed line).

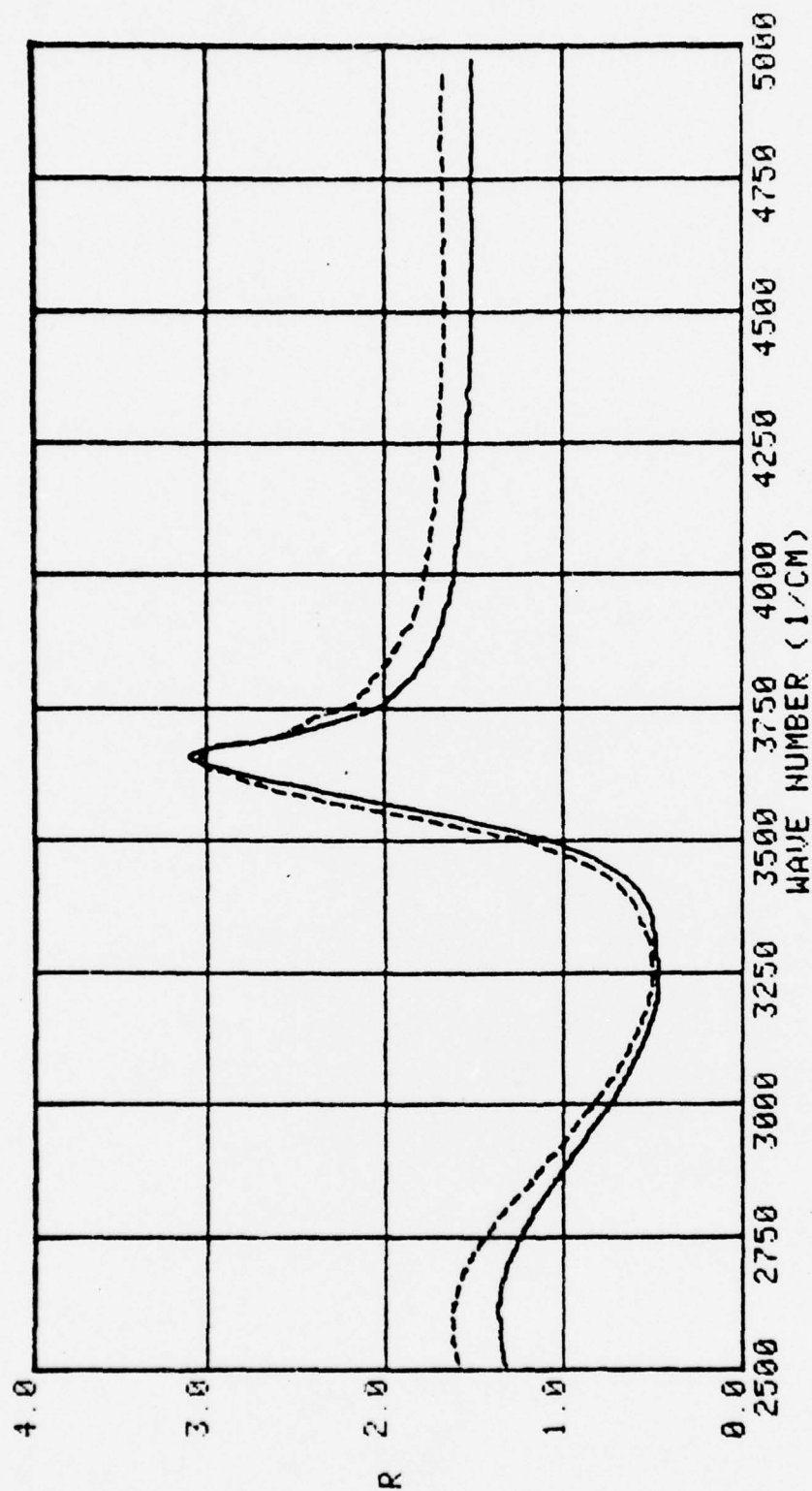


Figure 26. Near-normal incidence relative specular reflectance  $R(\nu)$  in the 2,500-5,000  $\text{cm}^{-1}$  spectral range for 85 percent aqueous solutions of  $\text{H}_3\text{PO}_4$  at  $25^\circ\text{C}$  (solid line) and  $-10^\circ\text{C}$  (dashed-line).

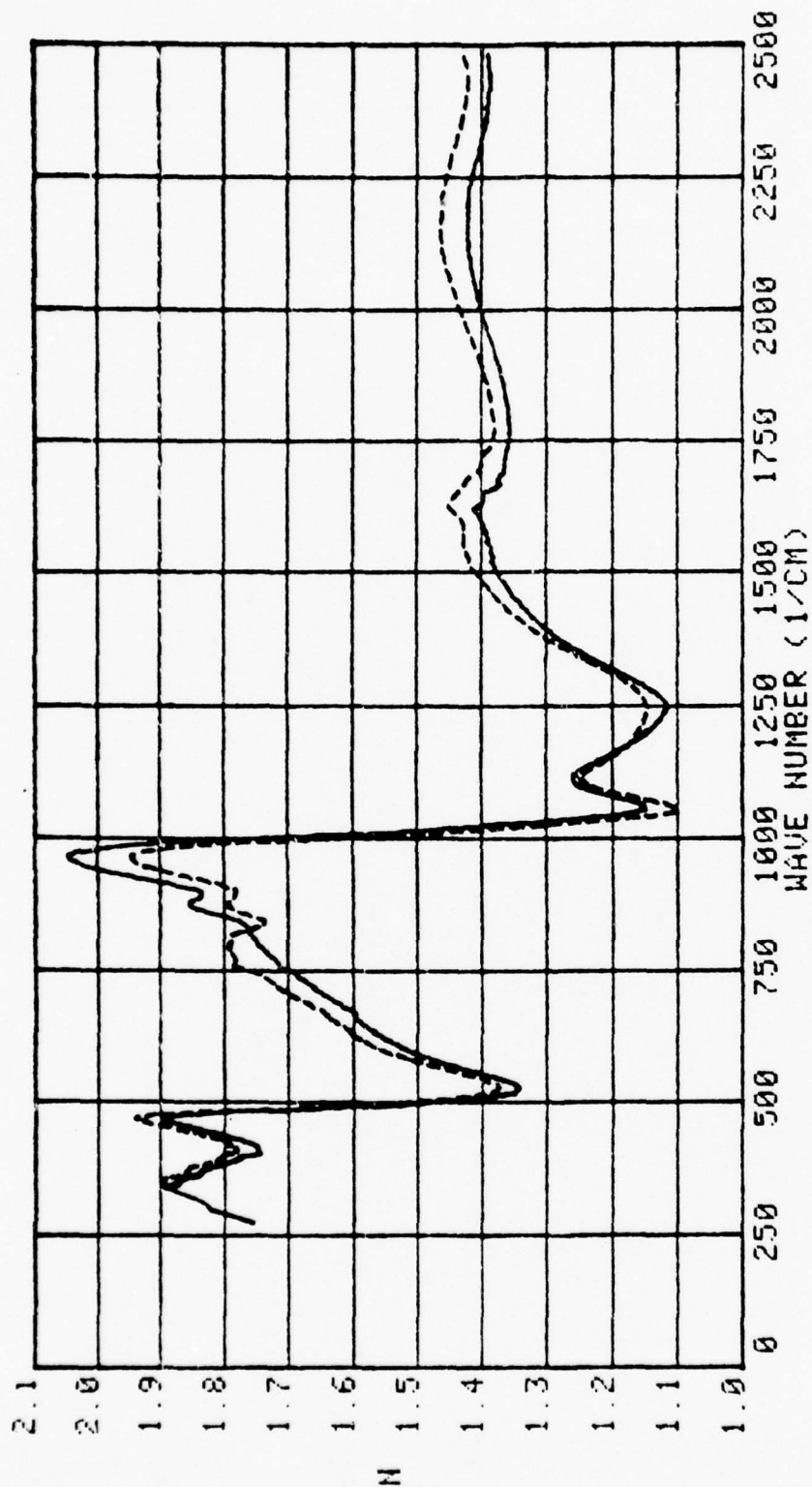


Figure 27. Index of refraction  $n(\nu)$  in the 300-2,500  $\text{cm}^{-1}$  spectral range for 85 percent aqueous solutions of  $\text{H}_3\text{PO}_4$  at  $25^\circ\text{C}$  (solid line) and  $-10^\circ\text{C}$  (dashed line).

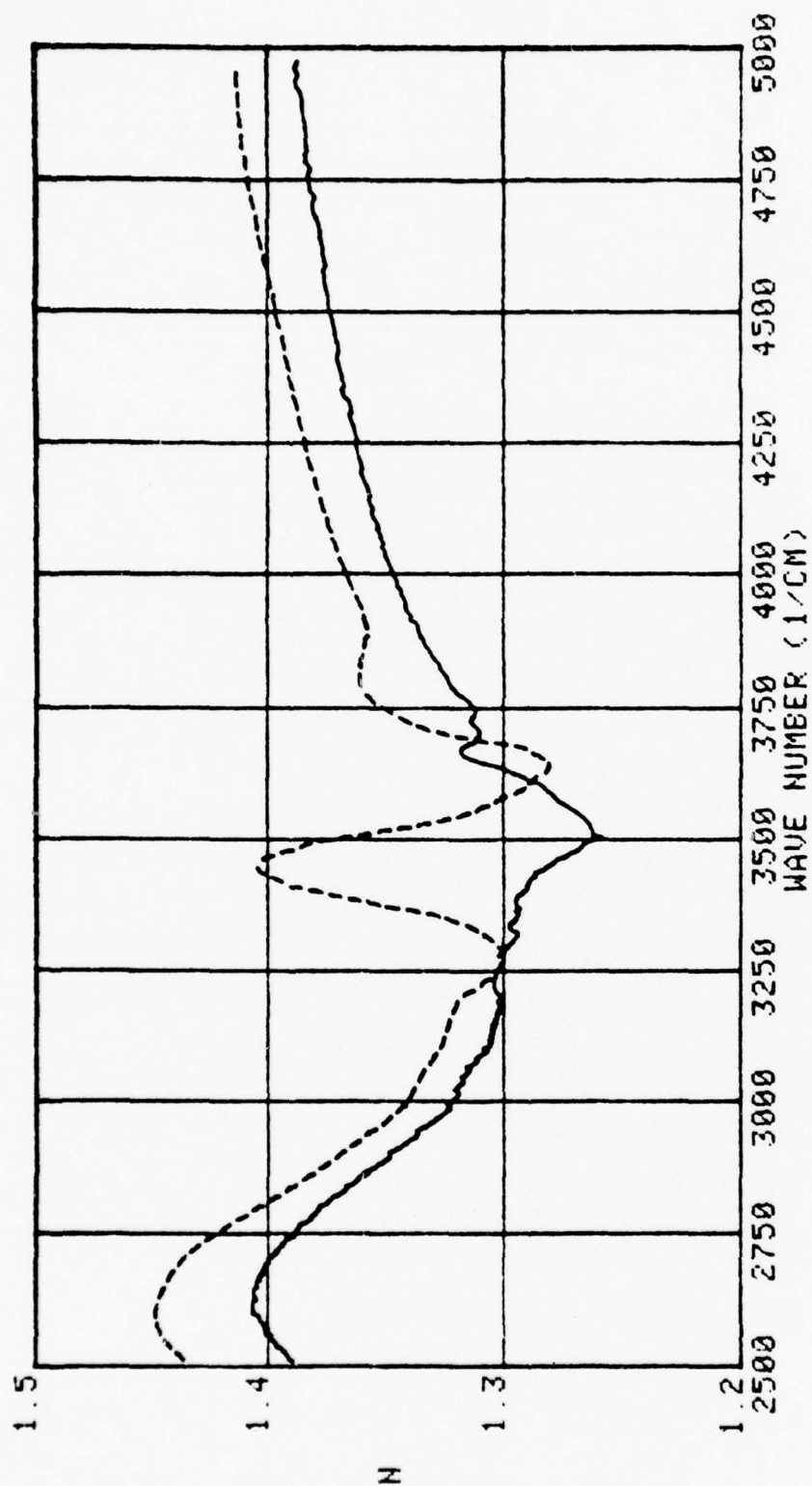


Figure 28. Index of refraction  $n(\nu)$  in the 2,500–5,000  $\text{cm}^{-1}$  spectral range for 85 percent aqueous solutions of  $\text{H}_3\text{PO}_4$  at  $25^\circ\text{C}$  (solid line) and  $-10^\circ\text{C}$  (dashed line).

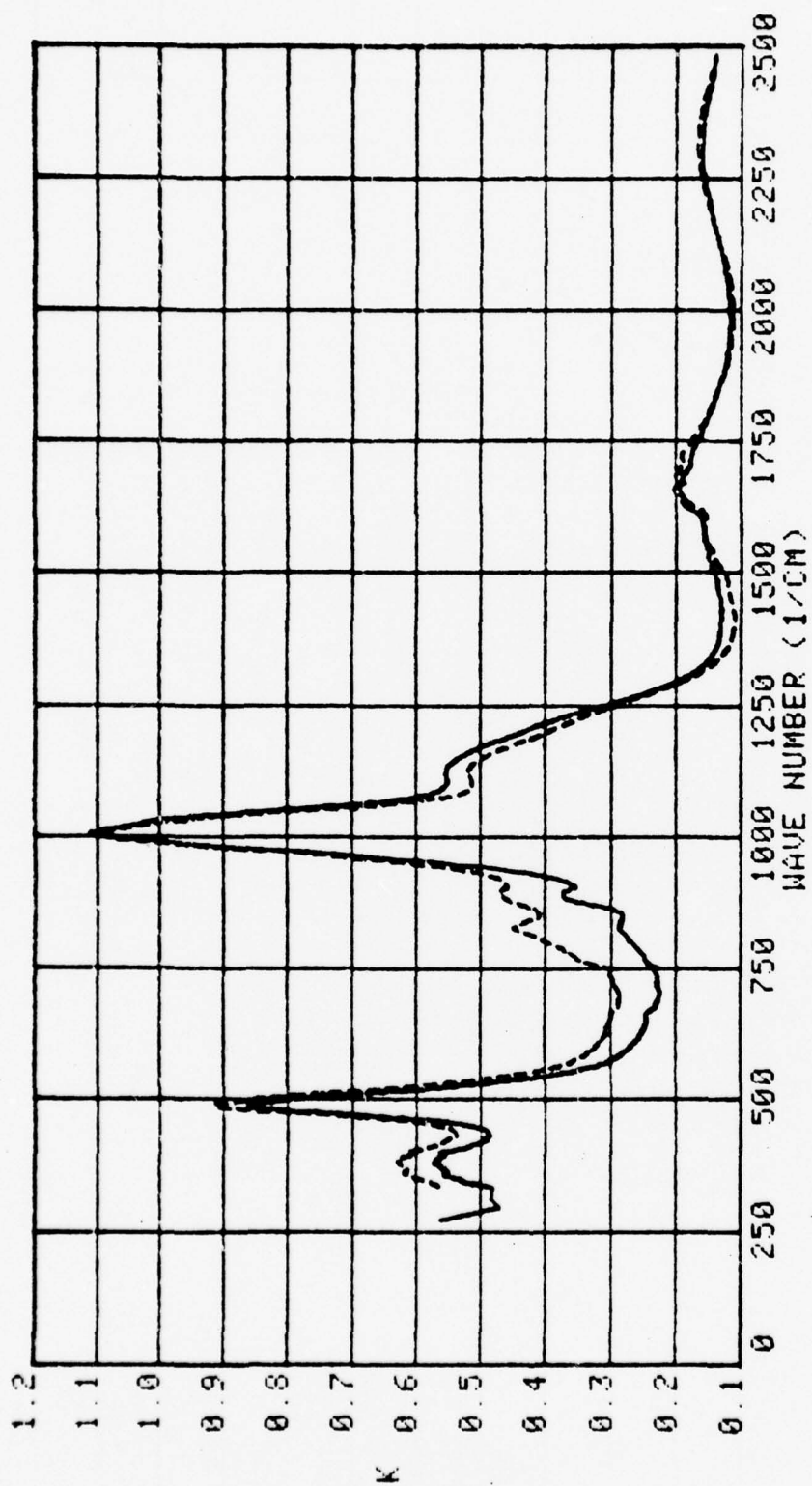


Figure 29. Extinction coefficient  $k(\nu)$  in the 300-2,500  $\text{cm}^{-1}$  spectral range for 85 percent aqueous solutions of  $\text{H}_3\text{PO}_4$  at  $25^\circ\text{C}$  (solid line) and  $-10^\circ\text{C}$  (dashed line).

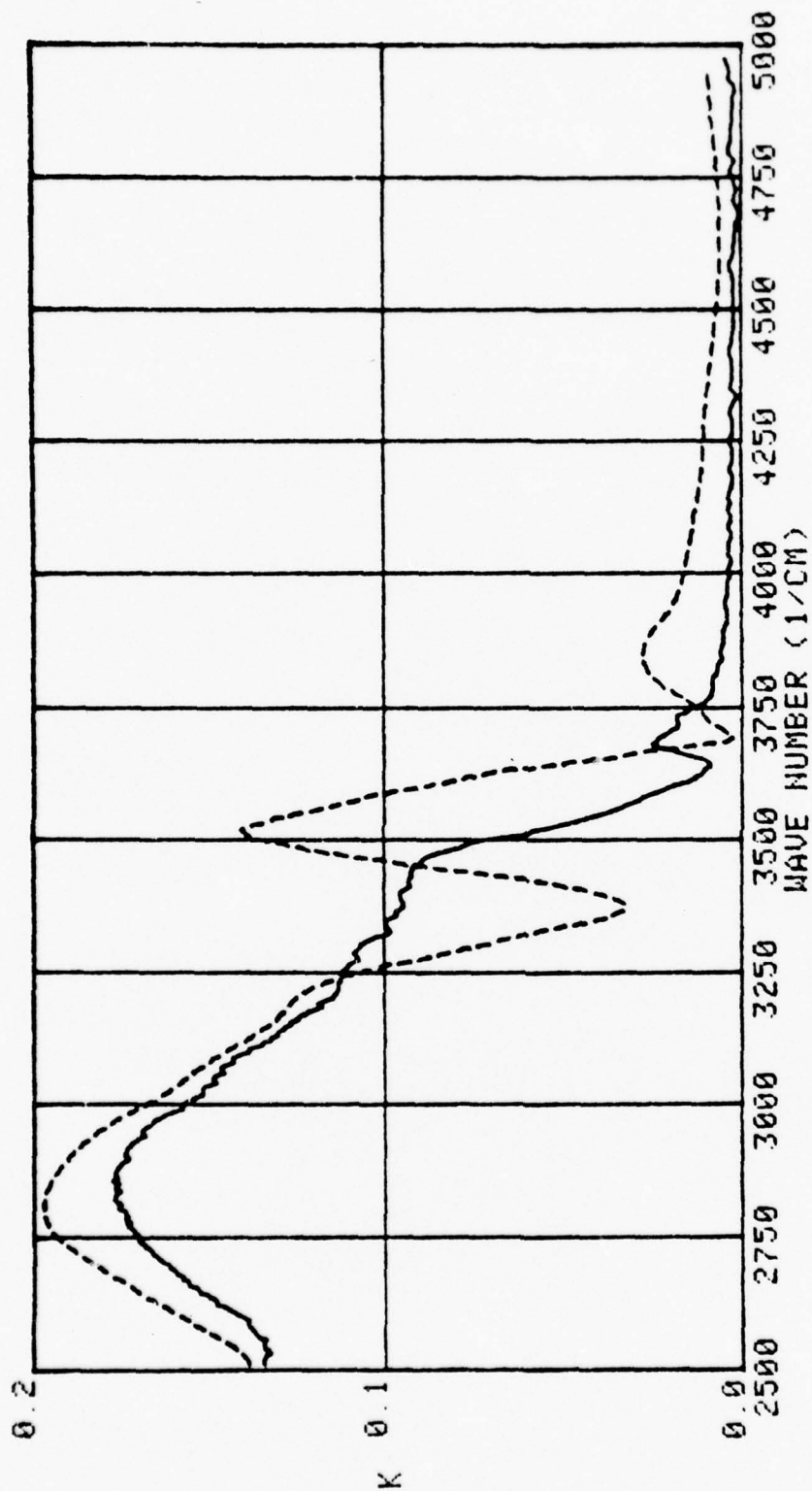


Figure 30. Extinction coefficient  $k(\nu)$  in the 2,500-5,000  $\text{cm}^{-1}$  spectral range for 85 percent aqueous solutions of  $\text{H}_3\text{PO}_4$  at  $25^\circ\text{C}$  (solid line) and  $-10^\circ\text{C}$  (dashed line).

described in Section V.A.2.c. to obtain  $N(\nu) = n(\nu) + ik(\nu)$  for each solution. Spectral values of  $N(\nu)$  for the 5, 10, 20, and 40 per cent solutions of  $H_3PO_4$  are presented graphically in Figs. 15-18, for the 50, 65, 75, and 85 per cent solutions of  $H_3PO_4$  in Figs. 21-24, and for the 85 per cent solution of  $H_3PO_4$  at  $25^\circ C$  and  $-10^\circ C$  in Figs. 27-30.

d. Discussion of Spectra of  $H_3PO_4$  Solutions

The degree of dissociation is greater for  $H_3PO_4$  solutions of less than about 1 M concentration. Thus, infrared active bands due to  $H_2PO_4^-$  should be relatively more prominent in the 5 and 10% solutions. One of the strongest bands for  $H_2PO_4^-$  occurs at  $1074\text{ cm}^{-1}$ . A small shoulder band at this position was observed in the 5, 10, and 20% solutions; for example, examine the  $k(\nu)$  spectra in Fig. 17. The  $1074\text{ cm}^{-1}$  band is not at all apparent in the solutions of greater concentration, even though in the 85% solution approximately 8.5% of the solution should be  $H_2PO_4^-$ . Therefore, we interpreted the spectra of the  $H_3PO_4$  solutions on the basis of infrared active bands of  $H_3PO_4$  and water. The central frequencies  $\nu(\text{cm}^{-1})$  and tentative assignments for the infrared active bands of  $H_3PO_4$  solutions are presented in Table V.

Table V. Central frequencies  $\nu(\text{cm}^{-1})$  of infrared active vibrational bands and tentative band assignments for  $\text{H}_3\text{PO}_4$  solutions.

Molecule	Assignment	$\nu(\text{cm}^{-1})$ for infrared bands of $\text{H}_3\text{PO}_4$ Solutions							
		5%	10%	20%	40%	50%	65%	75%	85%
$\text{H}_2\text{O}$	$\nu_1, \nu_3, 2\nu_2$	3,384	3,384	3,384	3,378	3,372	3,364	3,355	3,344
$\text{H}_3\text{PO}_4$	(E)O-H stretch					2,908	2,854	2,840	2,840
$\text{H}_3\text{PO}_4$	( $A_1$ )O-H stretch				2,358	2,298	2,294	2,290	2,294
$\text{H}_2\text{O}$	$\nu_2$	1,642	1,642	1,641	1,641	1,653	1,653	1,655	1,655
$\text{H}_3\text{PO}_4$	( $A_1$ )P-O stretch			1,173	1,169	1,151	1,134	1,134	
$\text{H}_3\text{PO}_4$	(E) $\text{PO}_3$ asym. str.		1,004	1,006	1,006	1,006	1,006	1,006	1,006
$\text{H}_3\text{PO}_4$	( $A_1$ ) $\text{PO}_3$ sym. str.					885	894	892	889
	?						825	826	827
$\text{H}_3\text{PO}_4$	( $A_1$ &E) $\text{PO}_3$ deform.				502	492	491	488	486
$\text{H}_3\text{PO}_4$	(E) $\text{PO}_3$ bend					376	377	377	376
$\text{H}_2\text{O}$	$\nu_L$	587	586	541					

#### 4. Aqueous Solutions of $\text{HNO}_3$

##### a. Objectives

The principal objectives for this investigation were:

- (1) to obtain, for aqueous solutions of  $\text{HNO}_3$ , spectral values of  $N(\nu) = n(\nu) + ik(\nu)$  which were suitable for computing Mie-scattering parameters, and (2) to measure central frequencies, half-widths, and band strengths of inter- and intramolecular infrared-active vibrational modes of liquid water,  $\text{HNO}_3$ , and molecular products due to dissociation of  $\text{HNO}_3$  in aqueous solutions. The methods whereby these objectives were accomplished were the same as those presented in Section V.A.2.a. Six nitric acid samples were investigated: 0.5, 1,

2, 4, 8, and 15.7 M solutions at 27°C.

Spectral values on  $N(\nu)$  for aqueous solutions of  $\text{HNO}_3$  are important because this acid is a common aerosol in the Earth's atmosphere.

The investigations as presented in this section were recently accepted for publication in The Journal of Chemical Physics.

b. Background Information for Discussion of  $\text{HNO}_3$  Solutions.

Here we present measurements of relative infrared reflectance spectra, computed values of spectral complex refractive index  $N(\nu) = n(\nu) + ik(\nu)$ , central wave-number positions of infrared vibrational bands, and measured strengths

$$S_b = \frac{1}{\rho_0} \int_{\text{band}} k(\nu) d\nu \quad (4)$$

of selected bands for 0.5, 1, 2, 4, 8, and 15.7 M aqueous solutions of nitric acid. In Eq. (4)  $S_b$  is the band strength,  $\rho_0$  is the molecular density ( $\text{mol./cm}^3$ ), and the integral is evaluated over the full width of the band. There have been many previous investigations of the infrared and Raman spectra of nitric acid. None of the previous investigations, however, were of the reflectance spectra, and none presented spectral values of  $N(\nu)$  for liquid nitric acid.

Investigations, prior to 1960, of the infrared and Raman spectra of nitric acid were previously reviewed and summarized by Stern et al.<sup>22/</sup> Some structural features of the  $\text{HNO}_3$  molecule were not well known at that time

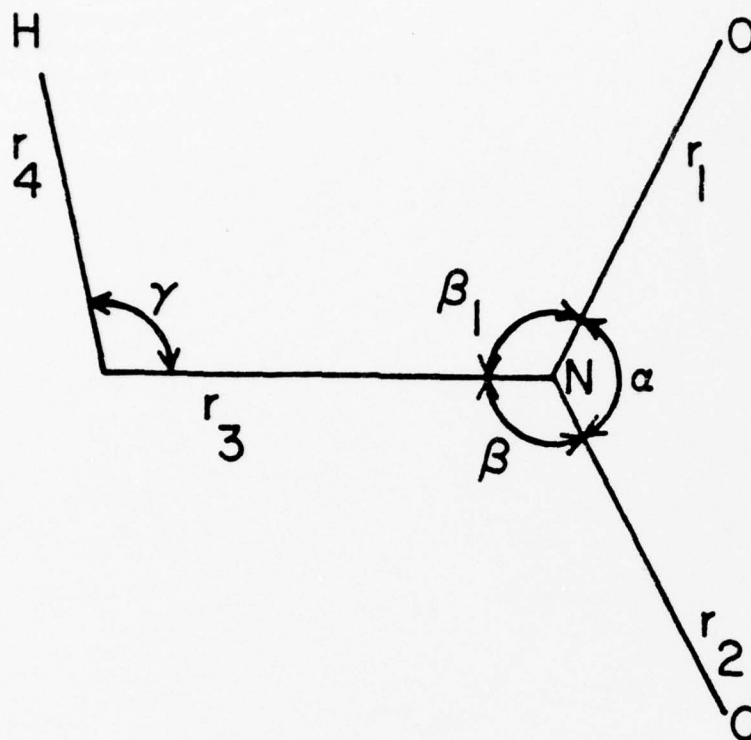


Figure 31. The structure of nitric acid:  $r_1 = 0.121$  nm,  
 $r_2 = 0.112$  nm,  $r_3 = 0.1405$  nm,  $r_4 = 0.0961$  nm,  
 $\alpha = 130^\circ 13'$ ,  $\beta_1 = 115^\circ 55'$ ,  $\beta_2 = 113^\circ 52'$ ,  
 $\gamma = 102^\circ 13'$  (from Ref. (23)).

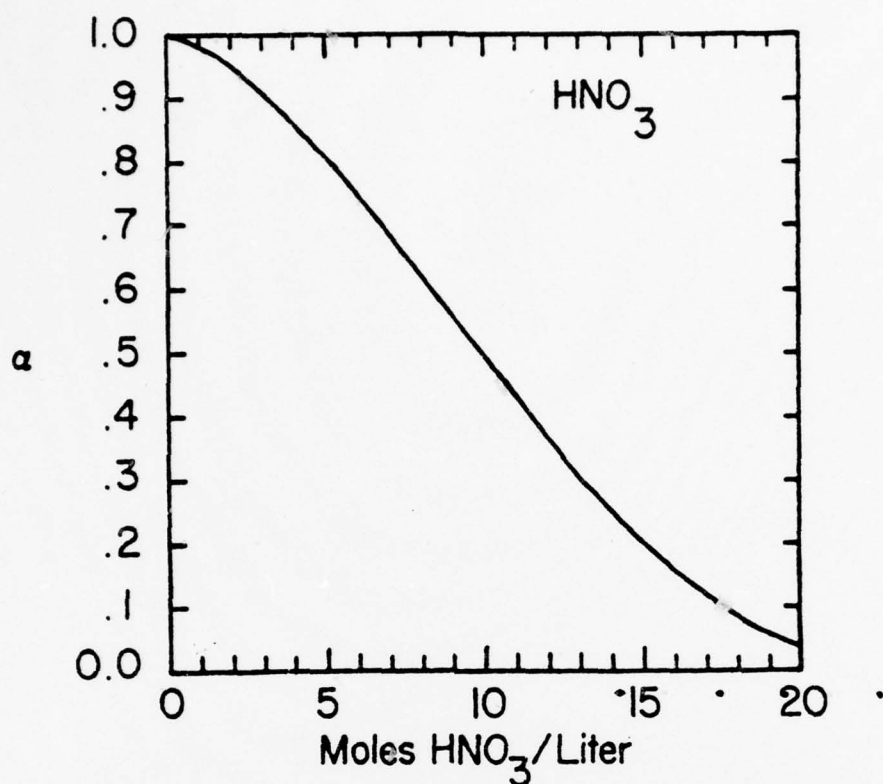


Figure 32. Degree of dissociation  $\alpha$  vs. molar concentration  $M$  of aqueous solutions of nitric acid. The dissociation of  $\text{HNO}_3$  in water follows Eq. (5) in the text.

and the molecule was therefore treated by some investigators as an  $\text{O}'\text{NO}_2$  planar system belonging to the  $\text{C}_{2v}$  point group. Thus there were several discrepancies in assignment of the fundamental vibrational bands of  $\text{HNO}_3$ .

In 1965 McGraw et al.<sup>23/</sup> reported a normal coordinate analysis of a planar nitric acid molecule belonging to the  $\text{C}_s$  point group and possessing the structure shown in Fig. 31. Such a molecule has nine fundamental vibrational modes. Seven modes are in-plane  $\text{A}'$  species and two modes are out-of-plane  $\text{A}''$  species. All modes are active in the infrared and Raman spectra. McGraw et al. compared the infrared absorption spectrum of nitric-acid vapor with results from the normal coordinate analysis. They made assignments of the nine fundamental bands and of several overtone and combination bands. Their assignments of the fundamental bands for nitric-acid vapor are valid yet today and are presented in the first, second, and fourth columns of Table VI.

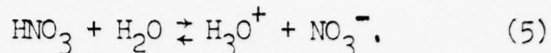
The assignment of infrared and Raman vibrational bands for aqueous solutions of nitric acid is more difficult for at least three reasons. One, the  $\text{HNO}_3$  monomer per se probably does not exist in the hydrogen-bonded structure of the liquid. Two, the liquid structure is not completely understood. And three, because  $\text{HNO}_3$  dissociates in aqueous solutions. A graph of  $\alpha$  the degree of dissociation of  $\text{HNO}_3$  in aqueous solutions<sup>24,25/</sup> as a function of molar concentration  $M$  is shown in Fig. 32. In aqueous solutions the dissociation is

Table VI. Previous band assignments for nitric-acid vapor and liquid.

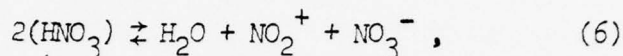
Mode (Species)	Vapor	Liquid	Assignment
$\nu_1(A')$	3550.0	3410	HO stretch
$\nu_2(A')$	1708.2	1675	$\text{NO}_2$ antisym. stretch
$\nu_3(A')$	1330.7	1395	HON bend
$\nu_4(A')$	1324.9	1303	$\text{NO}_2$ sym. stretch
$\nu_5(A')$	878.6	926	$\text{NO}_2$ deformation
$\nu_6(A')$	646.6	677	$\text{NO}'$ stretch
$\nu_7(A')$	579.0	612	$\text{ONO}'$ bend
$\nu_8(A'')$	762.2	771	$\text{NO}_2$ rock
$\nu_9(A'')$	455.8	485	HO torsion

Table VII. Molar concentration of nitric acid solutions, volume density  $\rho$  in  $\text{g/cm}^3$ , number of water molecules per acid molecule  $N_w/N_a$  prior to dissociation, degree of dissociation  $\alpha$ , and molar concentration of  $\text{HNO}_3$ ,  $\text{HO}_3^+$ ,  $\text{NO}_3^-$ , and  $\text{H}_2\text{O}$  after dissociation in the nitric acid solutions.

Solution	$\rho$	$N_w/N_a$	$\rho$	$\text{HNO}_3$	$\text{HO}_3^+$	$\text{NO}_3^-$	$\text{H}_2\text{O}$
0.5 M	1.015	109.3	0.99	0.005 M	0.495 M	0.495 M	54.16 M
1.0	1.032	53.9	0.97	0.03	0.97	0.97	52.85
2.0	1.065	26.1	0.95	0.10	1.90	1.90	50.27
4.0	1.130	12.2	0.85	0.59	3.41	3.41	45.34
8.0	1.249	5.2	0.61	3.12	4.88	4.88	36.48
15.7	1.413	1.5	0.165	13.11	2.59	2.59	20.97



In pure liquid nitric acid ( $\sim 24$  M) dissociation occurs by means of the autoionization process (or ionic self-dehydration process)



thus accounting for the greater electrical conductivity of the pure acid compared to that of aqueous solutions of very high nitric-acid concentration. The molar concentrations of  $\text{HNO}_3$ ,  $\text{H}_3\text{O}^+$ ,  $\text{NO}_3^-$ , and  $\text{H}_2\text{O}$  after dissociation in 0.5, 1, 2, 4, 8, and 15.7 M aqueous solutions of nitric acid are presented in Table VII. The concentrations of products of the dissociation were determined by use of Eq. (5) and the dissociation curve shown in Fig. 32.

Aqueous solutions of intermediate nitric-acid concentration (8-20 M), however, have Raman<sup>23,24/</sup> and infrared<sup>26,27/</sup> spectra closely similar to that of the vapor. In the spectra of the liquids there are also other vibrational bands observed which correspond to the dissociation products and to the liquid water. Previous assignments, by McGraw *et al.*,<sup>23/</sup> of fundamental vibrational bands based on Raman spectra of anhydrous nitric acid ( $\sim 24$  M) and aqueous solutions containing 95% (22.5 M) and 60% (13 M) nitric acid are shown in the first, third, and fourth columns of Table VI.

c. R(v) and N(v) Spectra of  $\text{HNO}_3$  Solutions.

Experimental methods for acquisition of the near-

normal incidence relative infrared reflectance spectra of the nitric-acid solutions were similar to those described in a previous paper,<sup>28/</sup> The relative reflectance spectra thus obtained are presented in Figs. 33 and 34. Relative spectral reflectance  $R(v)$  is defined as  $R(v) = R(v)_s / R(v)_w$ , where  $R(v)_s$  is the spectral reflectance of the nitric-acid solution and  $R(v)_w$  is the spectral reflectance of deionized and filtered water. Standard deviations based on three independent measurements of  $R(v)$  were generally  $\pm 0.005 R(v)$  but increased to about  $\pm 0.01 R(v)$  in spectral regions where atmospheric water vapor and carbon dioxide are strongly absorbing. The temperature of the water and the nitric-acid solutions was about  $27^\circ\text{C}$ .

The relative reflectance spectra were phase-shift analyzed by use of Kramers-Kronig techniques<sup>28,29/</sup> to obtain spectral values of  $N(v)$  which are presented graphically in Figs. 35-38. Uncertainties for  $N(v)$  obtained by these methods<sup>5,29/</sup> are typically as follows:  $\pm 0.01 n(v)$ ,  $\pm 0.02 k(v)$  for  $k(v)$  greater than 0.05, increase to about  $\pm 0.2 k(v)$  for  $k(v) = 0.01$ , and become much larger for  $k(v)$  less than 0.01.

d. Discussion of Spectra of  $\text{HNO}_3$  Solutions.

Water. Temporal clusters composed of several hydrogen-bonded  $\text{H}_2\text{O}$  molecules constitute the structure of liquid water. An infrared spectrum of liquid water is therefore interpreted in terms of bands associated with intramolecular vibrations of  $\text{H}_2\text{O}$  molecules and

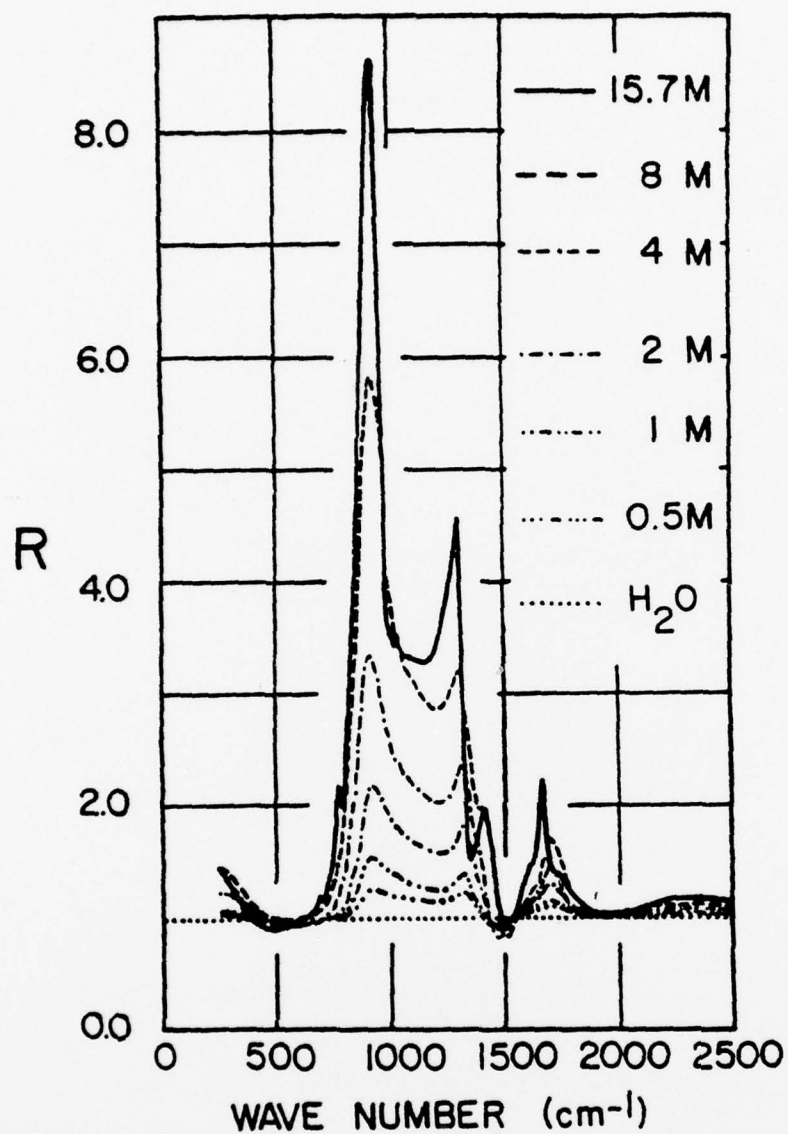


Figure 33. Near-normal incidence relative reflectance in the spectral region 310 to 2,500  $\text{cm}^{-1}$ , for 0.5, 1, 2, 4, 8, and 15.7 M aqueous solutions of nitric acid.

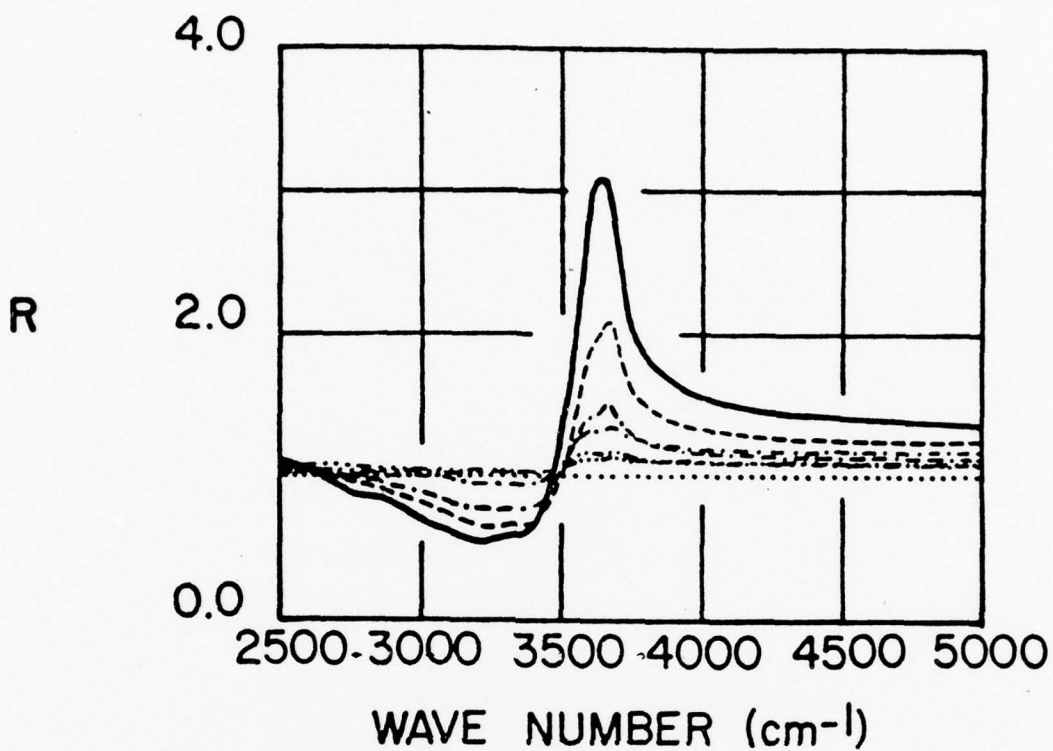


Figure 34. Near-normal incidence relative specular reflectance  $R(\nu) = R(\nu)_s / R(\nu)_w$  in the spectral region 2,500 to 5,000  $\text{cm}^{-1}$  for 0.5, 1, 2, 4, 8, and 15.7 M aqueous solution of nitric acid.

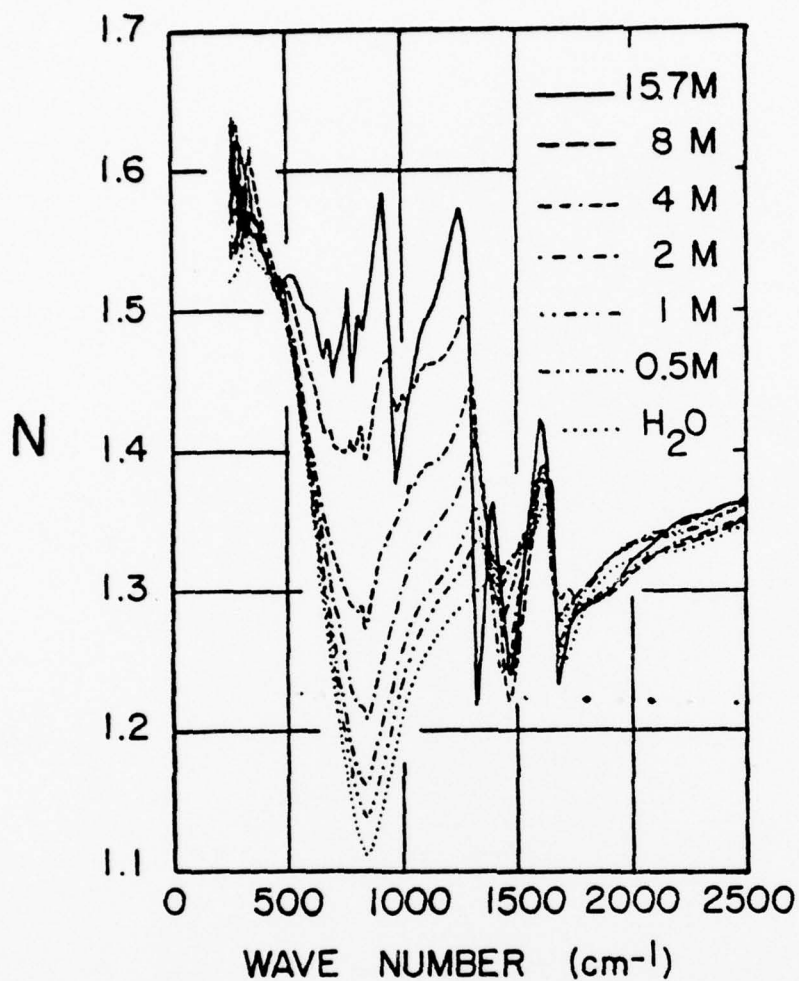


Figure 35. Index of refraction  $n(\nu)$  in the spectral region 310 to 2,500  $\text{cm}^{-1}$  for 0.5, 1, 2, 4, 8, and 15.7 M aqueous solutions of nitric acid:  $n(\nu)$  is the real part of  $N(\nu)$ .

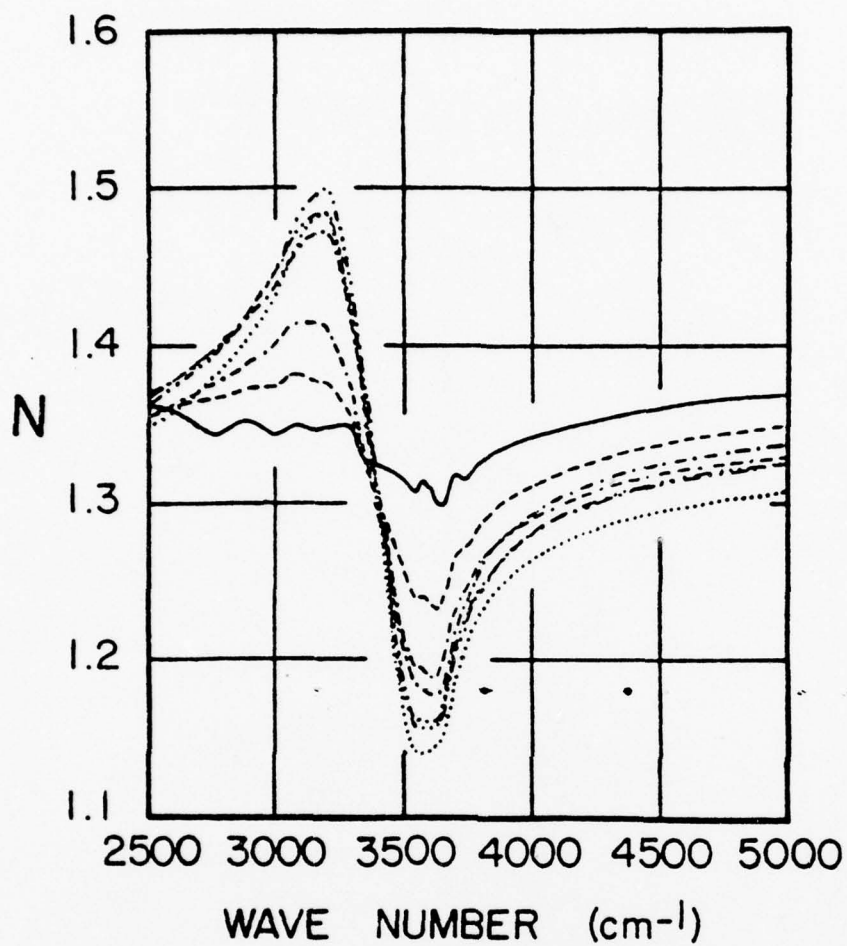


Figure 36. Index of refraction  $n(\nu)$  in the spectral region 2,500 to 5,000  $\text{cm}^{-1}$  for 0.5, 1, 2, 4, 8, and 15.7 M aqueous solutions of nitric acid:  $n(\nu)$  is the real part of  $N(\nu)$ .

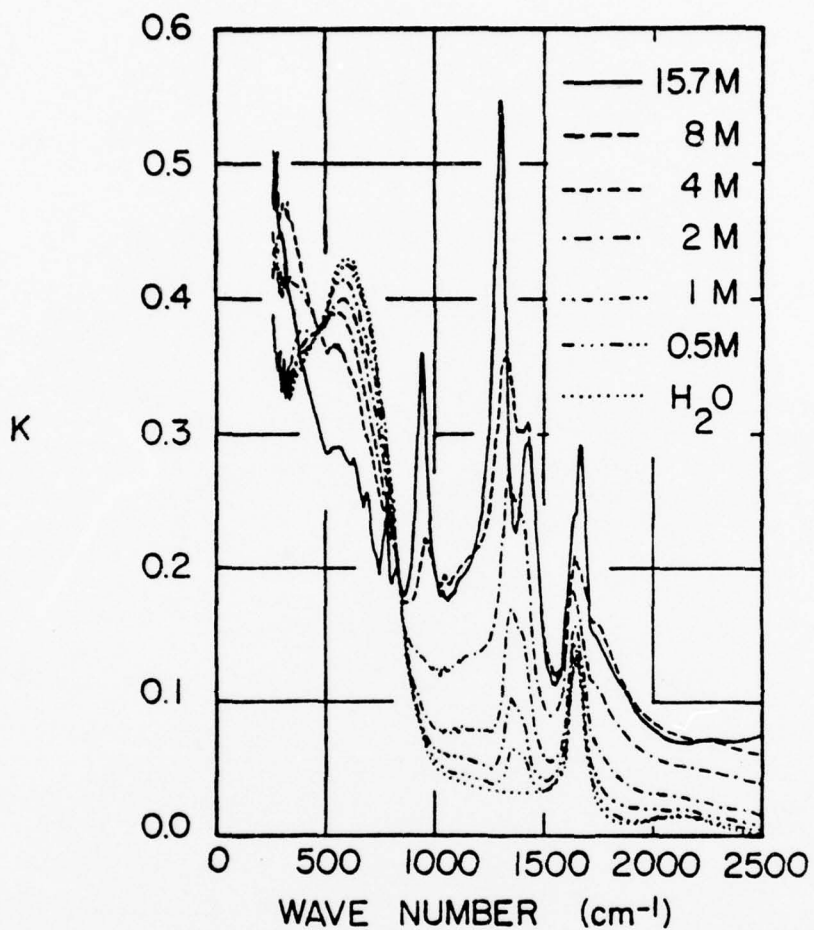


Figure 37. Extinction coefficient  $k(\nu)$  in the spectral region 310 to 2,500  $\text{cm}^{-1}$  for 0.5, 1, 2, 4, 8 and 15.7 M aqueous solution of nitric acid:  $k(\nu)$  is the imaginary part of  $N(\nu)$ .

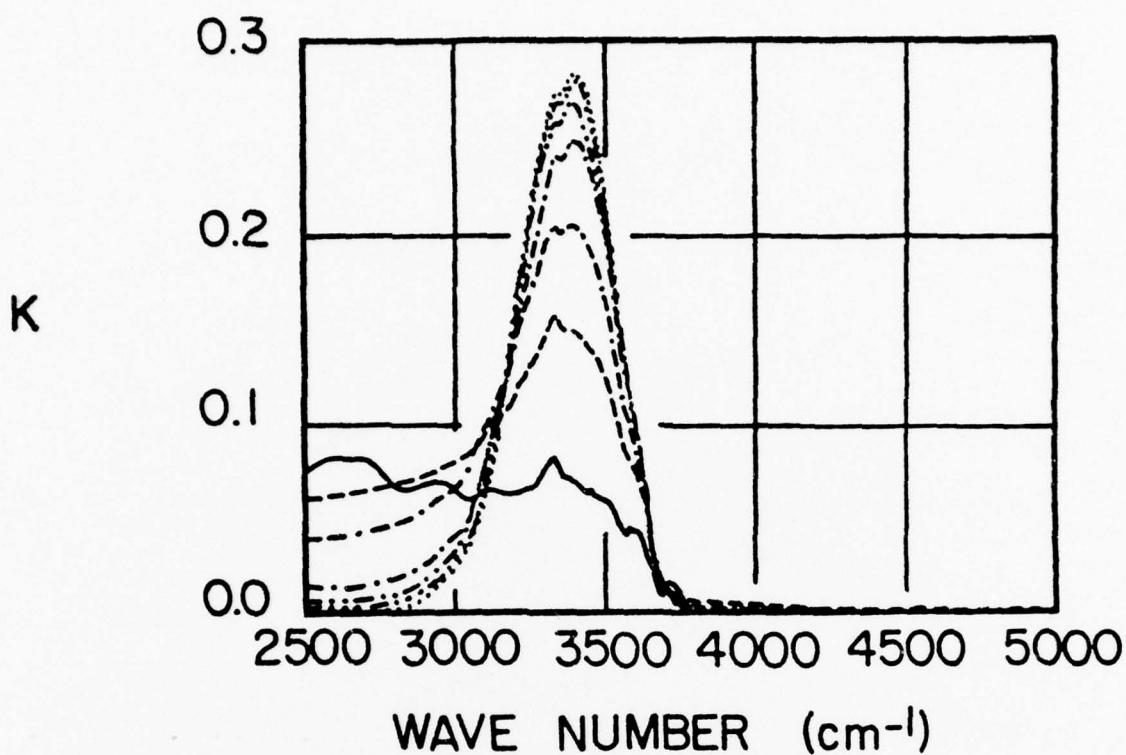


Figure 38. Extinction coefficient  $k(\nu)$  in the spectral region 2,500 to 5,000  $\text{cm}^{-1}$  for 0.5, 1, 2, 4, 8, and 15.7 M aqueous solutions of nitric acid:  $k(\nu)$  is the imaginary part of  $N(\nu)$ .

intermolecular lattice vibrations of the clusters. There are three intramolecular vibrations: the  $\nu_1$  symmetric and  $\nu_3$  antisymmetric O-H stretching motions, and the  $\nu_2$  O-H-O bending motion. The  $\nu_2$  band has a central frequency of  $1640 \text{ cm}^{-1}$ , a half-width of  $110 \text{ cm}^{-1}$ , and a band strength of  $(4.5 \pm 0.8) \times 10^{-22} \text{ cm}^2/\text{molecule}$ . The  $\nu_1$  and  $\nu_3$  stretching modes and the first overtone  $2\nu_2$ , which may be in Fermi resonance with  $\nu_1$  or  $\nu_3$ , produce broad overlapping bands. The  $\nu_1$ ,  $\nu_3$ , and  $2\nu_2$  bands are therefore grouped together in order to analyze the infrared spectrum of liquid water. Together these three bands form a broad composite band of central frequency  $\nu_{\text{max}}$ , half-width  $\Gamma$ , and band strength  $S_b$  as recorded in Table VIII.

The intermolecular vibrational modes are not well known. However, one structural model proposed by Bandekar and Curnutte<sup>30/</sup> consists of a central  $\text{H}_2\text{O}$  molecule hydrogen bonded with  $C_{2v}$  point-group symmetry in a tetrahedral cluster of 4 first and 12 second nearest neighboring  $\text{H}_2\text{O}$  molecules. A normal coordinate and Monte Carlo analysis of this structure,<sup>30/</sup> neglecting the intramolecular motion and degeneracies yielded six principal lattice vibrational modes with a total of 30 vibrational species. The principal lattice vibrations were  $75, 165, 219, 450, 550, \text{ and } 722 \text{ cm}^{-1}$ . Spectra obtained during the present investigation include only the  $450, 550, \text{ and } 720 \text{ cm}^{-1}$  modes. These three principal

Table VIII. Measurable parameters for intramolecular bands of selected nitric-acid solutions:  $\nu_{\max}$  is the central frequency,  $\Gamma$  is the half-width,  $k(\nu)_{\max}$  is the value of  $k(\nu)$  at  $\nu_{\max}$ , and  $S_b$  is the band strength.

Solution(M)	Molecule	Band	$\nu(\text{cm}^{-1})_{\max}$	$\Gamma(\text{cm}^{-1})$	$k(\nu)_{\max}$	$S_b(\text{cm}^2/\text{molecule})$
15.7	HNO <sub>3</sub>	$\nu_2(\text{A}')$	1672 $\pm$ 4	47 $\pm$ 8	0.292	1.70 $\pm$ 0.14 $\times 10^{-21}$
15.7	HNO <sub>3</sub>	$\nu_3(\text{A}')$	1429 $\pm$ 2	98 $\pm$ 6	0.294	2.0 $\pm$ 0.1 $\times 10^{-21}$
15.7	HNO <sub>3</sub>	$\nu_4(\text{A}')$	1304 $\pm$ 2	50 $\pm$ 5	0.546	4.7 $\pm$ 0.1 $\times 10^{-21}$
15.7	HNO <sub>3</sub>	$\nu_5(\text{A}')$	949 $\pm$ 2	49 $\pm$ 4	0.361	1.6 $\pm$ 0.1 $\times 10^{-21}$
15.7	HNO <sub>3</sub>	$\nu_6(\text{A}')$	691 $\pm$ 2	26 $\pm$ 6	0.256	0.22 $\pm$ 0.03 $\times 10^{-21}$
15.7	HNO <sub>3</sub>	$\nu_7(\text{A}')$	634 $\pm$ 2	-----	0.283	-----
15.7	HNO <sub>3</sub>	$\nu_8(\text{A}'')$	778 $\pm$ 2	15 $\pm$ 2	0.259	0.14 $\pm$ 0.04 $\times 10^{-21}$
15.7	HNO <sub>3</sub>	2 $\nu_4$	2633 $\pm$ 20	-----	0.082	-----
15.7	HNO <sub>3</sub>	2 $\nu_3$	2935 $\pm$ 20	-----	0.071	-----
15.7	NO <sub>3</sub> <sup>-</sup>	$\nu_2(\text{A}_2)$	820 $\pm$ 3	35 $\pm$ 10	0.198	-----
15.7	NO <sub>3</sub> <sup>-</sup>	$\nu_4(\text{E})$	730 $\pm$ 7	-----	-----	-----
0.5	NO <sub>3</sub> <sup>-</sup>	$\nu_3(\text{E})$	1350 $\pm$ 2	139 $\pm$ 10	0.065	16.7 $\pm$ 2.0 $\times 10^{-21}$
1.0	NO <sub>3</sub> <sup>-</sup>	$\nu_3(\text{E})$	1350 $\pm$ 2	157 $\pm$ 10	0.099	18.1 $\pm$ 2.0 $\times 10^{-21}$
8.0	H <sub>3</sub> O <sup>+</sup>	$\nu_2(\text{A}_1)$	1210 $\pm$ 40	-----	-----	-----
8.0	H <sub>3</sub> O <sup>+</sup>	$\nu_4(\text{E})$	1742 $\pm$ 15	180 $\pm$ 20	0.148	4.0 $\pm$ 0.5 $\times 10^{-21}$
0.0	H <sub>2</sub> O	$\nu_1, \nu_3, 2\nu_2$	3395 $\pm$	390 $\pm$	0.297	3.7 $\pm$ 0.1 $\times 10^{-21}$
0.0	H <sub>2</sub> O	$\nu_2$	1640 $\pm$	110 $\pm$	0.137	0.45 $\pm$ 0.08 $\times 10^{-21}$
0.0	H <sub>2</sub> O	$\nu_L$	580 $\pm$	500 $\pm$	0.443	7.2 $\pm$ 1.5 $\times 10^{-21}$

modes provide unresolved broad overlapping bands that are collectively referred to as the librational band  $\nu_L$ . Parameters for the  $\nu_L$  band are noted in Table VIII.

Nitric-Acid Solutions. The molar concentrations of molecular constituents  $\text{HNO}_3$ ,  $\text{H}_3\text{O}^+$ ,  $\text{NO}_3^-$ , and  $\text{H}_2\text{O}$  for the nitric-acid solutions are listed in Table VII. In the spectra for the 0.5, 1, 2, and 4 M solutions we primarily observed, in Figs. 33-38, spectral features due to liquid water. In Figs. 33 and 34 liquid water by definition has a relative reflectance  $R(\nu) = 1.0$  throughout the spectral range. The bands are easily seen in the spectra shown in Figs. 37 and 38. There were also secondary spectral features due to the strongest intramolecular vibrational modes of  $\text{NO}_3^-$  and  $\text{H}_3\text{O}^+$ .

The  $\text{NO}_3^-$  ion is planar with  $D_{3h}$  point-group symmetry, and thus possesses three infrared active vibrational mode  $\nu_2(A_2)$ ,  $\nu_3(E)$ , and  $\nu_4(E)$  at about 820, 1350, and 730  $\text{cm}^{-1}$ , respectively. The strongest vibrational modes is  $\nu_3(E)$  which is doubly degenerate. The  $\nu_3(E)$  mode is quite evident in the spectra for the 0.5, 1, 2, and 4 M solutions. Although the  $\nu_3(E)$  mode is doubly degenerate it appears in the present spectra as a doublet. Coordination of  $\text{NO}_3^-$  with  $\text{H}_2\text{O}$  molecules is probably responsible for removing the degeneracy. Parameters  $\nu_{\text{max}}$ ,  $\Gamma$ , and  $S_b$  measured for the  $\nu_3(E)$  mode

AD-A076 502

MISSOURI UNIV-KANSAS CITY DEPT OF PHYSICS  
MOLECULAR AND CRYSTALLINE ELECTROMAGNETIC PROPERTIES OF SELECTE--ETC(U)  
AUG 79 M R QUERRY

F/8 20/8

DAA629-76-8-185

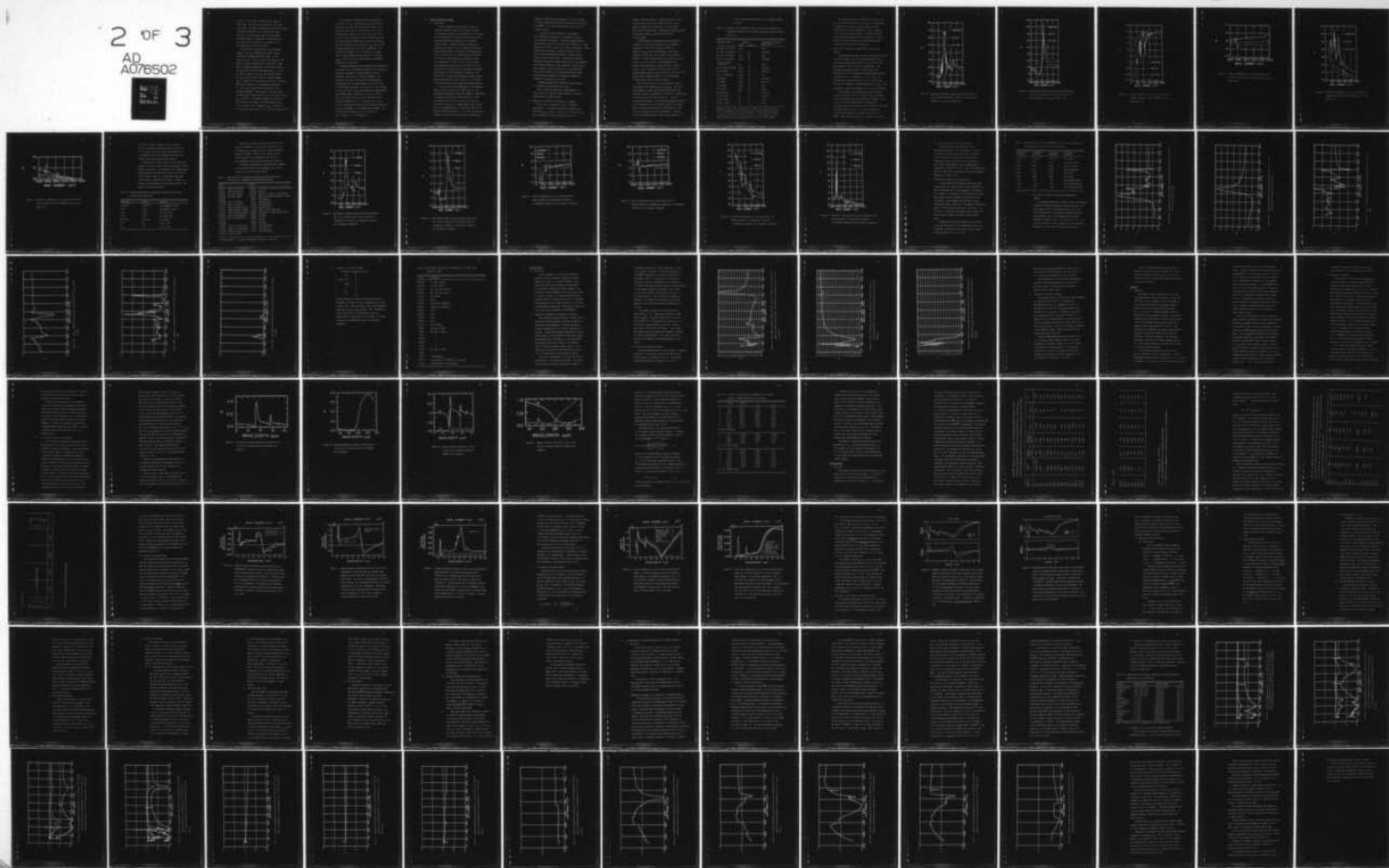
UNCLASSIFIED

ARO-13739.9-85X

NL

2 OF 3

AD  
A076502



of  $\text{NO}_3^-$  in the 0.5 and 1 M solutions are listed in Table VIII. The  $\nu_2(\text{A}_2)$  and  $\nu_4(\text{E})$  modes of  $\text{NO}_3^-$  are quite weak. They were not observable in previous infrared reflectance spectra<sup>4/</sup> of 0.5 M solutions of  $\text{NaNO}_3$ . The  $\nu_2(\text{A}_2)$  and  $\nu_4(\text{E})$  modes, however, were observed during the present investigation in the spectra for the 8 and 15.7 M solutions, e.g., see Fig. 38 for very weak bands at 820 and 730  $\text{cm}^{-1}$ .

The  $\text{H}_3\text{O}^+$  ion is pyramidal with  $\text{C}_{3v}$  point-group symmetry, and thus possesses four infrared active intramolecular vibrational modes  $\nu_1(\text{A}_1)$ ,  $\nu_2(\text{A}_1)$ ,  $\nu_3(\text{E})$ , and  $\nu_4(\text{E})$ . The  $\nu_1(\text{A}_1)$  and  $\nu_3(\text{E})$  bands are very broad and extend from about 2650 to 3380  $\text{cm}^{-1}$ . They were not observed specifically in the present spectra for the nitric acid solutions because the  $\nu_1$ ,  $\nu_3$ , and  $2\nu_2$  modes for  $\text{H}_2\text{O}$  occur in the same spectral region. The  $\nu_2(\text{A}_1)$  band of  $\text{H}_3\text{O}^+$  occurs at a central frequency  $\nu_{\text{max}} = 1210 \pm 40 \text{ cm}^{-1}$  in the spectrum for the 8 M solution, and is best observed as a low-frequency shoulder on the  $\nu_4(\text{A}')$  band of  $\text{HNO}_3$  which is discussed in the following paragraph. The presence of the  $\nu_2(\text{A}_1)$  band is also notable in the spectra for all the other solutions, e.g. see Fig. 38. The doubly degenerate  $\nu_4(\text{E})$  band of  $\text{H}_3\text{O}^+$  occurs as a shoulder on the high frequency side of the  $\nu_2$  band of  $\text{H}_2\text{O}$ . Parameters  $\nu_{\text{max}}$ ,  $\Gamma$ , and  $S_b$  for the  $\nu_2(\text{A}_1)$  and  $\nu_4(\text{E})$  bands of  $\text{H}_3\text{O}^+$  are listed in Table VIII.

The structure of the  $\text{HNO}_3$  molecule was discussed in Section V.A.4.b. Intramolecular vibrational bands associated with  $\text{HNO}_3$  were particularly evident in the spectra for the 8 and 15.7 M solutions. Of the nine intramolecular bands only the  $\nu_1(\text{A}')$  and  $\nu_9(\text{A}'')$  bands were not clearly identified. Both of these bands occur in spectral regions where liquid water also has bands. The  $\nu_7(\text{A}')$  band at central frequency  $\nu_{\text{max}} = 634 \pm 2 \text{ cm}^{-1}$  was the weakest band of  $\text{HNO}_3$  that was observed. The  $\nu_7(\text{A}')$  band, however, was not resolved to the extent that its band strength could be measured. Parameters  $\nu_{\text{max}}$ ,  $\Gamma$ , and  $S_b$  for the six other bands were measured and appear in Table VIII.

The band strengths  $S_b$  were determined from graphs such as those in Fig. 38 by manual decomposition of overlapping bands when necessary, by subtracting the continuum absorption, and by use of a manual planimeter. The strength of the  $\nu_4(\text{E})$  band of  $\text{H}_3\text{O}^+$  was determined by planimetry only the high-frequency half of the band and multiplying the result by a factor of 2. The strength of the  $\nu_2(\text{A}')$  band of  $\text{HNO}_3$  was determined by planimetry the combined areal contribution of the  $\nu_2(\text{A}')$  band of  $\text{HNO}_3$ , the  $\nu_2$  band of  $\text{H}_2\text{O}$ , and the  $\nu_4(\text{E})$  band of  $\text{H}_3\text{O}^+$ . The band strengths due to  $\nu_2$  of  $\text{H}_2\text{O}$  and  $\nu_4(\text{E})$  of  $\text{H}_3\text{O}^+$  at their appropriate molecular density were then subtracted from the measurement of the combined band strength. The resultant band strength for  $\nu_2(\text{A}')$  of  $\text{HNO}_3$  was

$$S_b = (1.70 \pm 0.14) \times 10^{-2} \text{ cm}^2/\text{molecule}.$$

## 5. Organic Liquids and Solids

### a. Objectives

Clouds composed of water droplets, which are stabilized against evaporation by surface coatings of long-chain alcohols, clouds composed of oil droplets, and clouds composed of small acrylic particles are of practical interest as obscurants in the infrared spectral region. Radiation transport through such clouds can be computed by use of classical or modified Mie-scattering theory. The spectral refractive index  $N(\nu) = n(\nu) + ik(\nu)$ , and a particle-size distribution, of the cloud's constituents are required to begin such computations. Values of  $N(\nu)$  in the infrared are available for water, but values of  $N(\nu)$  for oils, alcohols, and an acrylic were not previously available. The objective of the investigation reported in this section was to obtain the near-normal incidence relative reflectance spectra  $R(\nu)$  and values of  $N(\nu)$  for three oils, three solid alcohols, and polymethyl-methacrylate.

Oils selected for the investigation were commercial diesel fuel, No. 100 pale oil (light fog oil), and tetramethyl-tetraphenyl-trisiloxane (TMTPS). The TMTPS is commercially available as DOW Corning No. 704 Oil. In addition to its use as an obscurant, diesel fuel was chosen because it is a common aerosol which is present in the atmosphere due to incomplete combustion in internal-combustion engines. No. 100 pale oil was chosen because it is used by the Military as a screening-fog

material. TMIPTS was chosen because we wished to extend, into the infrared spectral region, some previous investigations<sup>31,32/</sup> of its optical properties in the ultraviolet spectral region.

Long-chain alcohols selected for investigation were 1-hexadecanol (palmityl), 1-octadecanol (stearyl), and 1-eicosanol (arachidyl). The melting temperatures of these alcohols are 49, 58.5, and 65.5°C, respectively. Their densities are 0.8176, 0.8124, and 0.8405, respectively. These particular alcohols were of interest because of their use in water-fog generating equipment, wherein they are melted in water at about 95°C. Compressed air bubbling vigorously through the water-alcohol mixture in the generator then produces steam-like clouds composed of alcohol-coated water droplets. As the droplets cool in the atmosphere the alcohol solidifies, thus forming irregularly shaped particles which, depending on the ambient temperature, possesses a liquid water or ice core.

Polymethyl-methacrylate (PMMA) was chosen because it is a readily available commercial acrylic.

Also, of basic interest was an interpretation of the  $R(\nu)$  and  $N(\nu)$  spectra of these materials in terms of intramolecular vibrational modes.

b. Background Information for Discussion of Organics

Diesel fuel is composed of a host of different hydrocarbons. Its primary constituents, however, are paraffins  $C_nH_{2n+2}$ , where  $n = 12-16$ . No. 100 pale oil has the consistency of a light lubricating oil and is

probably composed primarily of paraffins where  $n = 15-20$ .

The long-chain alcohols are closely related in their chemical composition and structure to the paraffins.

Their chemical formulas are: 1-hexadecanol  $\text{CH}_3(\text{CH}_2)_{14}\text{CH}_2\text{OH}$ , 1-octadecanol  $\text{CH}_3(\text{CH}_2)_{16}\text{CH}_2\text{OH}$ , and 1-eicosanol  $\text{CH}_3(\text{CH}_2)_{18}\text{CH}_2\text{OH}$ .

In 1963 Snyder and Schachtschneider published two papers<sup>33/</sup> on vibrational analysis of the n-paraffins.

A synopsis of their results appears in Table IX.

Paraffins  $\text{C}_n\text{H}_{2n+2}$  with  $n$  odd possess  $\text{C}_{2v}$  point group symmetry and those with  $n$  even possess  $\text{C}_{2h}$  point group symmetry. Infrared active species of  $\text{C}_{2v}$  are  $A_1$ ,  $B_1$ , and  $B_2$  and of  $\text{C}_{2h}$  are  $A_u$  and  $B_u$ . The asymmetric and symmetric stretching modes of  $\text{CH}_2$ , and  $\text{CH}_3$  to a lesser extent, in the  $2,929-2,849 \text{ cm}^{-1}$  region, and the HCH angular-bending modes of  $\text{CH}_2$  and  $\text{CH}_3$  in the  $1,376-1,473 \text{ cm}^{-1}$  region were of primary interest in this investigation of diesel fuel, fog oil, and the alcohols.

PMMA is the first ( $k = 1$ ) in the chemical series of polymethacrylates  $[\text{CH}_2\text{C}(\text{CH}_3)(\text{CO}_2 \text{C}_k \text{H}_{2k+1})]_n$ . The point group symmetry of PMMA varies with structure which can be either isotactic, syndiotactic, or atactic. Additionally, the structure can vary from one form to another in a particular PMMA sample. The infrared spectra and structure of PMMA remains as an open research topic,<sup>34/</sup> and assignments of vibrational species for infrared bands of PMMA could not be made during this investigation. However, most of the infrared bands of PMMA are characteristic of

various chemical groups shown in the preceding chemical formula.

Table IX. Infrared active vibrational modes, species, and frequencies of n-paraffins compiled from the normal coordinate analysis reported in Ref. (33).

Vibrational mode	Species*		Frequency of Frequency Range (cm <sup>-1</sup> )
	n-odd	n-even	
CH <sub>3</sub> asym. C-H stretch	A <sub>1</sub> , B <sub>1</sub>		2967
CH <sub>2</sub> asym. C-H stretch	B <sub>2</sub>	A <sub>u</sub>	2912-2929
CH <sub>3</sub> sym. C-H stretch	A <sub>1</sub> , B <sub>1</sub>	B <sub>u</sub>	2884
CH <sub>2</sub> sym. C-H stretch	A <sub>1</sub> , B <sub>1</sub>	B <sub>u</sub>	2849-2861
CH <sub>3</sub> out-of-plane <HCH bend	B <sub>2</sub>	A <sub>u</sub>	1465
CH <sub>3</sub> in-plane <HCH bend	A <sub>1</sub> , B <sub>1</sub>	B <sub>u</sub>	1446-1473
CH <sub>2</sub> <HCH bend	A <sub>1</sub> , B <sub>1</sub>	B <sub>u</sub>	1446-1473
CH <sub>3</sub> sym. <HCH bend	A <sub>1</sub> , B <sub>1</sub>	B <sub>u</sub>	1376
CH <sub>2</sub> wagging	A <sub>1</sub> , B <sub>1</sub>	B <sub>u</sub>	1174-1411
C-C stretch	A <sub>1</sub> , B <sub>1</sub>	B <sub>u</sub>	885-1132
CH <sub>3</sub> rocking	A <sub>1</sub> , B <sub>1</sub>	B <sub>u</sub>	895
<C-C-C bend	A <sub>1</sub> , B <sub>1</sub>	B <sub>u</sub>	0-535
CH <sub>2</sub> twist-rock	B <sub>2</sub>	A <sub>u</sub>	1175-1310
CH <sub>2</sub> rock-twist	B <sub>2</sub>	A <sub>u</sub>	719-1060
CH <sub>3</sub> -CH <sub>2</sub> torsion	B <sub>2</sub>	A <sub>u</sub>	0-153
CH <sub>2</sub> -CH <sub>2</sub> torsion	B <sub>2</sub>	A <sub>u</sub>	25-140

\*Paraffins C<sub>n</sub>H<sub>2n+2</sub> with n odd belong to the C<sub>2v</sub> point group and those with n even belong to the C<sub>2h</sub> point group. Infrared active species of C<sub>2v</sub> are A<sub>1</sub>, B<sub>1</sub>, B<sub>2</sub> and of C<sub>2h</sub> are A<sub>u</sub> and B<sub>u</sub>. All species of C<sub>2v</sub> are Raman active, but only species Ag and Bg of C<sub>2h</sub> are Raman active.

The chemical formula for TPTMS is  $(\text{CH}_3)(\text{C}_6\text{H}_5)_4\text{Si}_3\text{O}_2$ , and the infrared spectrum of this liquid is characterized by bands due to the methyl ( $\text{CH}_3$ ) groups, the phenyl ( $\text{C}_6\text{H}_5$ ) groups,  $\text{Si}-(\text{CH}_3)$  linkages,  $\text{Si} = (\text{C}_6\text{H}_5)$  linkages,  $\text{Si}-\text{O}$ , and many structural modes. At least 35 infrared active bands were observed for this material. A helpful review of infrared bands due to these chemical groups is provided by References (35) and (36).

c.  $R(\nu)$  and  $N(\nu)$  Spectra for Diesel Fuel, Fog Oil, and TMTPTS.

The measured near-normal incidence relative reflectance spectra for diesel fuel, fog oil, and TMTPTS(DC-704) in the spectral regions  $300-2,500 \text{ cm}^{-1}$  and  $2,500-5,000 \text{ cm}^{-1}$  are presented in Figs. 39 and 40, respectively. The relative reflectance spectrum of each material was analyzed by use of the Kramers-Kronig techniques described in Section V.A.2.c. to obtain  $N(\nu) = n(\nu) + ik(\nu)$  for each material. Spectral values of  $N(\nu)$  for diesel fuel, fog oil, and TMTPTS are presented graphically in Figs. 41-44.

d. Discussion of Spectra for Diesel Fuel, Fog Oil, and TMTPTS.

In the relative reflectance spectra, the spectral features near  $3,600 \text{ cm}^{-1}$  and  $1,640 \text{ cm}^{-1}$  are due primarily to liquid water which was the reflectance standard. Liquid water also has the infrared active intermolecular vibrational band of half-width  $500 \text{ cm}^{-1}$  centered at  $580 \text{ cm}^{-1}$ . The other features in the  $R(\nu)$  spectra correspond to infrared active bands of the diesel fuel, fog oil, or TMTPTS. The spectral features due to water do not appear

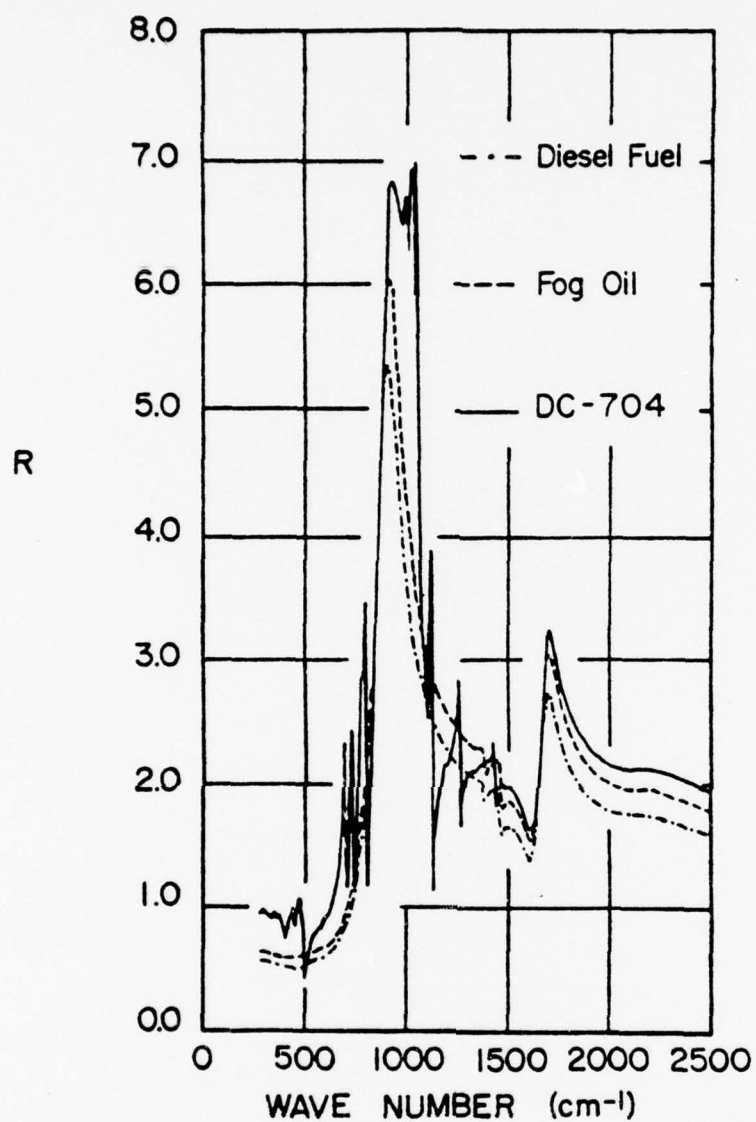


Figure 39. Near-normal incidence relative specular reflectance  $R(\nu)$  in the 300-2,500  $\text{cm}^{-1}$  spectral region for DC-704 (TMTPTS), fog oil, and diesel fuel.

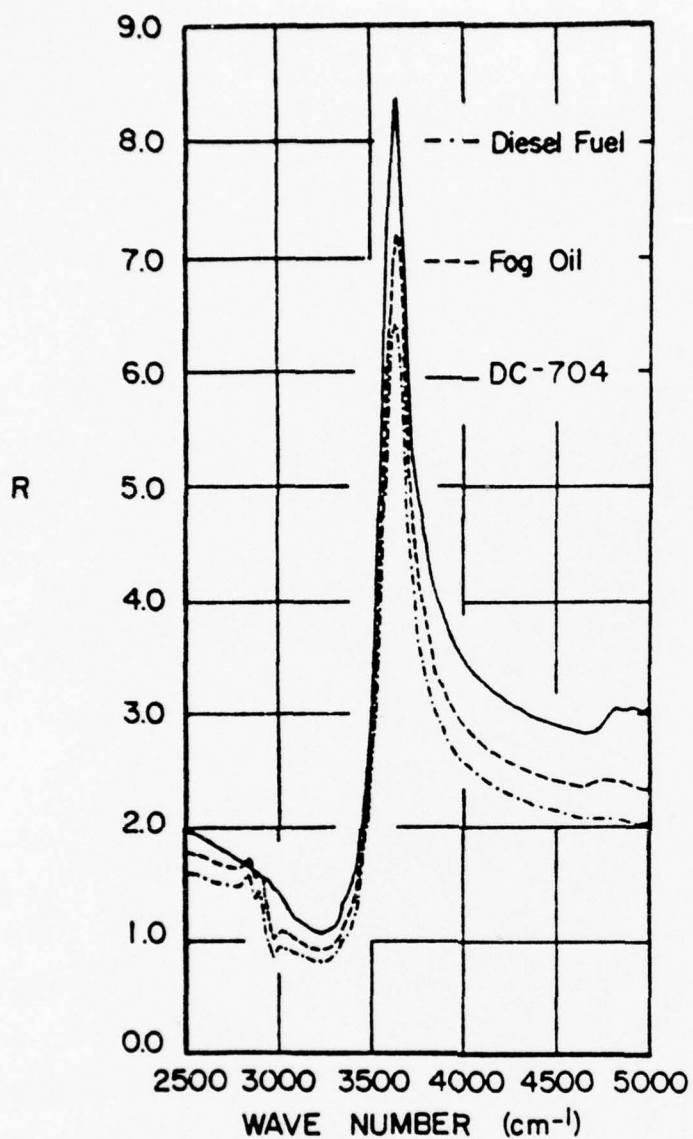


Figure 40. Near-normal incidence relative specular reflectance  $R(\nu)$  in the 2,500-5,000  $\text{cm}^{-1}$  spectral region for DC-704 (TMTPTS), fog oil, and diesel fuel.

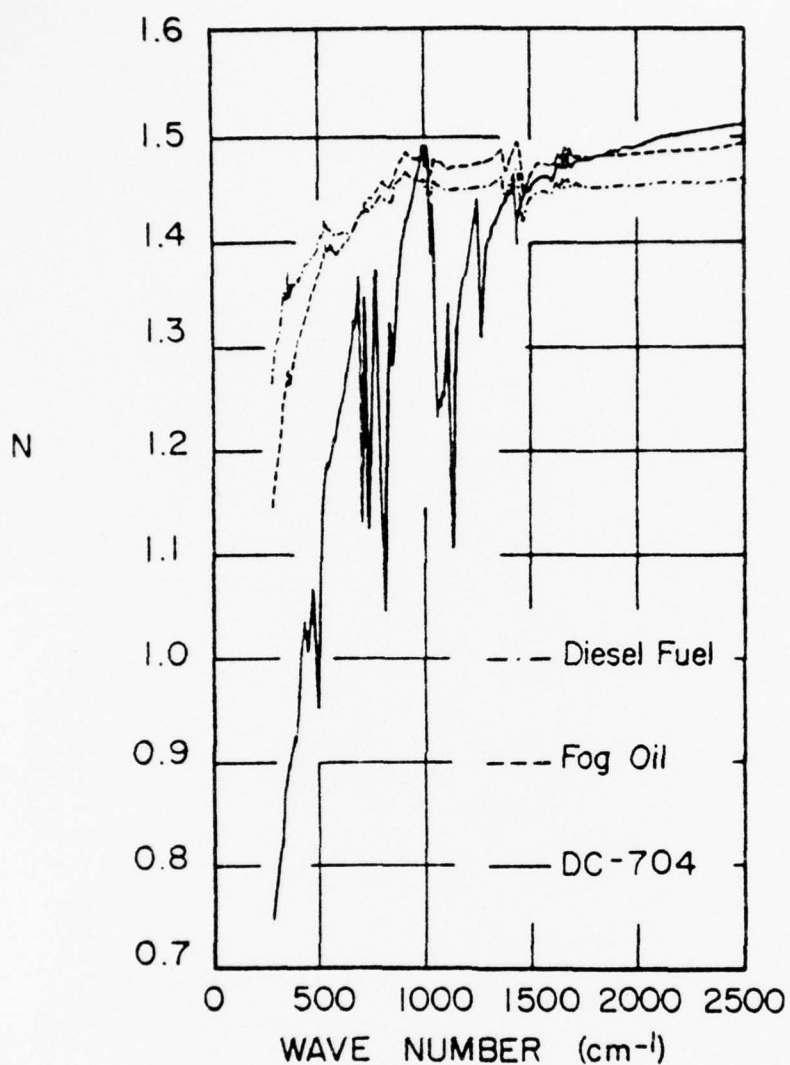


Figure. 41. Index of refraction  $n(\nu)$  in the  $300\text{--}2,500\text{ cm}^{-1}$  spectral region for DC-704 (TMPTS), fog oil, and diesel fuel.

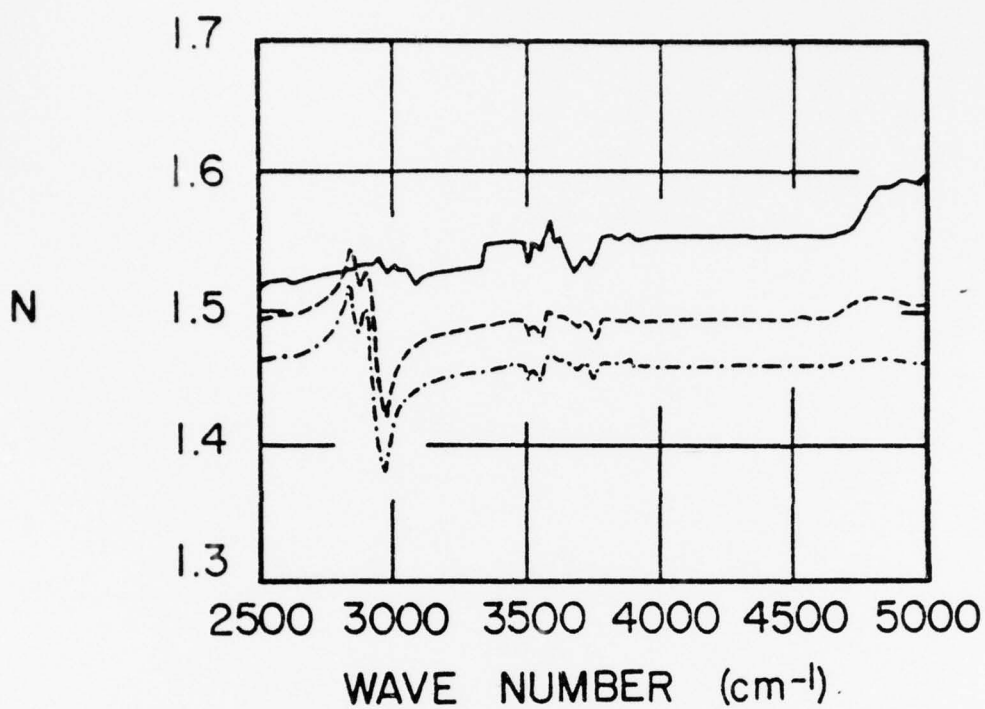


Figure 42. Index of refraction  $n(\nu)$  in the 2,500-5,000  $\text{cm}^{-1}$  spectral region for DC-704 (TMPTS), fog oil, and diesel fuel.

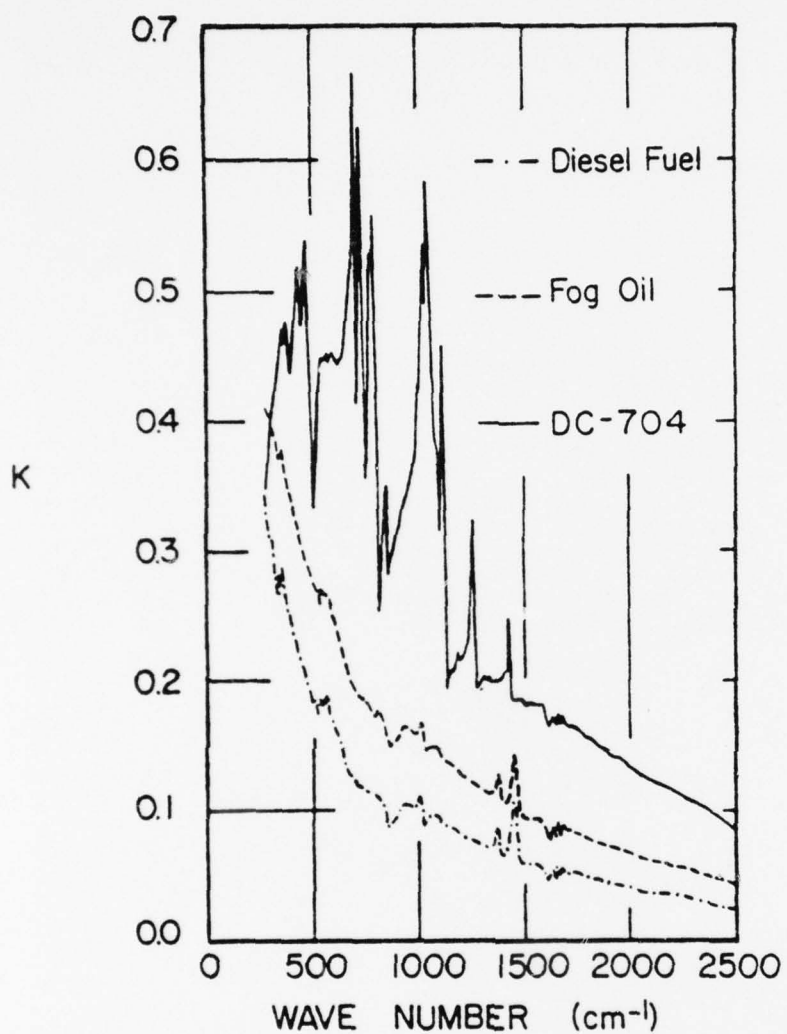


Figure 43. Extinction coefficient  $k(\nu)$  in the  $300\text{--}2,500\text{ cm}^{-1}$  spectral region for DC-704 (TMPTS), fog oil, and diesel fuel.

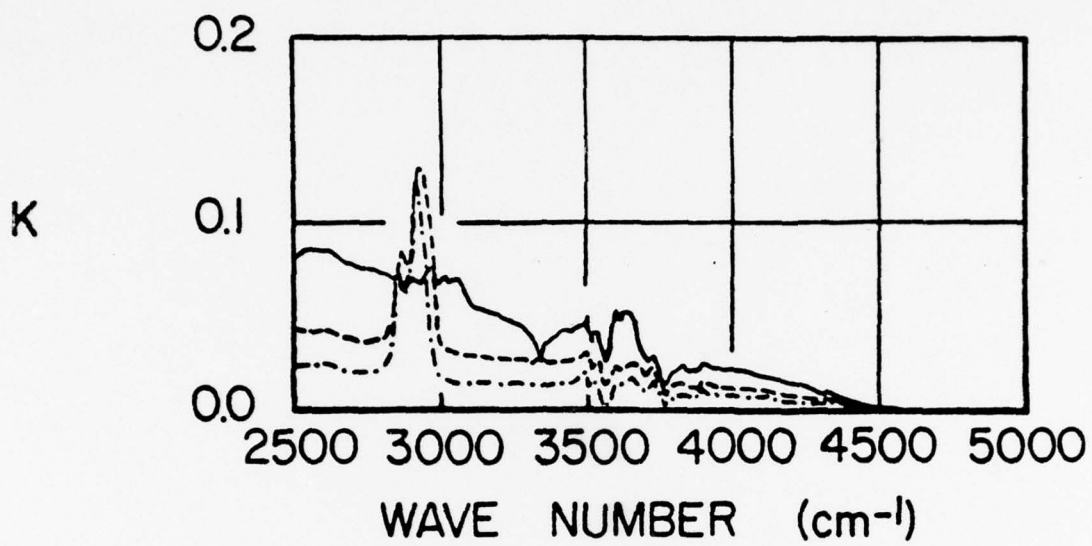


Figure 44. Extinction coefficient  $k(\nu)$  in the 2,500-5,000  $\text{cm}^{-1}$  spectral region for DC-704 (TMIPTS), fog oil, and diesel fuel.

in the  $N(\nu)$  spectra. However, the  $N(\nu)$  spectra should be uniformly smoothed through the 3,300-3,800  $\text{cm}^{-1}$  spectral region where the strong absorption due to atmospheric water vapor rendered these data less reliable than in adjoining spectral regions.

The spectra for diesel fuel and fog oil were quite similar as one would expect from prior knowledge of their chemical composition. The infrared active intramolecular bands observed in the spectra for diesel fuel and fog oil are listed in Table X. The molecular vibrations corresponding to these bands are listed in column 3 of Table X, and were obtained by consulting Table IX. The bands are all relatively weak.

Table X. Infrared active intramolecular bands observed in the spectra for Diesel Fuel and Fog Oil.

Diesel Fuel	Fog Oil	Vibration
2,920 $\text{cm}^{-1}$	2,924 $\text{cm}^{-1}$	$\text{CH}_2$ asymmetric stretch
2,857	2,857	$\text{CH}_2$ symmetric stretch
1,455	1,455	$\text{CH}_2$ HCH $\angle$ bend
1,375	1,376	$\text{CH}_3$ , HCH $\angle$ bend
900-1,000	900-1,000	C-C stretch
570	550	C-C-C $<$ bend
395	395	C-C-C $<$ bend

There are at least 35 infrared active bands in the spectra for TMTPS. A positive identification of all the bands was not possible without a normal coordinate analysis of TMTPS. However, we did assign the more obvious bands by use of References (35) and (36).

Our assignments were tabulated and appear in Table XI.

We have not determined the half-widths and strengths of the infrared bands of these materials, but we will during the follow-on-contract period.

Table XI. Infrared active intramolecular vibrational bands observed in the spectrum of tetramethyl-tetraphenyl-trisiloxane.

$\nu(\text{cm}^{-1})$		$\nu(\text{cm}^{-1})$	
3,056(W)	Phenyl C-H stretch	1,082(M)	Si-O-Si str. or phenyl in plane deform.
3,012(W)	Phenyl C-H stretch	1,041(Vs)	Si-O-Si
2,956(W)	CH <sub>3</sub> Asym. stretch	1,024(Vs)	Si-O-Si or phenyl in plane deform.
2,899(VW)	CH <sub>3</sub> sym. stretch	1,000(W)	Phenyl ring breathing (Star of David)
2,853(VW)		915(M)	CH <sub>3</sub> rocking
1,961(VW)	Comb. or overtone	840(S)	(CH <sub>3</sub> )-Si-(CH <sub>3</sub> )
1,877(VW)	Comb. or overtone	791(Vs)	(CH <sub>3</sub> )-Si-(CH <sub>3</sub> )
1,585(W)	Phenyl skeletal stretch	774(Vs)	(CH <sub>3</sub> )-Si-(CH <sub>3</sub> )
1,492(W)	Phenyl skeletal stretch	723(Vs)	Phenyl out of plane bend
1,427(M)	Phenyl skeletal stretch	693(Vs)	Phenyl out of plane skeletal band
1,409(W)	Asym. CH <sub>3</sub> deformation	663(M)	Si-(C <sub>6</sub> H <sub>5</sub> )
1,375(VW)	Sym. CH <sub>3</sub> deformation	595(M)	Si-O-Si
1,323(VW)		570(M)	Si-O-Si
1,301(VW)		468(Vs)	Si-(C <sub>6</sub> H <sub>5</sub> )
1,256(S)	Si-CH <sub>3</sub> & Si-(CH <sub>3</sub> ) str.	434(Vs)	(CH <sub>3</sub> )-Si-(C <sub>6</sub> H <sub>5</sub> ) <sub>2</sub>
1,187(W)	Phenyl in plane deform.	374(M)	Si-[O-(CH <sub>3</sub> )] <sub>2</sub>
1,156(VW)	Phenyl in plane deform.	351(M)	(CH <sub>3</sub> )-Si-(C <sub>6</sub> H <sub>5</sub> ) <sub>2</sub>
1,115(VS)	Si-C <sub>6</sub> H <sub>5</sub> stretch		

Vs = very strong, S = strong, M = medium, W = weak, VW = very weak

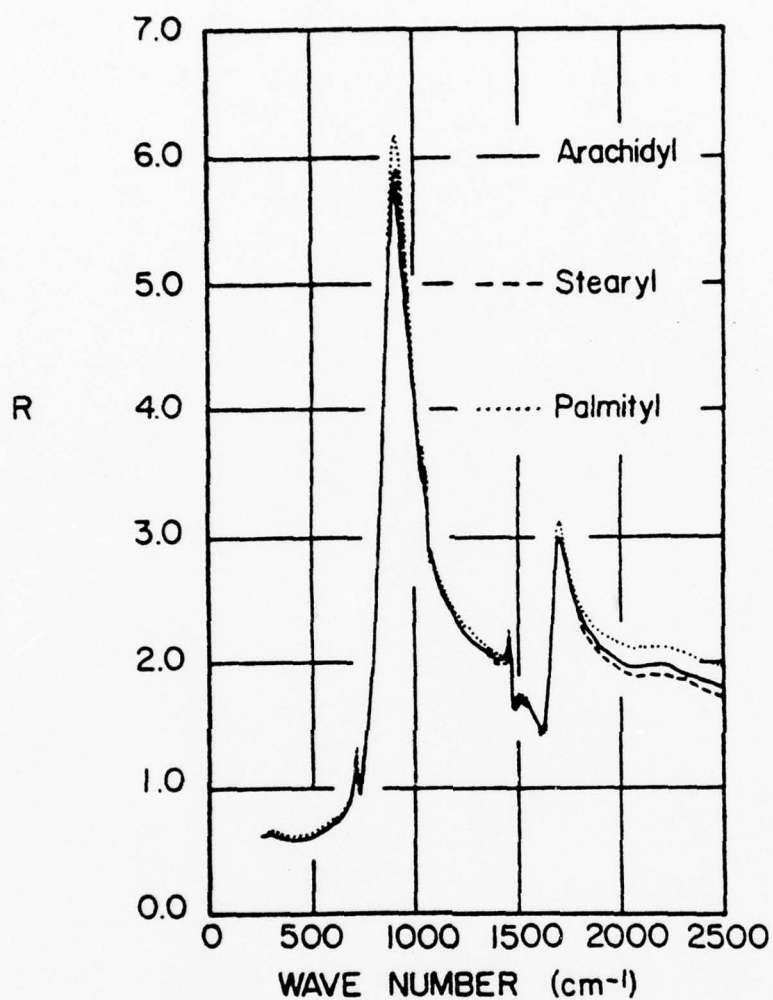


Figure 45. Near-normal incidence relative specular reflectance  $R(\nu)$  in the  $300\text{--}2,500\text{ cm}^{-1}$  spectral region for 1-hexadecanol (palmityl), 1-octadecanol (stearyl), and 1-eicosanol (arachidyl).

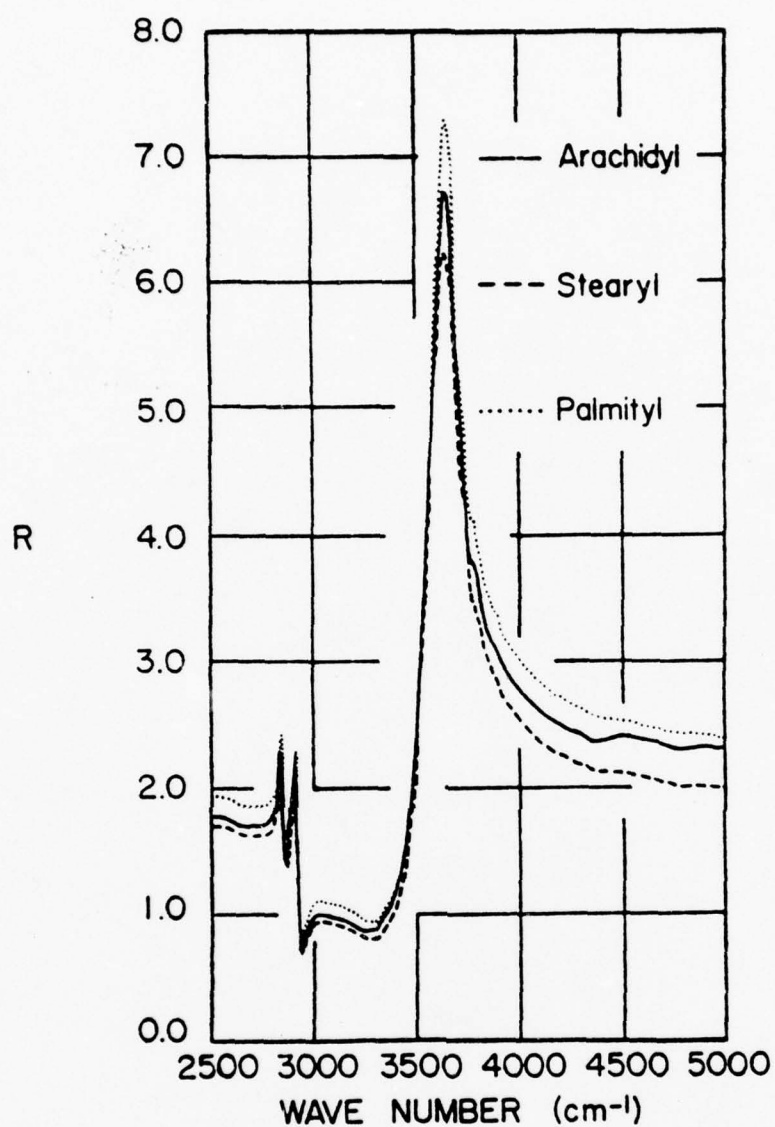


Figure 46. Near-normal incidence relative specular reflectance  $R(\nu)$  in the 2,500-5,000  $\text{cm}^{-1}$  spectral region for 1-hexadecanol (palmityl), 1-octadecanol (stearyl), and 1-eicosanol (arachidyl).

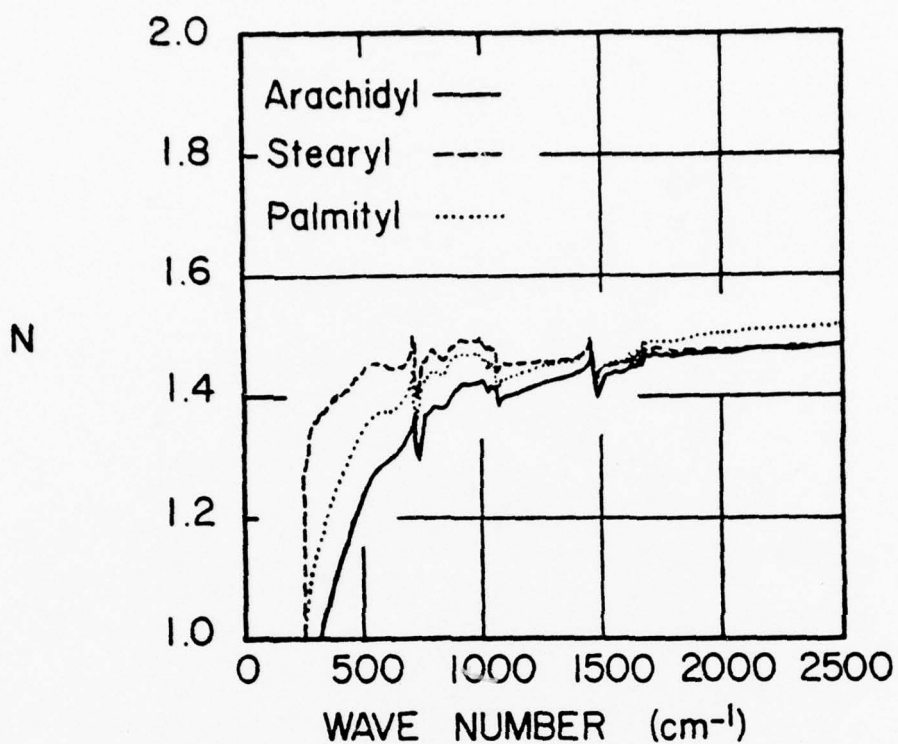


Figure 47. Index of refraction  $n(\nu)$  in the  $300\text{--}2,500\text{ cm}^{-1}$  spectral region for 1-hexadecanol (palmityl), 1-octadecanol (stearyl), and 1-eicosanol (arachidyl).

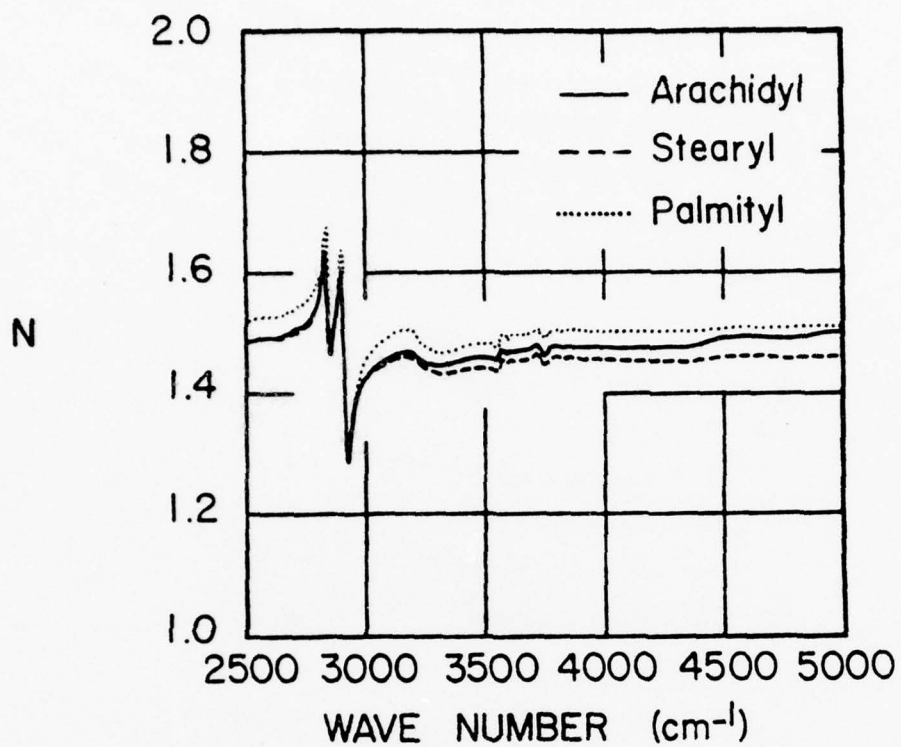


Figure 48. Index of refraction  $n(\nu)$  in the 2,500-5,000  $\text{cm}^{-1}$  spectral region for 1-hexadecanol (palmityl), 1-octadecanol (stearyl), and 1-eicosanol (arachidyl).

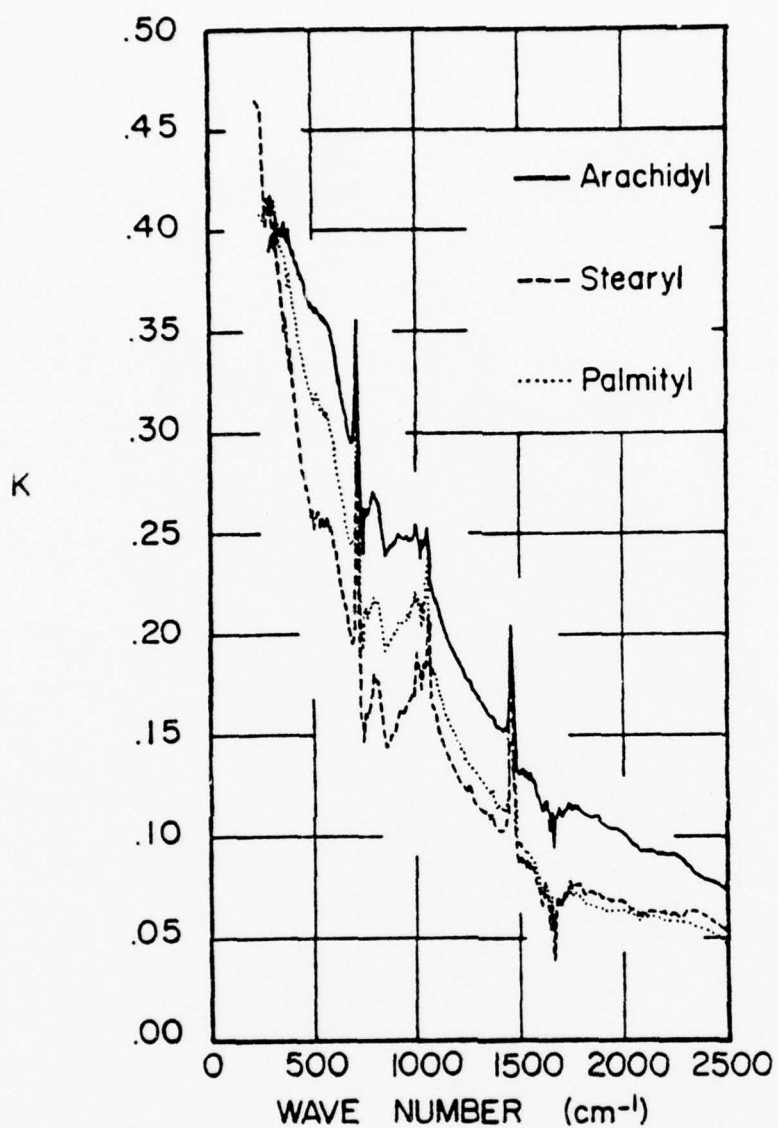


Figure 49. Extinction coefficient  $k(\nu)$  in the 300-2,500  $\text{cm}^{-1}$  spectral region for 1-hexadecanol (palmityl), 1-octadecanol (stearyl), and 1-eicosanol (arachidyl).

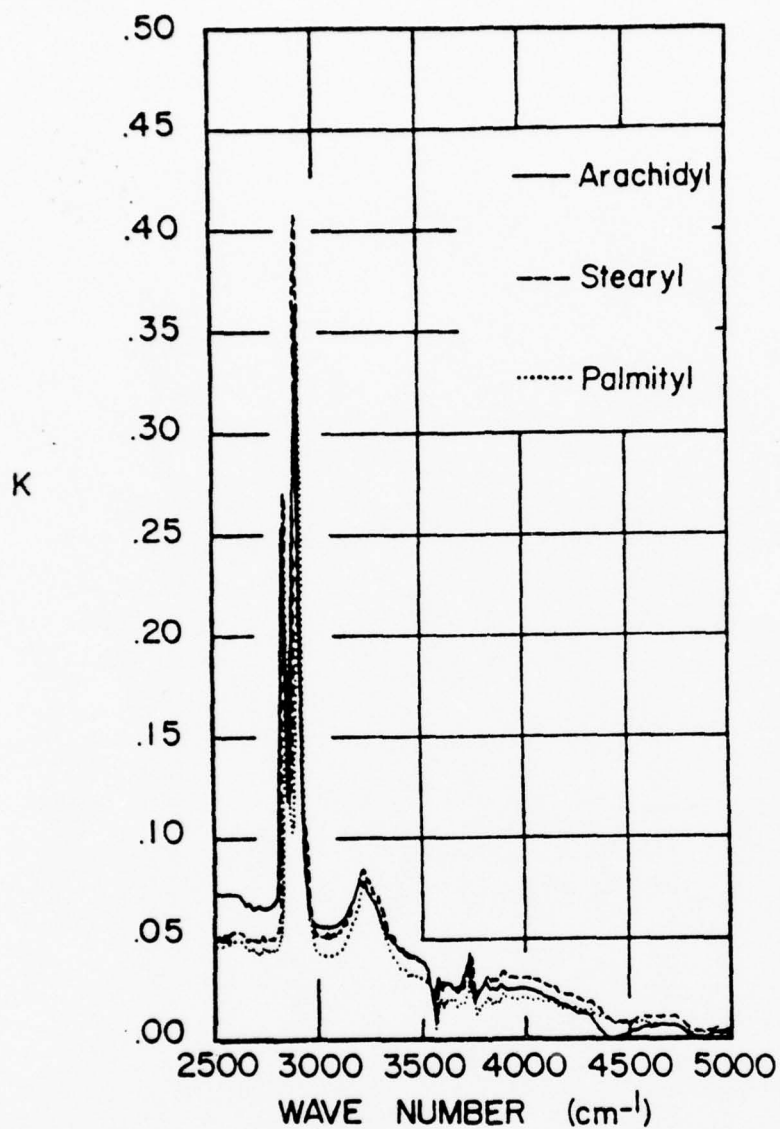


Figure 50. Extinction coefficient  $k(\nu)$  in the 2,500-5,000  $\text{cm}^{-1}$  spectral region for 1-hexadecanol (palmityl), 1-octadecanol (stearyl), and 1-eicosanol (arachidyl).

e.  $R(\nu)$  and  $N(\nu)$  Spectra of for Solid Alcohols.

The measured near-normal incidence relative reflectance spectra  $R(\nu)$  for 1-hexadecanol (palmityl), 1-octadecanol (stearyl), and 1-eicosanol (arachidyl) in the 300-3,500 and 2,500-5,000  $\text{cm}^{-1}$  regions are presented in Figs. 45 and 46. The  $R(\nu)$  spectrum of each alcohol was analyzed by use of Kramers-Kronig techniques to obtain  $N(\nu) = n(\nu) + ik(\nu)$  of each material. Spectral values of  $N(\nu)$  for these alcohols are presented graphically in Figs. 47-50.

f. Discussion of Spectra for Solid Alcohols.

In their structure and chemical composition these alcohols are very closely related to the n-paraffins, in that one hydrogen atom of the n-paraffin is replaced by an O-H member. The spectra of the alcohols thus include many features that are similar to the spectra of the n-paraffins. The strongest bands observed in these spectra are listed in Table XII. The number of vibrational modes for these alcohol molecules is  $9n$ , where  $n = 16$ , 18, and 20. Thus some of the bands listed in Table XII are actually an envelope of several closely spaced bands.

Although the point group symmetry of the alcohols is not the same as that of the corresponding n-even ( $C_{2h}$ ) n-paraffin, the bands in the alcohols can be assigned by using References (33) as a guide.

Table XII. Wave-number positions and assignments for the strongest infrared bands observed in the spectra of the alcohols.

1-hexadecanol (Palmityl)	1-octadecanol (stearyl)	1-eicosanol (Arachidyl)	Vibrational Assignment
3,228 $\text{cm}^{-1}$	3,228 $\text{cm}^{-1}$	3,228 $\text{cm}^{-1}$	O-H stretch
2,920	2,920	2,920	$\text{CH}_2$ asym. stretch
2,853	2,853	2,853	$\text{CH}_2$ sym. stretch
1,464	1,464	1,464	$-\text{CH}_2-$ deformation
1,061	1,063	1,060	C-C stretch
1,039	1,038	1,034	C-C stretch
801	801	800	$\text{CH}_2$ rocking-twisting
718	719	718	$\text{CH}_2$ rocking-twisting
572	578	576	C-C-C structural mode

g. R(v) and N(v) spectra for Polymethyl-methacrylate (PMMA).

The measured near-normal incidence relative reflectance spectrum for PMMA in the spectral regions  $300\text{--}2,500\text{ cm}^{-1}$  and  $2,500\text{--}5,000\text{ cm}^{-1}$  are presented in Figs. 51(a) and 51(b), respectively. The relative reflectance spectrum was analyzed by use of the Kramers-Kronig techniques described in Section V.A.2.c. to obtain  $N(v) = n(v) + ik(v)$  for this material. Spectral values of  $N(v)$  are presented graphically in Figs. 52(a), 52(b), 53(a), and 53(b).

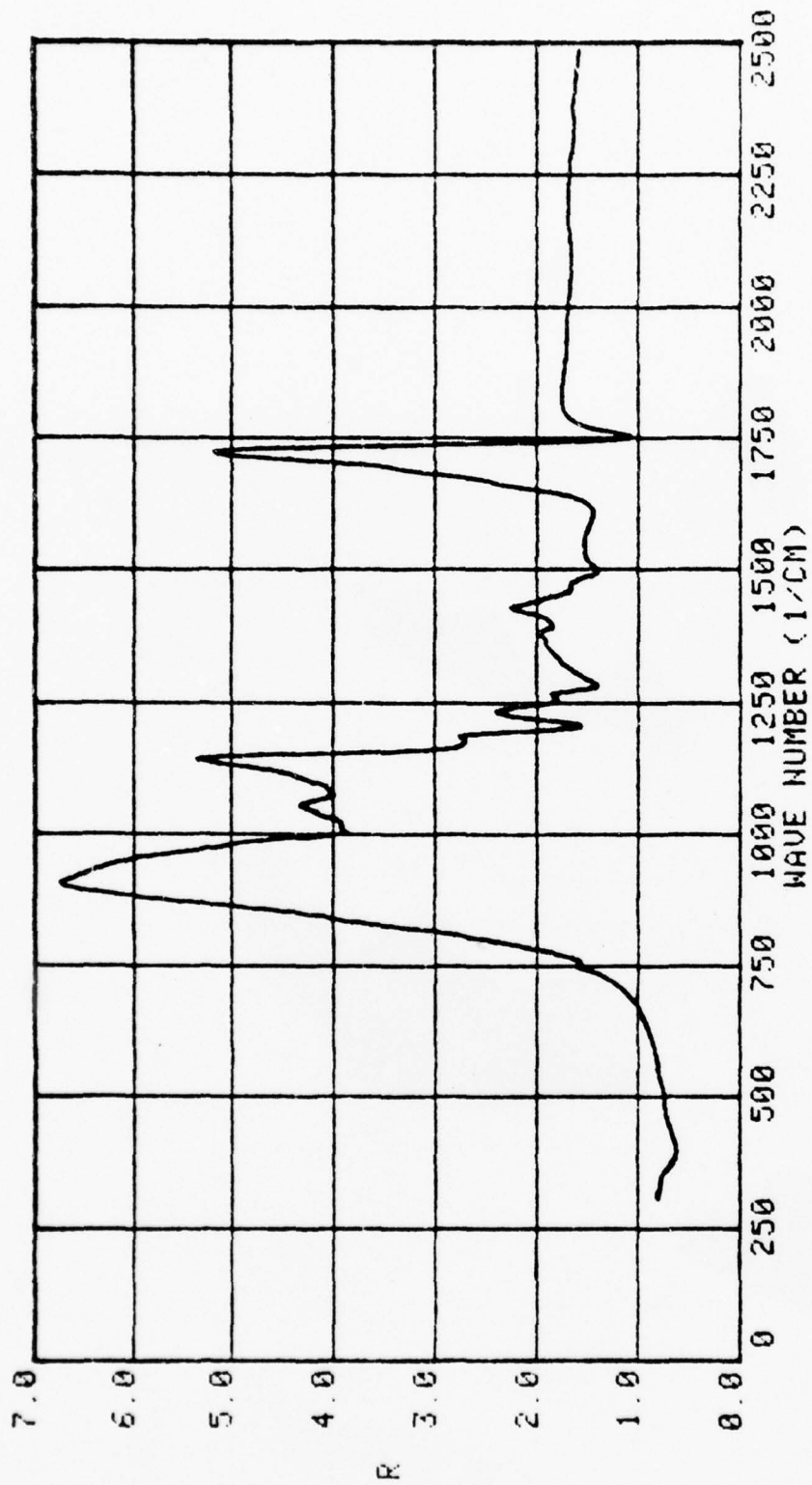


Figure 51(a). Near-normal incidence relative specular reflectance  $R(\nu)$  in the 300-2,500  $\text{cm}^{-1}$  spectral region for PMMA.

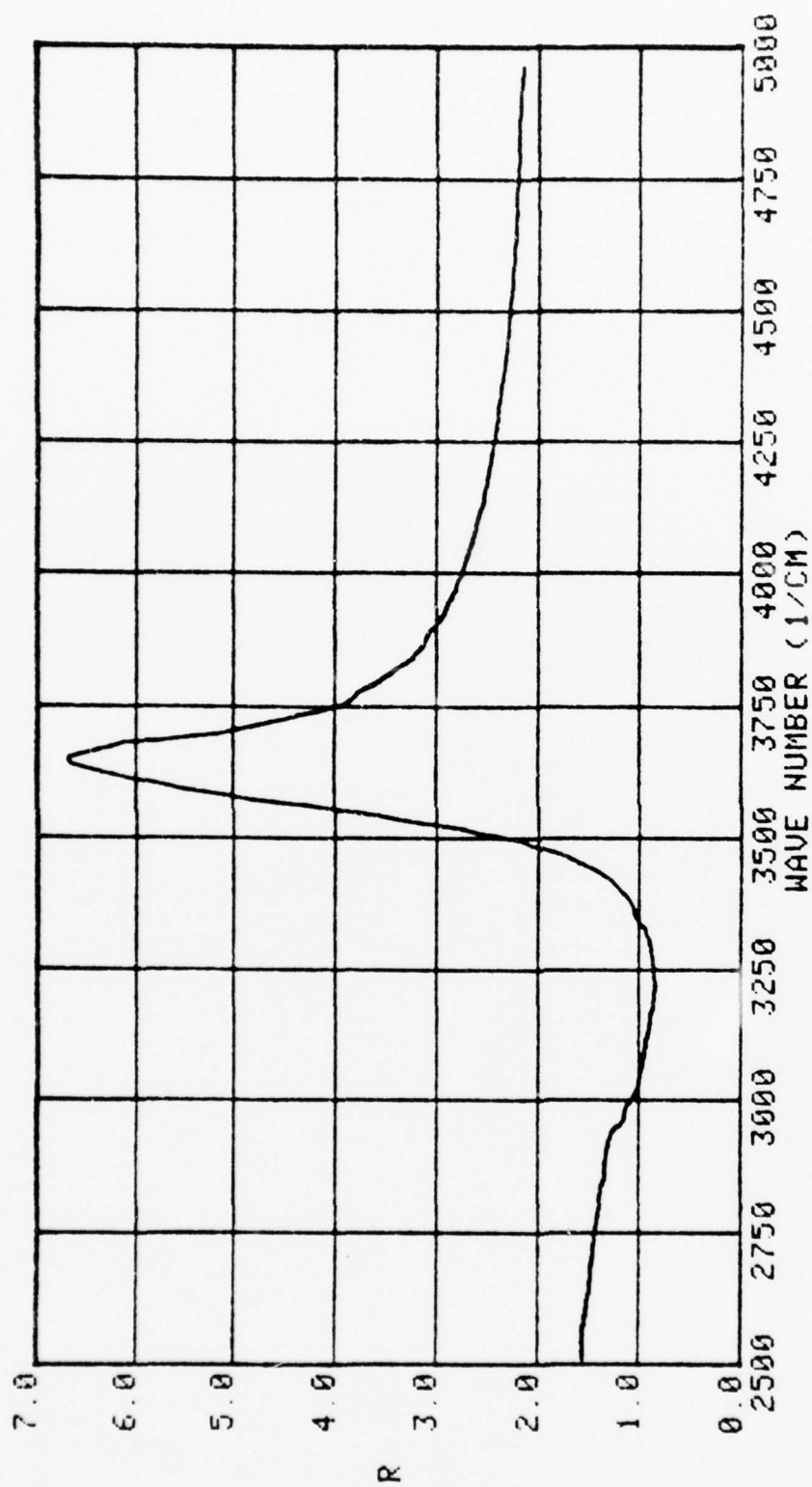


Figure 51(b). Near-normal incidence relative specular reflectance  $R(\nu)$  in the 2,500-5,000  $\text{cm}^{-1}$  spectral region for PMMA.

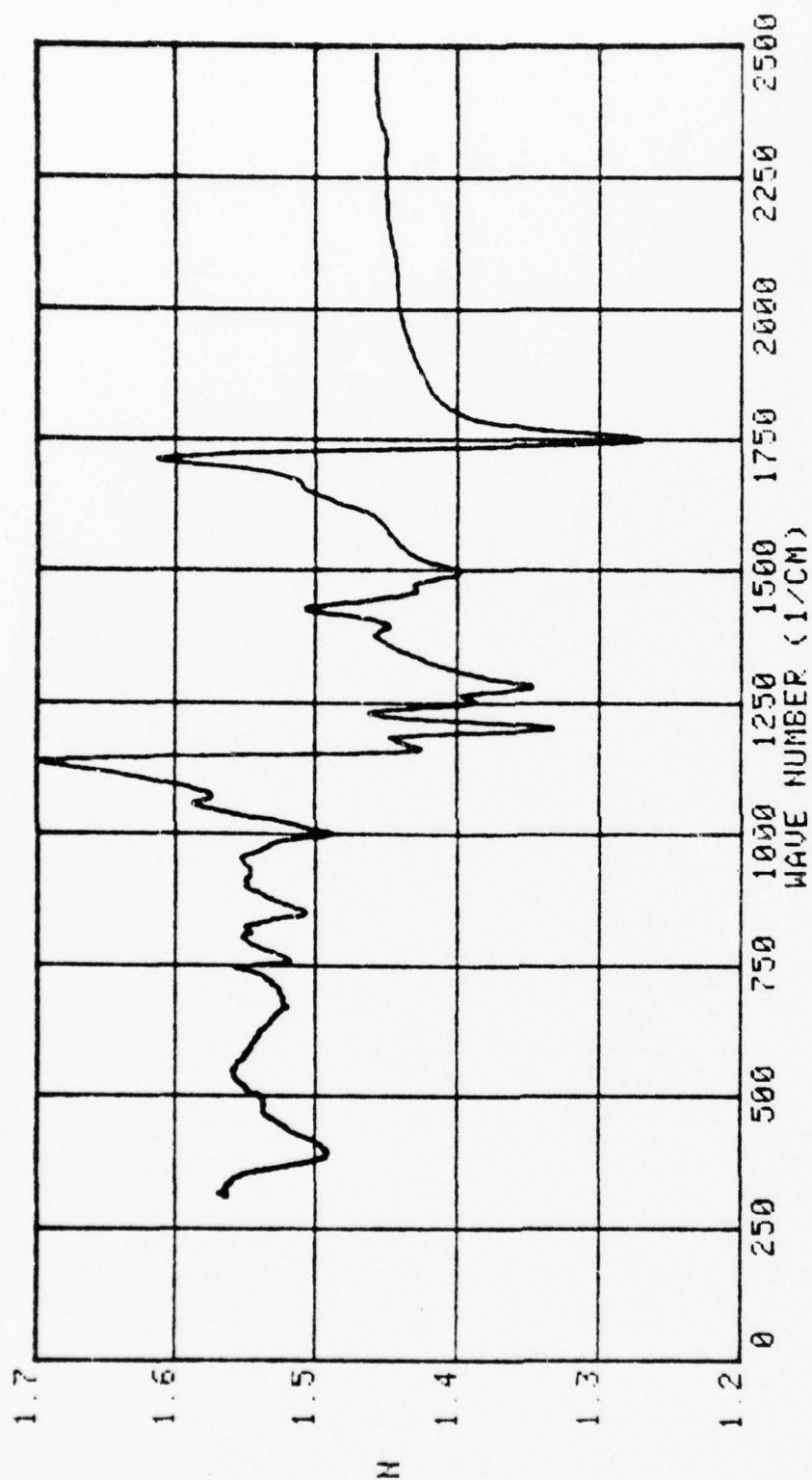


Figure 52(a). Index of refraction  $n(\nu)$  in the 300-2,500  $\text{cm}^{-1}$  spectral region for PMMA.

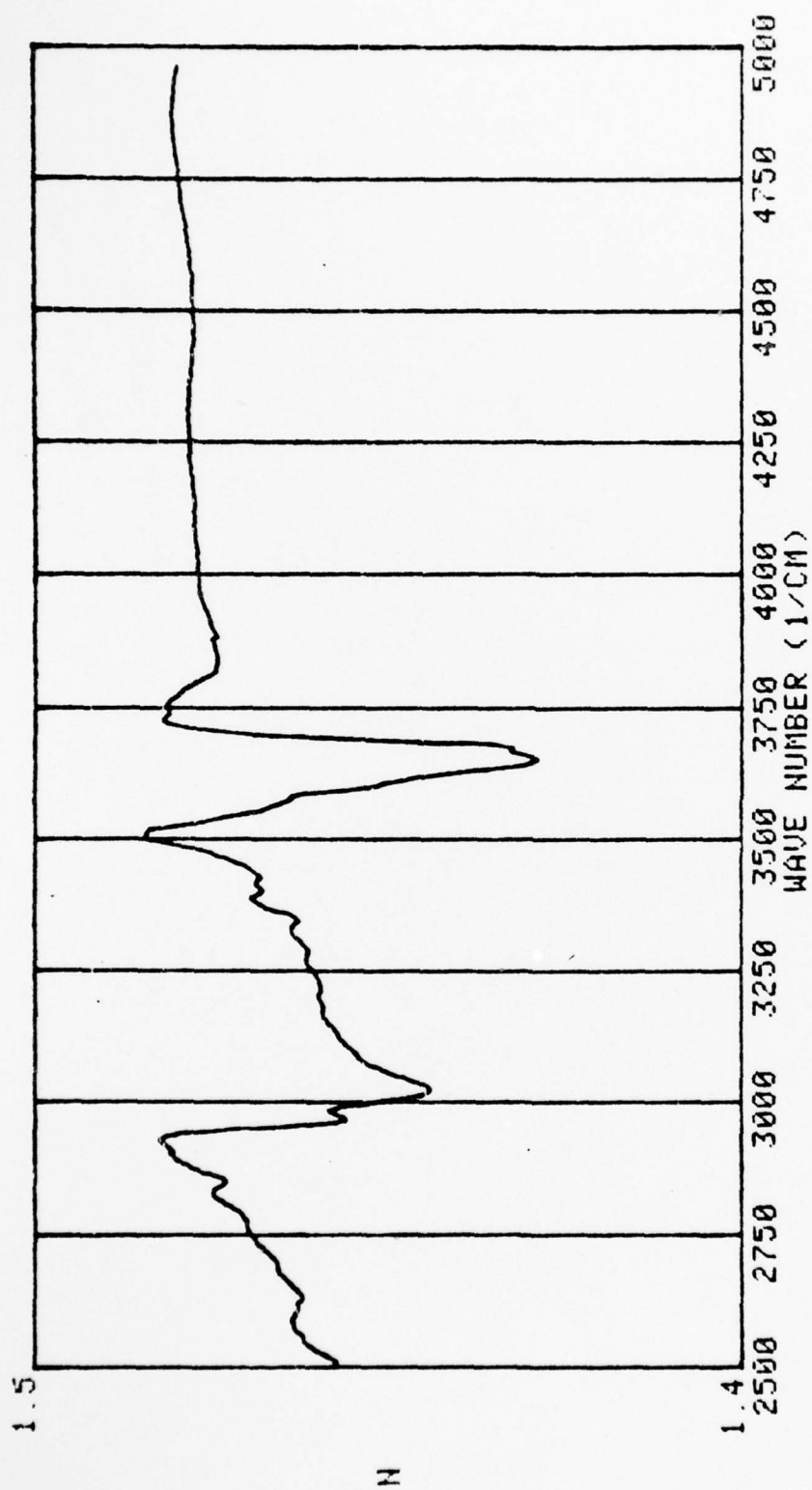


Figure 52(b). Index of refraction  $n(\nu)$  in the 2,500-5,000  $\text{cm}^{-1}$  spectral region for PMMA.

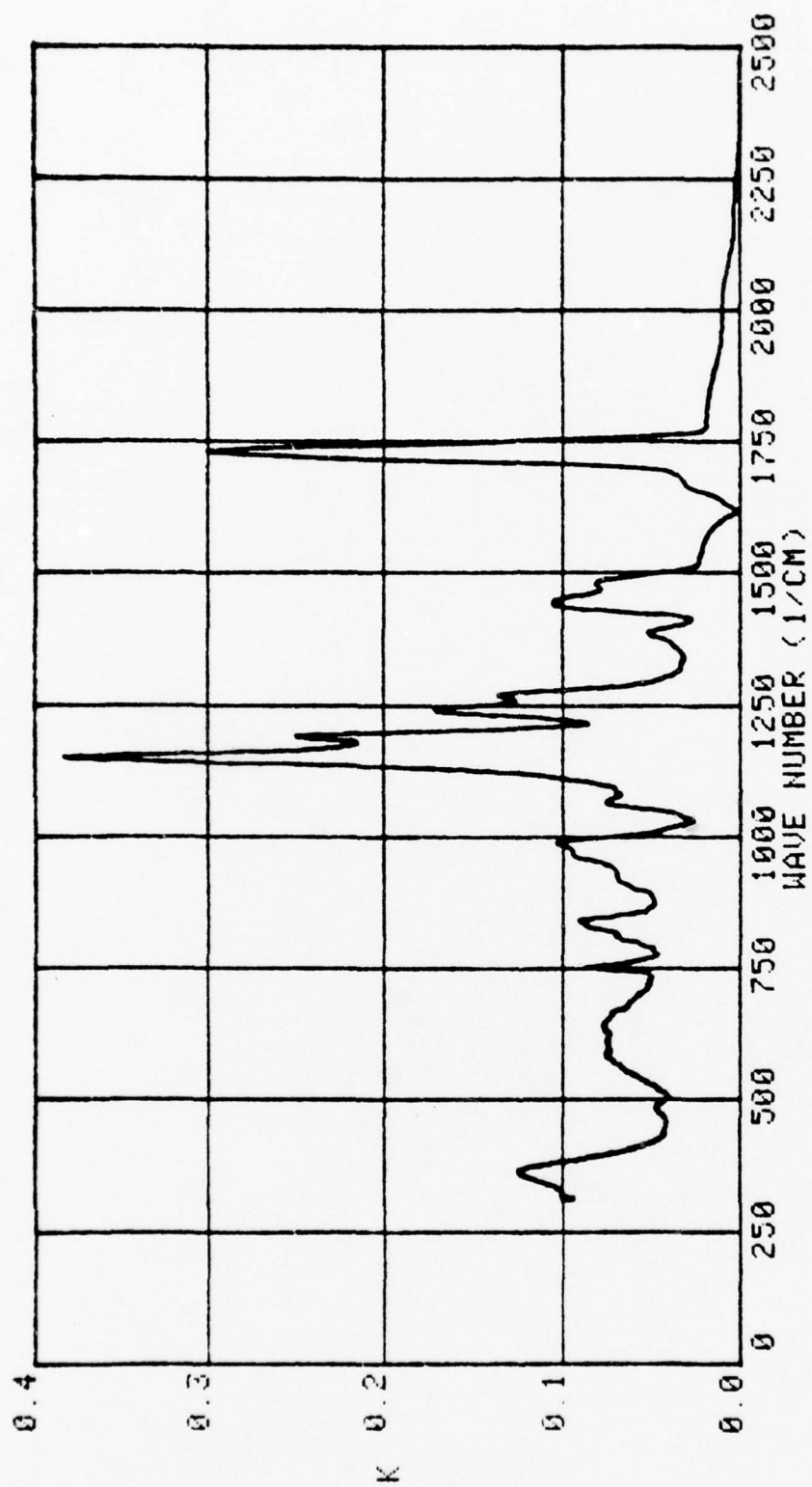


Figure 53(a). Extinction coefficient  $k(\nu)$  in the 300-2,500  $\text{cm}^{-1}$  spectral region for PMMA.

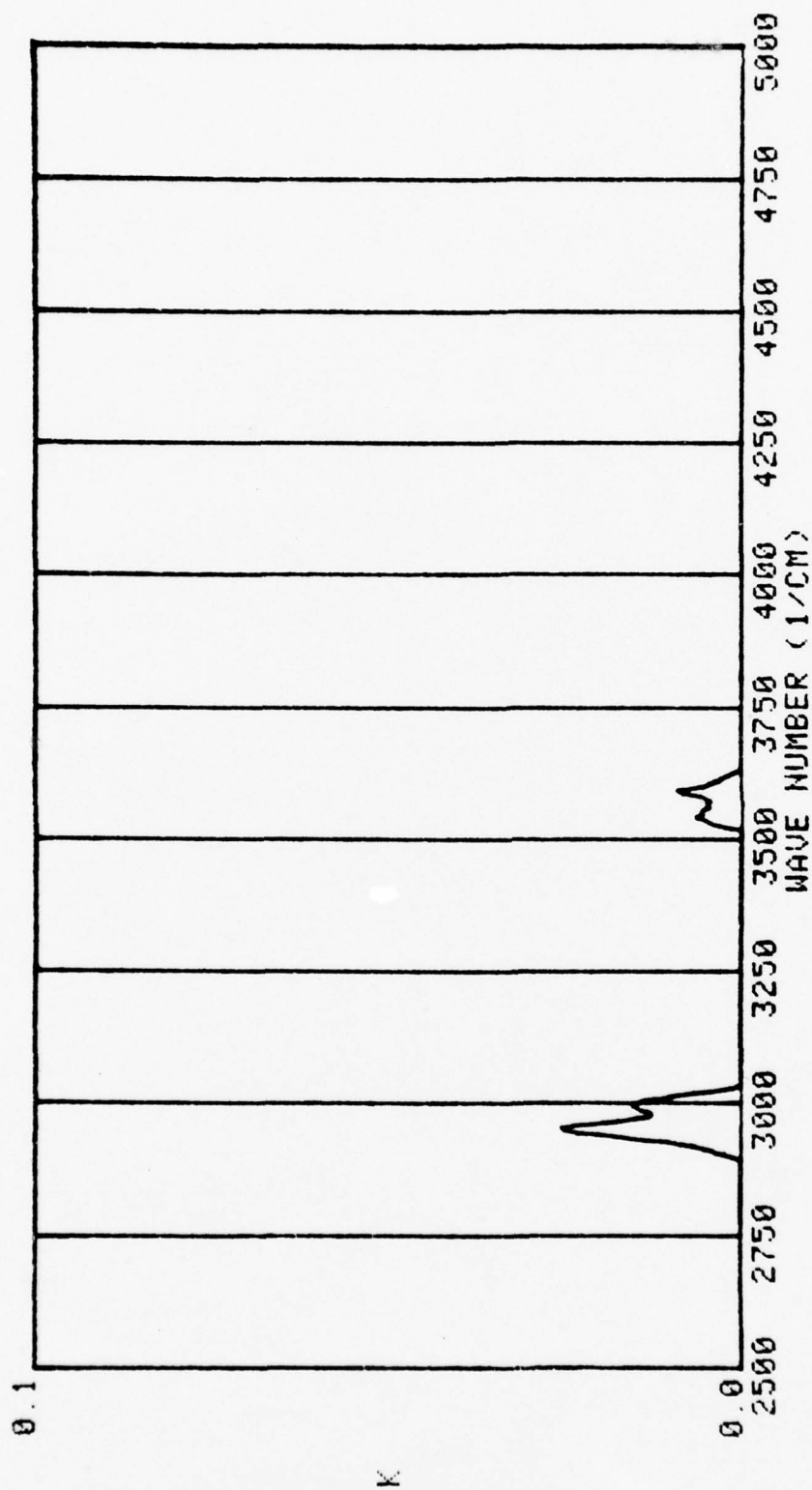
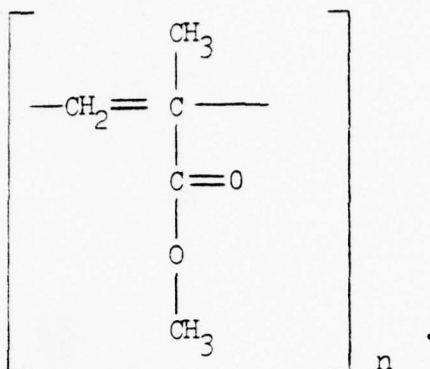


Figure 53(b). Extinction coefficient  $k(\nu)$  in the 2,500-5,000  $\text{cm}^{-1}$  spectral region for PMMA.

## h. Discussion of Spectra for PMMA,

The chemical formula for PMMA is



The most prominent infrared active bands observed in the spectrum of PMMA, and their assignments, are listed in Table XIII. There are weaker overtone and combination bands which are not listed in Table XIII. The bands at 3,591 and 3,552  $\text{cm}^{-1}$ , are believed to be due to a surface layer of water taken on by the PMMA. No attempt was made to dry the PMMA in order to confirm this assumption.

Table XIII. Wave-number positions and assignments for infrared bands  
observed in PMMA.

$\nu(\text{cm}^{-1})$	Assignment
3,591(VW)	H <sub>2</sub> O asym. stretch
3,552(VW)	H <sub>2</sub> O sym. stretch
2,994(W)	CH <sub>2</sub> & CH <sub>3</sub> asym. stretch
2,949(W)	CH <sub>2</sub> & CH <sub>3</sub> sym. stretch
1,730(s)	C=O stretch
1,479(M)	C-CH <sub>3</sub>
1,443(M)	C-CH <sub>3</sub> asym. deformation
1,385(W)	C-CH <sub>3</sub> sym. deformation
1,267(M)	C-O-C
1,239(M)	C-O-C
1,198(s)	C-O-C
1,147(s)	C-O-C
1,063(W)	C-C-C stretch
985(M)	CH <sub>3</sub> rock or twist
966(M)	CH <sub>3</sub> rock or twist
917(W)	?
840(M)	?
833(W)	?
810(W)	?
750(M)	CH <sub>3</sub> rock or twist
639(M)	?
586(M)	C-CH <sub>3</sub> wagging
476(W)	C-CH <sub>3</sub> deform. + C=O deform. + C-CH <sub>3</sub> wag.
359(M)	C-O-CH <sub>3</sub> deform. + C-CH <sub>3</sub> deform.

## 6. Natural Rutile

### a. Objectives

Clouds composed of dust particles constitute naturally occurring obscurants. Radiation transport through such clouds is of current interest. Thus, during this Grant period we began an investigation of the optical properties of natural minerals. The objective of this investigation, which continues during a follow-on contract, is to measure the near-normal incidence relative reflectance spectra  $R(\nu)$  of selected natural minerals, and to compute values of  $N(\nu)$  by use of Kramers-Kronig techniques. Natural Rutile ( $\text{TiO}_2$ ) was one of the minerals selected for investigation.

### b. Background Information for Discussion of Rutile.

The infrared reflectance spectra of Rutile, which is an optically uniaxial crystal, has been the subject of several prior investigations. The more significant of these investigations can be found in References (37) and (38). During those previous investigations Rutile crystals were cut and polished with faces both parallel and perpendicular to the C-axis. In one instance<sup>37/</sup> the polished crystals were etched in concentrated  $\text{H}_3\text{PO}_4$  to remove an anomalous surface layer. In the other case the crystals were annealed several hours at 1700 K to regenerate the surface after polishing.

During our investigation a Rutile crystal was cut perpendicular to the C-axis and polished. The crystal was not etched or annealed, because the unetched or

non-annealed surface most likely corresponds to Rutile in its natural environment. Previous investigations of Corundum<sup>39/</sup> demonstrated a decrease in reflectance in the spectral region of phonon modes for unetched or nonannealed crystals in comparison to the reflectance of crystals which were etched or annealed. The reflectance of the unetched crystals can diminish to 50% of that for the etched crystals in the spectral vicinity of the lattice phonons. This is precisely the effect we observed in our reflectance spectrum for Rutile when compared to the reflectance spectra in References (37) and (38).

The allowable infrared active phonon modes for Rutile are  $A_{2u} + 3E_u$ . Additionally, there is a Raman active  $A_{1g}$  mode. The  $E_u(TO)$  modes occur at ca. 189, 382, and  $508\text{ cm}^{-1}$ . The  $A_{2u}(TO)$  mode occurs at ca.  $172\text{ cm}^{-1}$  and the  $A_{2u}(LO)$  mode at ca.  $796\text{ cm}^{-1}$ . The  $A_{1g}$  mode occurs in the  $500\text{--}600\text{ cm}^{-1}$  region. The  $E_u$  modes are observed when the incident electromagnetic radiation is polarized perpendicular to the c-axis, and the  $A_{2u}$  mode when the radiation is polarized parallel to the c-axis.

c.  $R(\nu)$  and  $N(\nu)$  Spectra for Rutile.

The measured near-normal incidence relative reflectance spectrum  $R(\nu)$  for natural Rutile in the  $300\text{--}5,000\text{ cm}^{-1}$  spectral region is presented in Fig. 54. The relative reflectance spectrum was analyzed by use of the

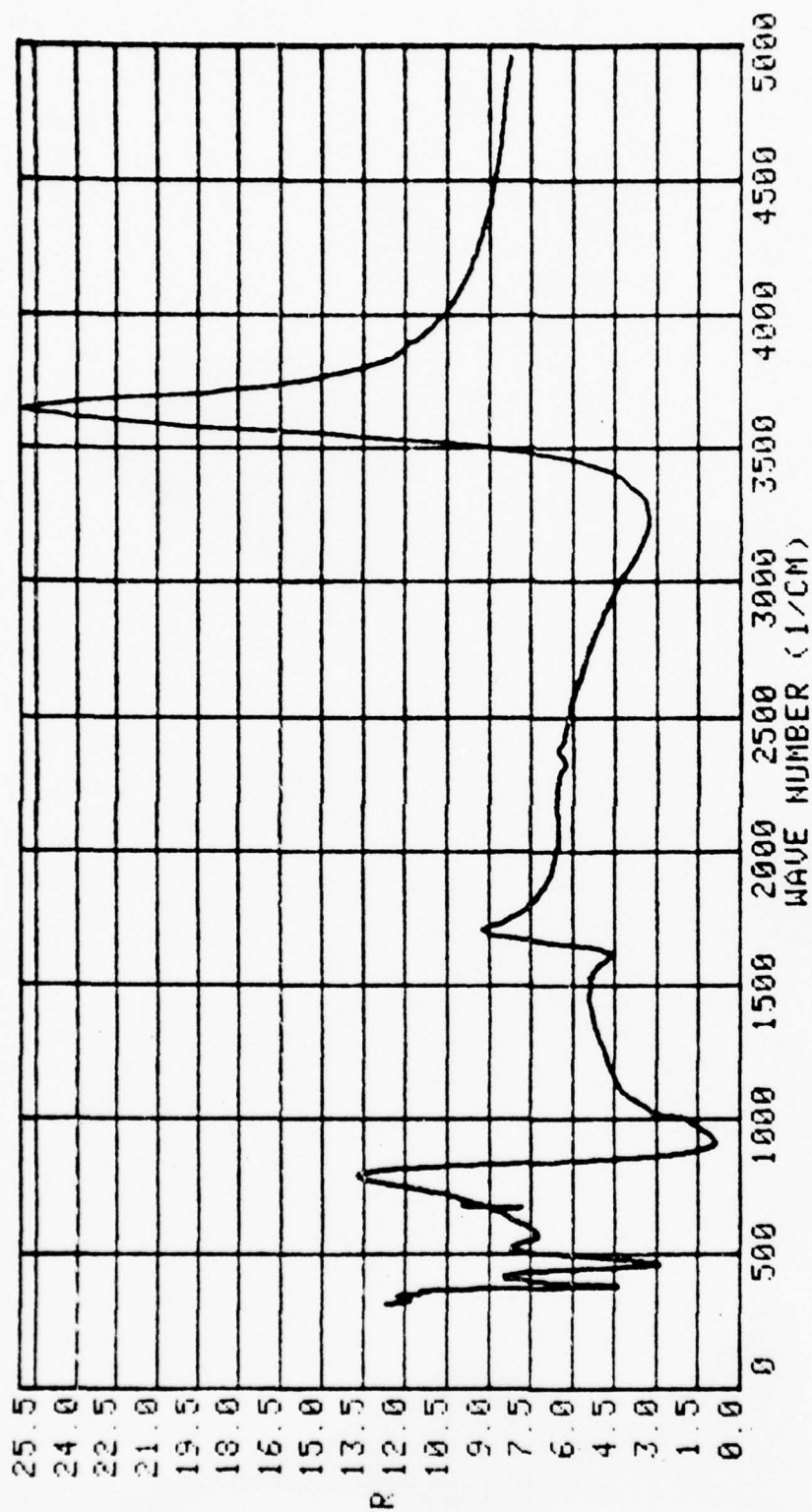


Figure 54. Near-normal incidence relative specular reflectance  $R(\nu)$  in the 300-5,000  $\text{cm}^{-1}$  region for natural Rutile ( $E_{1C}$ ). The sample was polished but was not etched or annealed.

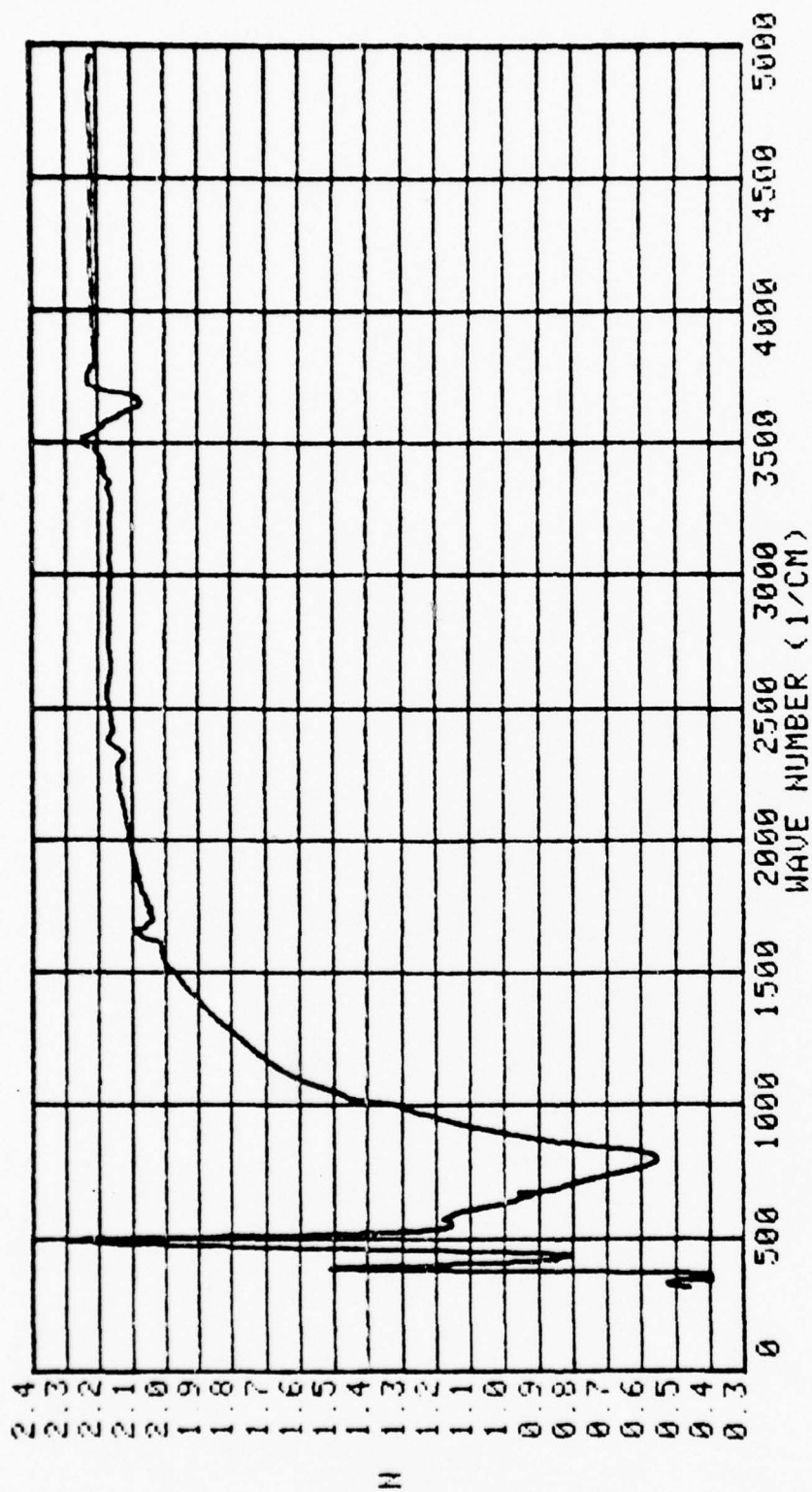


Figure 55. Index of refraction  $n(\nu)$  in the 300–5,000  $\text{cm}^{-1}$  spectral region for natural Rutile ( $E_{1C}$ ). The sample was polished but was not etched or annealed.

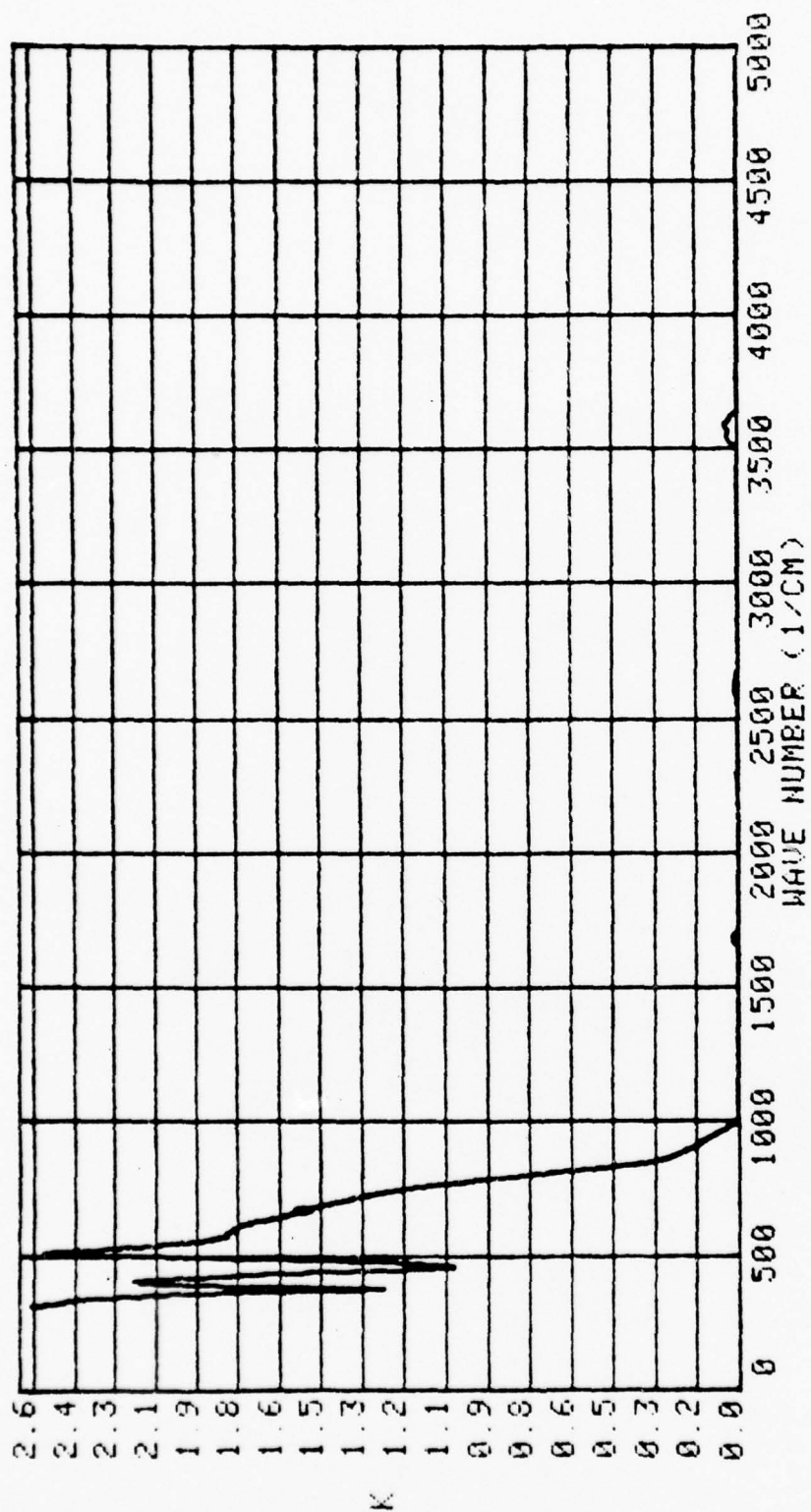


Figure 56. Extinction coefficient  $k(\nu)$  in the 300-5,000  $\text{cm}^{-1}$  spectral region for natural Rutile ( $E_1C$ ). The sample was polished but was not etched or annealed.

Kramers-Kronig techniques described in Section V.A.2.c. to obtain  $N(\nu)$  for this material. Spectral values of  $N(\nu)$  are presented graphically in Figs. 55 and 56.

These spectra are for the incident electromagnetic radiation polarized perpendicular to the C-axis of the Rutile sample. The sample was not etched or annealed after it was polished.

d. Discussion of Spectra of Rutile.

These spectra show to of the strong doubly degenerate  $E_u$  modes at 503 and 400  $\text{cm}^{-1}$ . The features are best observed in Fig. 56. Additionally, there is a secondary band at 594  $\text{cm}^{-1}$  which has previously been attributed to the  $A_{1g}$  mode. Although the  $A_{1g}$  mode is not infrared active in a pure Rutile crystal, it is observed in the infrared spectrum of natural crystals due to the presence of impurities. The  $A_{1g}$  mode could also be due, in part, to the lack of etching or annealing of the polished surface. There is also another weak unidentified mode at 670  $\text{cm}^{-1}$ .

When the Kramers-Kronig analysis was applied to  $R(\nu)$  for Rutile, small negative values of  $k(\nu)$  were obtained in the spectral regions ( $\nu \gtrsim 800 \text{ cm}^{-1}$ ) where this material is a weak absorber. In plotting the graph of  $k(\nu)$  in Fig. 56 the negative values were suppressed thus causing the unusual appearance of the  $k(\nu)$  spectrum in the region  $\nu \gtrsim 800 \text{ cm}^{-1}$ .

At the time these data were acquired we did not possess an adequate polarizer and therefore could not obtain the spectrum of the  $A_{2u}$  mode. We now have a polarizer and will continue this investigation during the follow-on contract.

## 7. Limestone

### a. Objectives

The advent of remote sensing by use of optical instruments mounted in ground stations, aircraft, and satellites, and an interest in the thermal budget of the planets, has produced an increasing interest in spectral values of the complex refractive index  $N(\lambda) = n(\lambda) + ik(\lambda)$  of materials commonly found on terrestrial and other planetary surfaces. The present investigation was undertaken to obtain spectral values of  $N(\lambda)_l$  for limestone which consists primarily of randomly oriented microcrystals of calcite. Other constituents of limestone are randomly oriented microcrystals of dolomite and organic fossil material. Limestone is relatively abundant in the terrestrial environment, but would be on other planetary surfaces only if biological conditions as we know them on earth once existed on those planets.

In the present investigation spectral values  $N(\lambda)_l$  are obtained in the following manner. First the near-normal incidence relative reflectance  $R(\lambda) = R(\lambda)_l / R(\lambda)_w$  of limestone  $l$ , with water  $w$  as the reflectance standard,

was measured throughout the 0.2-32.8- $\mu$ m wavelength region. Second, a Kramers-Kronig phase-shift dispersion analysis<sup>1,40/</sup> of  $R(\lambda)$  provided a spectrum  $\Delta\phi(\lambda)$  which is the difference in phase change for electromagnetic waves of wavelength  $\lambda$  reflected from the limestone and from the water standard. An algorithm<sup>1,40/</sup> that uses  $R(\lambda)$ ,  $\Delta\phi(\lambda)$ , the measured angle of incidence  $\theta$ , and known spectral values for the complex refractive index  $N(\lambda)_w$  of water then provided spectral values of  $N(\lambda)_l$ . Additionally, a classical Lorentz dispersion analysis of the absolute reflectance spectrum  $R(\lambda)_l$  of limestone yielded spectral values of the complex dielectric function  $\epsilon(\lambda)_l$  from which  $N(\lambda)$  were readily obtained.

The optical properties of natural minerals and rocks have been investigated by several other scientists. Aronson and Strong<sup>41/</sup> obtained Lorentz parameters in the infrared for muscovite mica, anorthosite, diopsidic pyroxenite, almandite-pyrope, garnet, and soda lime glass. Pollack et al.<sup>42/</sup> obtained Lorentz parameters for obsidian, basaltic glass, basalt, and andesite. Spitzer and Kleinman<sup>43/</sup> obtained Lorents parameters for the infrared lattice bands of quartz. Holland et al.<sup>44/</sup> measured infrared reflectance spectra in the 2-50- $\mu$ m wavelength region and computed  $N(\lambda)$  by use of Kramers-Kronig techniques for quartz, calcite, dolomite, fluorite, galena, sphalerite, brucite, magnetite, goethite, and hematite. Analysis of the optical

properties of minerals and rocks in the visible and infrared are also provided by Refs. (45)-(48).

b. Preparation of Samples.

Three samples of the Bethany Falls limestone, a prominent member of the Swope formation,<sup>49/</sup> were collected from the approximate center of Section 7-R32W-T49N in northeast Kansas City, Mo. All samples were prepared by standard polishing techniques. Following a final buffing with 0.1  $\mu$ m Linde B, the samples were examined for scratches and pits by use of a Vickers metalore microscope. The three polished limestone samples were slightly marred by pits and cracks due to the presence of natural vugs and joints. Modal analyses were performed by point counting in order to assess the impact of the pits and cracks on subsequent reflectance spectra. Modal analyses revealed 2.96 to 7.89 areal percent cavities with a mean areal percent of 4.60. Consequently, the reflectance spectra described hereinafter were increased by a factor of 1.04 to compensate for reduced specular reflectance due to the presence of pits and cracks, although this may be a function of wavelength and not a constant.

The Bethany-Falls samples consisted of dense fine-grained buff to gray mottled limestone. Calcite constituted greater than 99.7% of the samples, the remainder was sparse pyrite. Because the Bethany Falls limestone commonly contained dolomite in abundance,

this mineral was specifically searched for. However, results from both stained thin sections and x-ray diffraction disclosed no dolomite.

Texturally the samples were all very similar, typically containing 5-20  $\mu\text{m}$  irregular interlocking grains and no readily apparent preferred orientation. Some grains were as small as two microns and others were rare and widely dispersed clots of exceptionally large 40-200  $\mu\text{m}$  grains which appeared to be fossil fragments. A minor, but ubiquitous, dusting of two  $\mu\text{m}$  diameter pyrite grains was also present. Analysis of polished sections disclosed from 0.14 to 0.2 percent pyrite.

c.  $R(\lambda)$  and  $N(\lambda)$  Spectra for Limestone.

In the present investigation we measured relative reflectance  $R(\lambda) = R(\lambda)_l / R(\lambda)_w$ , where  $l$  and  $w$  denote limestone and water, respectively. Data were acquired in the following order: Z-W-L-W-L-W-L-W-Z, where Z indicates a spectral scan made when the beam of radiant flux was blocked just in front of the infrared source, W indicates a spectral scan made with the water standard  $w$  in the sample position, and each L indicates a sequence of three scans, one for each of the three limestone samples. After data were acquired throughout the 0.2-32.8  $\mu\text{m}$  spectral region the relative reflectance of the limestone samples was calculated as follows. First, the average of the two spectral scans Z was subtracted point by point from the other thirteen

spectral scans denoted by W and L. Second, the three spectral scans denoted by each L were averaged and ratioed to the average of the spectral scans W made just before and after spectral scans L. This procedure provided three relative reflectance spectra, one for each of the three groups of three spectral scans L, which were then averaged to provide a composite spectrum and standard deviations. The composite spectrum was then multiplied by 1.04 as indicated in the preceding Section. The absolute reflectance  $R(\lambda)_L$  of the limestone was provided by  $R(\lambda)_L = R(\lambda) R(\lambda)_W$ , where  $R(\lambda)_W$  was computed by use of the Fresnel equations and known values<sup>2/</sup> for  $N(\lambda)_W$ , and  $R(\lambda)$  designates the composite relative reflectance spectrum. The absolute reflectance spectrum  $R(\lambda)_L$  of limestone is shown in Figs. 57 and 58. The standard deviations were  $\pm 0.06 R(\lambda)_L$  in the spectral region beyond 25  $\mu\text{m}$ , and reduced to about  $\pm 0.01 R(\lambda)_L$  in the spectral region from 0.2 to 20  $\mu\text{m}$ .

Evidence of birefringence was not observed as the limestone samples were rotated while placed in the reflectometer; thus we treat limestone as a homogeneous isotropic material.

Spectral values of the complex refractive index  $N(\lambda)_L$  were obtained by use of the Kramers-Kronig algorithm described in Refs. (1) and (40). Values for  $N(\lambda)_L$  are presented in graphical form in Figs. 59 and 60.

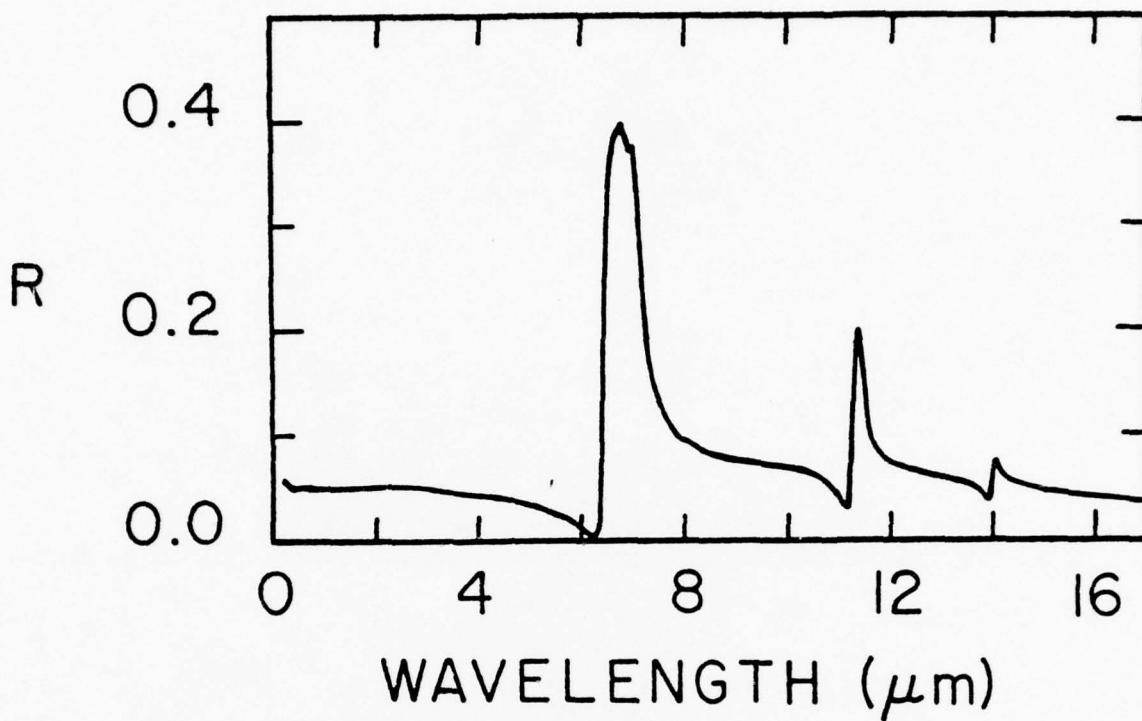


Figure 57. Near-normal incidence absolute reflectance  $R(\nu)$  in the 0.2-17  $\mu\text{m}$  spectral region for Bethany Falls Limestone.

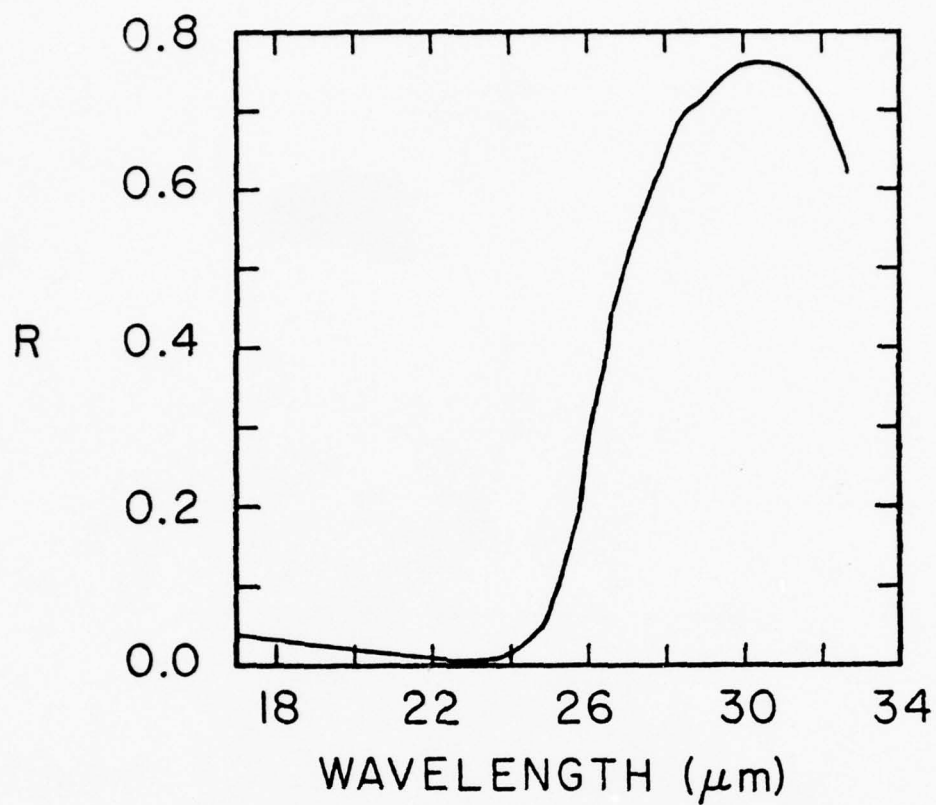


Figure 58. Near-normal incidence absolute reflectance  $R(\nu)$  in the 17-32.8  $\mu\text{m}$  spectral region for Bethany Falls Limestone.

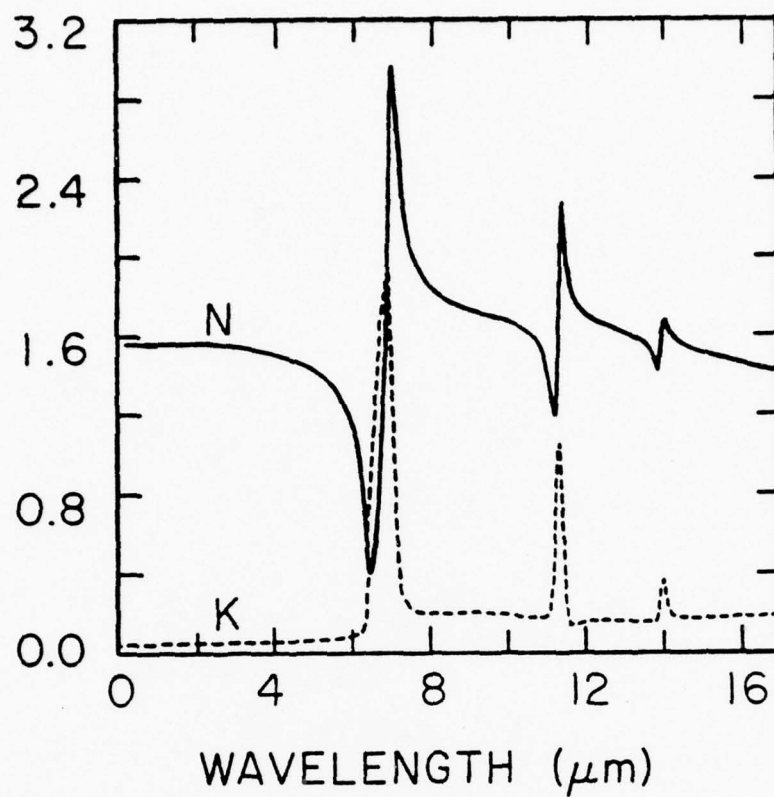


Figure 59. Complex refractive index  $N(\nu) + ik(\lambda)$  in the 0.2-17  $\mu\text{m}$  spectral region for Bethany Falls Limestone.

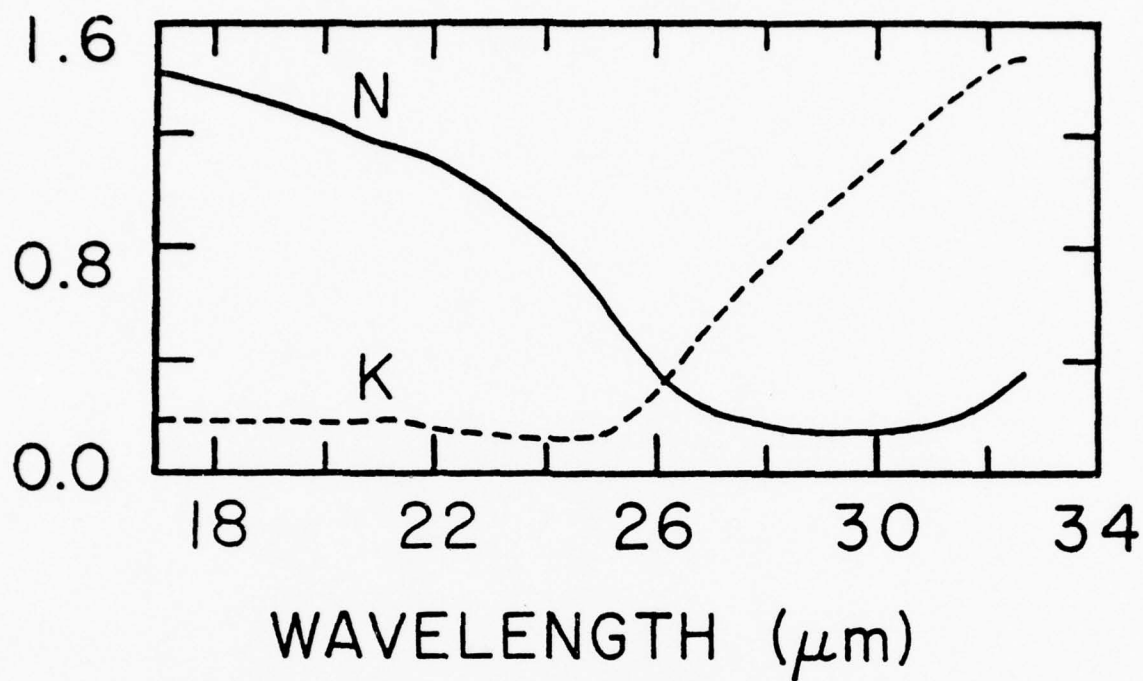


Figure 60. Complex refractive index  $N(\lambda) + ik(\lambda)$  in the 17-32.8  $\mu\text{m}$  spectral region for Bethany Falls Limestone.

Evaluation of the Kramers-Kronig dispersion relation requires an integration of  $R(\lambda)$  over the entire electromagnetic spectrum. Our data, however, extended only from 0.2 to 32.8  $\mu\text{m}$ . Thus we made the approximations that  $R(\lambda) = R(0.2 \mu\text{m})$  throughout the  $0 \leq \lambda \leq 0.2\text{-}\mu\text{m}$  region, and  $R(\lambda) = R(32.8 \mu\text{m})$  throughout the  $32.8 \leq \lambda \leq \infty\text{-}\mu\text{m}$  region. The latter assumption is open to serious inquiry because calcite, the primary constituent of limestone, possess other infrared active lattice bands at wavelengths greater than 32.8  $\mu\text{m}$ .

Spectral values of  $N(\lambda)_\ell$  were also obtained by use of classical Lorentz dispersion theory. According to the Lorentz theory the complex dielectric function  $\epsilon(\nu)$  at wavenumber  $\nu = \lambda^{-1}$  is given by

$$\epsilon(\nu) = \epsilon_\infty + \sum_j \frac{4\pi\rho_j\nu_j^2[(\nu_j^2 - \nu^2) + i\gamma_j\nu_j\nu]}{(\nu_j^2 - \nu^2)^2 + (\gamma_j\nu_j\nu)^2}, \quad (1)$$

where  $\epsilon_\infty$  is the high frequency dielectric constant,  $\rho_j$  is the strength of the  $j^{\text{th}}$  infrared active band,  $\nu_j = \lambda_j^{-1}$  is the central wave-number position of the  $j^{\text{th}}$  infrared active band, and  $\gamma_j$  is a damping coefficient. Lorentz parameters determined for limestone appear in Table XII. The relation between  $N(\lambda)_\ell$  and  $\epsilon(\lambda)_\ell$  is

$$\epsilon(\lambda)_\ell = N(\lambda)_\ell^2, \quad (2)$$

from which the real and imaginary parts of  $N(\lambda)_\ell = n(\lambda)_\ell + ik(\lambda)_\ell$  can be determined.

Table XIV. Classical dispersion theory parameters for carbonate minerals: Limestone, Calcite, and Dolomite.

$j$	$\lambda_j (\mu\text{m})$	$\nu_j (\text{cm}^{-1})$	$\rho_j$	$\gamma_j$
1	6.59	1517.5	0.005	0.020
2	6.83	1464.1	0.119	0.031
3	7.045	1419.4	0.245	0.025
4	11.47	871.8	0.052	0.011
5	14.11	708.7	0.010	0.0075
6	27.43	364.6	0.013	0.050
7	33.80	295.9	1.220	0.050
8	36.30	275.5	1.020	0.092
$\epsilon_\infty = 2.38$ , Limestone				
1	7.11	1406.5	0.634	0.0055
2	14.11	708.7	0.0183	0.0046
3	28.95	345.4	0.034	0.069
4	34.50	289.9	2.5	0.042
$\epsilon_\infty = 3.00$ , Calcite ( $E_{1C}$ )				
1	6.80	1470.6	0.025	0.010
2	6.94	1440.9	0.650	0.004
3	13.82	723.6	0.030	0.012
4	14.22	703.2	0.0275	0.007
5	25.00	400.0	0.009	0.010
6	27.00	370.4	0.075	0.025
7	28.10	355.9	2.220	0.044
$\epsilon_\infty = 3.50$ , Dolomite ( $E_{1C}$ )				

A comparison of values for  $N(\lambda)_\ell$  obtained by Kramers-Kronig techniques and by use of the Lorentz theory showed reasonable agreement in the spectral region from 0.2 to about 25  $\mu\text{m}$  and increasingly poor agreement as wavelength increased beyond 25  $\mu\text{m}$ . Both the real  $n(\lambda)_\ell$  and imaginary  $k(\lambda)_\ell$  parts of  $N(\lambda)_\ell$  were higher in the 25 - 32.8  $\mu\text{m}$  region for the Lorentz theory than for the Kramers-Kronig techniques. This difference in  $N(\lambda)_\ell$  beyond 25  $\mu\text{m}$  is attributed to the assumption that  $R(\lambda) = R(32.8 \mu\text{m})$  for the Kramers-Kronig technique in the spectral region  $32.8 \leq \lambda \leq \infty \mu\text{m}$ . The values of  $N(\lambda)_\ell$  in the region beyond 25  $\mu\text{m}$  as computed from the Lorentz theory are therefore preferred over those obtained from the Kramers-Kronig technique.

The regions of anomalous dispersion shown in the spectrum for  $n(\lambda)_\ell$ , and strong absorption shown in the spectrum of  $k(\lambda)_\ell$ , centered at wavelengths 7.00, 11.4, and 14.05 in Figs. 59 and 60 are characteristic of the ordinary and extra-ordinary rays in birefringent calcite ( $\text{CaCO}_3$ ).

## 8. Natural Waters

### a. Objectives

The complex refractive index is denoted by  $\underline{N} = n + ik$ , where italics denote a complex number,  $n$  is the index of refraction,  $k$  is the extinction coefficient, and  $i$  represents the square root of minus one. A quantitative

knowledge of spectral values of  $N$  for natural waters is presently of considerable interest to many scientists. Such knowledge has application to: (1) computer simulations of the transport of electromagnetic radiation through hydrosols, aerosols, and maritime fogs, (2) theoretical investigations of the energy and hydrological balance of the earth's lakes, oceans, and atmosphere, (3) remotely sensing the chemical quality of environmental waters,<sup>50/</sup> and (4) solar-energy development.<sup>51/</sup> We previously reported<sup>1,4,52/</sup> measurements of the relative reflectance spectra in the 2-20- $\mu$ m wavelength region of the infrared for individual aqueous solutions prepared with distilled water in the laboratory. The solutions contained NaCl, H<sub>2</sub>SO<sub>4</sub>, K<sub>2</sub>SO<sub>4</sub>, NH<sub>4</sub>H<sub>2</sub>PO<sub>4</sub>, NaNO<sub>3</sub>, or NaHCO<sub>3</sub>. Kramers-Kronig phase-shift dispersion analysis of the reflectance spectra for those solutions provided spectral values for  $N$ . We observed that monatomic ions such as Na<sup>+</sup>, Cl<sup>-</sup>, and K<sup>+</sup> perturbed the intra- and inter-molecular bonds of the liquid-water substances so that corresponding wavelength positions of infrared active fundamental vibrational and librational (lattice vibrational) modes were moderately shifted to shorter and longer wavelengths, respectively. We also explicitly identified twenty-one infrared active vibrational modes associated with SO<sub>4</sub><sup>-2</sup>, NH<sub>4</sub><sup>+</sup>, HSO<sub>4</sub><sup>-</sup>, H<sub>3</sub>O<sup>+</sup>, H<sub>2</sub>PO<sub>4</sub><sup>-</sup>, NO<sub>3</sub><sup>-</sup>, HCO<sub>3</sub><sup>-</sup>, or H<sub>2</sub>O. The half width  $\Gamma$ , central spectral position of each mode  $\lambda$ , mode (band) strength  $S_b$ , and maximum value of  $k$  were

Table XV<sup>a</sup>. Molecules, their fundamental infrared-active vibrational modes  $\nu$ , central wavelength  $\lambda(\mu\text{m})$  and wave number  $\bar{\nu}(\text{cm}^{-1})$ , full mode (band) width  $\Gamma$  at one-half  $k_{\text{max}}$ , and band strength  $RS_b$  relative to that for the combined  $\nu_1\nu_2$  modes of the water monomer<sup>b</sup>.

Molecule	Mode <sup>c</sup>	Central		Position $\bar{\nu}(\text{cm}^{-1})$	$\Gamma$		$RS_b$
		$\lambda(\mu\text{m})$	$\mu\text{m}$		$\mu\text{m}$	$\text{cm}^{-1}$	
H <sub>2</sub> O	$\nu_1(A_1), \nu_3(B_1)$	2.945	0.338	3,395	0.338	390	1.00 <sup>b</sup>
H <sub>2</sub> O	$\nu_2(A_1)$	6.060	0.404	1,650	0.404	110	0.13
H <sub>2</sub> O	$\nu_L$	17.2	14.9	580	14.9	500	1.97
SO <sub>4</sub> <sup>-</sup>	$\nu_3(F_2)$	9.049	0.58	1,105	0.58	71	7.29
SO <sub>4</sub> <sup>-</sup>	$\nu_4(F_2)$	6.901	0.20	1,449	0.20	42	0.62
HSO <sub>4</sub> <sup>-</sup>	$\nu_1(A_1)$	9.55	0.66	1,047	0.66	73	4.09
HSO <sub>4</sub> <sup>-</sup>	$\nu_3(A_1)$	~7.46		~1,340			weak
HSO <sub>4</sub> <sup>-</sup>	$\nu_3(E)$	8.40	0.69	1,190	0.69	98	4.65
HSO <sub>4</sub> <sup>-</sup>	$\nu_4(A_1)$	11.1	0.77	897	0.77	62	1.60
HSO <sub>4</sub> <sup>-</sup>	$\nu_4(E)$	16.9	0.60	592	0.60	21	0.87
H <sub>3</sub> O <sup>+</sup>	$\nu_4(E)$	5.75	0.846	1,739	0.846	256	1.16
H <sub>2</sub> PO <sub>4</sub> <sup>-</sup>	$\nu_1(A_1)$	11.4	0.47	873	0.47	36	0.47
H <sub>2</sub> PO <sub>4</sub> <sup>-</sup>	$\nu_3(A_1)$	9.30	0.26	1,075	0.26	30	1.89
H <sub>2</sub> PO <sub>4</sub> <sup>-</sup>	$\nu_3(B)$	8.68	0.56	1,152	0.56	74	1.75

Table XV (cont.)

$\text{H}_2\text{PO}_4^-$	$\nu_3(\text{B})$	10.6	940	0.48	42	1.56
$\text{NH}_4^+$	$\nu_3(\text{F}_2)$	3.15	3,175	0.32	34	4.87
$\text{NH}_4^+$	$\nu_4(\text{F}_2)$	6.90	1,449	0.20	42	0.62
$\text{NO}_3^-$	$\nu_3(\text{E})$	7.40	1,351	0.60	109	2.48
$\text{HCO}_3^-$	$\nu_2$	6.10	1,639	0.32	86	1.91
$\text{HCO}_3^-$	$\nu_3, \nu_4$	7.30	1,370	0.41	78	2.00
$\text{HCO}_3^-$	$\nu_1$	2.93	3,410	----	----	----

<sup>a</sup> Compiled from Querry et. al., 1974, 1976.

<sup>b</sup>  $S_B = 2.196 \text{ (cm-mole/liter)}^{-1}$  for the combined  $\nu_1\nu_3$  band of  $\text{H}_2\text{O}$ .

<sup>c</sup> A  $\equiv$  symmetric, B  $\equiv$  antisymmetric, E  $\equiv$  doubly degenerate, and F  $\equiv$  triply degenerate.

tabulated for each of the twenty-one modes. These parameters are presented collectively for the first time in Table XV. Band strengths were evaluated by use of

$$S_{bi} = a_i^{-1} \int_{\text{band}} \Delta k_i d\bar{\nu}, \quad (1)$$

where  $a_i$  (mole/liter) was the molecular density of the  $i^{\text{th}}$  constituent in the solution,  $\Delta k_i$  was the part of  $k$  due to a fundamental vibrational mode of the  $i^{\text{th}}$  constituent, and  $\bar{\nu} = \lambda^{-1}$  with  $\bar{\nu}$  as the wave number ( $\text{cm}^{-1}$ ) and  $\lambda$  the wavelength (cm). The integrals were evaluated over the spectral region of an infrared active band by planimetering appropriate areas on large graphs of  $\Delta k$  vs.  $\bar{\nu}$ . In Table XV relative band strengths  $RS_b$  were compiled based on the arbitrary choice  $RS_b = 1.00$  for the combined  $\nu_1(A_1)\nu_3(B_1)$  modes of  $\text{H}_2\text{O}$ ; the absolute band strength of these combined modes was  $S_b = 2.196$  ( $\text{cm mole/liter})^{-1}$ .  $\nu_1(A_1)$  denotes the symmetric OH stretch of the  $\text{H}_2\text{O}$  monomer and  $\nu_3(B_1)$  denotes the anti-symmetric OH stretching mode.

The investigations reported here had three objectives: (1) to measure the relative reflectance spectra in the infrared for saline natural waters containing both monatomic and polyatomic ions, (2) to compute and tabulate spectral values of  $N$  for these samples, and (3) to compare the relative reflectance spectra for the natural waters with reflectance spectra for aqueous solutions containing a single inorganic salt. Natural saline waters

Table XVI. Conductivity and results from chemical or spectrographic analyses of samples from San Francisco Bay (SFB), Pacific Ocean (PO), Great Salt Lake (GSL), phosphate mining area of Central Florida (CF), and the Dead Sea (DS). Chemical concentrations are specified in mg/liter.

The conductivity  $\sigma$  is specified as  $\mu\text{mhos/cm}$ , @25°C.

Ion	SFB	PO	GSL	CF	DS <sup>a</sup>
$\text{Ca}^{+2}$	360	400	210	1,100	16,300
$\text{Mg}^{+2}$	1,000	1,200	5,800	170	36,100
$\text{Na}^{+}$	8,000	10,000	52,000	2,100	38,500
$\text{K}^{+}$	340	420	4,000	300	6,500
$\text{NH}_3^{-}\text{N}$	<0.01	<0.01	<0.01		<0.01
$\text{HCO}_3^{-}$	124	142	514	1.6	230
$\text{SiO}_2$				230	
$\text{Cl}^{-}$	16,000	19,000	94,000	44	196,940
$\text{F}^{-}$				3,300	
$\text{SO}_4^{-2}$	2,200	2,700	12,000	870	580
$\text{NO}_3^{-}$	<0.1	0.1	<0.1		
$\text{PO}_4^{-3}$	0.03	0.04	2.3	17,000	
$\text{H}_2\text{PO}_4^{-}$				5,500	
$\text{CO}_3^{-2}$	6				

Table XVI (cont.)

Br <sup>-</sup> B Li Sr Fe	Spectrographic Analysis				4,600 30 12 240 0.09
	41,300	47,000	134,000	26,000	
$\sigma$					

<sup>a</sup> Data on ionic content from Neev and Emery (1967).

selected for investigation were obtained from the San Francisco Bay, Pacific Ocean, Atlantic Ocean, Great Salt Lake (Utah), Dead Sea (Israel), and an effluent pit adjacent to a phosphate mine in the Alafia river region of Central Florida. All samples, except the one from the Atlantic Ocean, were supplied by members or associates of the U.S. Geological Survey, EROS Program Office. Chemical and spectrographic analyses of the samples performed by chemists at USGS laboratories, and by Neev and Energy<sup>53/</sup> for the Dead-Sea sample, are presented in Table XVI.

b.  $R(\lambda)$  Spectra for Natural Waters.

The procedure for measuring the relative reflectance spectra of the natural water samples was identical to that used during our investigations of NaCl in water.<sup>52/</sup> Relative reflectance  $R_+$  is defined as  $R_+ = R_{+s}/R_{+w}$ , where the + subscript denotes radiant flux linearly polarized with the electric-field vector perpendicular to the plane of incidence, and  $R_{+s}$  and  $R_{+w}$  denote absolute specular reflectance of the natural water sample and the distilled water, respectively. Relative reflectance spectra throughout the 2-20- $\mu$ m region for the six water samples investigated are shown in Figs. 61-63. The angle of incidence was  $\theta = 70.03^\circ \pm 0.23^\circ$ . Each spectrum shown in Figs. 61-63 represents smoothed data obtained in the following manner. Averages  $\langle R_+ \rangle$  of three measurements of  $R_+$  were determined at consecutive 0.05- $\mu$ m intervals

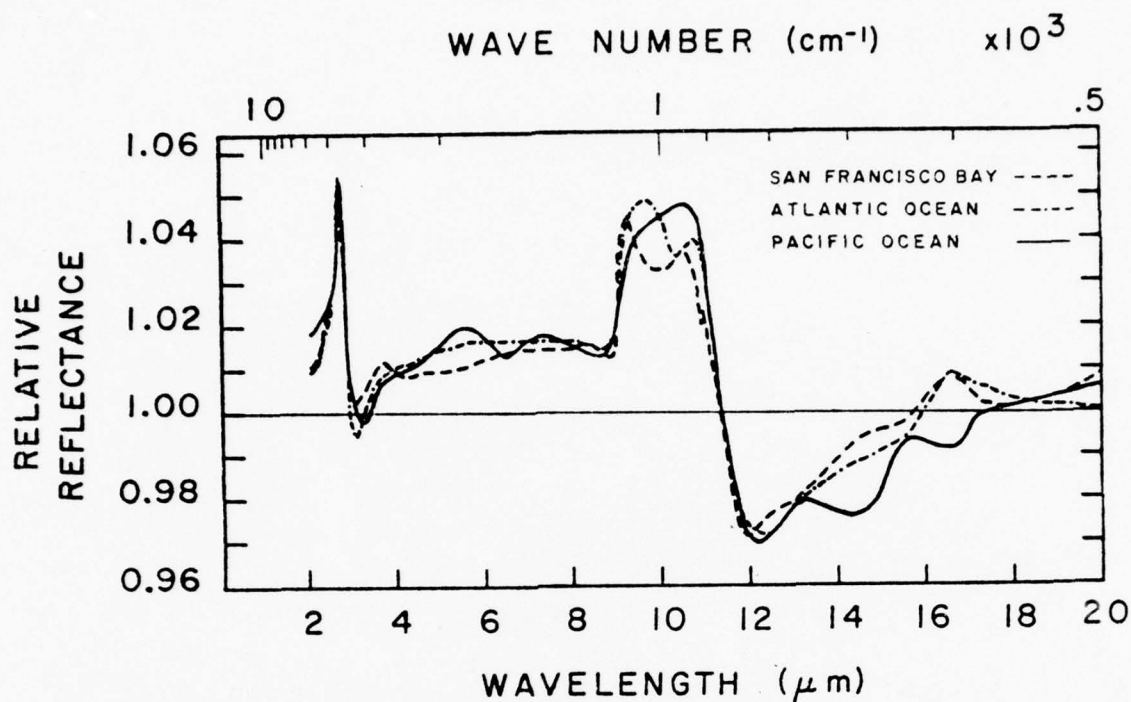


Figure 61. Measured relative reflectance spectra in the 2-20- $\mu\text{m}$  ( $5000\text{-}500\text{-cm}^{-1}$ ) spectral region for surface water samples from San Francisco Bay, Atlantic Ocean, and Pacific Ocean. The angle of incidence was  $70.03^\circ \pm 0.23^\circ$ . Distilled water was the standard reflector; its relative reflectance is 1.0 at all wavelengths. The radiant flux was linearly polarized with the electric-field vector perpendicular to the plane of incidence. Standard deviations are stated in the text.

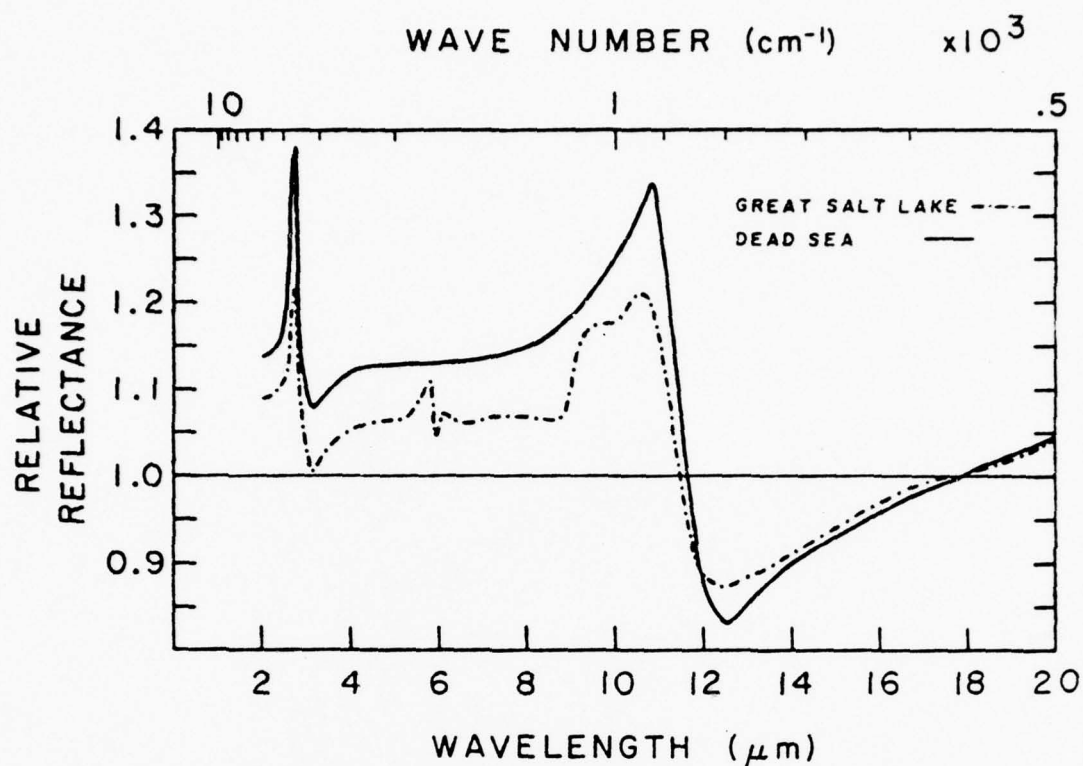


Figure 62. Measured relative reflectance spectra in the 2-20- $\mu\text{m}$  ( $5000\text{-}500\text{-cm}^{-1}$ ) spectral region for surface water samples from the Great Salt Lake (Utah) and the Dead Sea (Israel). The angle of incidence was  $70.03^{\circ} \pm 0.23^{\circ}$ . Distilled water was the standard reflector; its relative reflectance is 1.0 at all wavelengths. The radiant flux was linearly polarized with the electric-field vector perpendicular to the plane of incidence. Standard deviations are stated in the text.

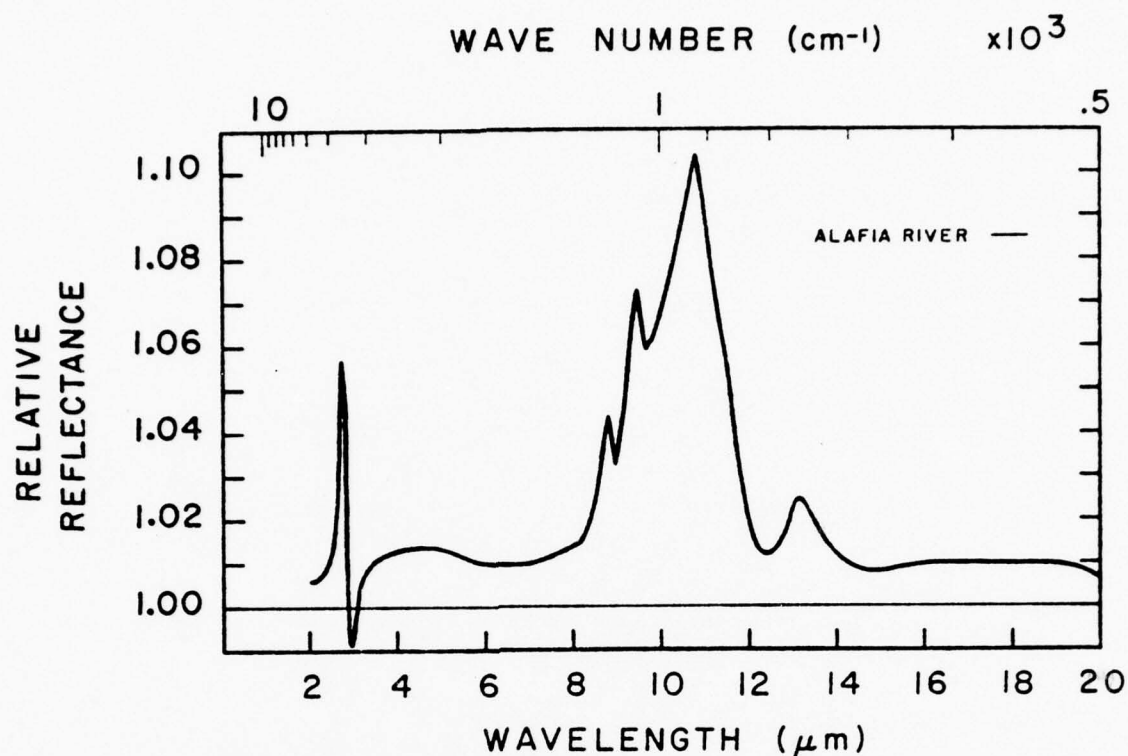


Figure 63. Measured relative reflectance in the 2-20- $\mu\text{m}$  ( $5000\text{-}500\text{-cm}^{-1}$ ) spectral region for a surface water sample from an effluent pit of a phosphate mine in the Alafia River Basin of Central Florida. The angle of incidence was  $70.03^\circ \pm 0.23^\circ$ . Distilled water was the standard reflector; its relative reflectance is 1.0 at all wavelengths. The radiant flux was linearly polarized with the electric-field vector perpendicular to the plane of incidence. Standard deviations are stated in the text.

throughout the 2-20- $\mu\text{m}$  region. The standard deviation for  $\langle R_+ \rangle$  was about  $\pm 0.008 \langle R_+ \rangle$ . In narrow spectral regions centered about the central positions of the fundamental infrared bands of atmospheric water vapor at 2.75 and 6.09  $\mu\text{m}$ , and atmospheric  $\text{CO}_2$  at 4.3 and 14.7  $\mu\text{m}$ , the standard deviations increased to about  $\pm 0.025 \langle R_+ \rangle$ . Our confidence in the data was then increased significantly by a critical examination and manual smoothing of a point-by-point plot of  $\langle R_+ \rangle$  vs. wavelength  $\lambda$ .

The spectral resolution  $\lambda/\Delta\lambda$  was from 125 to 200 throughout the 2-20- $\mu\text{m}$  region;  $\Delta\lambda$  represents the spectral slitwidth of the monochromator. Care was taken to keep the air-sample interface clean and free of standing waves. The temperature of the samples was about 300K<sup>0</sup>.

c.  $N(\lambda)$  Spectra for Natural Waters

Spectral values of  $N_s$  for the natural water samples, designated here by the subscript s, were calculated by use of a Kramers-Kronig (KK) algorithm applied to the relative reflectance spectra (Hale et. al. 1973, Querry et. al. 1974). KK analysis of a relative reflectance spectrum provides  $\Delta\phi_+ = \phi_{+w} - \phi_{+s}$ , the difference in phase shifts  $\phi_+$  for a monochromatic electromagnetic wave reflected from s the air-sample and w the air-water interfaces;

$$\Delta\phi(\lambda_0)_+ = \text{Prin.} \frac{\lambda_0}{\pi} \int_0^{\infty} \frac{\ln[\langle R(\lambda) \rangle_+]}{\lambda_0^2 - \lambda^2} d\lambda \quad .$$

(2)

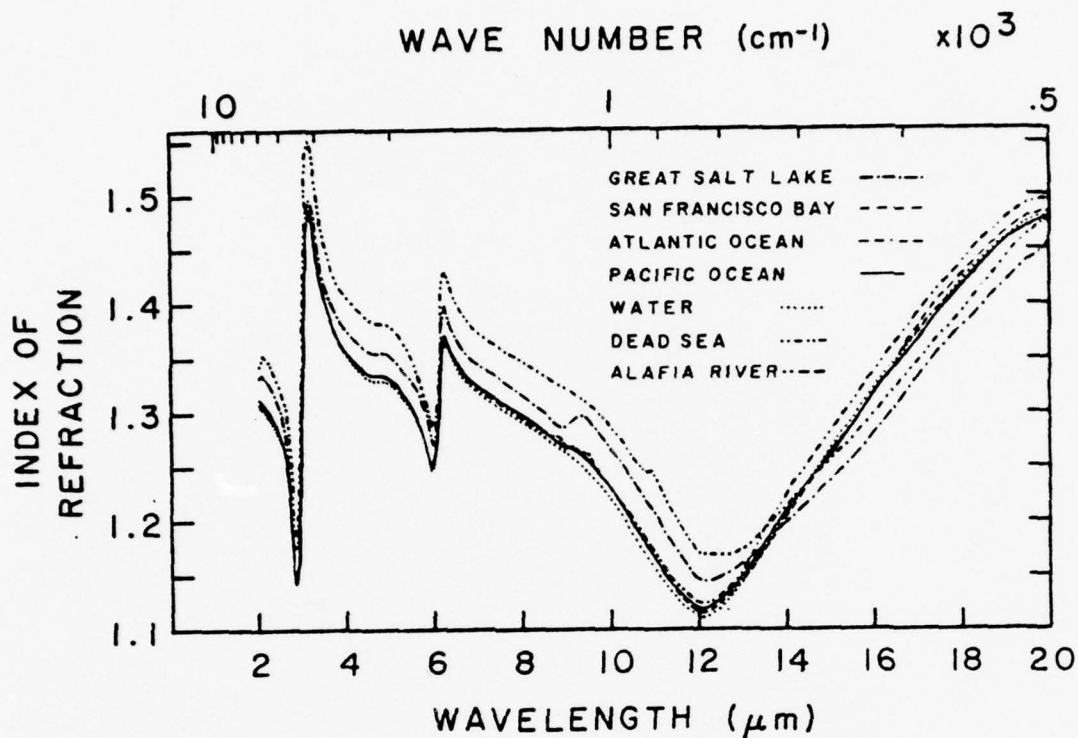


Figure 64. Index of refraction  $n$ , in the 2-20- $\mu\text{m}$  ( $5000\text{-}500\text{-cm}^{-1}$ ) region, for distilled water and for the six surface water samples. The algorithm consisting of Eqs. (2)-(12) was used to compute  $n$  from the measured relative reflectance spectrum for each surface water sample. The uncertainty is about  $\pm 0.01n$ . Data from Hale and Querry (1973) was used to plot  $n$  for water.

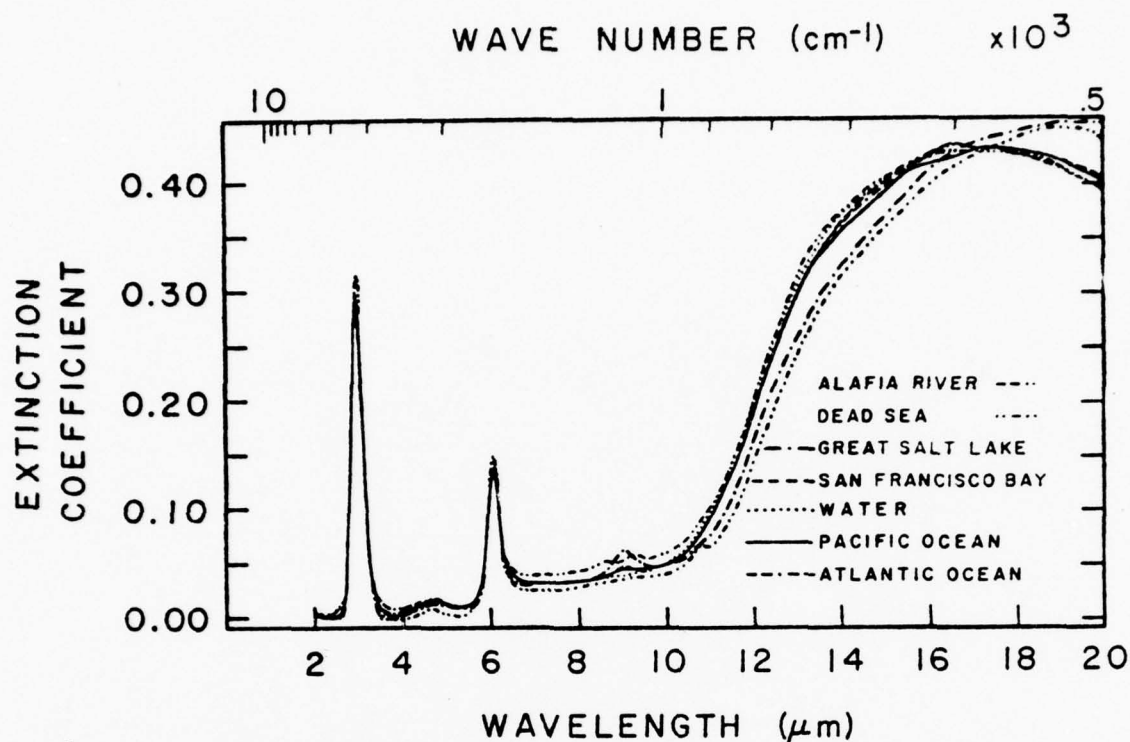


Figure 65. Extinction coefficient  $k$ , in the 2-20- $\mu\text{m}$  (5000-500- $\text{cm}^{-1}$ ) region, for distilled water and for the six surface water samples. The algorithm consisting of Eqs. (2)-(12) was used to compute  $k$  from the measured relative reflectance spectrum for each water sample. The uncertainties are about  $\pm 0.02k$  for  $k$  greater than 0.045, increase to about  $\pm 0.15k$  for  $k = 0.01$ , and become much larger for  $k$  less than 0.01. Data from Hale and Querry (1973) was used to plot  $k$  for water.

Prin. denotes the Cauchy principal value of the integral.

The smoothed reflectance spectra shown in Figs. 61-63 were used to compute values for  $\Delta\phi(\lambda_0)_+$ . Use of Eq. (2) requires a quantitative knowledge of the relative reflectance spectrum  $\langle R(\lambda)_+ \rangle$  for all  $\lambda$ . Measurements, however, were made only in the 2-20- $\mu\text{m}$  region. Because  $\langle R(\lambda)_+ \rangle$  was the relative reflectance of two aqueous substances, rather than the absolute reflectance, only a small negligible error in  $\Delta\phi(\lambda_0)_+$  was introduced by assuming for each spectrum that  $\langle R(\lambda)_+ \rangle$  was equal to  $\langle R(2 \mu\text{m})_+ \rangle$  and  $\langle R(20 \mu\text{m})_+ \rangle$  throughout the  $\lambda \leq 2 \mu\text{m}$  and  $\lambda \leq 20 \mu\text{m}$  regions, respectively.

The refractive index  $N_s = n_s + ik_s$  of the saline water samples were then determined by use of the algorithm from Querry *et al.*,<sup>1/</sup> and by use of  $N_w = n_w + ik_w$  for distilled water as tabulated by Hale and Querry.<sup>2/</sup> The angle of incidence was  $\theta = 70.03^\circ$ . The uncertainties were about  $\pm 0.01n_s$ , about  $\pm 0.02k_s$  for  $k_s$  greater than 0.045, increasing to about  $0.15k_s$  for  $k_s = 0.01$ , and became much larger for  $k_s$  less than 0.01. Graphical presentations of  $n_s$  and  $k_s$  vs.  $\lambda$  appear in Figs. 64 and 65, respectively.

d. Discussion of  $R(\lambda)$  Spectra for Natural Waters

The relative reflectance spectra for the six natural water samples are compared here with absolute and relative reflectance spectra previously obtained in our laboratory for individual 1, 3, or 5M aqueous solutions of NaCl

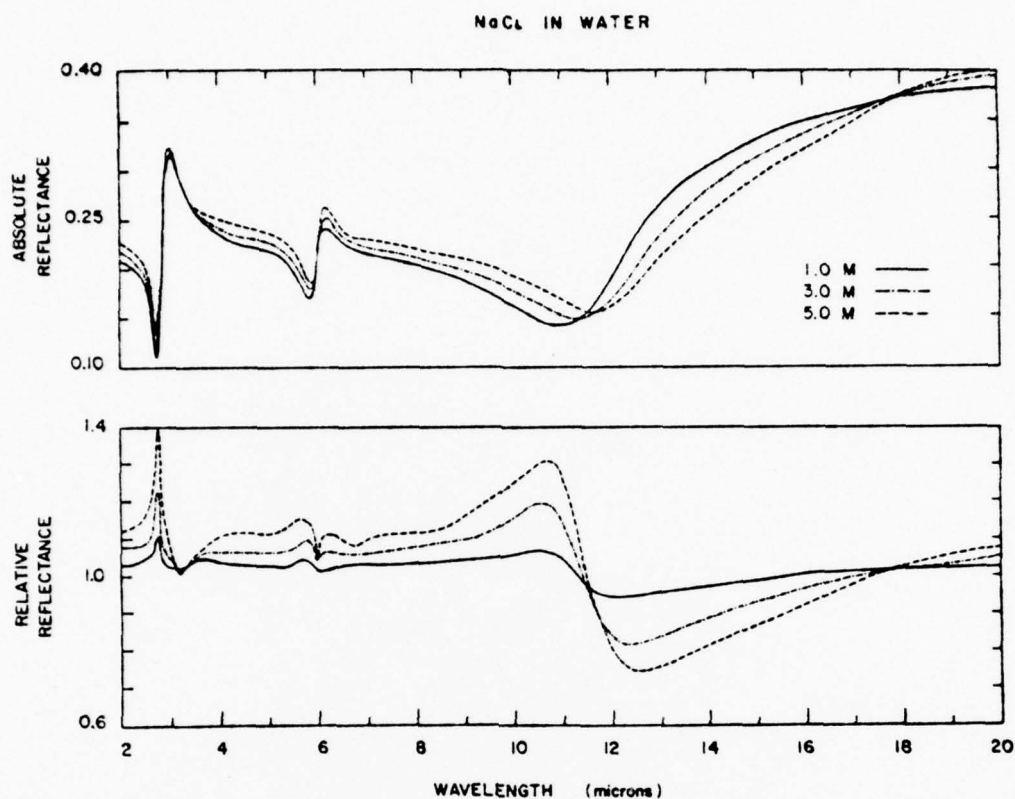


Figure 66. Measured relative reflectance (lower panel) and calculated absolute reflectance (upper panel) spectra in the 2-20- $\mu$ m region for aqueous solutions of 1, 3, and 5M NaCl content. The angle of incidence was  $70.03^\circ \pm 0.23^\circ$ . Distilled water was the standard reflector; its relative reflectance is 1.0 at all wavelengths. The radiant flux was linearly polarized with the electric-field vector perpendicular to the plane of incidence. The uncertainty in the relative reflectance is about  $\pm 0.008 \langle R_p \rangle$ . Reproduced by permission of M. R. Querry *et. al.*, *J. Opt. Soc. Am.*, **62**, 849-855, 1972.

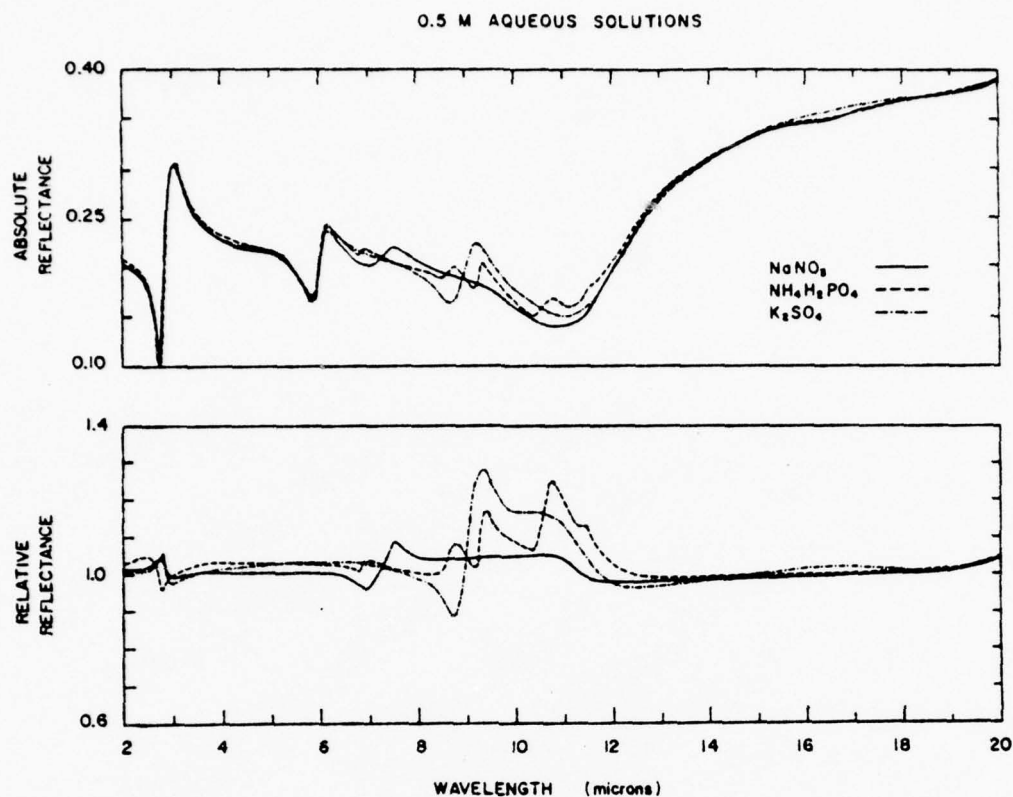


Figure 67. Measured relative reflectance (lower panel) and calculated absolute reflectance spectra (upper panel) in the 2-20- $\mu\text{m}$  region for individual 0.5M aqueous solutions containing  $\text{NaNO}_3$ ,  $\text{NH}_4\text{H}_2\text{PO}_4$ , or  $\text{K}_2\text{SO}_4$ . The angle of incidence was  $70.03^\circ \pm 0.23^\circ$ . Distilled water was the standard reflector; its relative reflectance is 1.0 at all wavelengths. The radiant flux was linearly polarized with the electric-field vector perpendicular to the plane of incidence. The uncertainty in the relative reflectance was about  $\pm 0.008 \langle R_r \rangle$  before the data were smoothed.

and for individual 0.5M aqueous solutions of  $\text{NaNO}_3$ ,  $\text{K}_2\text{SO}_4$ , or  $\text{NH}_4\text{H}_2\text{PO}_4$ . Reflectance spectra for these aqueous solutions appear in Figs. 66 and 67. First, we very briefly review salient characteristics of those reflectance spectra of the solutions that contain an individual chemical compound.

# (1) Individual Aqueous Solutions

## (a) Liquid Water

The  $\text{H}_2\text{O}$  monomer has three fundamental infrared active vibrational modes which are evident at different spectral positions:

$\nu_1(\text{A}_1)$ . . . symmetric OH stretch. . . 3.10  $\mu\text{m}$ ,

$\nu_2(\text{A}_1)$ . . . breathing motion. . . 6.10  $\mu\text{m}$ , and

$\nu_3(\text{A}_1)$ . . . antisymmetric OH stretch. . . 2.90  $\mu\text{m}$ .

Liquid water also possesses infrared active lattice vibrations which are known as librations. One librational mode is due to hindered oscillations of an entire  $\text{H}_2\text{O}$  monomer that is instantaneously hydrogen bonded in a tetrahedral cage of its four nearest neighbors.<sup>54,55/</sup> This librational mode is designated  $\nu_L$  and is spectrally centered at 17.2  $\mu\text{m}$ . Other librational modes are centered at wavelengths greater than 20  $\mu\text{m}$ .

Parameters for the oscillatory modes of water comprise the first three lines of Table XV. In Figs. 66 and 67 the interaction of electromagnetic radiation with the vibrational

and librational modes of water cause the respective decrease and increase in absolute reflectance on the short and long wavelength sides of the central spectral position for each mode. We previously tabulated the spectral complex refractive index of water<sup>2/</sup> at about 298°K.

(b) Sodium Chloride in Water

Sodium chloride goes into solution as monatomic ions  $\text{Na}^+$  and  $\text{Cl}^-$ . There are no molecular vibrational modes for the monatomic ions. As NaCl content of an aqueous solution is increased, however, the central positions of some infrared active modes of  $\text{H}_2\text{O}$  shift slightly to other wavelength positions. Querry et. al.<sup>52/</sup> observed the following wavelength shifts:

-0.009  $\mu\text{m}$ . . . combined  $\nu_1\nu_3$  . . . 3M NaCl,  
 -0.026  $\mu\text{m}$ . . . combined  $\nu_1\nu_3$  . . . 5M NaCl,  
 +0.145  $\mu\text{m}/\text{M}$ . . . libration  $\nu_L$ . . . 1, 3, 5M NaCl.

Shifting of the central wavelength positions of the oscillatory modes of  $\text{H}_2\text{O}$  and liquid water was the principal cause of the structure observed in the relative reflectance spectra of 1, 3, and 5M NaCl solutions shown in Fig. 66. One mole of NaCl contains 22.99g of Na and 35.45g of Cl.

## (c) Potassium Sulfate in Water

Potassium sulfate goes into aqueous solution as monatomic  $K^+$  and polyatomic  $SO_4^{2-}$ . The sulfate ion has infrared active  $\nu_3(F_2)$  and  $\nu_4(F_2)$  modes centered at 9.05 and 6.90  $\mu m$ , respectively. We note from Table XV that the infrared strength of the  $\nu_3(F_2)$  mode of  $SO_4^{2-}$  is about 11.76 times greater than that of the  $\nu_4(F_2)$  mode. In the relative reflectance spectrum shown in Fig. 67 for 0.5M  $K_2SO_4$  in water, the predominant feature is the effect of the strong  $\nu_3(F_2)$  band in the 8-12  $\mu m$  region. The much weaker  $\nu_4(F_2)$  band is barely evident in the 14.9-19  $\mu m$  region. In the absolute reflectance spectrum the  $\nu_3(F_2)$  mode of  $SO_4^{2-}$  causes the respective increase and decrease in reflectance on the short and long wavelength sides of this mode's central position. One mole of  $K_2SO_4$  contains 78.2g of K and 96.1g of  $SO_4$ .

## (d) Ammonium Phosphate (Monobasic) in Water

$NH_4H_2PO_4$  goes into aqueous solution as polyatomic ions  $NH_4^+$  and  $H_2PO_4^-$ . The ammonium ion has infrared active  $\nu_3(F_2)$  and  $\nu_4(F_2)$  modes centered at 3.15 and 6.90  $\mu m$ , respectively. Again the  $\nu_3(F_2)$  mode has greater infrared band strength than the  $\nu_4(F_2)$  mode (see column seven, Table XV). The effect of the  $\nu_3(F_2)$  mode of  $NH_4^+$  is difficult to see in spectra of aqueous

solutions because it is an NH-oscillation occurring at nearly the same spectral position as the combined  $\nu_1\nu_3$  modes of  $\text{H}_2\text{O}$ . The effect of the  $\nu_4(\text{F}_2)$  mode of  $\text{NH}_4^+$  appears at about  $6.90\text{ }\mu\text{m}$  as a small dip and then increases in both the relative and absolute reflectance spectra shown in Fig. 67 for a 0.5M solution of  $\text{NH}_4\text{H}_2\text{PO}_4$ .

$\text{H}_2\text{PO}_4^-$  possesses four infrared active vibrational modes of moderate band strength. They are listed in Table XV as  $\nu_1(\text{A}_1)$ ,  $\nu_3(\text{A}_1)$ ,  $\nu_3(\text{B})$ ,  $\nu_3(\text{B})$ . The effects of these vibrational modes are easily identified when their spectral position listed in Table XV are compared with the absolute and relative reflectance spectra in Fig. 67. One mole of  $\text{NH}_4\text{H}_2\text{PO}_4$  contains 18g of  $\text{NH}_4$  and 97g of  $\text{H}_2\text{PO}_4$ .

(e) Sodium Nitrate in Water

Sodium nitrate dissolves in water as  $\text{Na}^+$  and  $\text{NO}_3^-$ . The nitrate ion possesses a  $\nu_3(\text{E})$  mode centered at  $7.4\text{ }\mu\text{m}$ . The effect of the  $\nu_3(\text{E})$  mode appears as a respective decrease and then increase in absolute and relative reflectance on the short and long wavelength sides of the central position at  $7.4\text{ }\mu\text{m}$ . This effect is easily seen in the spectra shown in Fig. 67 for 0.5M  $\text{NaNO}_3$ . One mole of  $\text{NaNO}_3$  contains 22.99g of Na and 62g of  $\text{NO}_3$ .

## (2) Natural Saline Waters

The foregoing discussion of the reflectance spectra of aqueous solutions containing a single chemical compound, together with the molecular parameters in Table XV, and the chemical analyses shown in Table XVI for the natural waters, make the analysis of the reflectance spectra for the natural waters a relatively simple task.

### (a) San Francisco Bay, Pacific Ocean, Atlantic Ocean

The water samples from the San Francisco Bay and the Pacific Ocean contained monatomic ions  $\text{Ca}^{+2}$ ,  $\text{Mg}^{+2}$ ,  $\text{Na}^+$ ,  $\text{K}^+$ , and  $\text{Cl}^-$  and polyatomic ions  $\text{HCO}_3^-$  and  $\text{SO}_4^{-2}$ . The concentration of monatomic ions was equivalent to about 0.45M for the San Francisco Bay sample, and about 0.53M for the Pacific-Ocean sample. The concentration of polyatomic ions was about 0.002M for  $\text{HCO}_3^-$  and about 0.025M for  $\text{SO}_4^{-2}$ . We believe, although it was not measured, that the Atlantic-Ocean sample had a similar chemical composition.

The relative reflectance spectra are shown in Fig. 61 for these three water samples. The spectra exhibit all the spectral characteristics or relative reflectance spectra for aqueous solutions containing monatomic ions, e.g. the spectra for 1, 3, and 5M NaCl solutions shown in Fig. 66. At  $2.75 \mu\text{m}$  is a prominent peak due to shifting of the combined  $\nu_1\nu_3$  modes of

H<sub>2</sub>O when the monatomic ions are present in the sample. In the 8-11- $\mu$ m intervals the relative reflectance of these three samples increases, then decreases in the 11-12 $\mu$ m interval, and then begins to generally increase again beyond 12  $\mu$ m; this is caused in part by the monatomic ions shifting the  $\nu_L$  modes of liquid water to greater wavelengths. The effect of the  $\nu_3(F_2)$  mode of  $SO_4^{-2}$  at 9.05  $\mu$ m was also partially responsible for the increased reflectance in the 8-11- $\mu$ m interval of the relative reflectance spectra for these three samples. The effect of the  $HCO_3^-$  ion is not discernable in these spectra.

(b) Great Salt Lake (Utah)

The water sample from the Great Salt Lake contained monatomic ions  $Ca^{+2}$ ,  $Mg^{+2}$ ,  $Na^+$ ,  $K^+$ , and  $Cl^-$  and polyatomic ions  $HCO_3^-$  and  $SO_4^{-2}$ . The total concentration of monatomic positive and negative ions was about 2.65M. The concentration of  $HCO_3^-$  was 0.008M; and for  $SO_4^{-2}$  was 0.125M.

The relative reflectance spectrum for this sample is shown in Fig. 62. The spectrum contains the prominent peak at 2.75  $\mu$ m due a shifting to shorter wavelengths of the combined  $\nu_1 \nu_3$  modes of H<sub>2</sub>O. In the 8-11- $\mu$ m interval the relative reflectance increases, then decreases in the 11-12.5- $\mu$ m interval, and then generally increases

again beyond 12.6 $\mu$ m; this is caused in part by the  $\nu_L$  mode of liquid water being shifted to greater wavelengths in this sample. The effect of the  $\nu_3(\text{F}_2)$  mode of  $\text{SO}_4^{-2}$  centered at 9.05  $\mu$ m is particularly evident in the 8-11- $\mu$ m interval when the relative reflectance spectrum for this sample is compared to that for  $\text{K}_2\text{SO}_4$  shown in Fig. 67. The effect of the  $\nu_2$  mode of  $\text{HCO}_3^-$  is just beginning to appear at 6.10  $\mu$ m in the spectrum for this sample. Also, the combined effect of  $\nu_3\nu_4$  at 7.3  $\mu$ m for  $\text{HCO}_3^-$  is barely discerable in the spectrum.

(c) Dead Sea (Isreal)

Chemical composition for the sample from the Dead Sea was obtained from the publication by Neev and Emery,<sup>53/</sup> because spectrographic techniques, exclusively, were utilized at the USGS Laboratory to analyze this sample; see Table XIV. The sample, therefore, probably contained monatomic ions  $\text{Ca}^{+2}$ ,  $\text{Mg}^{+2}$ ,  $\text{Na}^+$ ,  $\text{K}^+$ ,  $\text{Cl}^-$ ,  $\text{Br}^-$ , plus relatively small amounts of metals. The concentration of monatomic ions in such a water sample is equivalent to about 5.60M each for total negative ions and for total positive ions.  $\text{HCO}_3^-$  content was probably about 0.003M, and  $\text{SO}_4^{-2}$  content about 0.006M.

The relative reflectance spectrum for this sample is shown in Fig. 62. The spectrum possesses only those features characteristic of a solution containing monatomic ions. There is a great similarity in the spectrum for this sample and the relative reflectance spectrum shown in Fig. 66 for a 5M NaCl solution. The effects of vibrational modes for  $\text{HCO}_3^-$  and  $\text{SO}_4^{2-}$  are not discernable in the spectrum for the sample from the Dead Sea.

(d) Phosphate Effluent Pit (Central Florida)

This water sample contained monatomic ions  $\text{Ca}^{+2}$ ,  $\text{Mg}^{+2}$ ,  $\text{Na}^+$ ,  $\text{K}^+$ ,  $\text{Cl}^-$ , and  $\text{F}^-$ . The relative reflectance spectrum shown in Fig. 3 for this sample has the sharp peak at 2.75  $\mu\text{m}$  which is due to shifting of the combined  $\nu_1\nu_3$  modes of  $\text{H}_2\text{O}$ . The presence of the smaller  $\text{F}^-$  ion causes the combined  $\nu_1\nu_3$  modes of  $\text{H}_2\text{O}$  to shift to longer wavelengths,<sup>56/</sup> whereas  $\text{Cl}^-$  causes a shift to shorter wavelengths.

This water sample also contained polyatomic ions  $\text{SO}_4^{2-}$  in relatively small concentrations and contained  $\text{PO}_4^{3-}$  and  $\text{H}_2\text{PO}_4^-$  in much larger concentrations. The  $\text{PO}_4^{3-}$  ion has infrared active modes  $\nu_3(\text{F}_2)$  at about 10  $\mu\text{m}$  and  $\nu_4(\text{F}_2)$  at 19.4  $\mu\text{m}$ . The  $\nu_3(\text{F}_2)$  mode is stronger in infrared activity than the  $\nu_4(\text{F}_2)$  mode.  $\text{H}_2\text{PO}_4^-$  has the four infrared active modes listed in Table XV, and has additional

infrared active modes  $\nu_4(A_1)$ ,  $\nu_4(B_1)$ , and  $\nu_4(B_2)$  which were not observed in the spectrum of  $\text{NH}_4\text{H}_2\text{PO}_4$  shown in Fig. 67. The prominent peak in the 8-12  $\mu\text{m}$  interval of the reflectance spectrum shown in Fig. 63 is caused by the  $\nu_3(F_2)$  mode of  $\text{PO}_4^{3-}$  and the  $\nu_1(A_1)$ ,  $\nu_3(A_1)$ ,  $\nu_3(B_1)$ ,  $\nu_3(B_2)$  modes of  $\text{H}_2\text{PO}_4^-$ .

In the relative reflectance spectrum, as shown in Fig. 63 for this sample, there is a small peak in the 12-14- $\mu\text{m}$  interval. The small peak is tentatively attributed to a vibrational mode of  $\text{SiO}_2$ , which also appears as a strong band in the absorption spectra of natural silicates such as  $\alpha$ -quartz, Chert, and Opal.<sup>57/</sup>

## B. Investigations of Infrared Transmittance of Powdered Materials.

### 1. Objectives

As previously stated in Section V.A.b., the complex refractive index  $N(\nu)$  of natural minerals is a current interest to some scientists. To obtain adequate specular reflectance measurements, however, requires a crystal sample of approximate minimum dimensions of 1 cm. Many natural minerals, particularly the clays, do not occur as large homogeneous crystals that can be cut and polished. Samples of such materials must, therefore, be investigated in a powdered form.

The objectives of this investigation are: (1) to measure either a reflectance or transmittance spectrum of the powdered material, and (2) to obtain spectral values of  $N(\nu)$  from the measured spectrum.

### 2. Background Information for Discussion of Powdered Materials

The acquisition and analysis of optical reflectance or transmittance spectra of polished single crystals is relatively simple when compared to acquisition and analysis of optical spectra for powders which are composed of small amorphous or crystalline particles. Although group-theory analysis remains a valid means for predicting the optical activity of molecular vibrations or phonons in small amorphous or crystalline particles, the acquisition of appropriate optical spectra and its subsequent analysis is complicated by diffraction, interference and total internal reflectance effects which are characteristic of the particle-size distribution, particle shape, random or preferred orientation of uniaxial or biaxial

crystals, and the relative spatial distribution of the particles within the powdered material. The Kramers-Kronig analysis is a valid means for analyzing specular reflectance spectra and fractional transmittance spectra, but is not validly applied to diffuse reflectance spectra which is typical of powders. Dispersion-theory analysis is a valid means for determining  $N(\nu)$  of the powders provided there exists an adequate theory for computing the measured optical properties of the powders. A wholly satisfactory method of acquisition and analysis of optical spectra must account for all of these things. Currently no such wholly satisfactory method exists, but several methods are now practiced with varying degrees of success in research laboratories.

One method, developed by Ebersol<sup>58/</sup> and his colleagues, requires simultaneous measurements of the particle-size distribution and of scattering and attenuation of laser radiation by airborne particulates which continuously flow through a test chamber. The particle-size distribution is measured by use of a Knollenberg counter. Mie-scattering computations, assuming spherical-particles are present, are then empirically adjusted until a best fit to the observed optical data is obtained; thereby providing a value for  $N(\nu)$  at the single frequency  $\nu$  of the laser radiation. Presently the principal objections to this method are (1) its reliance on the Knollenberg counter, (2) the spherical-particle assumption, and (3) its limited spectral extent in the infrared.

A second method<sup>59/</sup> is application of Fourier transform spectroscopy in the  $300\text{--}1400\text{ cm}^{-1}$  spectral range to measure diffuse emittance or reflectance spectra of loose powders whose chemical composition, crystalline structure, and spectral values of  $N(\nu)$  are known. The spectral values of  $N(\nu)$  are known from previous investigations of the optical properties of large single crystals. The measured spectra are then compared with spectra computed from a theory<sup>60/</sup> for the spectral reflectance and emittance of particulate materials. The theory, which is initiated with the known values of  $N(\nu)$  and known particle sizes and shapes, yields a favorable comparison with measured spectra. In principal this theory could be mathematically inverted so that its application to the measured spectra would yield  $N(\nu)$ . In practice, however, the inversion would be extremely difficult and one would probably resort to empirical adjustments of  $N(\nu)$  until a best fit to the measured spectra is obtained from the theory.

A third method is to press the particulate material in a transparent matrix and then measure the fractional transmittance of the matrix plus the particulate material relative to the transmittance of the matrix alone. In the infrared KBr and CsI, and in the far infrared polyethylene, are the preferred substances for the transparent matrix. This method was used by Volz<sup>61,62/</sup> to obtain  $N(\nu)$  in the  $250\text{--}4,000\text{ cm}^{-1}$  spectral range for Sahara dust, volcanic pumice, ammonium

sulfate, flyash, and other aerosols such as soot and sea salt. The principal objections to this method are (1) the particulate material is embedded in a matrix whose refractive index thereby alters the relative refractive index of the particulate material, (2) the attenuation coefficient obtained from the fractional transmittance is the sum of the absorption and scattering coefficients, and (3) the scattering coefficient is altered due to the presence of the matrix. However, this method does yield quantitative data over a wide spectral range. This was the method whereby powdered materials were investigated during the last months of this grant.

A fourth method is a variation of the third method which was outlined in the preceeding paragraph. Rather than pressing the powder within a matrix as in method three, one spreads the powder loosely (about 5 per cent packing fraction) on a substrate. Electrostatic attraction binds the powder to the surface of the substrate, which is typically KRS-5, crystalline quartz, or soft polyethylene. The transmittance spectrum of the substrate with the particulate material is measured relative to the transmittance spectrum of the substrate alone. This avoids objections (1) and (3) as mentioned for the third method, but objection (2) still holds for short wavelength electromagnetic waves. At longer wavelengths, i.e. wavelengths much greater than the diameters of the individual particles, Maxwell-Garnett theory<sup>63/</sup> allows one to compute the measured transmittance spectrum of the powder if  $N(v)$  is known for the bulk material. In those cases where  $N(v)$  is not known for the bulk, i.e. in the

proposed investigations, one empirically adjusts  $N(\nu)$  until a best fit to the measured spectrum is obtained.

A fifth method is to compact the particulate material under pressure thereby producing a solid sample that can be polished, and then measure the specular reflectance spectrum. Schatz<sup>66/</sup> utilized this method to measure the total reflectance of unpolished compacted powders composed of transparent or opaque particles as a function of the compacting pressure. Using pressures from  $6.9 \times 10^6 \text{ N/m}^2$  to  $4.8 \times 10^8 \text{ N/m}^2$  ( $10^3$  to  $7 \times 10^4 \text{ psi}$ ) he found that powders composed of transparent particles underwent a large decrease in reflectance as the pressure was increased, and powders composed of opaque particles increased in reflectance as the pressure was increased. As a powder is compacted its optical properties approach those of a large bulk sample of the amorphous or polycrystalline material. This method has some merit in investigations of optical properties provided (1) some practical compacting pressure is reached above which the reflectance does not vary, (2) the compacted powder can be pressed with a polished die or can be polished so that specular reflectance can be measured, (3) the crystalline structure remains unchanged for the individual small crystals, and (4) the small crystals are known to be either randomly or preferentially oriented. The Kramers-Kronig analysis would be valid when applied to the specular reflectance spectrum of the polished compacted powder. This is the method whereby we are investigating powdered materials during the follow-on contract.

### 3. $T(\nu)$ Spectra for Powdered Materials Pressed in KBr Pellets

Materials investigated were those listed in Table XVII. Relative transmittance spectra  $T(\nu) = T(\nu)_s / T(\nu)_m$  were measured, where  $T(\nu)_s$  denotes the fractional transmittance for a KBr pellet containing the powdered material and  $T(\nu)_m$  denotes the fractional transmittance for a KBr pellet without powdered material. The  $T(\nu)$  spectra are presented in graphical form for the various materials in the Figures listed in column 4 of Table XVII.

Table XVII. Powdered materials pressed in KBr pellets for which relative transmittance  $T(\nu)$  was measured.

Material	Concentration*	Spectral Range	$T(\nu)$
Montmorillonite	$10^{-2}$ , $10^{-3}$ , $10^{-4}$	300-5,000 $\text{cm}^{-1}$	Fig. 68
Colemanite	$10^{-2}$ , $10^{-3}$ , $10^{-4}$	300-5,000	Fig. 69
Kernite	$10^{-2}$ , $10^{-3}$ , $10^{-4}$	300-5,000	Fig. 70
Kaolin	$10^{-2}$ , $10^{-3}$ , $10^{-4}$	300-5,000	Fig. 71
Lampblack	$2 \times 10^{-5}$	300-5,000	Fig. 72
Active Charcoal	$2 \times 10^{-5}$	300-5,000	Fig. 73
Wood Charcoal	$2 \times 10^{-4}$	300-5,000	Fig. 74
Aluminum	$2 \times 10^{-2}$	1,665-5,000	Fig. 75
Kaolin	$2 \times 10^{-2}$	1,665-5,000	Fig. 76
Montmorillonite	$2 \times 10^{-2}$	1,665-5,000	Fig. 77
Colemanite	$2 \times 10^{-2}$	1,665-5,000	Fig. 78
Illite	$2 \times 10^{-2}$	1,665-5,000	Fig. 79
Kernite	$2 \times 10^{-2}$	1,665-5,000	Fig. 80

\*See following section for a discussion of the concentrations.

### 4. Discussion of $T(\nu)$ Spectra for Powdered Materials

The KBr pellets containing the powdered materials were prepared as follows. For the first four materials listed in

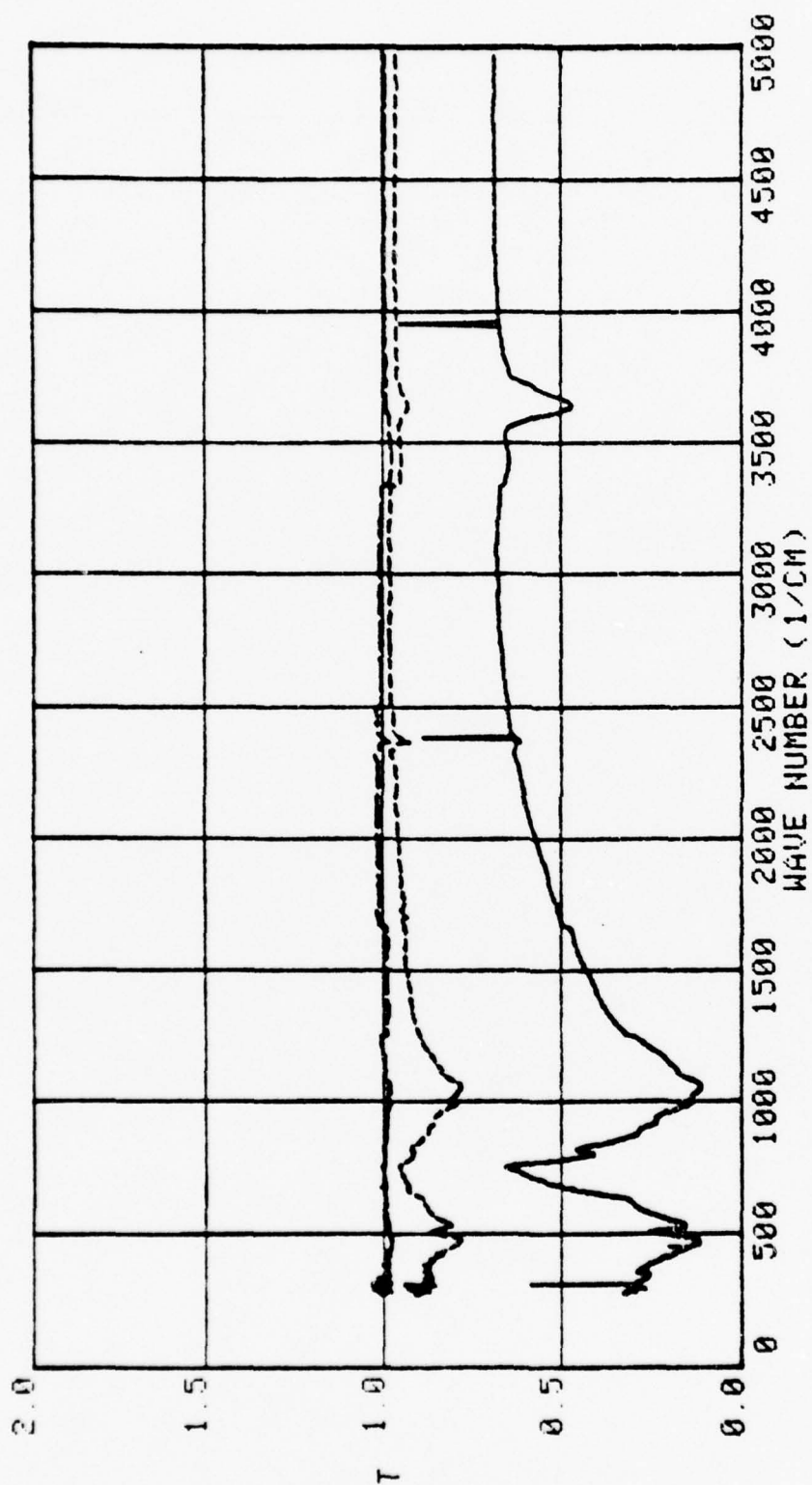


Figure 68. Relative transmittance spectra  $T(\nu)$  in the 300-5,000  $\text{cm}^{-1}$  spectral region for Montmorillonite at concentrations of  $10^{-2}$  (solid line),  $10^{-3}$  (short-dashed line), and  $10^{-4}$  (long-dashed line) in KBr pellets.

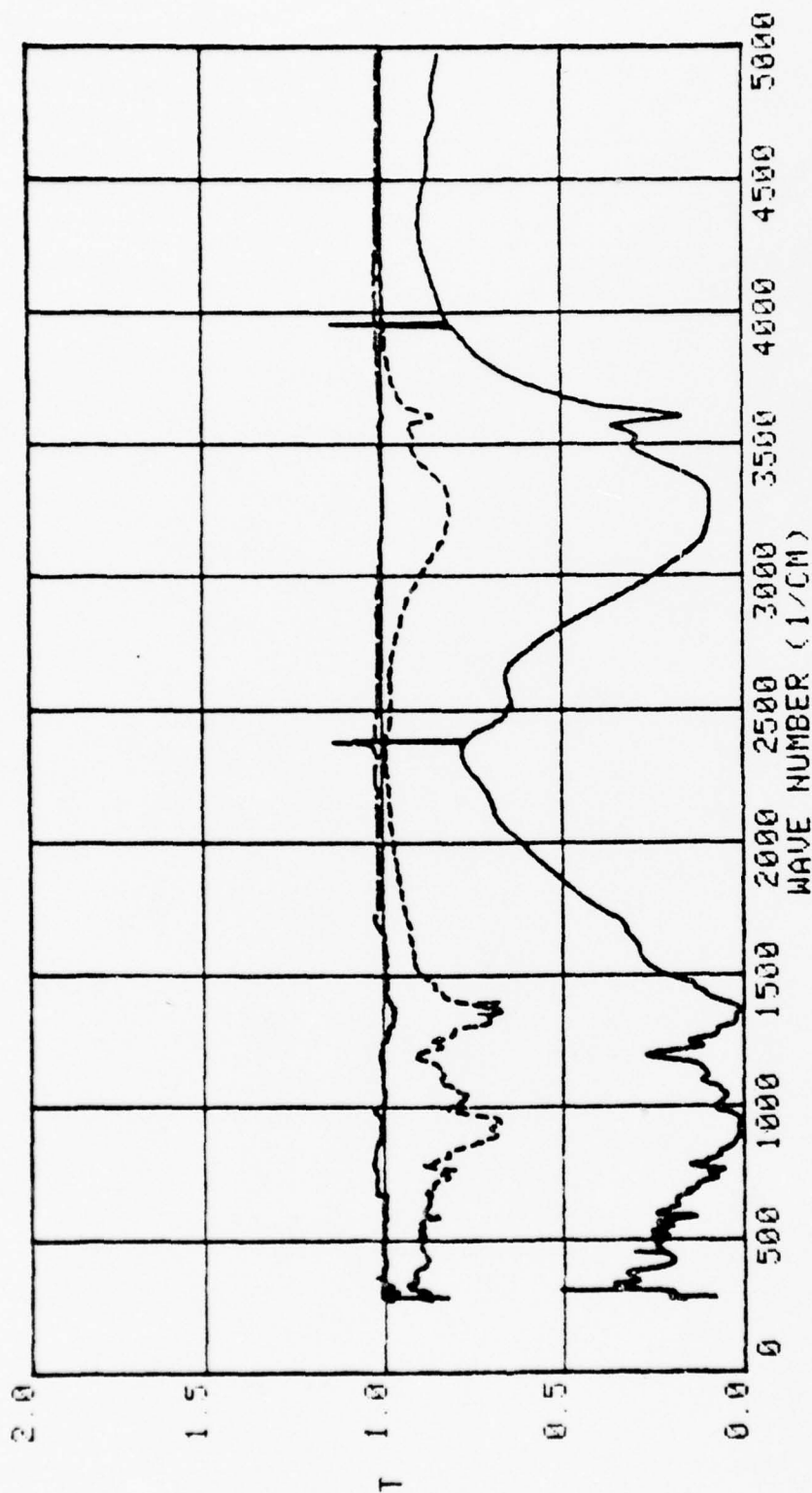


Figure 69. Relative transmittance spectra  $T(\nu)$  in the 300-5,000  $\text{cm}^{-1}$  spectral region for Colemanite at concentrations of  $10^{-2}$  (solid line),  $10^{-3}$  (short-dashed line), and  $10^{-4}$  (long-dashed line) in KBr pellets.

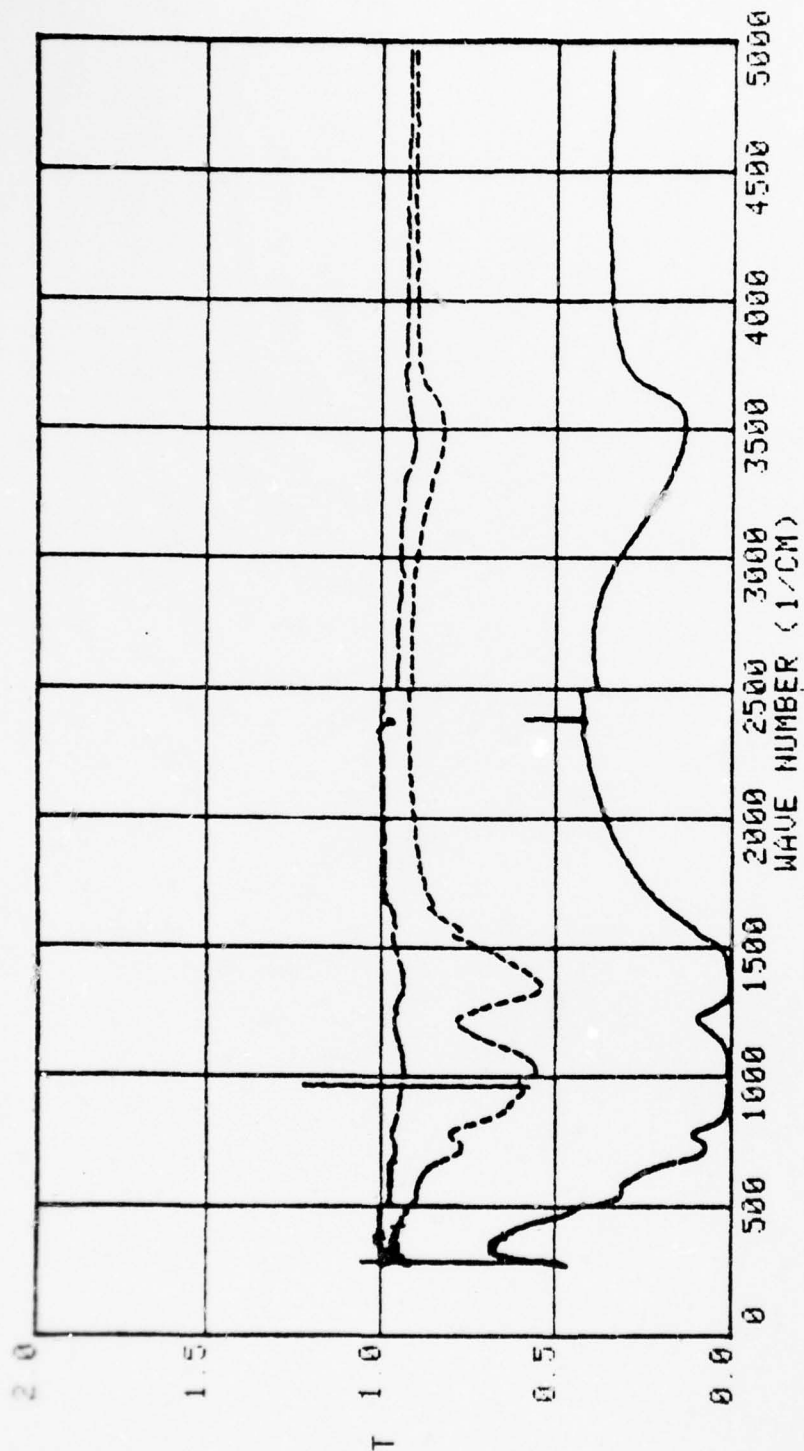


Figure 70. Relative transmittance spectra  $T(\nu)$  in the 300-5,000  $\text{cm}^{-1}$  spectral region for Kernite at concentrations of  $10^{-2}$  (solid line),  $10^{-3}$  (short-dashed line), and  $10^{-4}$  (long-dashed line) in KBr pellets.

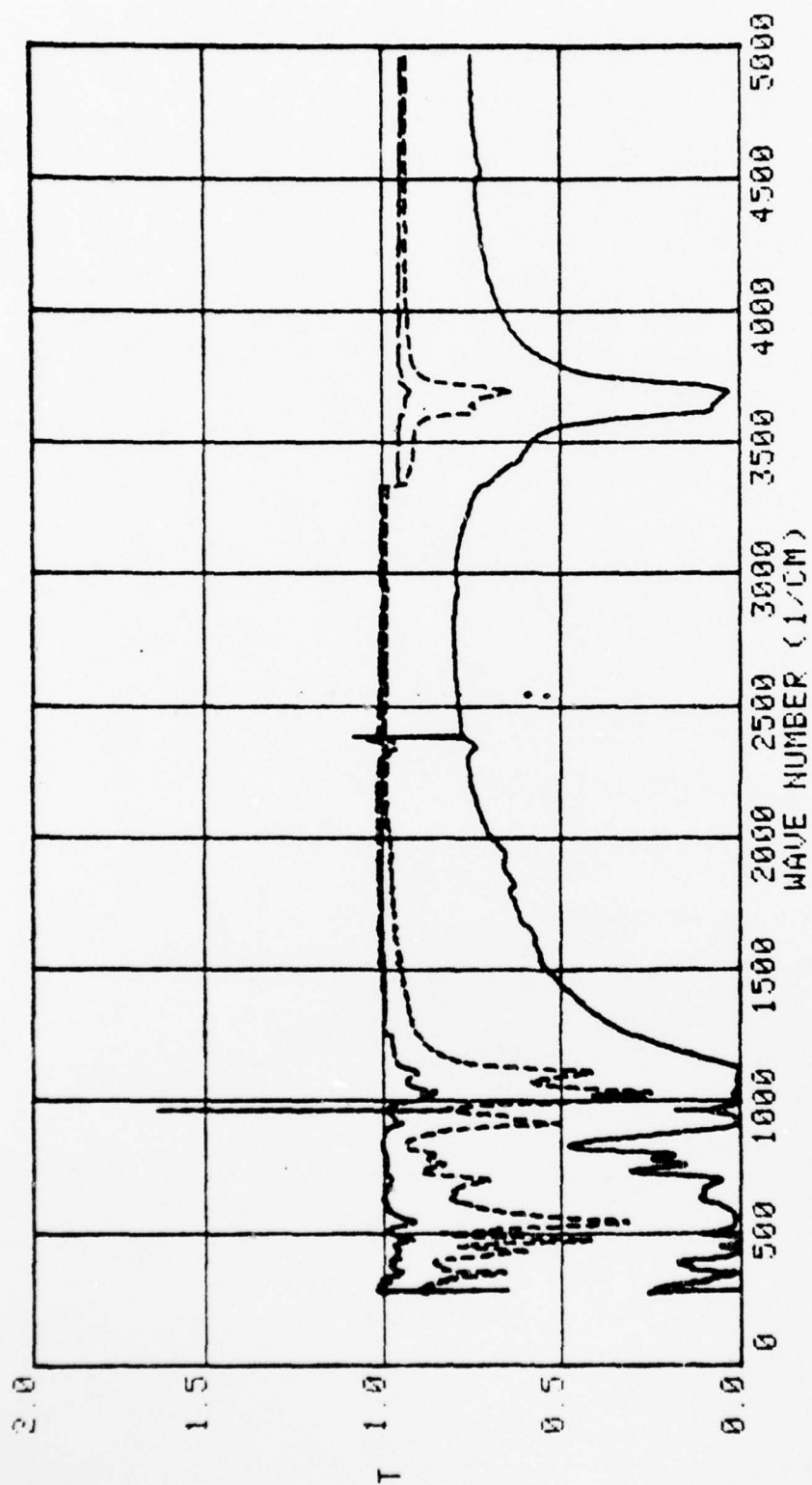


Figure 71. Relative transmittance spectra  $T(\nu)$  in the 300-5,000  $\text{cm}^{-1}$  spectral region for Kaolin at concentrations of  $10^{-2}$  (solid line),  $10^{-3}$  (short-dashed line), and  $10^{-4}$  (long dashed line) in KBr pellets.

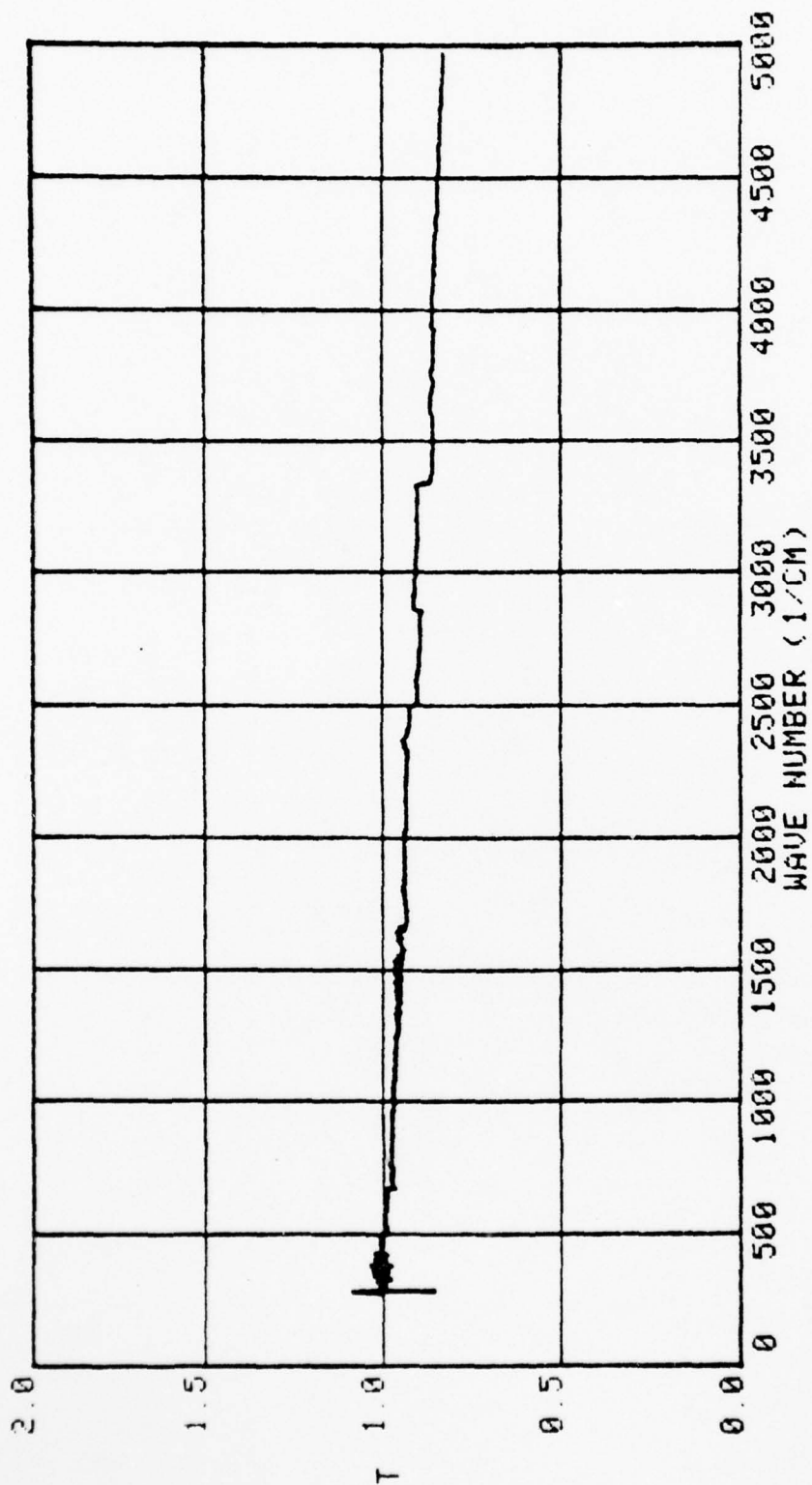


Figure 72. Relative transmittance spectrum  $T(\nu)$  in the  $300\text{--}5,000\text{ cm}^{-1}$  spectral region for Lampblack at a concentration of  $2 \times 10^{-5}$  in KBr pellets.

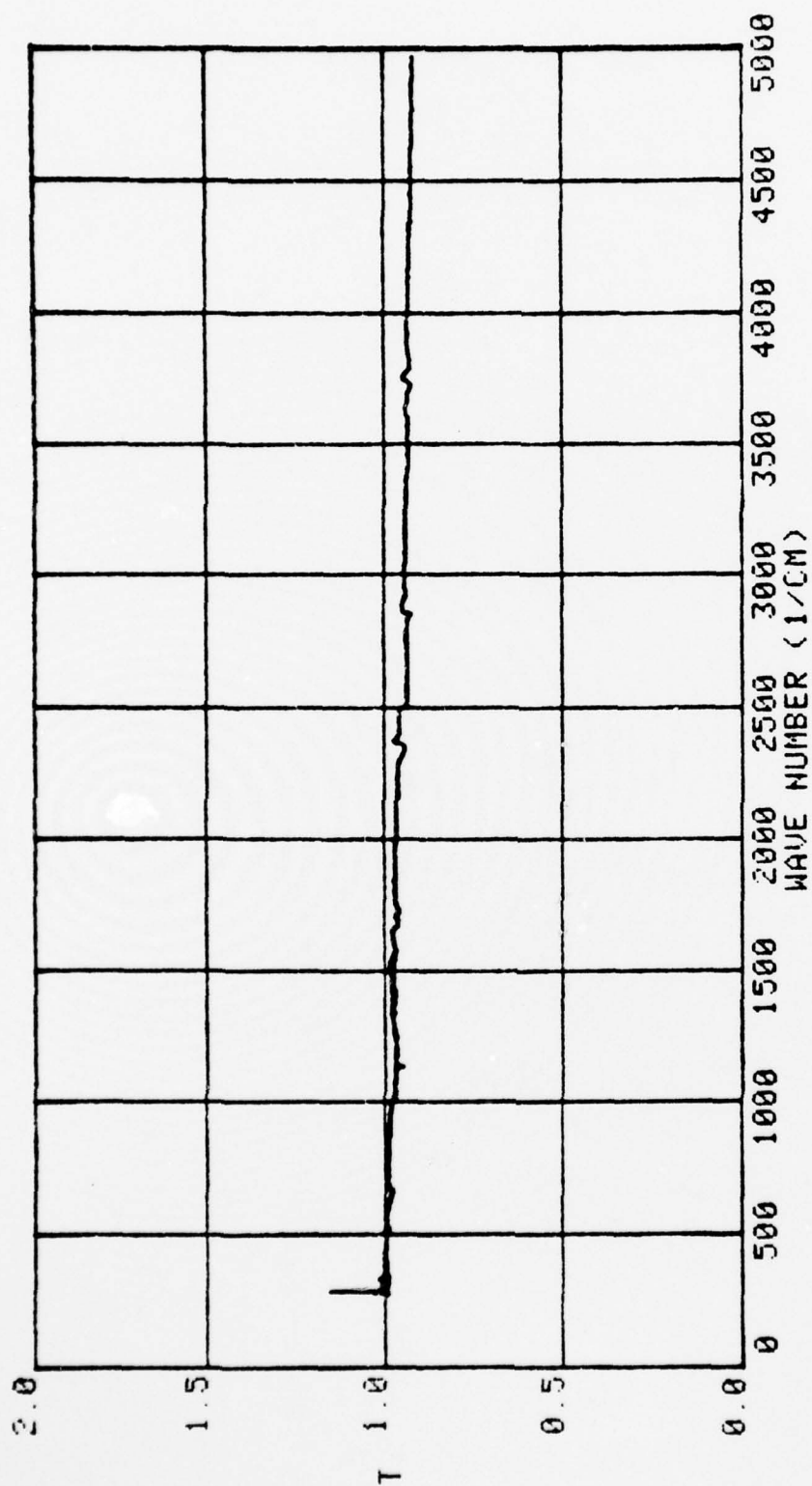


Figure 73. Relative transmittance spectrum  $T(\nu)$  in the 300-5,000  $\text{cm}^{-1}$  spectral region for activated charcoal at a concentration of  $2 \times 10^{-5}$  in KBr pellets.

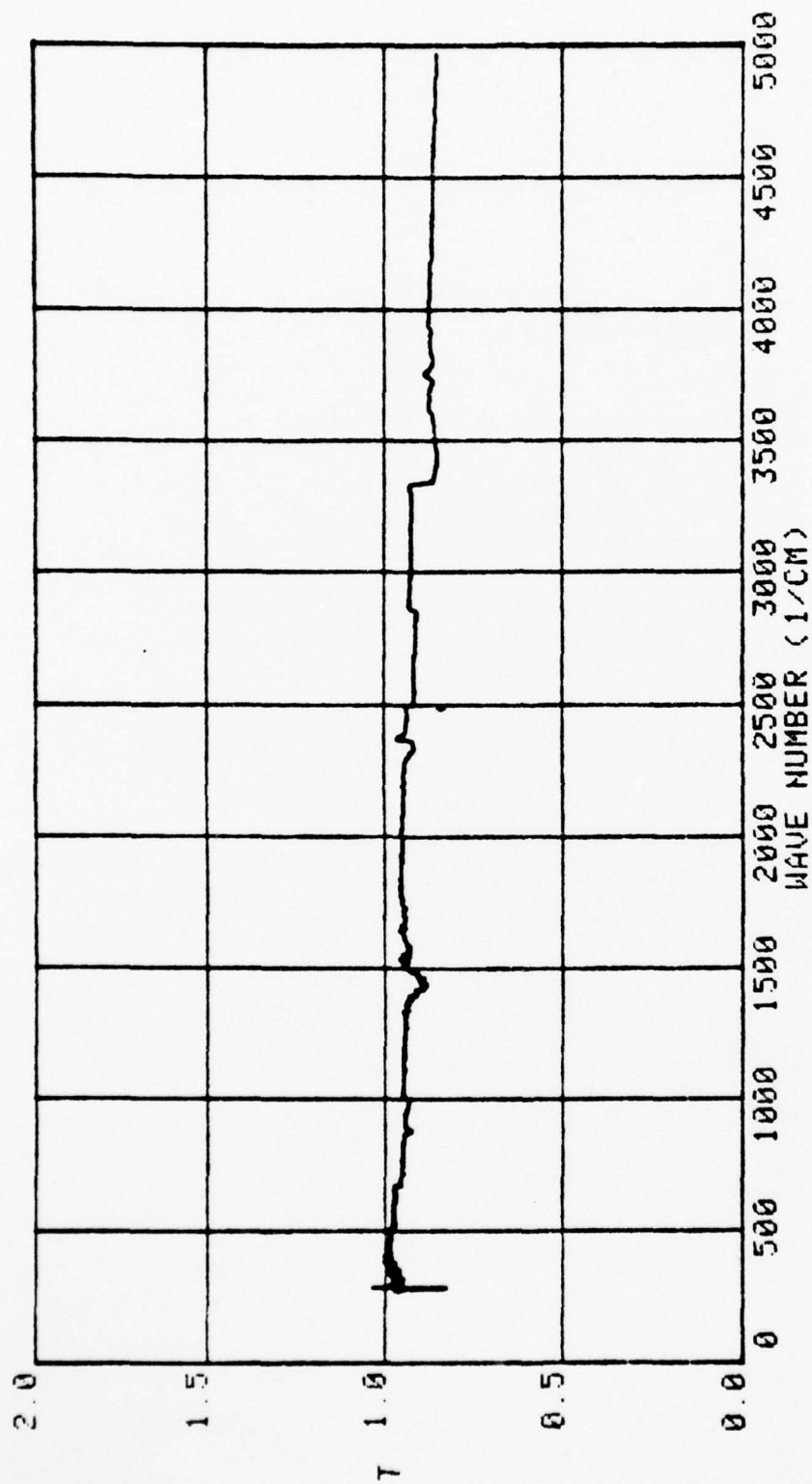


Figure 74. Relative transmittance spectrum  $T(\nu)$  in the 300-5,000  $\text{cm}^{-1}$  spectral region for wood charcoal at a concentration of  $2 \times 10^{-4}$  in KBr pellets.

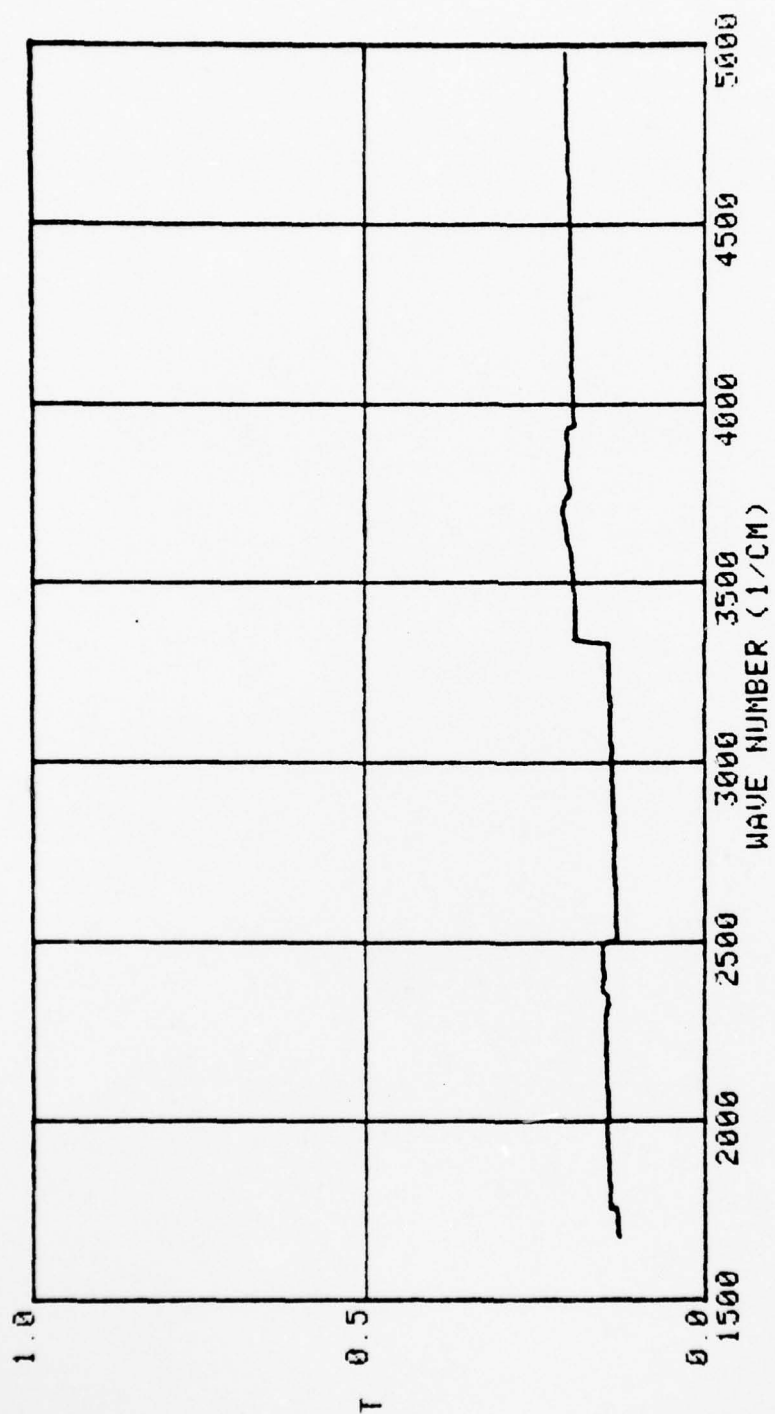


Figure 75. Relative transmittance spectrum  $T(\nu)$  in the 1,665-5,000  $\text{cm}^{-1}$  spectral region for Aluminum powder at a concentration of  $2 \times 10^{-2}$  in KBr pellets.

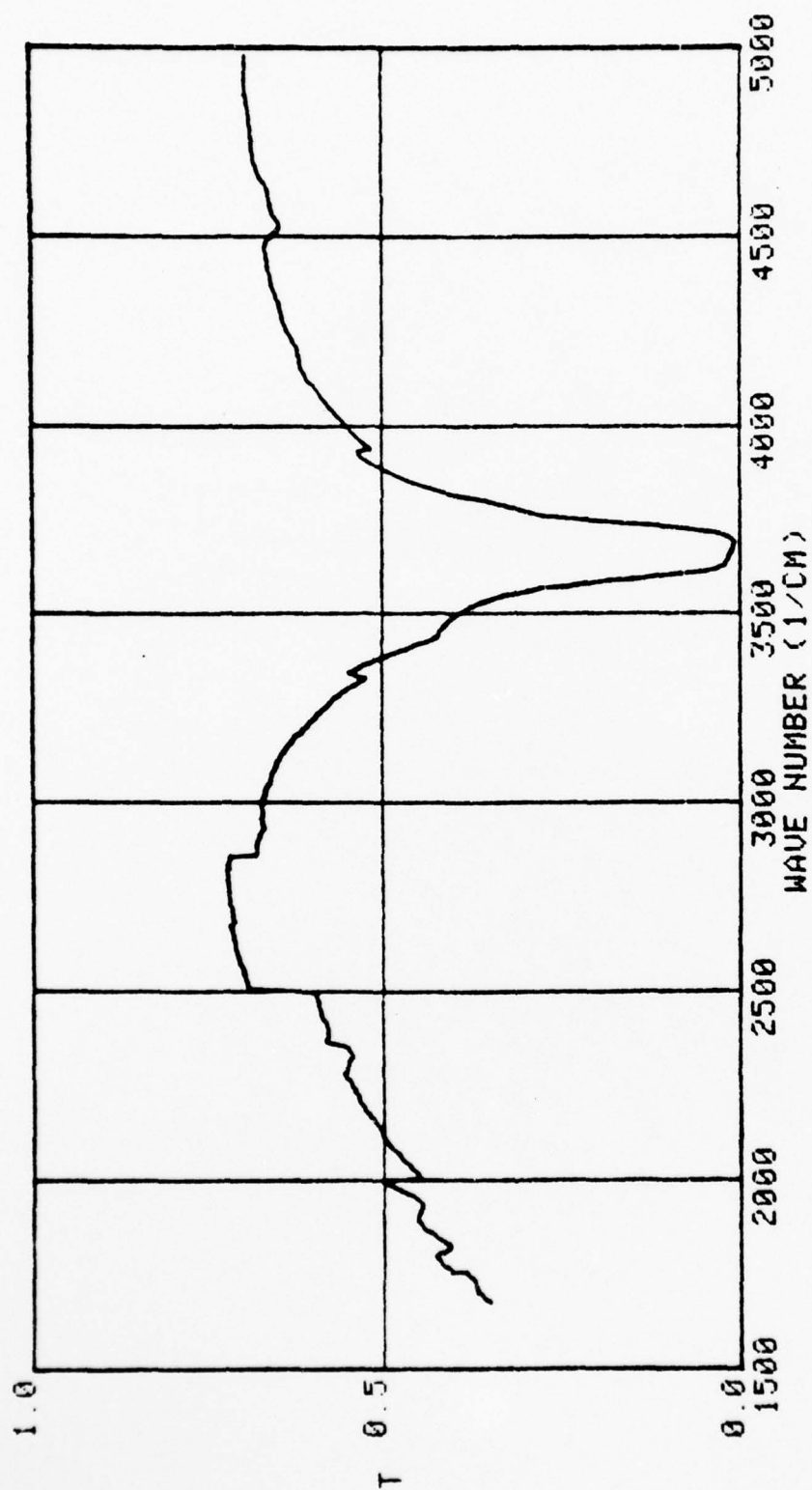


Figure 76. Relative transmittance spectrum  $T(\nu)$  in the 1,665-5,000  $\text{cm}^{-1}$  spectral region for Kaolin at a concentration of  $2 \times 10^{-2}$  in KBr pellets.

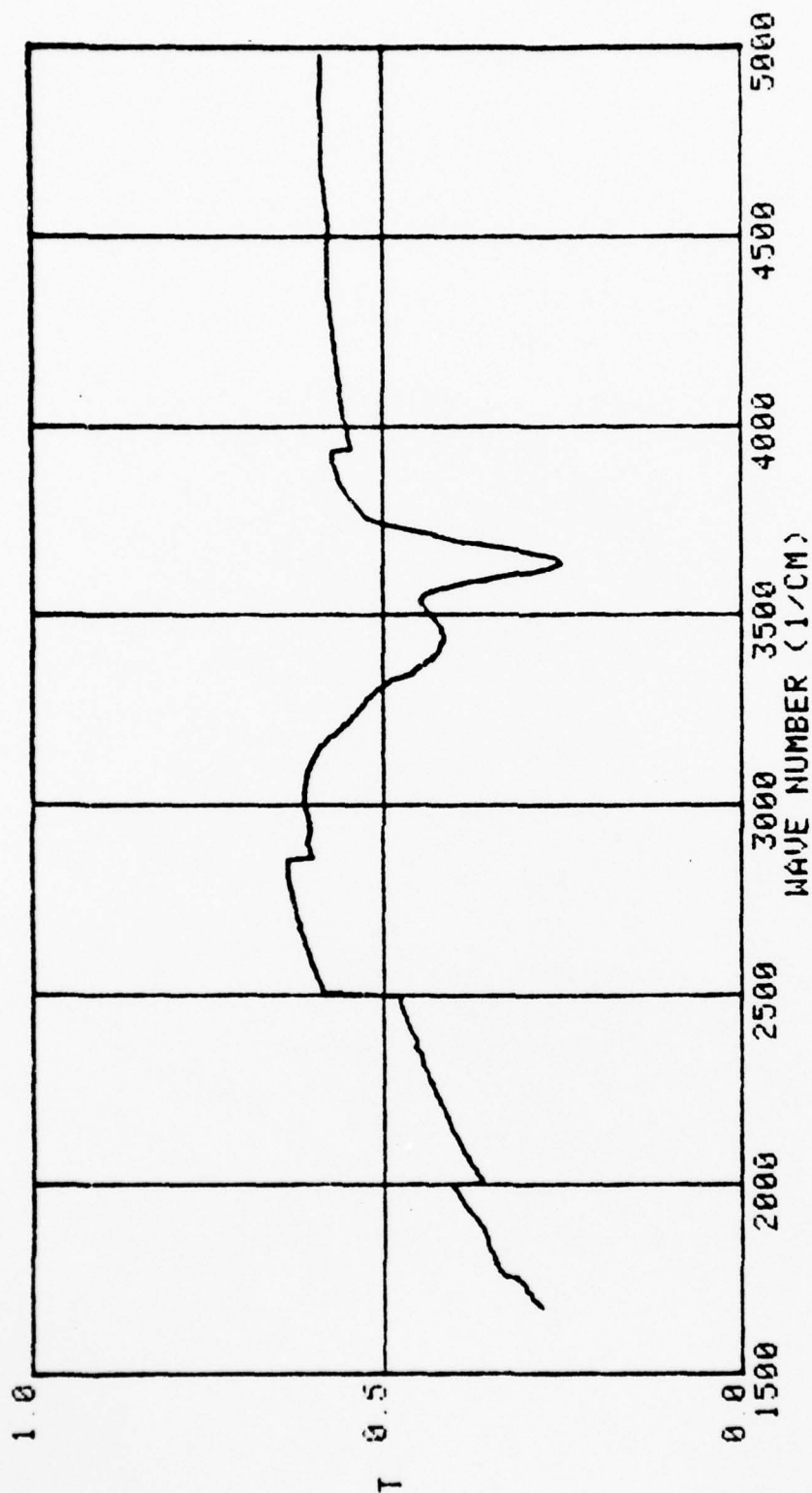


Figure 77. Relative transmittance spectrum  $T(\nu)$  in the  $1,665\text{--}5,000\text{ cm}^{-1}$  spectral region for Montmorillonite at a concentration of  $2 \times 10^{-2}$  in KBr pellets.

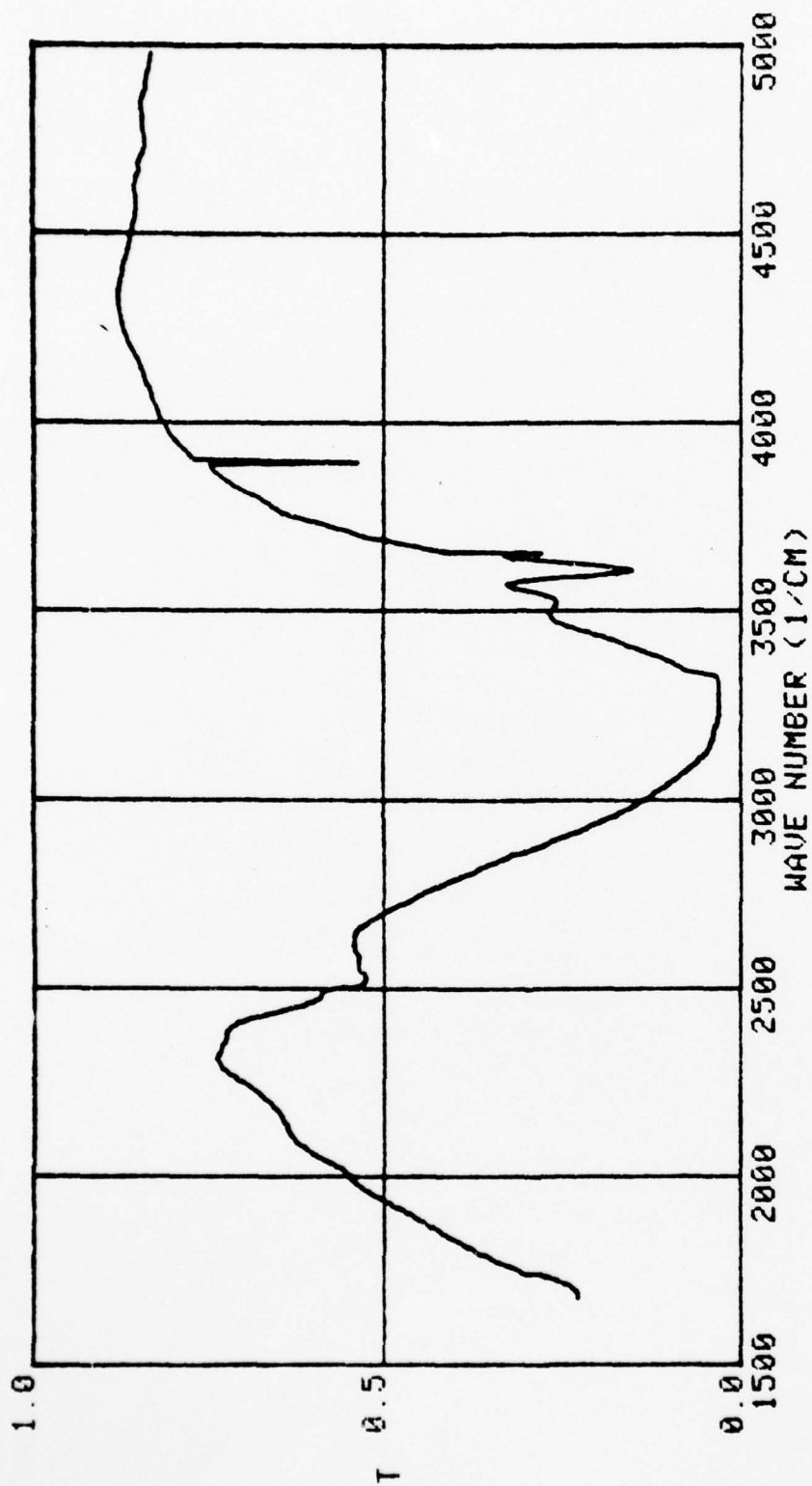


Figure 78. Relative transmittance spectrum  $T(\nu)$  in the  $1,665\text{--}5,000\text{ cm}^{-1}$  spectral region for Colemanite at a concentration of  $2 \times 10^{-4}$  in KBr pellets.

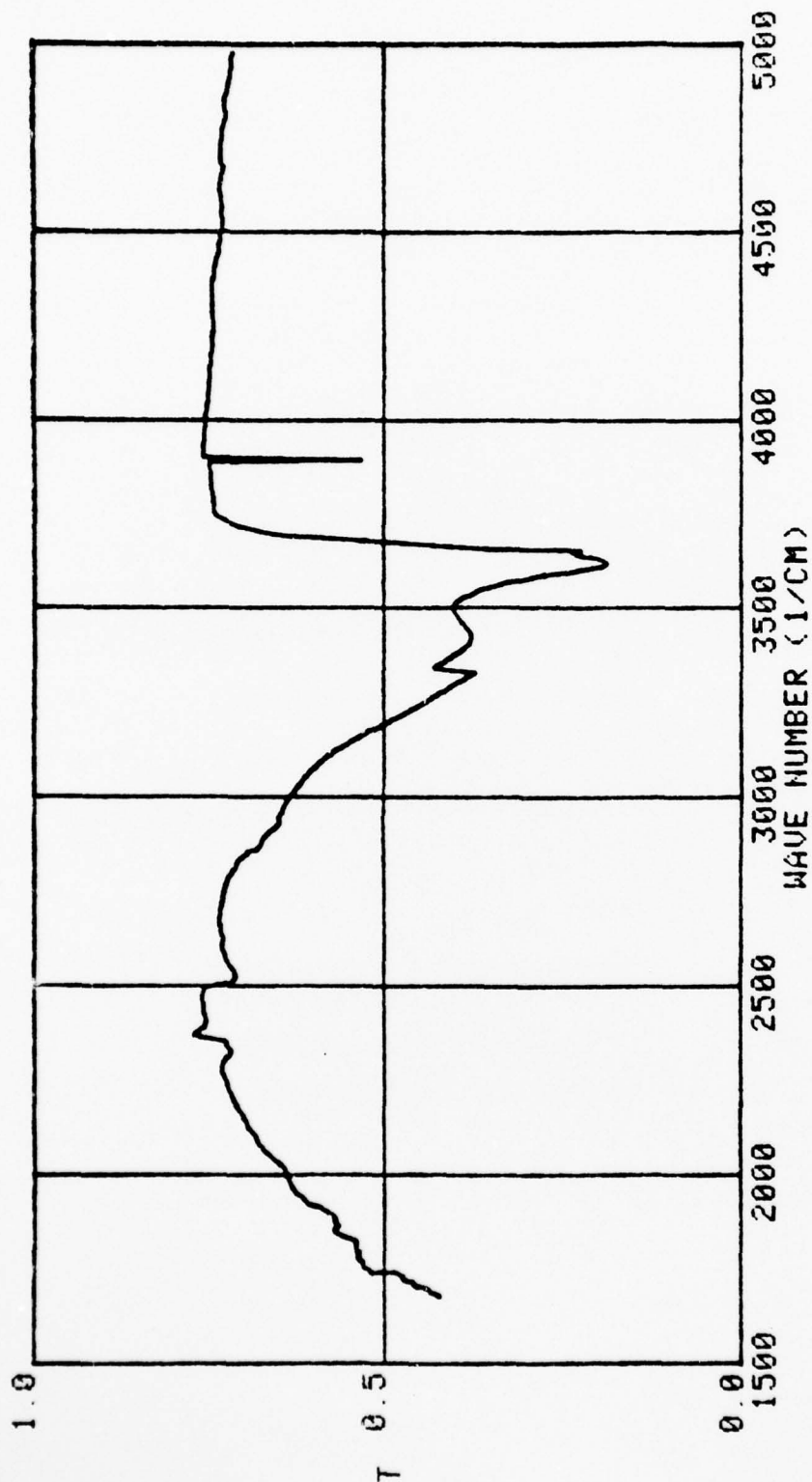


Figure 79. Relative transmittance spectrum  $T(\nu)$  in the  $1,665\text{--}5,000\text{ cm}^{-1}$  spectral region for Illite at a concentration of  $2 \times 10^{-2}$  in KBr pellets.

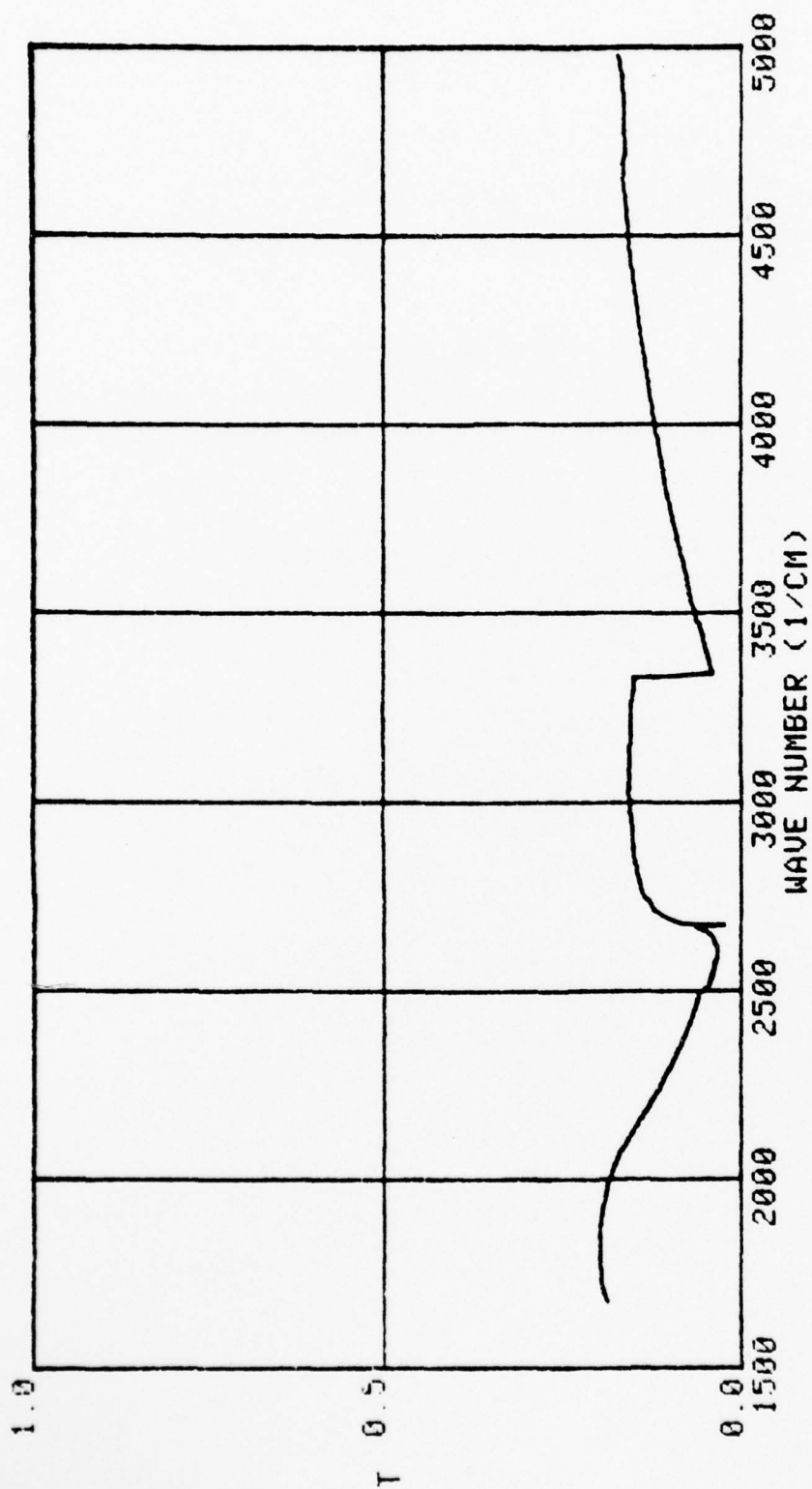


Figure 80. Relative transmittance spectrum  $T(\nu)$  in the 1,665-5,000  $\text{cm}^{-1}$  spectral region for Kernite at a concentration of  $2 \times 10^{-2}$  in KBr pellets.

Table XVII, a stock mixture consisting of 1 part powder per 100 parts KBr (6g of KBr) was prepared. This provided the  $10^{-2}$  concentration. Serial dilution of portions of the stock mixture then provided the  $10^{-3}$  and  $10^{-4}$  concentrations. A similar serial dilution process provided the concentrations for lampblack, activated charcoal, and wood charcoal. The remaining six materials in Table XVII were prepared by mixing 0.12g of powdered material with 6g of KBr.

Each pellet was prepared by use of 300 mg of KBr or powder + KBr. The pellets were pressed in a polished die at a pressure of 87,000 psi. The pellets were  $1.30 \pm 0.03$  mm in diameter and  $0.842 \pm 0.015$  mm thick. Just prior to pressing the pellet, about 500mg of the powder--KBr mixture was reground by use of a vibromill. The 300mg required for the pellet was then obtained from this reground material. All powdered materials, except the KBr, were obtained from Wards Scientific.

Montmorillonite is an optically biaxial material whose chemical composition is  $\text{Al}_2\text{Si}_4\text{O}_{10}(\text{OH})_2 \cdot n\text{H}_2\text{O}$ . The  $T(\nu)$  spectra for this material are presented in Figs. 68 and 77.

Colemanite is an optically biaxial material whose chemical composition is  $\text{Ca}_2\text{B}_6\text{O}_{11} \cdot 5\text{H}_2\text{O}$ . The  $T(\nu)$  spectra for this material are presented in Figs. 69 and 78. The colemanite and montmorillonite spectra both show the O-H stretching bands in the  $3,300 \text{ cm}^{-1}$  region. We did not make a group analysis of these minerals, and therefore did not assign the bands in the lower wave-number region.

Kernite is an optically biaxial material whose chemical composition is  $\text{Na}_2\text{B}_4\text{O}_7 \cdot 4\text{H}_2\text{O}$ . The  $T(\nu)$  spectra for this material are shown in Figs. 70 and 80. The O-H stretch bands are also apparent in the spectra of this material.

Kaolin is an optically biaxial material whose chemical composition is  $\text{Al}_2\text{Si}_2\text{O}_5(\text{OH})_4$ . The  $T(\nu)$  spectra for this material are shown in Figs. 71 and 76.

Lampblack consists of opaque carbon soot particles. The  $T(\nu)$  spectrum for this material is shown in Fig. 72. Note the absence of infrared active bands for this material.

Activated charcoal also consists of opaque particles. Its  $T(\nu)$  spectrum is shown in Fig. 73. Again there is an absence of infrared active bands.

Wood charcoal was more transparent than lampblack or activated charcoal, and there is one weak infrared active band near  $1,450 \text{ cm}^{-1}$ . The  $T(\nu)$  spectrum for this material is shown in Fig. 74.

Aluminum powder consists of optically opaque particles. The  $T(\nu)$  spectrum for this material is shown in Fig. 75. Again there is an absence of infrared active bands.

Illite is an optically biaxial material whose variable chemical composition is  $\text{K}_{1-x}\text{Al}_2\text{Si}_{3+x}\text{Al}_{1-x}\text{O}_{10}(\text{OH})_2$ . The  $T(\nu)$  spectrum for this material is shown in Fig. 79.

Attempts to determine attenuation cross sections from these  $T(\nu)$  spectra yielded inconsistent results for reasons discussed in Section V.B.2.

The powdered materials whose  $T(\nu)$  spectra have been presented here are currently being investigated by use of

reflectance methods during the follow-on contract.

The  $T(\nu)$  spectra shown in Figures 68-80 constitute raw data which have not been corrected for random errors picked up during data transmission (anomalous sharp spikes), and the use of practional transmitting sector wheels during data acquisition (abrupt discontinuities in the spectra).

AD-A076 502

MISSOURI UNIV-KANSAS CITY DEPT OF PHYSICS F/6 20/8  
MOLECULAR AND CRYSTALLINE ELECTROMAGNETIC PROPERTIES OF SELECTE--ETC(U)  
AUG 79 M R QUERRY DAA629-76-8-185

**UNCLASSIFIED**

**ARO-13739.9-85X**

NL

3 OF 3

AD  
A076502

END  
DATE  
FILMED

12-79

DDC

## C. References for Sections V.A. and V.B.

1. M. R. Querry, R. C. Waring, W. E. Holland, L. M. Earls, M. D. Herrman, W. P. Nijm, and G. M. Hale, J. Opt. Soc. Am. 64, 39 (1974).
2. G. M. Hale and M. R. Querry, Appl. Opt. 12, 555 (1973).
3. J. Bandekar and B. Curnutte, J. Mol. Spectrosc. 58, 169 (1975).
4. M. R. Querry, R. C. Waring, and W. E. Holland, J. Opt. Soc. Am. 66, 830 (1976).
5. M. R. Querry, W. E. Holland, R. C. Waring, L. M. Earls, and M. D. Querry, J. Geophys. Res. 82, 1425 (1977).
6. P. Rhine, D. Williams, G. M. Hale, and M. R. Querry, J. Phys. Chem. 78, 238 (1974).
7. P. Rhine, D. Williams, G. M. Hale, and M. R. Querry, J. Phys. Chem. 78, 1405 (1974).
8. D. E. Irish, Chap. 9, "Vibrational Spectral Studies of Electrolyte Solutions and Fused Salts," Ionic Interactions from Dilute Solutions to Fused Salts, Vol. 2, ed. S. Petrucci, Academic Press, (New York, 1971), pp. 239-246.
9. I. Nakagawa and T. Shimanouchi, Spectrochim. Acta 20, 429 (1964).
10. D. E. Irish, B. McCarroll, and T. F. Young, J. Chem. Phys. 39, 3436 (1963).
11. D. E. Irish and T. F. Young, J. Chem. Phys. 43, 1765 (1965).
12. B. Gilbert, Bull. Soc. Chim. Belges 76, 493 (1967).
13. D. F. C. Morris, E. L. Short, and D. N. Waters, J. Inorg. Nucl. Chem. 25, 975 (1963).

14. C. O. Quicksall and T. G. Spiro, *Inorg. Chem.*, 5, 2232 (1966).
15. J. K. Wilmhurst, *J. Chem. Phys.*, 39, 1779 (1963).
16. A. Loewenschuss, A. Ron, and O. Schnepf, *J. Chem. Phys.*, 49, 272 (1968).
17. R. F. Kruh and C. L. Standley, *Inorg. Chem.*, 1, 941 (1962).
18. D. E. Irsih and M. H. Brocker, "Raman and Infrared Spectral Studies of Electrolytes," *Advances in Infrared and Raman Spectroscopy*, Vol. 2, ed. R. J. H. Clark and R. E. Hester, Heyden (London, 1976).
19. E. Matijevic, J. P. Crouch, and M. Kerker, *J. Phys. Chem.*, 66, 111 (1962).
20. C. M. Preston and W. A. Adams, *Can. J. Spectry.*,     , (1978).
21. A. C. Chapman and L. E. Thirlwell, *Spectrochim. Acta* 20, 937 (1964).
22. S. A. Stern, J. T. Mullhaupt, and W. B. Kay, *Chem. Revs.* 60, 185 (1960).
23. G. E. McGraw, D. L. Bernitt, and I. C. Hisatsune, *J. Chem. Phys.*, 42, 237 (1965).
24. T. F. Young, L. F. Maranville, and H. M. Smith, "Raman Spectral Investigations of Ionic Equilibria in Solutions of Strong Electrolytes," The Structure of Electrolytic Solutions, ed. W. J. Hamer, Wiley (New York, 1959), pp. 35-63.
25. The curve in Fig. 2 of this paper is based on Values of  $\alpha$  obtained from Figs. 2 and 3 of Reference 3. The values of  $\alpha$  are the results of Raman spectroscopic analysis of aqueous solutions of nitric acid by A. A. Krawetz, Thesis, Univ. of Chicago, 1955.

26. H. Cohn, C. K. Ingold, and H. G. Poole, J. Chem. Soc. (London), Part 4, 4272 (1952).
27. D. E. Bethell and N. Sheppard, J. Chem. Phys. 21, 1421 (1953).
28. I. L. Tyler and M. R. Querry, J. Chem. Phys. 68, 1230 (1978).
29. G. M. Hale, W. E. Holland, and M. R. Querry, Appl. Opt. 12, 48 (1973).
20. J. Bandekar and B. Curnutte, J. Mol. Spectrosc. 58, 169 (1975).
31. G. D. Kerr, M. W. Williams, R. O. Birkhoff, and L. R. Painter, J. Appl. Phys. 42, 4258 (1971).
32. B. L. Sowers, M. W. Williams, R. N. Hamm, and E. T. Arakawa, J. Appl. Phys. 42, 4254 (1971).
33. R. G. Snyder and J. H. Schachtschneider, Spectrochim. Acta. 19, 85 (1963) and Spectrochim Acta 19, 117 (1963).
34. H. Tadokoro and M. Lobayashi, "Vibrational Spectroscopy," Chap. 2, Polymer Spectroscopy, ed. D. O. Hummel, Verlag Chemie (Weinheim/Berstr., 1974).
35. L. J. Bellamy, The Infrared Spectra of Complex Molecules, vol. 1, Third Edition, John Wiley & Sons (New York, 1975).
36. A. L. Smith, Spectrochim. Acta 19, 849 (1960).
37. W. G. Spitzer, R. C. Miller, D. A. Kleinman, and L. E. Howarth, Phys. Rev. 126, 1710 (1962).
38. F. Gervais and B. Piriou, Phys. Rev. B 10, 1642 (1974).
39. A. S. Barker, Jr., Phys. Rev. 132, 1474 (1963).
40. George M. Hale, Wayne E. Holland, and Marvin R. Querry, Appl. Opt. 12, 48 (1973).

41. J. R. Aronson and P. F. Strong, Appl. Opt., 14, 2914 (1975).
42. James B. Pollack, Owen B. Toon, and Bishun N. Khare, Icarus 19, 372 (1973).
43. W. G. Spitzer and D. A. Kleinman, Phys. Rev., 121, 1324 (1961).
44. Wayne E. Holland, Marvin R. Querry, and Raymond M. Coveney, Jr., "Measurements of spectral reflectance and optical constants of selected rock samples for application to remote sensing of soil moisture," Completion Report, U.S. Dept. of Commerce grant 04-4-158-27, available from Nat. Tech. Inform. Serv., Springfield, Va. 22151.
45. Howard P. Ross, Joel E. M. Adler, and G. R. Hunt, Icarus 11, 46 (1969).
46. Robert D. Watson, Remote Sensing of Environ., 2, 95 (1972).
47. Graham R. Hunt and John W. Salisbury, and John W. Salisbury, Mod. Geo. 1, 283 (1970).  
Graham R. Hunt, John W. Salisbury, and Charles J. Lenhoff, Mod. Geo. 2, 195 (1971).
48. John M. Hunt, Mary P. Wisherd, and Lawrence C. Bonham, Anal. Chem. 22, 1478 (1950).
49. W. B. Howe and J. W. Koenig, "The Stratigraphic Succession of Missouri," 185 p., Mo. Geo. Sur. and Water Res. 40, 2nd Ser., 100 (1961).
50. Querry, M. R., Contribution to Chap. 19 "Water resources assessment," pp. 1493-1497, Manual of Remote Sensing, Vol. 2, ed. R. G. Reeves, Am. Soc. Photogrammetry, Falls Church, Va. (1975).
51. Chappell, T. I., and R. M. White, Appl. Phys. Letters 28, 422-423, 1976.

52. Querry, M. R., and R. C. Waring, W. E. Holland, G. M. Hale, and W. Nijm, J. Opt. Soc. Am. 62, 849-855, 1972.
53. Neev, D., and K. D. Emery, Chemical characteristics of the dead sea water, pp. 63-81, The Dead Sea, Bull. no. 41, State of Israel, Ministry of Development, Geological Survey, 1967.
54. Bryan, J. B., and B. Curnutte, J. Mol. Spectry. 41, 512-533, 1972.
55. Walrafen, G. E., Contribution as Chap. 5, Raman and infrared spectral investigations of water structure, pp. 151-214, Water: a Comprehensive Treatise, Vol. I, ed. F. Franks, Plenum Press, New York, 1972.
56. Rhine, P., D. Williams, G. M. Hale, and M. R. Querry, J. Phys. Chem. 78, 238-246, 1974.
57. Hunt, J. M., M. P. Wisherd, and L. C. Bonham, Analytical Chem. 22, 1478-1497 (1950).
58. J. F. Ebersol, Aerodyne Research Inc., Bedford, Ma. 01730, (private conversations), and J. F. Ebersol et al. J. Opt. Soc. Am. 68, 1358 (1978).
59. J. R. Aronson and A. G. Emslie, Appl. Opt. 12, 2573 (1973).
60. A. G. Emslie and J. R. Aronson, Appl. Opt. 12, 2563 (1973).
61. F. E. Volz, Appl. Opt. 12, 564 (1973).
62. F. E. Volz, Appl. Opt. 11, 755 (1972).
63. J. C. Maxwell-Garnett, Phil. Trans. R. Soc. Lond. 203, 385 (1904); 205, 237 (1906).
64. E. A. Schatz, J. Opt. Soc. Am. 56, 389 (1966).

#### D. Other Investigations

1. Split-pulse laser method for measuring attenuation coefficients of transparent liquids: Application to deionized filter water in the visible region

Marvin R. Querry, Philip G. Cary, and Richard C. Waring  
Department of Physics, University of Missouri-Kansas City,  
Kansas City, Mo. 64110

##### a. Abstract

Attenuation coefficients  $\alpha(\lambda)$  for collimated quasimonochromatic radiation passing through deionized filtered water were measured throughout the 418.6 to 640.3 nm wavelength region by use of a split-pulse laser method which employs reference and sample cells arranged in a geometry similar to that of a Michelson interferometer. The radiant source was a pulsed wavelength-tunable dye laser possessing a relatively short coherence time. This paper includes descriptions of theoretical and experimental techniques applicable to the split-pulse laser method, and includes a tabulation of  $\alpha(\lambda)$  measured for deionized filtered water at  $26.4 \pm 1.7^\circ\text{C}$ .

b. Introduction

From a survey of the scientific literature<sup>1/</sup> on the complex refractive index  $N(\lambda) = n(\lambda) + ik(\lambda)$  of liquid water, and from a recent article by Kopelevich,<sup>2/</sup> we became increasingly aware of considerable variations in the values measured by various investigators<sup>3-12/</sup> for the attenuation coefficient  $\alpha(\lambda) = 4\pi k(\lambda)/\lambda$  of liquid water in the visible region where  $\alpha(\lambda)$  is the order of from  $10^{-3}$  to  $10^{-4}$ . Although such variations in  $\alpha(\lambda)$  are in part directly attributable to varying quantities of particulates and dissolved chemicals in water samples, different experimental methods and procedures can also introduce variations in measured values of  $\alpha(\lambda)$ . Some problems that arise in conventional absorption spectroscopy are the following: (1) incorrect determination of reflectance of cell windows by measuring reflectance losses for an empty cell and applying those measurements to a filled cell, (2) insufficient collimation of radiant flux from an extended source thus precluding the use of adequate length cells to provide attenuation of from 20 to 80% of the incident radiant flux, (3) insufficient collimation thus allowing radiant flux to be reflected from the side walls of long cells, (4) temporal variations in the brightness of the radiant source during single-beam long-path investigations where transmittance must be measured at different times through two or more cells of different length, and (5) additional signal from a photomultiplier detector due to stray light reaching the detector. Although these problems, if anticipated, can be overcome in conventional spectroscopy by proper experimental techniques they do constitute points of serious concern in the measurement of the attenuation

coefficients of transparent liquids.

The principal objective of this investigation was to develop an experimental method that overcame the five problems listed above. The problems were overcome in the following manner. A wavelength tunable dye laser was chosen as the radiant source thus assuring proper collimation of radiant flux and elimination of stray light. Reflectance at the end windows of the absorption cells was accounted for by choosing a split-beam experimental apparatus that was similar in geometry to a Michelson interferometer. Temporal variations in the brightness of the radiant source were considered by choosing a pulsed dye laser, rather than a CW dye laser, as the radiant source and applying repetitive single-pulse ratioing techniques by use of a dual channel boxcar integrator. Also, a pulsed dye laser with a relatively small coherence length was chosen thereby avoiding interference fringes in optical components of the experimental apparatus. The split-pulse laser method that we developed, based on the preceeding choices, for measuring  $\alpha(\lambda)$  of highly transparent liquids is presented in the following sections. The method is presented by describing its application to measuring  $\alpha(\lambda)$  for deionized filtered water.

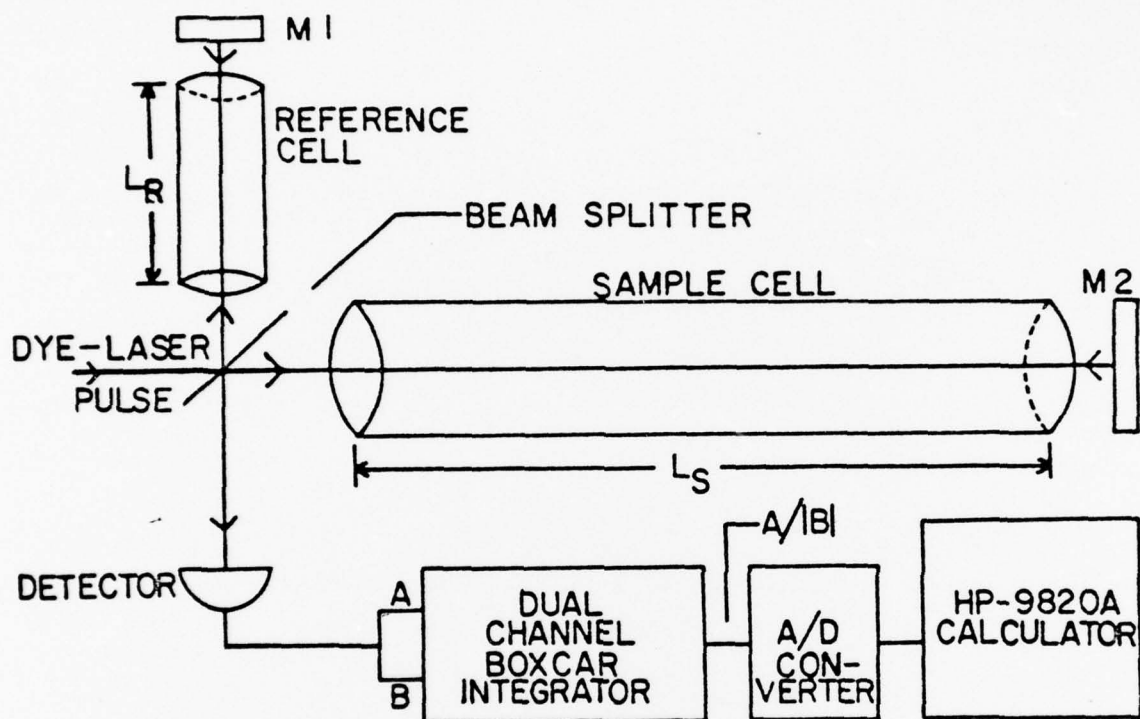


Figure 81

A block diagram of the instrumentation used to measure the attenuation coefficient  $\alpha(\lambda)$  of deionized filter water in the 418.6- to 640.3-nm region. Further details are provided in Section II.

### c. Experimental Methods

The radiant source for this experiment was a wavelength tunable dye laser<sup>13/</sup> which was optically pumped by an AVCO C950 pulsed nitrogen laser. Pulses from the dye laser were of about 10 nsec duration, were from 1 nm to 2 nm in spectral width, and had with a repetition rate of 50 pps. Radiant flux from the dye laser was passed through a limiting aperture and was then further collimated by a converging lens in order to retain the radiant flux well within the sample and reference cells described hereinafter. After passage through the convergent lens the beam of radiant flux encountered the beam splitter depicted in Fig. 81 where it was split into two beams. One beam, that reflected by the splitter, then passed through a reference cell of length  $L_r = 24.3$  cm, and the other beam, that transmitted by the splitter, passed through a sample cell of length  $L_s = 499.1$  cm. The reference and samples cells were both filled with purified deionized water which was previously passed through a 0.22  $\mu$ m Millipore filter to remove macroscopic particulates. The beam passing through the reference cell, and the beam passing through the sample cell, then encounter plane mirrors  $M_1$  and  $M_2$ , respectively, where they were reflected back through the respective cells to again encounter the beam splitter. After the second encounter with the beam splitter that portion of the reference-cell beam transmitted by the splitter, and that portion of the sample-cell beam reflected by the splitter, were incident on a single ITT FW114A photodiode detector. The cells were slightly misaligned relative to the direction of propagation of radiant flux so that radiant flux reflected from both surfaces of the cell windows was not incident on the detector.

Due to the difference in length of the two cells, the pulse of radiant flux passing through the sample cell lagged the pulse passing through the reference cell by about 40 nsec at the detector. The signal from the detector was applied to a Princeton Applied Research (PAR) model 162 dual channel boxcar integrator equipped with two PAR-164 integrator modules. Gate A of the integrator was adjusted to sense the signal associated with the pulse passing through the sample cell, and gate B was adjusted to sense the signal associated with the pulse passing through the reference cell. The gate widths were about 10 nsec. The integrator provided an output signal  $A(\lambda)/B(\lambda)$  to the input of a PAR-260 analog/digital converter, where  $A(\lambda)$  and  $B(\lambda)$  are proportional to the radiant intensity. The output from the PAR-260 was then applied to a Hewlett-Packard 9820 programmable calculator where data were printed on paper tape and were also stored on cassette magnetic tapes. The calculator was programmed to compute the attenuation coefficient

$$\alpha(\lambda) = \frac{1}{2(L_r - L_s)} \ln[A(\lambda)/B(\lambda)] \quad (1)$$

As explained in the following Section, Eq. (1) is deemed to be valid for analysis of data from this experiment.

Each cell was constructed from cylindrical pyrex tubing of 4.1 cm nominal inside diameter. End windows for all cells were cut from the same plate of pyrex glass so they would have the same transmission and reflection properties. The end windows were fused to the pyrex tubing by the glassblower thus avoiding the use of O-rings or any material other than glass. An inlet/outlet tube, also of pyrex glass, was fused to the side wall near each end of each cell. The cells were initially cleaned with chromic acid,

then with Alconox, and were then flushed many times with clean deionized filtered water. The entire cleaning procedure was applied twice to each cell. Care was taken to keep the outer surfaces of the windows clean and dust free.

Clean deionized filtered water was sealed inside the cells for about 180 days prior to serious attenuation measurements, thus allowing microscopic air and vapor bubbles to dissipate. The bubbles were initially observed in the path of the laser beam as profuse scattering centers.

Sullivan,<sup>5/</sup> who used a 60-cm long cell made from acrylic plastic and equipped with pyrex windows sealed with o-rings, noted that in 24 hours the fractional transmittance of freshly distilled water decreased from  $88.5\% \pm 1\%$  to 80% or less at a wavelength of 470 nm. Because Sullivan attributed the decrease in fractional transmittance to the deterioration of the optical purity of distilled water, we were concerned about possible leaching of the pyrex cells by deionized water. However, no systematic increase or decrease in the fractional transmittance of the deionized water was observed throughout the 413.6- to 640.3-nm region during the four months when we were making several measurements of the spectral attenuation. If leaching did occur, then it reached equilibrium during the initial 180 days that the deionized water was sealed in the pyrex cells, or the leached borosilicates did not affect the absorption measurements.

Three types of beam splitters were tried before a satisfactory one was obtained. The first was a thin pellicle with a partially reflecting coating on one surface. The pellicle was unsatisfactory because its thickness was less than the coherence length of the laser pulse, and interference fringes were observed as the laser was scanned through the region of wavelength tunability. The second was a mirror type (Edmund Sci. #578) beam

splitter with a partially reflecting coating on one side of a 5-mm thick glass flat. The second beam splitter was unsatisfactory because the sample-cell and reference-cell laser beams were not subject to exactly the same net optical treatment after interacting twice each with the beam splitter. A 6-mm thick glass optical flat proved to be a very satisfactory beam splitter. Additionally, mirrors  $M_1$  and  $M_2$  were interchanged several times and the measured attenuation remained the same each time.

The temperature of the water was maintained at  $26.4 \pm 1.7^\circ\text{C}$ .

#### d. Theoretical Background

The macroscopic form of Maxwell's equations and the corresponding constitutive relations, in cgs gaussian units, applied to an infinite, homogeneous, linear, isotropic, magnetic, conducting medium which is free of net electric charge provides the wave equations

$$(\nabla^2 - \frac{4\pi\mu\sigma}{c^2} \frac{\partial}{\partial t} - \frac{\mu\epsilon}{c^2} \frac{\partial^2}{\partial t^2})\psi = 0, \quad (2)$$

where  $\psi$  is any one of the components of the electric field intensity  $\vec{E}$  or the magnetic field intensity  $\vec{H}$ ,  $c$  is the speed of electromagnetic waves in vacuum,  $\mu$  is the relative magnetic permeability,  $\epsilon$  is the dielectric function which originates from the physical behavior of bound charge,  $\sigma$  is the electrical conductivity which is attributed to free charge carriers responding to the incident electromagnetic wave, and  $\omega = 2\pi c/\lambda$  is the angular frequency. Equation (2) has a plane monochromatic wave solution

$$\vec{E} = \vec{E}_0 e^{i(\vec{\kappa} \cdot \vec{r} - \omega t)}, \quad (3)$$

$$\vec{H} = c(\vec{\kappa} \times \vec{E})/\mu\omega, \quad (4)$$

$$\kappa = \frac{\mu\epsilon\omega^2}{c^2} + i 4\pi\frac{\mu\sigma\omega}{c^2}, \quad (5)$$

$$\left. \begin{matrix} \kappa_r \\ \kappa_i \end{matrix} \right\} = \left\{ \frac{\pm\gamma + \sqrt{\gamma^2 + \delta^2}}{2} \right\}^{1/2} \quad (6)$$

$$\gamma = [\omega^2(\mu_r\epsilon_r - \mu_i\epsilon_i) - 4\pi\omega(\mu_i\sigma_r + \mu_r\sigma_i)]/c^2, \quad (7)$$

$$\delta = [\omega^2(\mu_i\epsilon_r + \mu_r\epsilon_i) + 4\pi\omega(\mu_r\sigma_r - \mu_i\sigma_i)]/c^2, \quad (8)$$

where subscripts  $r$  and  $i$  denote real and imaginary parts, respectively. The

complex refractive index  $N = n + ik$  of the material medium is defined as the ratio of  $c$ , the speed of electromagnetic waves in vacuum where  $\epsilon = 1$ ,  $\mu = 1$ , and  $\sigma = 0$  for all  $\omega$ , to the phase velocity  $v_p = \omega/\kappa$  of the electromagnetic wave in the material medium:

$$n + ik = c(\kappa_r + i\kappa_i)/\omega \quad (9)$$

For simplicity we have dropped the functional notation. The absorption of electromagnetic flux moving in the  $+z$ -direction from  $z_0$  to  $z$  is

$$I = I_0 e^{-\alpha_a(z-z_0)}, \quad (10)$$

where  $\alpha_a = 2\kappa_i$ , and  $I$  and  $I_0$  are radiant intensities at  $z$  and  $z_0$ , respectively. The parameter  $\alpha_a$  in Eq. (10) represents a true absorption coefficient corresponding to the electromagnetic properties  $\mu$ ,  $\epsilon$ , and  $\sigma$  of the material responding to the incident electromagnetic wave. In the visible region of the electromagnetic spectrum we assume for liquid water that  $\mu = 1$ ,  $\sigma = 0$ ,  $\epsilon_i \ll \epsilon_r$ , and  $\epsilon_r = n^2$  so that; by use of Eqs. (5), (7), and (8);

$$\kappa^2 = (\omega^2 + i2b\omega)/a, \quad (11)$$

where

$$a^2 = c^2/\epsilon_r, \text{ and} \quad (12)$$

$$b = (\omega\epsilon_i)/(2\epsilon_r). \quad (13)$$

In practical situations, especially in investigations of liquid water, the incident electromagnetic radiation is absorbed and is also scattered. The measured attenuation of electromagnetic radiation by water, therefore, is described by

$$I = I_0 e^{-(\alpha_a + \alpha_s)(z-z_0)}, \quad (14)$$

where  $\alpha_a$  is the absorption coefficient of Eq. (10), and  $\alpha_s$  is the attenuation coefficient due to scattering. The scattering coefficient  $\alpha_s$  is comprised of the sum of two contributions:

$$\alpha_s = \alpha_{ps} + \alpha_{ms}, \quad (15)$$

where  $\alpha_{ps}$  is an attenuation coefficient due to scattering by microscopic particles, and  $\alpha_{ms}$  is an attenuation coefficient due to molecular scattering, i.e., Rayleigh scattering due to local thermal fluctuations in the molecular density.

The attenuation coefficient  $\alpha(\omega)_{ms}$  for electromagnetic radiation of angular frequency  $\omega$  may be calculated by use of the Einstein-Smoluchowski equation

$$\alpha(\omega)_{ms} = \frac{k'T\beta}{6\pi} \left( \frac{\omega}{c} \right)^4 \left| \frac{[\epsilon(\omega)-1][\epsilon(\omega)+2]}{3} \right|^2, \quad (16)$$

where  $k'$  is the Boltzmann constant,  $T$  is the absolute temperature, and  $\beta = 4.508 \times 10^{-11} \text{ cm}^2/\text{dyne}$  is the isothermal compressibility of water at  $26.4^\circ\text{C}$ . In the visible region where  $\epsilon(\omega) = n(\omega)^2$  for water we have

$$\alpha(\omega)_{ms} = \frac{k'T\beta}{54\pi} \left( \frac{\omega}{c} \right)^4 \{[n(\omega)^2-1][n(\omega)^2+2]\}^2. \quad (17)$$

Values of  $n(\omega)$  for water are readily interpolated from those given in Ref. (1).

In the present investigation we measure, by use of Eq. (14) the total attenuation coefficient  $\alpha = \alpha_a + \alpha_s$  of liquid water for electromagnetic radiation from a pulsed dye laser. Pulses from the dye laser are about 10 nsec duration and of spectral width  $\Delta\omega = 8 \times 10^{12} \text{ sec}^{-1}$  at  $\omega = 2.73 \times 10^{15} \text{ sec}^{-1}$  (640nm), and  $\Delta\omega = 1.7 \times 10^{12} \text{ sec}^{-1}$  at  $\omega = 4.5 \times 10^{15} \text{ sec}^{-1}$  (418nm). The coherence time for the laser radiation is  $\tau_0 = 2\pi/\Delta\omega$ . As such pulses of electromagnetic radiation propagate through the water they are attenuated and the shape of the pulses may also be distorted. We now examine the possible distortion. The pulses are regarded as quasimonochromatic radiation in that mathematically they are a Fourier superposition of a finite but continuous

spectral distribution of plane electromagnetic waves. Stratton<sup>14</sup> has provided the mathematical rigor for examining the behavior of such pulses; to wit

$$\begin{aligned}\psi(z,t) = & \frac{1}{2} e^{bz/a} f(t+z/a) + \frac{1}{2} e^{-bz/a} f(t-z/a) \\ & + \frac{a}{2} e^{-bt} \int_{t-z/a}^{t+z/a} f(\beta) e^{b\beta} J_0 \left[ (b/a) \sqrt{z^2 - a^2(t-\beta)^2} \right] d\beta \\ & + \frac{a}{2} e^{-bt} \int_{t-z/a}^{t+z/a} F(\beta) e^{b\beta} J_0' \left[ (b/a) \sqrt{z^2 - a^2(t-\beta)^2} \right] d\beta, \quad (18)\end{aligned}$$

where  $\psi(z,t)$  is a cartesian component of  $\vec{E}$  or  $\vec{H}$ ,  $z$  is the distance measured from  $z=0$  along the axis of propagation,  $J_0[(b/a)\sqrt{z^2 - a^2(t-\beta)^2}]$  is the zero-order Bessel function and its argument,  $J_0'$  is the partial derivative of  $J_0$  with respect to  $z$ ,  $f(t) = \psi(0,t)$ ,  $F(t) = (\partial\psi/\partial z)_{z=0}$ , and  $b$  and  $a$  are defined by Eqs. (13) and (12), respectively. We assume a simple model for quasi-monochromatic radiation of the form

$$\vec{E} = \vec{E}_0 e^{i(\vec{k} \cdot \vec{r} - \omega t + \phi(t))}, \quad (19)$$

where  $\phi(t)$  is a random step function of period  $\tau_0$  the coherence time, and of range  $0 \leq \phi(t) \leq 2\pi$ . Equation (19) represents a sequence of finite waves, each with wave vector  $\vec{k}$ , coherence time  $\tau_0 = 2\pi/\Delta\omega$ , but with randomly differing phases  $\phi(t)$ . Next, we consider one of the finite waves in the sequence indicated by Eq. (19). We represent a component of  $\vec{E}$  or  $\vec{H}$  by a wave moving in the  $+z$ -direction as

$$\psi(z,t) = A(e^{ikz} + e^{-ikz})e^{-i\omega t} \quad (20)$$

for  $|t| \leq \tau_0/2$ , and

$$\psi(z,t) = 0 \quad (21)$$

for  $|t| > \tau_0/2$ . We thus find that Eq. (18) becomes

$$\begin{aligned} \psi(z,t) = A(e^{[bz/a - i\omega(t+z/a)]} + e^{[-bz/a - i\omega(t-z/a)]}) \\ + aAe^{-bt} \int_{t-z/a}^{t+z/a} e^{(b-i\omega)\beta} J_0 \left[ (b/a) \sqrt{z^2 - a^2(t-\beta)^2} \right] d\beta, \end{aligned} \quad (22)$$

where the pulse moving in the  $+z$ -direction is the one of interest for our application. The integral in Eq. (22) represents the distortion of the pulse in time  $t$  at position  $z$ . By use of data from Ref. (1) we note that

$$2 \times 10^{10} \text{ cm/sec} < a < 3 \times 10^{10} \text{ cm/sec}, \quad (23)$$

$$2b/a = \alpha_a < 4 \times 10^{-3} \text{ cm}^{-1}. \quad (24)$$

In the present investigation the pulse propagates a maximum distance of 10m in the water, but by conservatively using  $z = 20$  m, we find the value of the integral in Eq. (22) to be on the order of  $A \times 10^{-6}$ . However, the amplitude  $A$  of the pulse propagating 20 m in water is attenuated to only something on the order of  $A \times 10^{-2}$ . Thus, for the present investigation, any distortion of the pulse by the water is at least four orders of magnitude less than the attenuation, and we can quite accurately represent the pulse moving in the  $+z$ -direction by

$$\psi(z,t)_+ = \begin{cases} A e^{-bz/a} e^{i\omega(t-z/a)}, & |t| \leq \tau_0/2 \\ 0, & |t| > \tau_0/2 \end{cases} \quad (25)$$

The attenuation of radiation described by Eq. (25) is

$$I = I_0 e^{-2bz/a} \quad (26)$$

The absorption coefficient for water, therefore, is  $\alpha_a = 2b/a$ , and  $2b/a = 2\kappa_1$  provided  $\mu = 1$ ,  $\sigma = 0$ , and  $\epsilon(\omega)_i \ll \epsilon(\omega)_r$  as was previously assumed for water in the visible region.

As a final point, we note that when quasimonochromatic radiation is incident on two boundary surfaces between three electromagnetically dissimilar media (e.g. air/glass/water) multiple reflections at the boundaries of the intermediate material can provide constructive and destructive interference of the electromagnetic radiation. No interference is observed, however, when the coherence time  $\tau_0$  is less than the time required for the radiation to traverse two thicknesses of the intermediate material.<sup>15/</sup> The smallest separation of two such boundaries in the present investigation was 3.17 mm, the thickness of the pyrex windows at the end of the cells containing the water. The minimum time for radiation to propagate through a single thickness of a glass window was about  $10\tau_0$ . Interference effects, therefore, were not observed during this experiment.

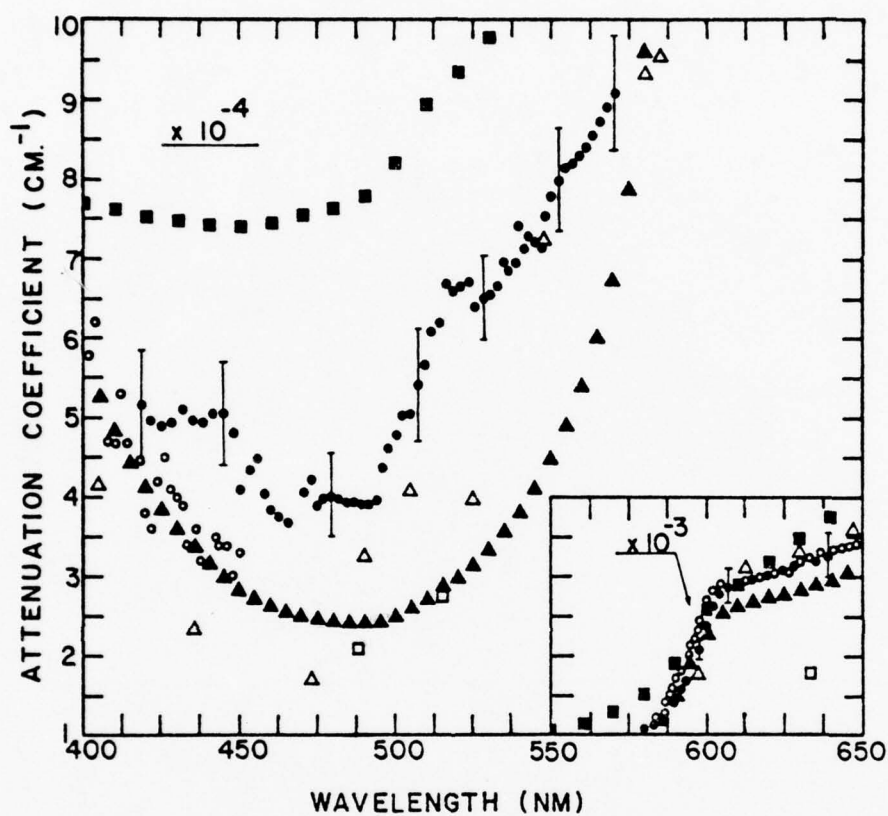


Figure 82. A graphical comparison of  $\alpha(\lambda)$  (solid circles) from the present investigation with  $\alpha(\lambda)$  and  $\alpha(\lambda)_a$  obtained by previous investigators. Further details are provided in Section IV.

TABLE XVIII. Wavelength  $\lambda$ , attenuation coefficients  $\alpha(\lambda)$ , Rayleigh scattering coefficients  $\alpha(\lambda)_{\text{ms}}$ , the sum of the absorption coefficient  $\alpha(\lambda)$  and the particle scattering coefficient  $\alpha(\lambda)_{\text{ps}}$ , and wavenumber  $\lambda^{-1}$  for deionized filtered water.

$\lambda$ nm	$\alpha(\lambda)$ $\text{cm}^{-1}$	$\alpha(\lambda)_{\text{s}}$ $\text{cm}^{-1}$	$\alpha(\lambda)_{\text{a}} + \alpha(\lambda)_{\text{ps}}$ $\text{cm}^{-1}$	$\lambda^{-1}$ $\text{cm}^{-1}$
418.6	$5.161 \times 10^{-4}$	$5.015 \times 10^{-5}$	$4.659 \times 10^{-4}$	23889.2
421.9	4.960	4.855	4.475	23702.3
425.2	4.890	4.701	4.420	23518.3
428.4	4.944	4.557	4.488	23342.7
431.7	5.088	4.415	4.647	23164.2
434.9	4.975	4.282	4.547	22993.8
438.2	4.937	4.150	4.522	22820.6
441.5	5.040	4.022	4.638	22650.1
444.7	5.046	3.904	4.656	22487.1
448.0	4.811	3.786	4.432	22321.4
450.4	4.108	3.703	3.738	22202.5
453.5	4.353	3.599	3.993	22050.7
455.9	4.473	3.521	4.121	21934.6
458.3	4.045	3.445	3.700	21819.8
460.6	3.840	3.374	3.503	21710.8
463.0	3.753	3.302	3.423	21598.3
465.4	3.692	3.232	3.369	21486.9
468.3	4.076	3.150	3.761	21353.8
470.7	4.061	3.084	3.753	21245.0
473.0	4.220	3.022	3.918	21141.6
475.0	3.889	2.969	3.592	21052.6
477.3	3.997	2.910	3.706	20951.2
479.6	4.008	2.853	3.723	20850.7
481.8	3.981	2.799	3.701	20755.5
484.2	3.933	2.742	3.659	20652.6

TABLE XVII II, Continued

195

486.6	3.935	2.686	3.666	20550.8
489.0	3.919	2.632	3.656	20449.9
491.4	3.933	2.578	3.675	20350.0
493.8	3.985	2.527	3.732	20251.1
495.7	4.374	2.487	4.125	20173.5
497.9	4.618	2.441	4.374	20084.4
500.3	4.754	2.393	4.515	19988.0
502.5	5.031	2.349	4.796	19900.5
504.8	5.046	2.305	4.815	19809.8
507.2	5.412	2.260	5.186	19716.1
509.5	5.662	2.218	5.440	19627.1
511.8	6.084	2.177	5.866	19538.9
514.2	6.198	2.135	5.985	19447.7
516.6	6.699	2.093	6.490	19357.3
518.9	6.631	2.055	6.425	19271.5
521.2	6.662	2.017	6.460	19186.5
523.6	6.722	1.979	6.524	19098.5
525.9	6.408	1.943	6.214	19015.0
528.2	6.507	1.908	6.316	18932.2
530.4	6.553	1.875	6.365	18853.7
532.8	6.650	1.840	6.466	18768.8
535.0	6.943	1.809	6.762	18691.6
536.6	6.851	1.787	6.672	18635.9
538.2	6.942	1.764	6.766	18580.5
539.7	7.413	1.744	7.239	18528.8
541.2	7.134	1.724	6.962	18477.5
542.8	7.278	1.703	7.108	18423.0
544.3	7.255	1.683	7.087	18372.2

TABLE XVIII. Continued

545.8	7.179	1.664	7.013	18321.7
547.8	7.539	1.639	7.375	18254.8
550.1	7.783	1.610	7.622	18178.5
552.4	7.994	1.584	7.836	18102.8
554.5	8.135	1.560	7.979	18034.3
556.8	8.226	1.534	8.073	17959.8
559.0	8.314	1.510	8.163	17889.1
561.2	8.425	1.487	8.276	17819.0
563.4	8.572	1.464	8.426	17749.4
565.6	8.748	1.441	8.604	17680.3
567.7	8.930	1.420	8.788	17614.9
570.0	9.092	1.397	8.925	17543.9
580.3	$1.085 \times 10^{-3}$	1.298	$1.072 \times 10^{-3}$	17232.5
582.5	1.139	1.278	1.126	17167.4
584.6	1.222	1.259	1.209	17105.7
586.8	1.323	1.239	1.311	17041.6
588.9	1.434	1.220	1.422	16980.8
591.0	1.562	1.202	1.550	16920.5
593.2	1.698	1.184	1.686	16857.7
595.4	1.864	1.166	1.852	16795.4
597.5	2.085	1.148	2.074	16736.4
599.7	2.372	1.131	2.361	16675.0
601.9	2.639	1.114	2.628	16614.1
604.0	2.798	1.099	2.787	16556.3
606.2	2.865	1.083	2.854	16496.2
609.1	2.913	1.063	2.902	16417.7
611.2	2.939	1.048	2.929	16361.3
613.3	2.959	1.034	2.949	16305.2
615.5	2.985	1.019	2.975	16247.0

TABLE XVIII. Continued

617.6	3.010	1.005	3.000	16191.7
619.7	3.028	$9.917 \times 10^{-6}$	3.018	16136.8
621.8	3.051	9.784	3.041	16082.3
623.9	3.077	9.652	3.067	16028.2
626.1	3.111	9.514	3.101	15971.9
628.2	3.139	9.381	3.130	15918.5
630.3	3.163	9.250	3.154	15865.5
632.4	3.200	9.121	3.191	15812.8
634.5	3.224	8.995	3.215	15760.4
636.7	3.263	8.865	3.254	15706.0
638.9	3.283	8.737	3.274	15651.9
640.3	3.311	8.657	3.302	15617.7

### e. Experimental Results

The HP9820 calculator was programmed to compute attenuation coefficients  $\alpha(\lambda) = \alpha(\lambda)_a + \alpha(\lambda)_{ps} + \alpha(\lambda)_{ms}$  by use of Eq. (1). Five independent measurements of  $A(\lambda)/B(\lambda)$  were made at each of several wavelength positions from which five values for  $\alpha(\lambda)$  were obtained. Values of  $\alpha(\lambda)$  presented in the second column of Table XVIII are averages of the five independent measurements. The experimental error, expressed as percentages of  $\alpha(\lambda)$ , were  $\pm 13\%$  in the wavelength region from 418.6 to 509.5 nm, and  $\pm 8\%$  in the wavelength region from 511.8 to 640.3 nm. Scattering coefficients  $\alpha(\lambda)_{ms}$  due to thermal density fluctuations were computed by use of Eq. (17). Values thus obtained for  $\alpha(\lambda)_{ms}$  appear in the third column of Table XVIII. Values for the coefficient  $\alpha(\lambda)_a + \alpha(\lambda)_{ps}$  appear in the fourth column of Table XVIII. Wavelength  $\lambda$  and wave number  $\lambda^{-1}$  appear in the first and fifth columns of Table XVIII, respectively.

The attenuation coefficients  $\alpha(\lambda)$  measured during the present investigation are designated by solid circles in Fig. 2, where they are graphically compared with values of  $\alpha(\lambda)$  and  $\alpha(\lambda)_a$  obtained by previous investigators. The open circles in Fig. 2 represent  $\alpha(\lambda)$  of distilled water measured by Sullivan.<sup>5/</sup> The open triangles represent  $\alpha(\lambda)$  for sea water which were obtained from absorption spectra measured by Clark and James.<sup>9/</sup> The solid squares designate  $\alpha(\lambda)$  computed for clear lake and clear ocean water by Tyler et al.<sup>10/</sup> The solid triangles designate  $\alpha(\lambda) = 4\pi k(\lambda)/\lambda$  computed from  $k(\lambda)$  chosen by Hale and Querry<sup>1/</sup> for distilled water at 25°C.

And, the open squares designate data obtained for deionized filtered water by Hass and Davisson<sup>16/</sup> who used adiabatic laser calorimetry to measure only  $\alpha(\lambda)_a$ .

In the spectral region from 418.6 to 580 nm,  $\alpha(\lambda)$  from the present investigation are intermediate to those previously computed for clear natural water<sup>10/</sup> and distilled water.<sup>1,5/</sup> This is due to scattering by microscopic particles which are generally more abundant in natural water than in deionized filtered water, and are more abundant in deionized filtered water than in distilled water. In the spectral region from 582 to 610 nm  $\alpha(\lambda)$  from the present investigation are slightly less than  $\alpha(\lambda)$  obtained by Sullivan for distilled water, and are less than  $\alpha(\lambda)$  computed by Tyler et al. for clear natural water. In the spectral region from 610 to 640.3 nm  $\alpha(\lambda)$  from the present investigation agree very well with  $\alpha(\lambda)$  obtained by Sullivan for distilled water, are about 11 percent greater than  $\alpha(\lambda)$  from Hale and Querry, and are less than  $\alpha(\lambda)$  computed for clear natural water.

Therefore, the split-pulse laser method described in this paper provides a convenient means for measuring the attenuation coefficients of highly transparent liquids.

## f. References for Section V.D.1.

1. G. M. Hale and M. R. Querry, Appl. Opt. 12, 555 (1973).
2. O. V. Kopelivich, Opt. Spectrosc. 41, 391 (1977).
3. N. G. Jerlov, Optical Oceanography, (Elsevier, Amsterdam, 1968), pp. 47-62.
4. R. M. Goody, Atmospheric Radiation 1: Theoretical Basis, (Oxford Univ. Press, London, 1964), pp 415-416.
5. S. A. Sullivan, J. Opt. Soc. Am. 53, 962 (1963).
6. J. Lenoble and B. Saint-Guilly, Compt. Rend. 240, 954 (1955).
7. K. Kondratyev, Radiation in the Atmosphere, Vol. 12, Internat. Geophys. Series (Academic Press, New York, 1969), pp. 107-123.
8. J. A. Curcio and C. C. Petty, J. Opt. Soc. Am. 41, 302 (1951).
9. G. L. Clark and H. R. James, J. Opt. Soc. Am. 29, 43 (1939).
10. J. E. Tyler, R. C. Smith, and W. H. Wilson, J. Opt. Soc. Am. 62, 83 (1972).
11. N. P. Grudinkina, Opt. Spectrosc. 1, 658 (1956).
12. H. R. James and E. A. Birge, Trans. Wisc. Acad. Sci. 31, 1 (1938).
13. M. R. Querry, Contribution as Chap. 5-2, Tunable Laser Spectroscopy, Methods of Experimental Physics, Spectroscopy, Vol. 13, Part B, ed. Dudley Williams, (Academic Press, New York, 1976) pp. 309-311.
14. J. A. Stratton, Electromagnetic Theory, (McGraw-Hill, New York, 1941), pp. 297-309.

15. P. G. Cary, M. S. Thesis, Univ. of Mo.-Kansas City (1976).
16. M. Hass and J. W. Davisson, J. Opt. Soc. Am. 67, 622 (1977).

## 2. Optical Properties of Crystalline Graphite ( $E_{1C}$ ).

### a. Introduction

A search of the scientific literature on the optical properties of carbon in any spectral region provided experimental data from which the imaginary part of  $N(\xi) = n(\xi) + ik(\xi)$  could be determined in the  $10^{-3}\text{ev} \leq \xi \leq 10^6\text{ev}$  spectral region. By use of high and low energy approximations the  $k(\xi)$  spectrum thus obtained was defined piecewise analytically over the entire electromagnetic spectrum. Compton scattering and pair production were ignored in the high energy approximations. Kramers-Kronig analysis of the  $k(\xi)$  spectrum provided values for  $n(\xi)$ , which along with knowledge of  $k(\xi)$  were used to compute the reflectance spectrum, the relative dielectric function, and the energy loss function. The evaluation of five different sum rules showed the data to be of high quality.

Graphite is an optically uniaxial material. In the infrared spectral region, therefore, two  $k(\xi)$  spectra are required to completely specify the optical constants. The search of the scientific literature, however, provided a  $k(\xi)$  spectrum only for the electric vector of the electromagnetic wave linearly polarized perpendicular to the c-axis of the graphite crystal. The results here are only for the case  $E_{1C}$ . In the energy region above  $\xi = 1\text{ ev}$  this constraint of  $E_{1C}$  is not pertinent.

These investigations of graphite are based on a M.S. Thesis (UMKC, 1979) by Mr. Roy Holt.

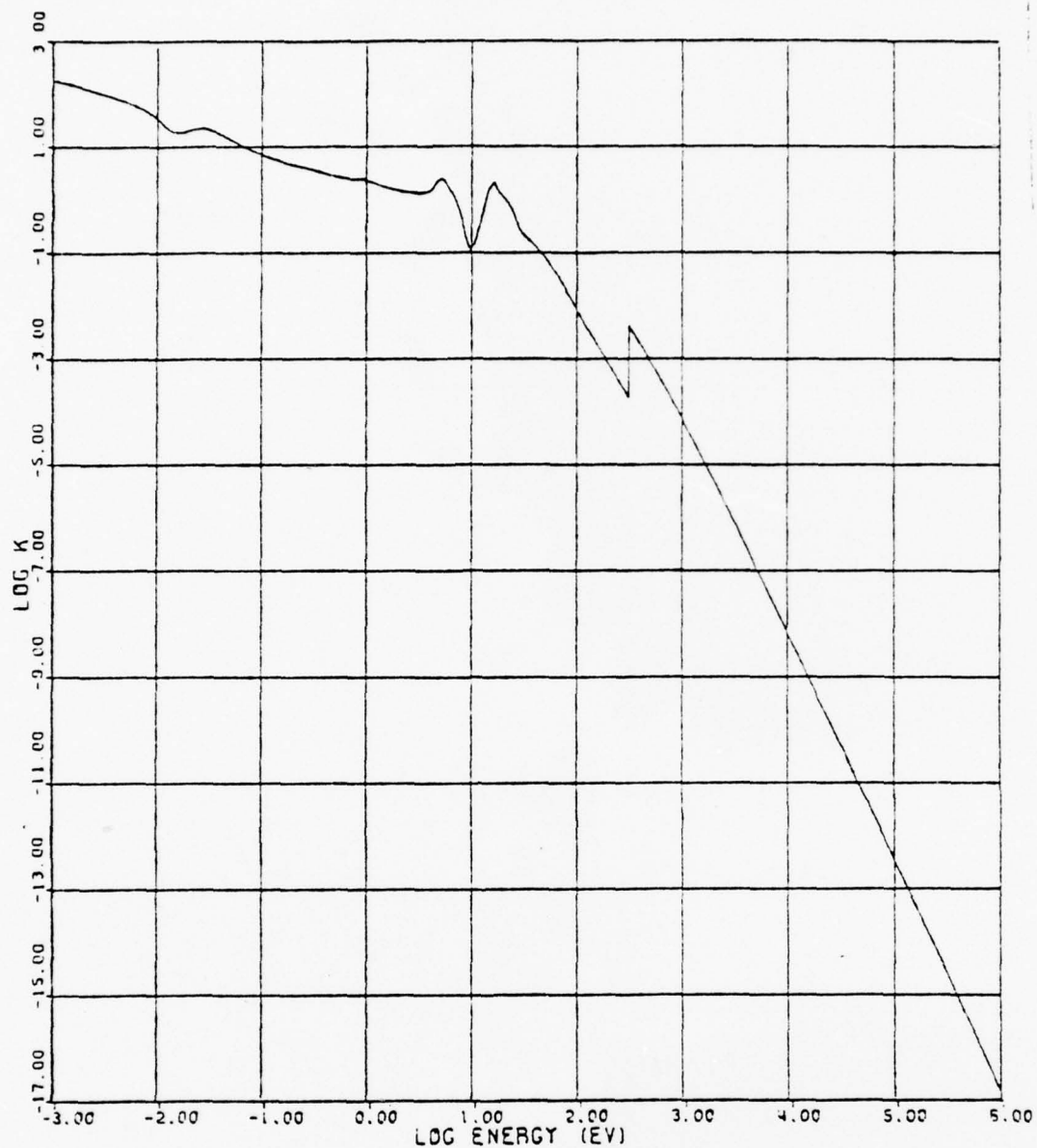


Figure 83. A graphical presentation of  $\log [k(\xi)]$  vs.  $\log(\xi)$  in the  $10^{-3} - 10^{+6}$  ev spectral region. Values for  $k(\xi)$  were compiled from the scientific literature.

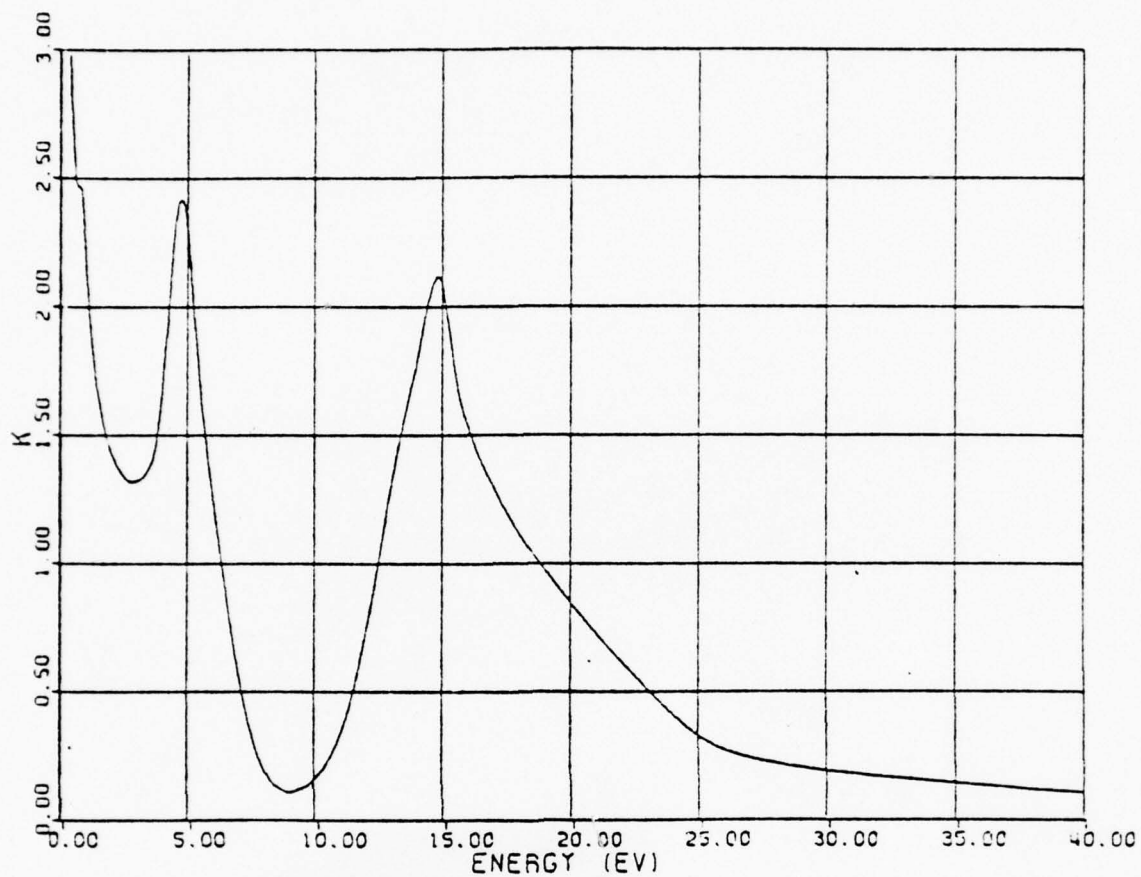


Figure 84. A graphical presentation of  $k(\xi)$  vs.  $\xi$  in the  $10^{-3}$ -40 ev spectral region. Values of  $k(\xi)$  were compiled from the scientific literature.

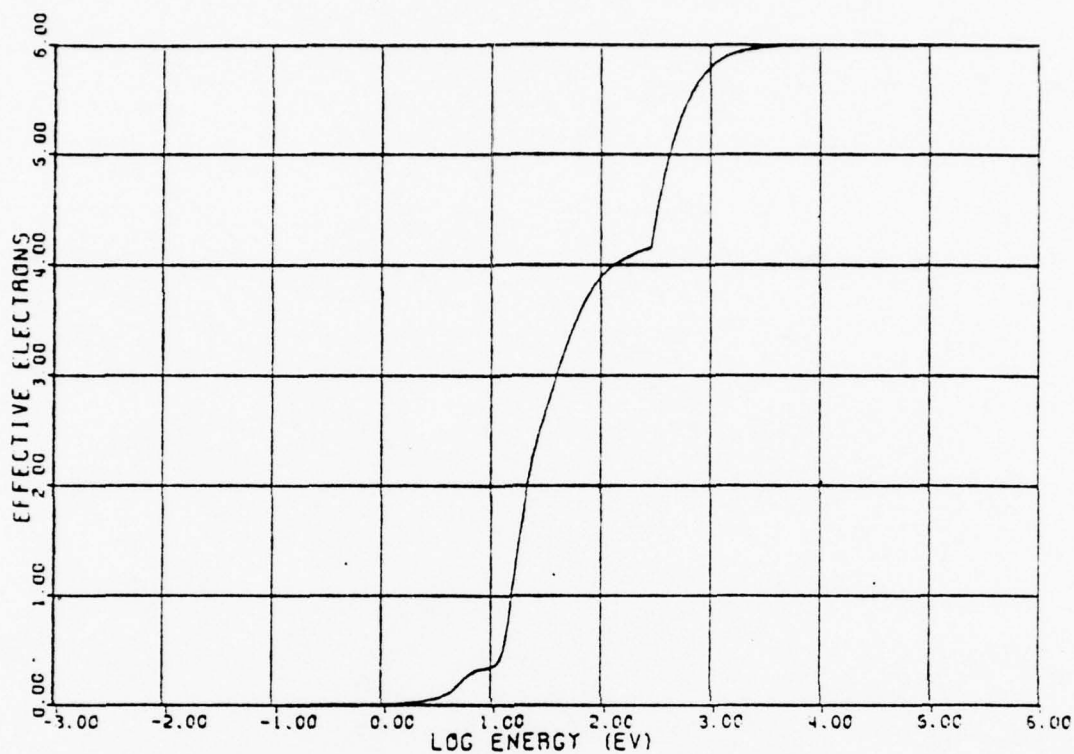


Figure 85. A graphical presentation of  $Z(\xi_0)$  vs.  $\log(\xi_0)$   
for the electron sum rule

$$Z(\xi_0) = \frac{m}{n^2 \pi^2 \epsilon_0^2} \int_{0.001 \text{ ev}}^{\xi_0} \xi k(\xi) d\xi.$$

b. Spectra for Graphite

The  $k(\xi)$  spectrum for graphite obtained from about 30 papers in the scientific literature is presented in Fig. 83., where the base 10 logarithm of  $k(\xi)$  vs.  $\xi$  is plotted. For purposes of comparison with other data the conversion  $\lambda(\mu\text{m}) = (1.24 \text{ m eV}/\xi(\text{eV}))$  may be helpful to the reader. There is some structure in the far infrared region ( $10^{-1}$ - $10^{-2}$  eV), valence and conduction electronic bands near 5 eV and 15 eV, and the x-ray k-absorption edge in the  $10^{+2}$ - $10^{+3}$  region. The  $k(\xi)$  spectrum in the  $10^{-3}$ -40 eV range is presented in Fig. 84, where the electronic bands are very vivid at ca. 5 eV and 10 eV.

One sum rule evaluated to test the quality of the  $k(\xi)$  spectrum was

$$Z(\xi_0) = \frac{m}{\hbar^2 \pi^2 n e^2} \int_{0.001 \text{ eV}}^{\xi_0} \xi k(\xi) d\xi ,$$

where  $Z(\xi_0)$  is the effective number of electrons/atom contributing to the  $k(\xi)$  spectrum in the region 0.001 eV to  $\xi_0$ ,  $m$  is the electron rest mass,  $\hbar$  is Planck's constant divided by  $2\pi$ ,  $n$  is the number of atoms per unit volume, and  $e$  is the charge of the electron. In the limit as  $\xi_0 \rightarrow \infty$ , for graphite  $Z(\xi_0 \rightarrow \infty) = 6$  the number of electrons/carbon atom. A spectrum depicting the evaluation of the  $Z(\xi_0)$  sum rule for the  $k(\xi)$  spectrum of graphite is shown in Fig. 85, where  $Z(\xi_0)$  vs.  $\log(\xi_0)$  is plotted. Note that in the region between  $10^2$  eV and  $10^3$  eV the  $Z(\xi_0)$  reaches a value of 6 and then remains constant for about 2.5 orders of magnitude in  $\xi_0$ . This sum rule, together with the evaluation of four other different sum rules, gave us considerable confidence

in the  $k(\xi)$  spectrum,

A Kramers-Kronig analysis of the  $k(\xi)$  spectrum provided  $n(\xi)$  for graphite. A plot of  $\log[n(\xi)]$  vs.  $\log(\xi)$  in the energy range from  $10^{-3}$  ev to  $10^6$  ev is presented in Fig. 86. And,  $n(\xi)$  vs.  $\xi$  in the energy range from  $10^{-3}$  ev to 40 ev is presented in Fig. 87. The normal incidence reflectance spectrum  $R(\xi)$  was computed by use of the Fresnel equations and the knowledge of  $k(\xi)$  and  $n(\xi)$ . The spectrum  $R(\xi)$  vs.  $\xi$  in the energy range from  $10^{-3}$  ev to 40 ev is presented in Fig. 88.

The reader is referred to Mr. Holt's M.S. Thesis for a more detailed discussion of the physics associated with this investigation.

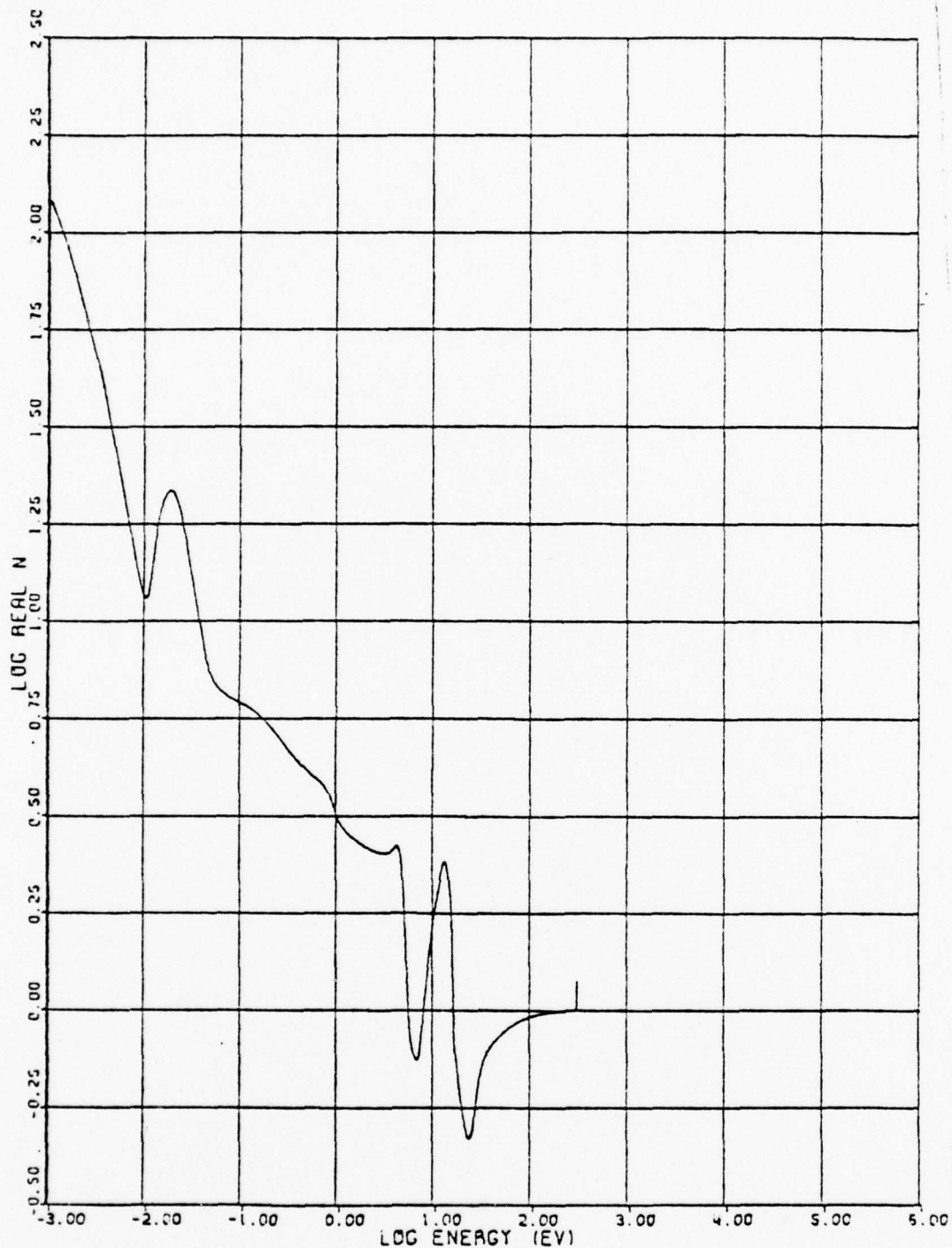


Figure 86. A graphical presentation of  $\log[n(\xi)]$  vs.  $\xi$  in the  $10^{-3}$ - $10^6$  ev spectral region.  $n(\xi)$  is the real part of the complex refractive index:  $N(\xi) = n(\xi) + ik(\xi)$ . The blip on the curve in the  $10^2$ - $10^3$  ev region is real, and is the contribution from the K-edged absorption in carbon.

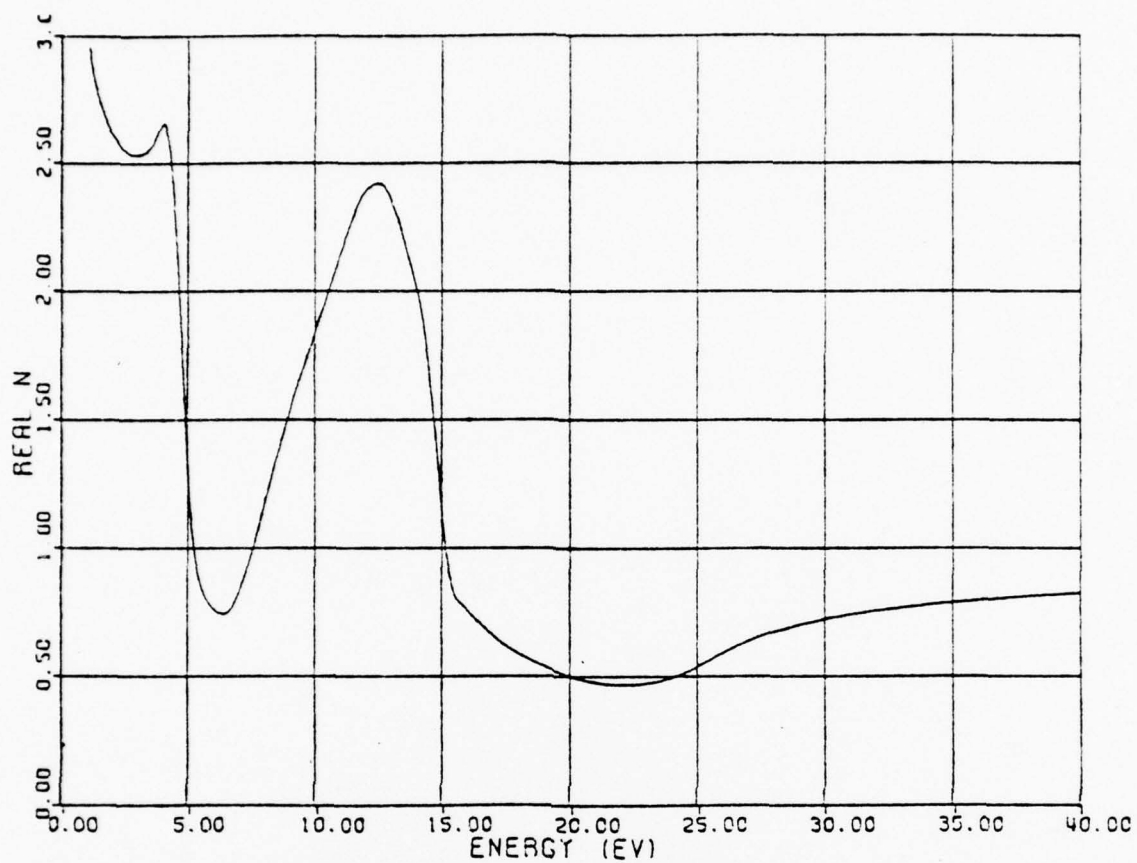


Figure 87. A graphical presentation of  $n(\xi)$  vs.  $\xi$  in the  $10^{-3}$ -40 eV spectral region.  $n(\xi)$  is the real part of the complex refractive index  $N(\xi) = n(\xi) + ik(\xi)$ .

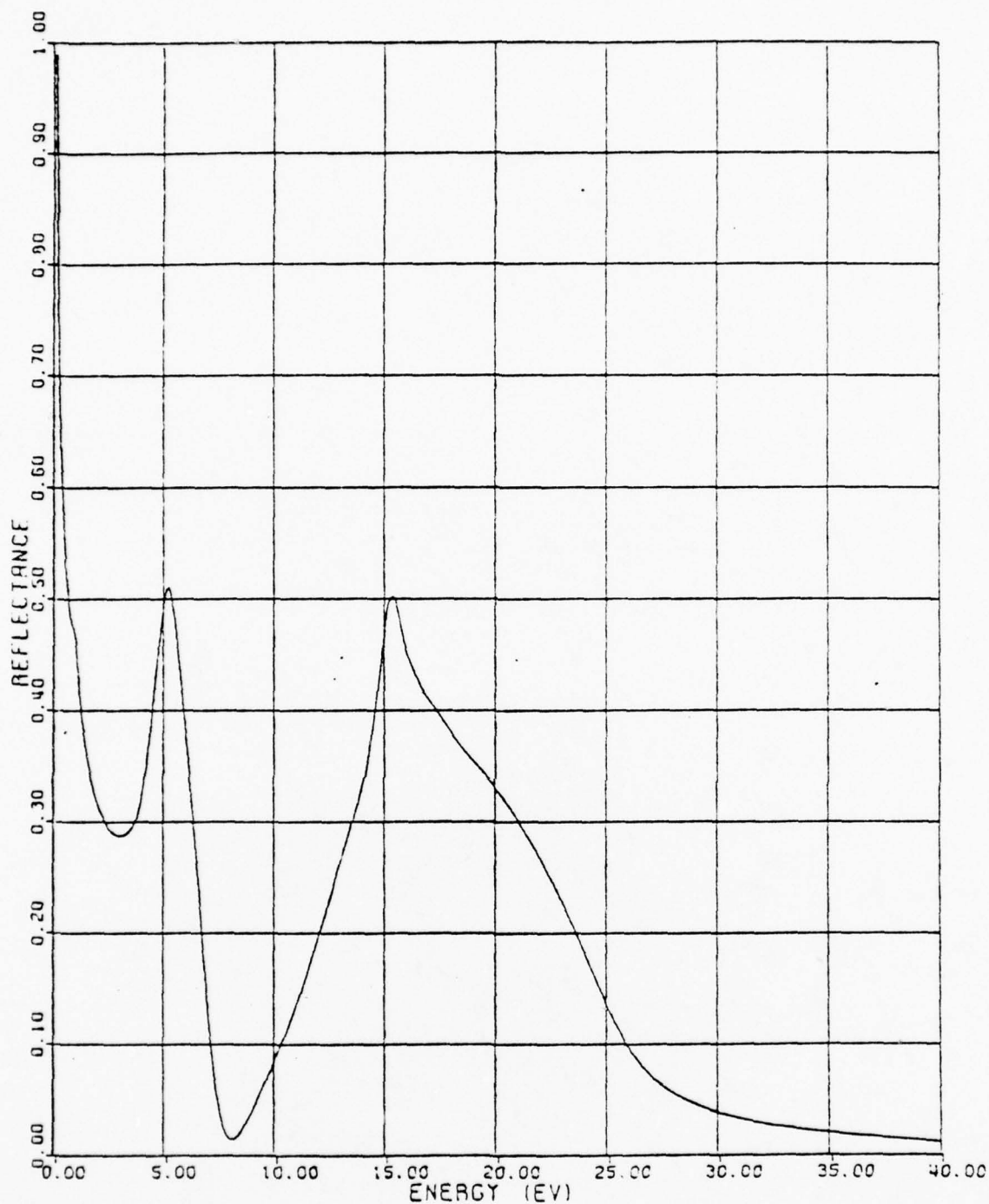


Figure 88. The normal incidence absolute reflectance of graphite ( $E_{1C}$ ) in the  $10^{-3}$ -40 eV spectral region. The reflectance spectrum was computed by use of the appropriate Fresnel equation and values of  $N(\xi) = n(\xi) + ik(\xi)$  obtained during this investigation.

3. Thin Wedge-Shaped Cell for Highly Absorbent Liquids\*

I. L. Tyler, G. Taylor, and Marvin R. Query

University of Missouri-Kansas City,

Department of Physics, Kansas City, Mo. 64110

a. Abstract

We describe the construction, physical function, and use of a wedge-shaped cell for measuring the Lambert absorption coefficient of highly absorbent liquids. Liquids are held in the cell by surface tension thus avoiding the use of seals. The cell is simple in its design and is about as convenient to use as an ordinary cuvette.

b. Introduction

The fractional spectral transmittance  $T(\nu, z)$  for electromagnetic radiation of frequency  $\nu$  passing through an absorption cell containing a volume of liquid of thickness  $z$  is

$$T(\nu, z) = t(\nu)_a^2 t(\nu)_l^2 \exp[-2d\alpha(\nu)_w - z\alpha(\nu)_l] , \quad (1)$$

where  $t(\nu)_a$  is the spectral transmittance at the air-window interfaces,  $t(\nu)_l$  is the spectral transmittance at the window-liquid interfaces,  $\alpha(\nu)_w$  and  $\alpha(\nu)_l$  are the Lambert absorption coefficients of the window material  $w$  and the liquid  $l$ , and  $d$  is the thickness of each of two similar cell windows. Two measurements of  $T(\nu, z)$  made with electromagnetic radiation of the same frequency  $\nu$  and with the same cell windows, but with different thicknesses  $z_1$  and  $z_2$  of the absorbing liquid, provide

$$\alpha(\nu)_l = \ln[T(\nu, z)/T(\nu, z_2)]/(z_2 - z_1) \quad (2)$$

In spectral regions where liquids are highly absorbent measurements of  $\alpha(\nu)_l$  require differences in thicknesses in the range  $0 < (z_2 - z_1) \leq 200 \mu\text{m}$ .

Robertson and Williams<sup>1/</sup> previously described the use of a unique absorption cell wherein liquid water was contained in a small wedge shaped volume between two optically flat infrared transmitting windows of  $\text{CaF}_2$  or KRS-5. Neoprene strips were used to seal the edges of the cell. The wedge varied uniformly

from zero thickness at its vertex to 20- $\mu$ m thickness at its base, which was determined by use of interferometric techniques. The cell was then oriented with the window surfaces perpendicular to the optic axis of a spectrophotometer system. As the cell was translated in a direction perpendicular to the optic axis the wedge-shaped volume presented uniformly increasing thicknesses  $z$  of water to a convergent beam of infrared radiant flux. In this manner Robertson and Williams used Eq. (2) to determine  $\alpha(\nu)_\lambda$  for water throughout a broad region of the infrared spectrum.

The cell described by Robertson and Williams was, at inception, novel in its application and it served their purposes well. There are at least three things, however, that limit its versatility for general use with liquids other than water. First, the cell was assembled and then sealed as a fixed unit with a relatively small vertex angle, thus requiring a Beckman variable-pathlength cell<sup>2/</sup> for use with liquids possessing a Lambert absorption coefficient less than about 50  $\text{cm}^{-1}$ . Second, the presence of the neoprene seals would make it difficult to flush the cell when changing samples, and the seals would also be a potential source of contaminants. The seals, however, would prevent evaporation of the liquid sample. And third, during use the cell was oriented so that possible interference fringes would be parallel to the entrance slit of the spectrophotometer.

This orientation required a careful evaluation of the effect of interference fringes during measurements on liquids for which the Lambert absorption coefficient was relatively low and for which the index of refraction was significantly different from that of the cell windows. The cell we have designed, constructed, and used avoids the foregoing shortcomings by use of means described in the following sections.

#### c. Description of the Cell

An exploded view of our wedge shaped absorption cell and cell holder is shown in Fig. 89. The dimensions provided in the following description are dictated by the dimensions of the cell windows; thus minor alterations may be required if one chooses windows with different dimensions. The cell comprises:

a square stainless steel base 1 measuring  $7.6 \times 7.6 \times 0.95$  cm

with a rectangular hole measuring  $5.4 \times 2.7 \times 0.95$  cm centered therethrough as shown in Fig. 89;

two  $2.2 \times 2.2$  cm riser mounts 2' and 2'' attached to base 1 by use of machine screws as shown in Fig. 89;

toggle clamps<sup>3/</sup> 3' and 3'' mounted on 2' and 2'', respectively;

spring plungers<sup>4/</sup> 4' and 4'' mounted in the heads of 3' and 3'', respectively;

two rectangular stainless steel blocks 5' and 5'' measuring

$2.5 \times 1.3 \times 0.95$  cm with two threaded holes through their sides for receiving set screws 6' and 7', and 6'' and 7'', respectively, and with 5' and 5'' mounted on base 1 as shown in Fig. 89;

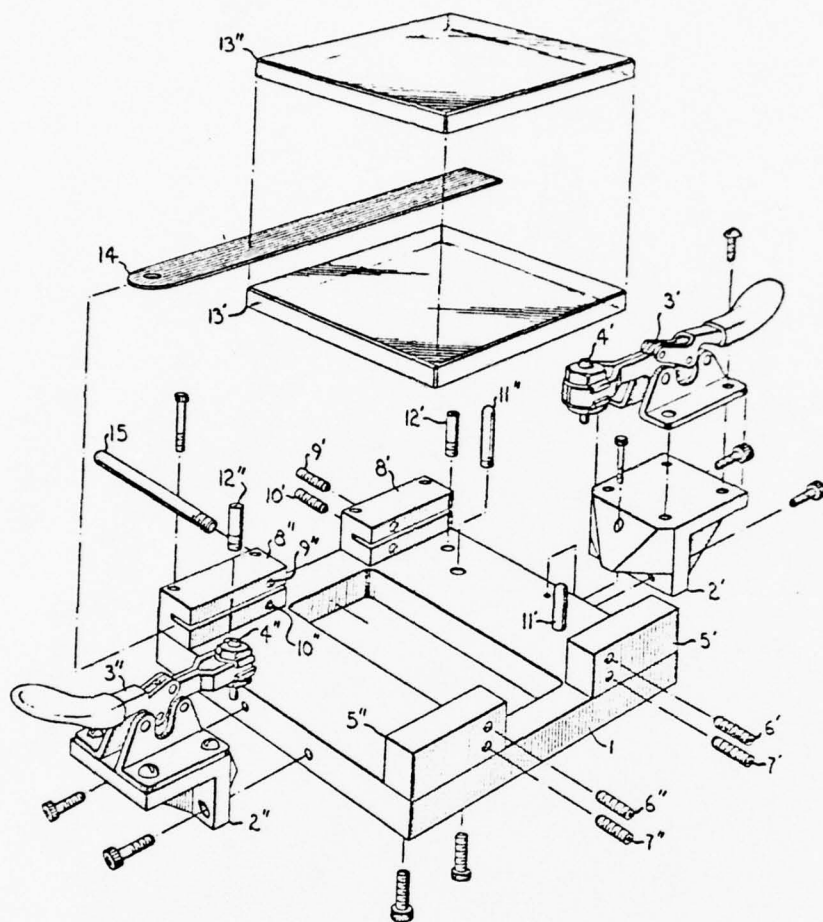


Figure 89. An exploded drawing of components comprising a thin, wedge-shaped cell for measuring the Lambert absorption coefficient of highly absorbent liquids. The windows determine the cell dimensions.

two rectangular stainless steel blocks 8' and 8'' measuring  $2.5 \times 1.3 \times 0.95$  cm, with two threaded holes in each for receiving threaded ball plungers<sup>3/</sup> 9' and 10', and 9'' and 10'', respectively, with a slot 0.8 cm deep and 0.16 cm wide in each block, and with 8' and 8'' mounted on base 1 as shown in Fig. 89;

two stainless steel posts 11' and 11'' each 0.32 cm in diameter and 1.6 cm long mounted 2.5 cm and 2.2 cm from edges of base 1 as shown in Fig. 89;

two posts 12' and 12'' each 0.32 cm in diameter and 0.95 cm long, and mounted 0.6 cm and 1.9 cm from edges of base 1 near blocks 8' and 8'', respectively;

two square optically flat windows<sup>5/</sup> 13' and 13'' measuring  $5.09 \times 5.08 \times 0.64$  cm;

a segment of machine shop feeler stock<sup>6/</sup> 14 measuring about  $9.5 \times 1.3$  cm and of a thickness suitable to the needs of the investigator; and

a handle 15 centered and mounted on a side surface of base 1 which provides a means for holding the cell for translation.

The cell is assembled empty as follows. The bottom surface of window 13' rests flat against the top surface of base 1 so that 13' is squarely centered on and covering the rectangular hole in base 1. The rounded ends of set screws 7' and 7''

contact one edge of window 13'. The ball ends of ball plungers 10' and 10'' contact the opposite edge of 13' thus acting as a resilient means for holding 13' in place. Window 13' easily snaps in place when a slight force is applied near the edge that contacts 10' and 10''. The slots in 8' and 8'' receive the segment of feeler stock 14 as indicated in Fig 89. A portion of the lower surface of 14 rests flat against the top surface of window 13' as indicated in Fig. 89. Posts 12' and 12'' retain 14 in slots 8' and 8''. The second window 13'' is then gently pressed in position so that one bottom edge of 13'' contacts the top surface of window 13' thus forming the vertex of a wedge-shaped volume between 13' and 13''. The opposite edge of window 13'' rests flat against the upper surface of feeler stock 14 thus forming the base of the wedge-shaped volume between 13' and 13''. Rounded ends of set screws 6' and 6'' contact one edge of window 13''. The ball ends of ball plungers 9' and 9'' contact the opposite edge of 13'' thus providing a resilient means for holding 13'' in place. Set screws 6' and 6'' are advanced slightly more than screws 7' and 7'' so that the edge of window 13'' rests on the flat upper surface of window 13'. One side of windows 13' and 13'' are each in contact with posts 11' and 11''. Toggle clamps 3' and 3'' are then closed so that spring plungers 4' and 4'' gently but resiliently contact points on the top surface of window 13''; this secures contact between 1 and 13', 13' and 14, 13'' and 14, and 13' and 13''.

After assembly, the vertex angle of the wedge-shaped volume between windows 13' and 13'' was measured by use of a He-Ne laser interferometer. We determined by repeatedly assembling and disassembling the cell that the vertex angle of the wedge shaped volume was reproducible to better than  $\pm 0.3$  per cent if windows 13' and 13'' were not rotated or interchanged.

A liquid is placed in the cell during assembly in the following manner. A few droplets of liquid are deposited on the upper surface of window 13' near the edge that forms the vertex of the wedge-shaped volume between 13' and 13''. Window 13'' is then gently pressed in position thus deforming the liquid so it fills the wedge-shaped volume between 13' and 13''. Toggle clamps 3' and 3'' are then closed. Most feeler stock is made of ordinary steel so care must be exercised to avoid overfilling the cell when corrosive liquids are used.

During use, we place the cell just in front of the entrance slit of a Perkin -Elmer El Ebert monochromator so that the vertex is uppermost and so that window 13' is perpendicular to a beam of convergent radiant flux that passes through the rectangular hole in base 1. The limiting aperture of the optical system is formed horizontally by the entrance slit of the monochromator, which is continuously adjustable from 10 to  $10^4$   $\mu\text{m}$ , and is formed vertically by a 0.64 cm wide slit milled in a plate placed between the cell and the entrance slit. Thus, possible interference fringes

from the wedge-shaped volume between windows 13' and 13'' are perpendicular to the entrance slit. The cell is translated vertically by use of an xy-translating stage. Interference effects are thereby avoided when the entrance slit is narrowed for investigations requiring greater spectral resolution.

d. Calculation of Maximum Cell Thickness

Fig. 90 is two cross-sectional drawings wherein the windows, feeler stock of thickness  $D$ , and liquid sample are shown in the vertical orientation in which the cell is used for measurements of  $\alpha(v)_\ell$ . The liquid is retained in the cell by surface tension  $\gamma_{w\ell}$  of the liquid in contact with the cell windows,  $\gamma_{\ell v}$  of the liquid in contact with its vapor, and  $\gamma_{wv}$  of the vapor in contact with the cell windows. Fig. 90a shows the liquid completely filling the vertex region as it does when retained in the cell. Fig. 90b shows a virtual downward displacement  $x$  of the top surface of the liquid from the vertex. The corresponding virtual change in surface potential energy  $\Delta\epsilon$ , per unit length of liquid in a direction perpendicular to the plane of Fig. 90, and to first order in  $x$ , is

$$\Delta\epsilon = [D\gamma_{\ell v}/L + 2(\gamma_{wv} - \gamma_{w\ell})]x, \quad (3)$$

where  $x$  and  $L$  are shown in Fig. 2.  $\Delta\epsilon$  is positive for liquids that wet the windows because  $(\gamma_{wv} - \gamma_{w\ell}) \sim \gamma_{\ell v}$  for such liquids.

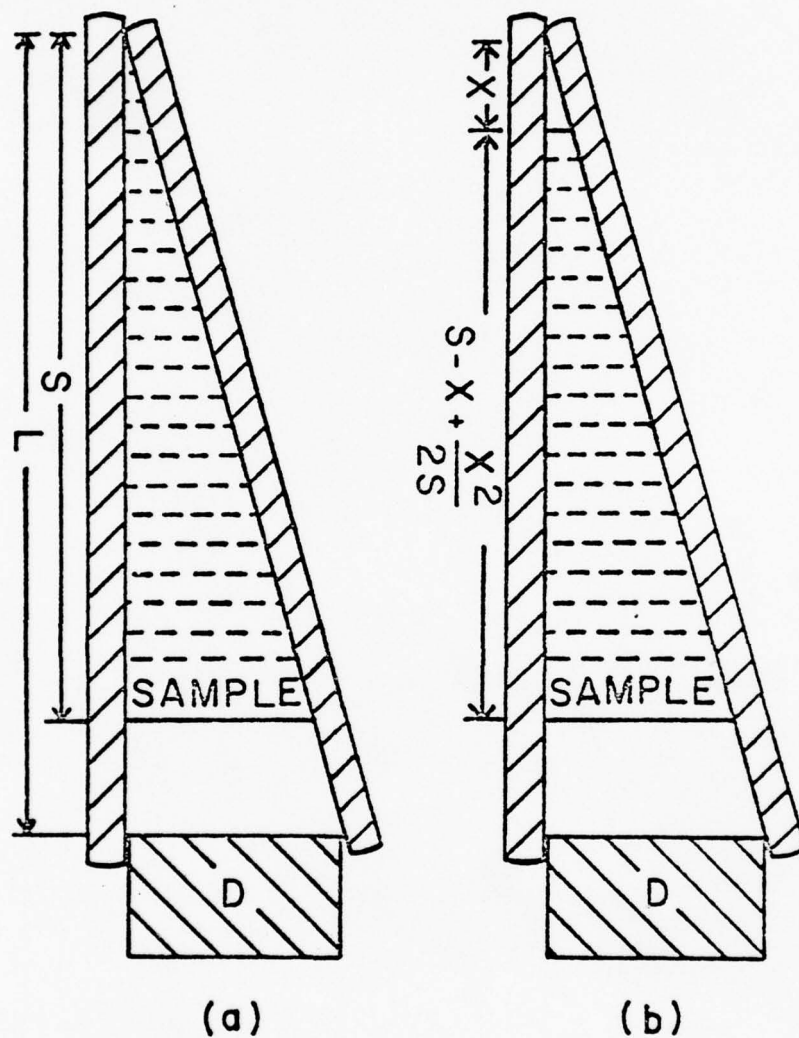


Figure 90. Cross-sectional view of the cell windows, liquid sample, and feeler-stock spacer shown in the vertical orientation in which the cell is used. In (a) the sample fills the vertex region between the windows. In (b) the sample is virtually displaced a distance  $x$  from the vertex.

Furthermore, in the right-hand side of Eq. (3) the first term is orders of magnitude less than the second term. The upward force on the liquid due to surface tension is provided by the negative derivative of  $\Delta\epsilon$  with respect to  $x$ . The weight  $W$  of the liquid, per unit length is

$$W = DS^2\rho g/2L, \quad (4)$$

where  $S$  is shown in Fig. 2A,  $\rho$  is the volume density, and  $g$  is the acceleration due to gravity. The maximum value of  $D$  occurs when the upward force due to surface tension is equal in magnitude to the downward force  $W$ . Thus we find, letting  $S$  equal to  $L$

$$D_{\text{MAX}} \equiv 4\gamma_{lv}/L\rho g. \quad (5)$$

Maximum values of  $D$  calculated by use of Eq. (5) for some common liquids retained in a cell with glass windows for which  $L = 5$  cm are presented in Table XIX. However, our experience is that liquids are retained in the cell even when values of  $D$  are about 30% larger than those calculated by use of Eq. (5). This is probably due to surface tension effects at the vertex where the two windows are in contact, as well as to our ignoring the first term in Eq. (3).

#### e. Some Experimental Results

Table XX presents values of  $\alpha(v)_2$  that we measured for 20, 30, and 40 per cent aqueous solutions of zinc chloride and for 50, 65, 75, and 85 per cent phosphoric acid at

TABLE XIX

Calculated upper bounds for the cell thickness  $D$  for some common solvents. Values were obtained using Eq. (5) with  $L = 5$  cm.

Solvent	$D[\mu\text{m}]$
Acetone	240
Benzene	270
Carbon Tetrachloride	140
Ethyl Alcohol	230
Water	590

TABLE XX

Lambert absorption coefficients  $\alpha(\nu)_\ell$  and values for  $k(\nu)_\ell = \alpha(\nu)_\ell / 4\pi\nu$  at  $\nu = 4444.4 \text{ cm}^{-1}$  for aqueous solutions of  $\text{ZnCl}_2$  and for phosphoric acid.

Sample	$\alpha(\nu)_\ell$	$k(\nu)_\ell$
20% $\text{ZnCl}_2$	$22.06 \pm 0.08 \text{ cm}^{-1}$	$(3.950 \pm 0.014) \times 10^{-4}$
30% $\text{ZnCl}_2$	$21.73 \pm 0.07$	$(3.891 \pm 0.012)$
40% $\text{ZnCl}_2$	$21.64 \pm 0.08$	$(3.874 \pm 0.015)$
50% $\text{H}_3\text{PO}_4$	$75.29 \pm 1.56$	$(13.48 \pm 0.28)$
65% $\text{H}_3\text{PO}_4$	$93.99 \pm 0.39$	$(16.83 \pm 0.07)$
75% $\text{H}_3\text{PO}_4$	$108.40 \pm 0.22$	$(19.41 \pm 0.04)$
85% $\text{H}_3\text{PO}_4$	$117.28 \pm 0.34$	$(21.00 \pm 0.06)$

$\nu = 4444.4 \text{ cm}^{-1}$ . Values of  $k(\nu)_\ell = 4\pi\nu\alpha(\nu)_\ell$ , the imaginary part of the complex refractive index  $\hat{N}(\nu) = n(\nu) + ik(\nu)$ , are also presented in Table XX. We use values of  $k(\nu)_\ell$  at  $\nu = 4444.4 \text{ cm}^{-1}$  in a double subtractive Kramers-Kronig analysis of reflectance spectra to determine  $\hat{N}(\nu)$  for the zinc chloride solutions<sup>7/</sup> and for the phosphoric acids<sup>8/</sup> throughout the spectral region  $270 \leq \nu \leq 5000 \text{ cm}^{-1}$ .

#### f. Conclusion

We constructed and tested a wedge shape absorption cell which is extremely versatile. By use of the cell one can easily and accurately measure the Lambert absorption coefficient of highly absorbent liquids. The provision of a variable apex angle permits cell parameters to be optimized for any given sample. The cell can be used to measure absorption in any spectral region because several different sets of windows are freely interchangeable. And, the cell is relatively inexpensive to construct and maintain.

g. References for Section V.D.3.

\*

Supported in part by the U.S. Army Research Office.

1. C. W. Robertson and D. Williams, J. Opt. Soc. Am. 61, 1316 (1971).
2. K. F. Palmer and D. Williams, J. Opt. Soc. Am. 64, 1107 (1974).
3. Manufactured by De-Sta-Co. Division, Dover Corp., Detroit, Mich. 48203.
4. Manufactured by Vlier Engineering Corp., Burbank, Calif. 91505.
5. No. A-45-302-0, Oriel Corp., Stanford, Conn. 06902.
6. No. 667, L. S. Starrett Co., Athol, Mass. 01331.
7. I. L. Tyler and M. R. Querry, Bull. Am. Phys. Soc. 22, 641 (1977).
8. M. R. Querry, I. L. Tyler, and W. E. Holland, Bull. Am. Phys. Soc. 22, 641 (1977).

#### 4. Microprocessor controlled Interface for a Desktop Calculator

##### a. Abstract

We have designed and constructed a microprocessor-based interface/controller which significantly expands the capabilities of a programmable desktop calculator. With the aid of the unit, a calculator such as the Hewlett-Packard Model 9820 equipped with an xy-plotter and cassette tape deck (a) controls an optical spectrometer, (b) reads and stores optical data from the spectrometer, (c) transmits data to a central computer via a TSO terminal, and (d) receives data from the central computer and plots them on the xy plotter. The techniques employed are quite general and the system, as built, can be used to automate a wide variety of laboratory equipment. The capability of communicating with the central computer also makes the system a convenient substitute for a "CALCOMP" plotter.

b. Introduction

(1) Control of Experimental Equipment.

In the past year or so there has been a marked increase in the number of commercial instruments which perform a fixed number of specified complicated experimental operations. The heart of the control system for these units is a microcomputer (MC). Usually the only feature which makes these instruments more than their predecessors is the automation provided by the MC and associated electronics. Therefore automation of a laboratory procedure often involves replacing perfectly good laboratory equipment with expensive new equipment for the sake of a small amount of control electronics. In addition one may later find that the fixed number of control algorithms provided by the new instrument no longer are sufficient.

To avoid these problems some investigators have begun to construct MC-based control units for their existing equipment.<sup>1/</sup> The controllers are inexpensive and can be quite versatile but they may require more familiarity with microprocessor programming procedures than is reasonable for these who use the equipment only occasionally. They also are not well-adapted for performing intricate decision-making procedures sometimes required during experiments.

The ideal control unit would be one which was easy for anyone to operate and yet retained the versatility of a user-programmable MC. The newest generation of desktop, programmable calculators approaches this ideal but only at a very high cost (\$12,000-\$15,000).

Table XXI

List of abbreviations used in the text

Abbreviation	Full Description
AC	CPU accumulator register
CC	Central computer
CI	Communications Interface
CPU	MC central processing unit
ECI	Experimental Control Interface
FP1	Front Panel of CI
FP2	Front Panel of ECI
HP 9820	Hewlett-Packard Model 9820 calculator
$\overline{\text{LD}}$	Load-in-memory strobe pulse from CPU
MC	Microcomputer
PAD	Peripheral Address Decoder
ROM	CC read-only memory
RWM	CC read-write memory
SDS	Serial Data Switcher
SM	Stepper motor
SMD	Serial Mode Decoder
$\overline{\text{ST}}$	Store-in-memory strobe pulse from CPU
SR	ECI shift registers
UART	Universal asynchronous receiver-transmitter

We have chosen an alternative, less expensive, approach. An MC is utilized as an interface between experimental equipment and one of the previous generation of desktop calculators -- a Hewlett-Packard Model 9820 (HP 9820). In this approach the MC is programmed to interpret and to carry out a specified set of commands entered on the calculator. The entered commands are in simplified mnemonic form thus permitting anyone familiar with the calculator to automate experimental procedures once the MC has been programmed. Furthermore, the calculator can be programmed in the usual way to determine, for example, the sequence of scan increment sizes to scan a spectrometer linearly in wavelength or in wavenumber. Because the desktop calculator retains its normal operating capabilities, it can also carry out complicated mathematical calculations on experimental data during an experimental run. These calculations can then be used to modify the experimental procedure automatically during the run. For example, it is possible for an operator, familiar only with the standard calculator programming procedures, to program a routine which automatically locates absorption peaks, rescans through these peaks with enhanced resolution, and finally calculates relative peak heights, widths, and areas.

## (2) Communication with a Central Computer

An additional advantage of the interface we have constructed is that it can be used to connect the programmable calculator to a central computer (CC) via a modem and telephone circuit. This not only permits the rapid transmission of experimental data stored on cassette tapes but also permits the CC to send the results of calculations back to the calculator. There are, of course, many instances

when a medium-resolution plot of computer calculations is much preferable to the standard computer printout. The delays and other aggravations involved in obtaining a "CALCOMP" plot of CC calculations are well known. Our interface permits us to plot CC output directly on the plotter accessory of the calculator. The time required to obtain a plot of 400 datum points with a resolution of better than 0.25% is thirty seconds -- a significant improvement over the usual "CALCOMP" turnaround time.

### c. system design

An interconnection diagram of the various units comprising the complete system is shown in Fig. 91. The additions described in this article are those enclosed within the dotted lines. The Communication Interface (CI) contains the microprocessor chip<sup>2/</sup>, 1/2 K of read-only memory, and 3 K of read-write memory as well as the decoders, associated electronics, and switches referred to in the next subsection. The Experiment Control Interface (ECI) is under direct control of the CI. It facilitates operation of the spectrometer and data acquisition system but can be omitted at the expense of additional software. The system was expressly constructed for use with the HP 9820 but could be modified for use with any ASCII-coded programmable calculator equipped with parallel data input/output capability.

In the following subsections we describe first the principles utilized in communicating between the various units in the system and secondly the function of the two interfaces.

#### (1) Principles of Operation

For the purposes of this discussion the MC can be represented as a box with three sets of lines emanating from it -- sixteen address lines, two control lines, and eight data lines. As indicated in Fig. 92, the MC itself consists of three sections. The first is the central processing unit (CPU) which contains an accumulator (AC) and several general purpose registers each capable of holding one 8-bit binary data byte. The second is a random access or read-write memory (RWM) which contains a large number of 8-bit memory cells each labeled with a 16-bit binary address. The third is a read-only memory (ROM) which

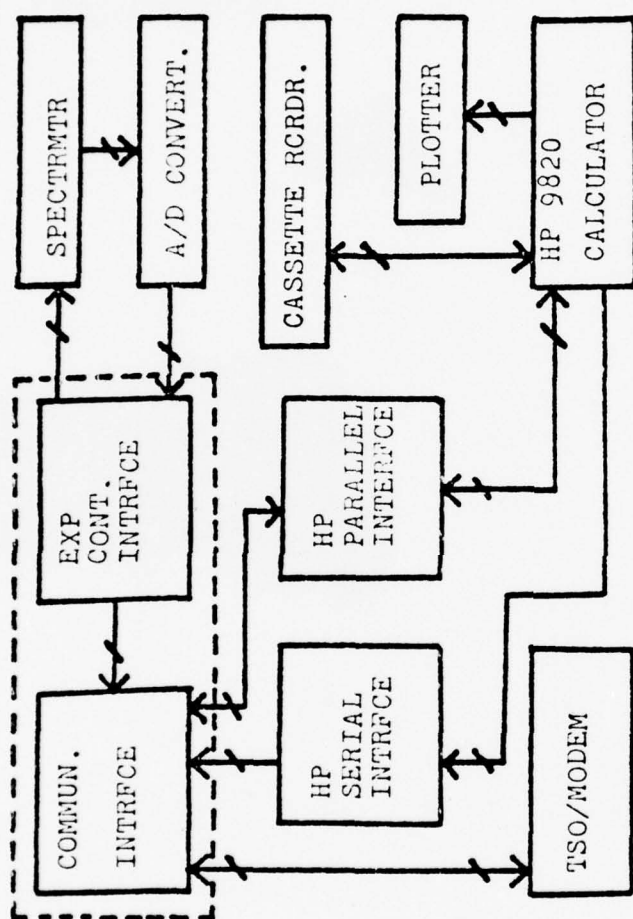


Figure 91. The interconnection diagram for the calculator/microprocessor interface system.

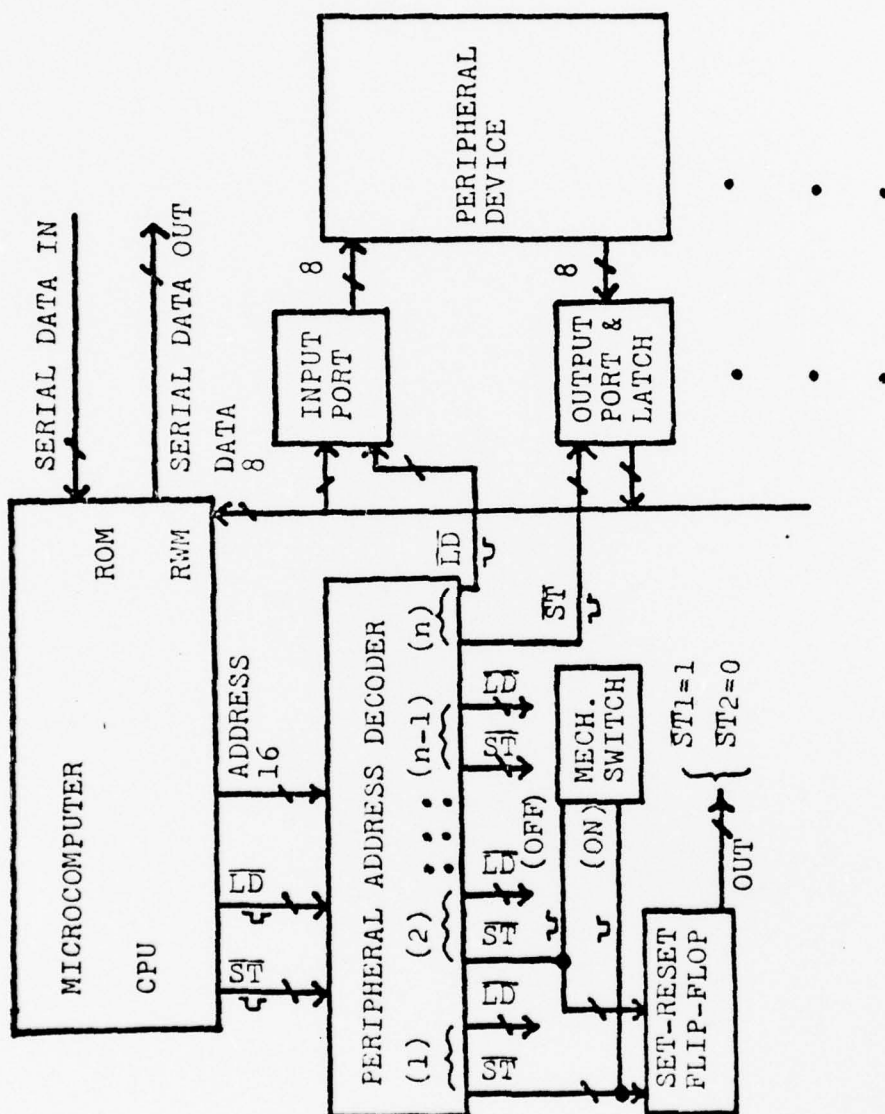


Figure 92. A block diagram indicating the electronic principles employed to control peripheral devices.

contains permanent data used to program the microcomputer. The CPU is connected internally to the ROM and RWM by the address and data lines discussed above.

During the execution of a program the CPU transfers data from the RWM into its registers, performs logical and arithmetic operations on these data, and restores the modified data to the original or some other address in the RWM. The procedure for programming the MC to perform desired operations is not important here.<sup>3/</sup> What is important is to note how the CPU communicates with the RWM and how this communication procedure can be utilized to enable the CPU to communicate with peripheral devices.

In sending data from the AC to one of the addressed memory cells in the RWM the CPU first enters the address of that cell on the 16 address lines which internally connect the CPU and RWM. Then it puts the data in the AC onto the data lines. Following this the CPU strobes the  $\overline{ST}$  (store) control line low for one microsecond. This strobing of the control line effects the transfer of the data on the 8-data lines into the specified RWM cell. Loading data from a specified WRM register into the AC register is accomplished as follows: The CPU sends an address via the address lines to the RWM and then strobes the load control line ( $\overline{LD}$ ) low for one microsecond. When  $\overline{LD}$  is low the WRM puts the data in the addressed cell onto the data lines. When  $\overline{LD}$  goes high the CPU loads these data into the AC.

Because the address, strobe, and data lines are externally accessible it is possible to substitute external devices -- peripherals -- for some of the memory cells. Usually the substitution is for cells with addresses 1000000000000000 to 1111111111111111. Each peripheral can

have as many as eight input/output leads for each address register it replaces. This procedure is called memory-mapped I/O (input/output).

Peripherals are interfaced to the microcomputer by the method shown in Fig. 92. First input and output ports (buffers) controlled by the  $\overline{LD}$  and  $\overline{ST}$  pulses from the CPU are interposed between the microcomputer parallel data lines and the peripheral device. These prevent the peripherals from interfering with data appearing on these lines during normal operation of the MC. Secondly, a peripheral address decoder (PAD) consisting of standard decoder chips is connected to the strobe and address lines coming from the MC. The PAD routes the  $\overline{LD}$  and  $\overline{ST}$  pulses to an appropriate pair of outputs corresponding to the memory address placed by the CPU on the address lines at the time the pulse appears. The control pulse is then directed to an input port ( $\overline{ST}$ ) or output port ( $\overline{LD}$ ) of the peripheral with the same address, thereby activating the port and effecting transfer of data between the peripheral and the MC data lines.

As an example of how this interfacing can be used we consider the operation of a stepper motor (SM). A typical SM has four windings, a, b, c, and d, each of which is energized and de-energized in a prescribed sequence to advance the rotor. Letting a logic 1 (+5v) represent an energized winding and logic 0 (0V) represent a de-energized winding, clockwise shaft rotation can be achieved by cyclic repetition of the four patterns 0101, 0110, 1010, and 1001. In these four binary numbers the least significant bit represents winding a and so forth. The SM windings can then be wired, through power amplifiers, to four of the eight output data lines from an addressed output port and latch. Operation of the SM then simply requires programming the MC to send the data prescribed above, at a rate proportional to the

desired SM speed, to the address of the output port.

In practice most peripheral devices require more than one address for operation. For example data communication between the MC and the CC is effected through a universal asynchronous receiver-transmitter (UART) chip. The chip receives data from CC in series form at a rate of  $300 \text{ bits sec}^{-1}$ . Only after a full 8-bits of data have been received can the UART transmit these data in parallel via the data lines to the MC. It is therefore necessary for the MC to wait until it receives an indication from the UART that the data are ready before it executes a  $\overline{\text{LD}}$  command to the UART data address. For this reason the UART is equipped with status lines. These lines are connected to an output port with another address. During the execution of a subroutine to receive data from the CC the MC is programmed to load and analyze the data from the UART status address repeatedly until these data indicate that real data are available at the UART data output port.

Similarly the HP 9820 parallel interface communicates with the MC via two addresses, the second serving for status communication.

A simple way to control a wide variety of devices is shown connected to outputs (1) and (2) of the PAD in Fig. 91. This is an on-off switch consisting of a set-reset flip-flop which is driven to logic 1 (ON) by a  $\overline{\text{ST}}$  command from the MC to its "ON" address and to a logic 0 (OFF) by a  $\overline{\text{ST}}$  command to its "OFF" address. The advantage of this device is that it is a simple matter to include a mechanical switch circuit in a manner such that the last action taken -- mechanical- or MC derived -- determines the state of the output. Such an arrangement is very convenient in the operation of electromagnetic clutches, etc. If AC power must be controlled the set-reset flip-flop can be used to drive a solid state relay.

## (2) Circuit Description

In this section we describe the circuitry using only block diagrams. Detailed circuit diagrams are available from the authors on request.

### (a) Communications Interface

A block diagram of the MC CI is shown in Fig. 93. Input lines terminating in bubbles represent control strobe lines which originate in the PAD (upper left) and are used to activate input and output ports. Broad open lines represent parallel data lines. All such lines are buffered by input or output ports before connecting with the MC bidirectional parallel data lines whether shown explicitly or not. Broad dark lines represent buffered device status lines.

The HP 9820 is connected to the system through both parallel and serial interfaces. The serial interface is used only to transmit data from the calculator to the central computer. As discussed earlier, data from the CC is transmitted serially at  $300 \text{ bits sec}^{-1}$ . The HP 9820 cannot receive serial data faster than  $260 \text{ bits sec}^{-1}$  hence the UART chip is used as an intermediary. Serial data are received by the UART. Once a full 8-bit byte has been received it is transmitted in parallel form to the HP 9820.

The Serial Data Switcher (SDS) is worth considering in greater detail. Commercial computer devices often interface with RS-232 logic (1 = -10v, 0 = +10v). For completely automated operation it necessary that the MC be capable of mediating communication not only between TTL peripherals (1 = +5v, 0 = 0v) but also between TTL and RS-232 peripherals. This is accomplished by converting all RS-232 input signals to TTL by means of RS-232 line receiver chips. All internal switching is then effected by the microcomputer in TTL via the Serial Mode Decoder (SMD). The SMD converts

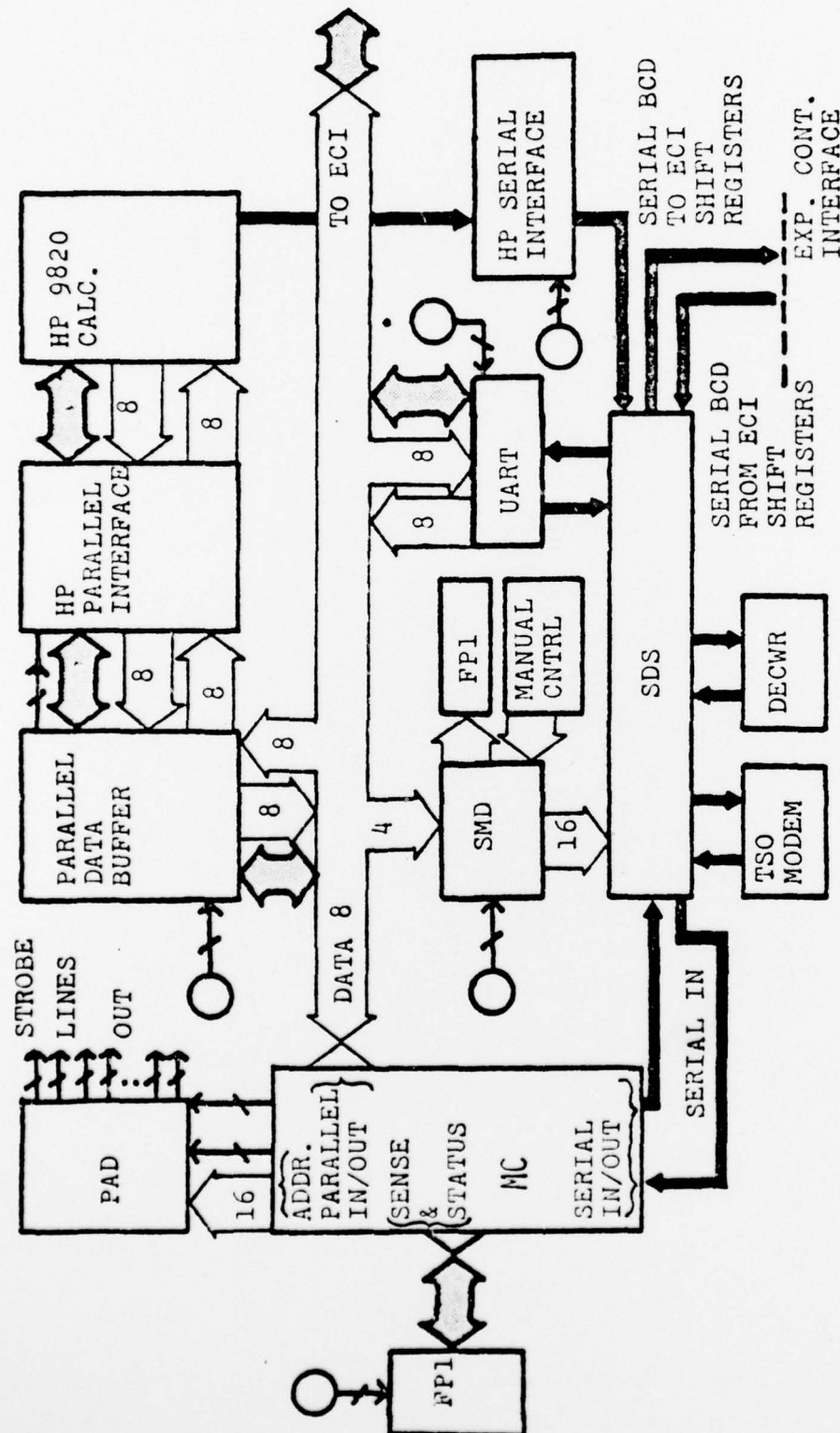


Figure 93. A block diagram of the Communications Interface.

the four least significant bits on the data line into their BCD equivalent when the SMD address is strobed. The TTL portion of the SDS consists of a number of logic gates. These gates are controlled by the SMD BCD output. Each BCD digit thus selects one of 16 possible gate configurations each determining a particular routing of serial data from peripherals through the SDS and out to other peripherals. Finally those data routed out to RS-232 peripherals are converted back to RS-232 by means of RS-232 line drivers before leaving the SDS.

This approach provides a general method for doing any degree of complex MC-controlled switching using low-cost TTL components. Switching between RS-232 devices is normally cumbersome and expensive requiring reed relays or manual switches. A well-shielded junction box, however, is not subject to noise levels requiring  $\pm 10V$  logic. Thus by converting to TTL for switching one can reduce costs by an order-of-magnitude without sacrificing reliability.

#### (b) Experimental Control Interface

A block diagram of the Experiment Control Interface (ECI) is shown in Fig. 94. The same conventions are used in this diagram as were used in Fig. 93. Thus, each block in the diagram to which bubbles are attached represents a memory mapped I/O device, and so forth.

The ECI is under direct control of the MC. The MC, in turn, is under the control of the HP 9820 calculator. The MC is programmed to check repetitively for ASCII-coded parallel input (commands) from the HP 9820. Once the command is received the MC analyzes the command characters and then jumps to that particular subroutine stored in the RWM required to execute the command. Execution involves sending, in the proper sequence, one or more  $\overline{ST}$  commands to memory addresses of

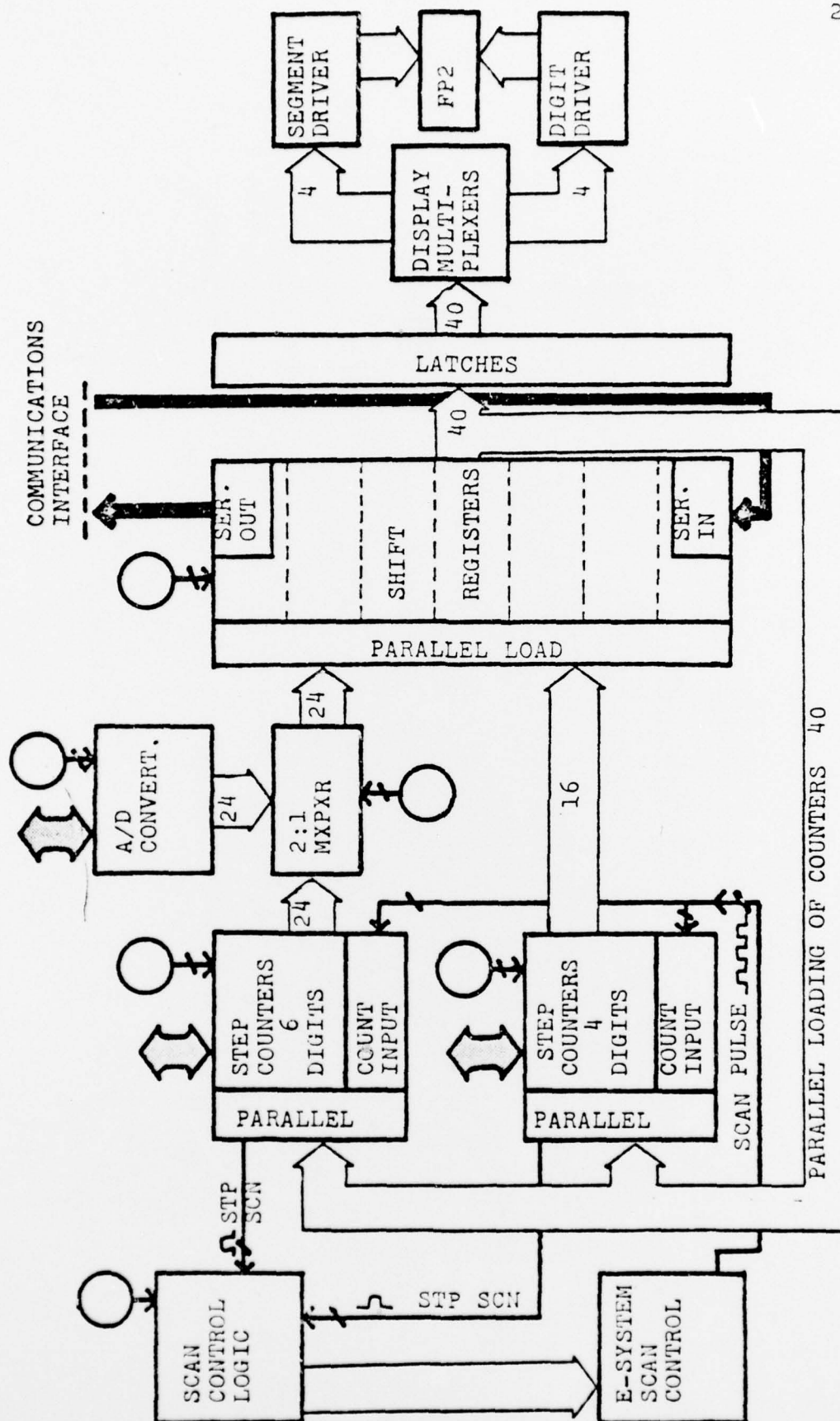


Figure 94. A block diagram of the Experimental-Control Interface.

peripherals in the ECI. Once the subroutine is executed the MC again begins a repetitive check for new commands from the HP 9820. This provides interlocked operation between the MC program and the HP 9820 program.

The ECI is currently being used to control a Perkin-Elmer El monochromator and a data acquisition system. The monochromator grating is scanned by an SM drive. The processed signal from the monochromator detector is digitized by a PAR Model 260 A/D converter under control of memory mapped I/O signals.

As was stated in the introduction, the versatility of the MC-HP 9820 combination allows anyone familiar with the HP 9820 programming procedures to automate extremely complicated scan routines. This is accomplished by utilizing the HP 9820 to perform complex calculations and, on the basis of these calculations, to determine a desired wavelength and wave-number region to be scanned as well as the number of scans and spacing of data points. The MC then need only be programmed to execute a very small number of commands such as "scan up n steps" or "read the A/D converter". Each such command is written in mnemonic form and the operator is supplied with this short list of "calculator keyboard operations" in addition to the calculator's usual keyboard functions.

In what follows we describe the operation of the ECI by listing the HP 9820 mnemonic commands, following each with a short command description and finally listing the sequential operations carried out by the system to effect the command.

SUxxxx:<sup>4/</sup> Scan up xxxx steps where xxxx ranges from 0000 to 9999.

- a) The number xxxx is series-loaded from the MC into the ECI shift registers (SR).

- b) This number is parallel-loaded into the ECI latches for front panel display and into the ECI  $\Delta$  Step Counter.
- c) The MC activates the SM scan via the ECI Scan Control Logic. The pulses running the SM are also directed to the  $\Delta$  Step Counter and to the Step Counter. Each pulse decrements the number in the  $\Delta$  Step Counter by one digit. When this number reaches zero a pulse is generated within the  $\Delta$  Step Counter. This pulse is directed to the Scan Control Logic where it serves to stop the scan. The MC monitors the Scan Control Logic unit to determine when the Scan has stopped.<sup>5/</sup>
- d) Each pulse received by the Step Counter increments the number stored there by one digit. At the end of the scan the MC parallel-loads this number, via the 2:1 multiplexer and SR into the Latches for front panel display.

SD xxxx: Scan down xxxx steps.

The sequential operations are the same as SUxxxx except for obvious changes.

RA: Read the A/D converter.

- a) The MC commands the A/D converter to digitize the signal voltage appearing at its input.
- b) These digitized data are parallel-loaded via the 2:1 multiplexer into the SR.
- c) From the SR the data are loaded serially into the MC.
- d) The MC waits for an input (read) command from the HP 9820 after which it sends the data in parallel to the HP 9820 for analysis or storage.

RS: Read Step Counter and transmit the number to the HP 9820.

- a) The number in the Step Counter is parallel-loaded into the SR via the 2:1 Multiplexer.
- b) From the SR the number is serial-loaded into the MC.
- c) The MC then waits for an input (read) command from the HP 9820 after which it sends the number in parallel to the HP 9820.

P xxxx: Pause for xxx.x seconds where xxx.x ranges from 000.1-999.9.

The MC is equipped by the manufacturer with a pause command in the ROM. The subroutine for this command simply translates the P xxx.x into the equivalent assembler command.

The following commands are effected by a single ST command to the appropriate peripheral addresses

CS Clear Step Counter and Step Counter Display.

CD Clear  $\Delta$  Step Counter and  $\Delta$  Step Counter Display.

A Turn on External Alarm to alert operator.

CA Turn off External Alarm.

#### (c) Operational Problems

We conclude this section with a discussion of some unexpected problems which were encountered in the operation of this interface system and of how these problems were overcome.

- (1) Echo during direct derial communication between the HP 9820 and the CC.

The HP 9820 Serial Interface cannot be used without the SDS to receive signals directly from the CC. This is because all received signals are echoed back out to the CC via the HP serial output line

and interfere with the CC operation. Even though the HP 9820 is not used to receive data directly from the CC it is used to receive "handshake" signals. By routing HP 9820 serial input/output through the SDS this interference can be avoided. The SDS logic circuit simply blocks the serial output channel when it is placed in the HP 9820 serial input mode by the MC.

(ii) Interference of "handshake" operations between the HP 9820 and CC.

In the transmission of data from the HP 9820 to the CC it is necessary both for the CC to be notified when one line of data has been entered on the TSO terminal and for HP 9820 to be notified when the entered data have been received. We utilize the standard "handshake" signals between TSO and CC for this purpose. Thus when the HP 9820 has entered a full line of data on the Decwriter terminal it terminates the data with the ASCII equivalent of CNTL/D entered on the keyboard. As usual, when the CC has received these data it unlocks the TSO keyboard, returns the carriage, and advances the paper with the ASCII equivalent of CR/LF (carriage return/line feed) entered on the keyboard. The HP 9820 is programmed to look for the ASCII characters CR/LF. When these are received it begins entering another line of data on the keyboard, and so forth.

A problem arises because when the HP 9820 sends serial data it first enters them in parallel on internal shift registers. It then proceeds to execute the next programmed command while these data are being shifted out serially. Normally the next programmed command would be to receive the CR/LF signal from the CC; but this involves having the SDS block the HP serial output channel before the serial output data have left the shift registers. This problem

can be avoided by programming the HP 9820 to execute several "mark-time" operations between the send data and receive data commands.

(d) Performance

The microprocessor-based interface/controller has been in operation for over two years. It has proven to be extremely versatile and virtually trouble-free. The construction process itself was not trivial but an undergraduate with a solid background in digital electronics should be able to build a similar unit as a summer project. The cost of the components required would be about \$800.

e. References for Section V.D.4.

- a) This work supported by the UMKC Research Council and by the U. S. Army Research Office.
- b) Present address: General Electric Electronics Lab, Bldg. 3, Electronics Park, Syracuse, N.Y.
1. Charles L. Pomernacki, Rev. Sci. Instrum. 48 (11), 1420 (1977).
2. We used a SC/MP microprocessor manufactured by National Semiconductor Corp, Santa Clara, CA. Complete microprocessor-plus-memory boards are now available from a number of manufacturers.
3. See for example, W. J. Weller, Assembly Lend Programming for Small Computer, (Lexington Books, Lexington, MA., 1975).
4. In order to transmit the ASCII characters SUxxxx via the HP 9820 parallel interface the actual keyboard operations are FMT "SUxxxx"; WRT 8 where 8 is the Select-Code for the HP Parallel Interface.
5. The procedure described here is primarily "hardware controlled" and differs from the "software controlled" stepper motor scan procedure described earlier in this article. However, we found during the course of construction of this unit that software-dominated control is usually preferable in terms of total time required for construction and programming.